Physics-Based Modelling of Erosion at the Catchment Scale

Dissertation

der Mathematisch-Naturwissenschaftlichen Fakultät

der Eberhard Karls Universität Tübingen

zur Erlangung des Grades eines

Doktors der Naturwissenschaften

(Dr. rer. nat.)

vorgelegt von

Karim Norouzi Moghanjoghi

Aus Salmas, Iran

Tübingen

2016

Gedruckt mit Genehmigung der Mathematisch-Naturwissenschaftlichen Fakultät der Eberhard Karls Universität Tübingen.

Tag der mündlichen Qualifikation:	05.12.2016
Dekan:	Prof. Dr. Wolfgang Rosenstiel
1. Berichterstatter:	Prof. Todd A. Ehlers
2. Berichterstatter:	Dr. Claus Haslauer

I hereby testify that this monograph is written by me and the work of others are acknowledged by providing a reference whereever they were used.

Tübingen Karim Norouzi Moghanjoghi

Acknowledgement

I would like to thank my supervisor, Prof. Todd A. Ehlers, for being very supportive during the time I was doing this research. This research also benefited from the advice of Prof. Olaf A. Cirpka. The initial model setup was made possible with the help of Dr. Claus Haslauer by acquiring the data needed for the region of study from DWD. The HydroGeoSphere team also provided support and were very diligent in responding to the code modification requests. Diane von Gunten was very helpful with the trouble shooting of the input files to the HydroGeoSphere. I also would like to extend my gratitude to the entire IRTG members from the first and second cohort for being a great team and providing a learning and research atmosphere that helped me enrich my understanding of the scientific research.

Abstract

The study of erosion is motivated by the prediction and prevention of soil loss from agricultural lands, the rehabilitation of mining and hazardous waste sites and to improve our understanding of the Earth surface response to changing climate and anthropogenic land use. This dissertation contributes to our understanding of erosion by investigating the effects of unsaturated zone hydrologic processes, rainfall distribution, and vegetation on erosion in the catchment scale. Methods used in this study include an integrated surface and subsurface hydrological model augmented with a sediment transport model for fluvial sediment transport. The hydrology model solves the diffusive wave equation on the surface and Richards equation in the subsurface domain, with an exchange water flux term that couples the surface and subsurface. Sediment transport is calculated using water depth on the surface which couples sediment transport and hydrological processes. This coupling of sediment transport with hydrology allows investigation of the parameters that govern the hydrologic response of the catchment and their relation to erosion. The surface topography is updated at short regular intervals so that the flow fields accommodate the new topography and the system co-evolves in time. The coupling of erosion to the surface water flux allows an accurate prediction of hill-slope and river channel erosion for the scenarios investigated in this study. The coupled hydrologic and erosion models are used to evaluate three hypotheses. The effects of variations in the precipitation times series with a fixed annual precipitation on the surface erosion are investigated in the first hypothesis. Results indicate a large difference in model predicted erosion rates for variations in precipitation intensity, duration and dry intervals. More specifically, increase of mean intensity by multiple of two can increase bed shear stress by about 10%. The spatial distribution of the erosion is also shown to be dependent on the precipitation patterns. The high intensity and longer duration events produce erosion throughout the catchment. High intensity and short duration events produce large bed shear on the upstream regions where the slopes are steeper. The low intensity, longer duration and shorter dry intervals do not produce a significant amount of bed shear stress anywhere in the catchment as the precipitation mostly evaporates or infiltrates into the subsurface.

The second hypothesis investigates the effects of vegetation cover and duration of the growth season on the erosion and bed-load discharge from the catchment. Simulations with identical climate and hydrological properties were conducted with different forest vegetations that have different patterns of growth, canopy size and root depth. The forest types studied are categorized as forests containing mostly Deciduous, Coniferous and Hardwood trees. Changes in the canopy density affect the surface albedo and potential evapotranspiration. Results indicate that the ground water table elevation changes and responds differently for each vegetation type. At the growth season, the water table in the Deciduous forest is about $0.5m$ lower than Coniferous water table depth. The transpiration of the plants affect the subsurface levels and runoff generation mechanism change accordingly. It is shown that the Hardwood forests discharge about 5% less sediment than the Deciduous or Coniferous forests. The third hypothesis

investigates the effects of the climate change and anthropogenic induced reduction in the vegetation density on erosion. This hypothesis is evaluated by wild fire and logging induced reduction of canopy size. The reduction in canopy changes hydrological response of the catchment and subsequently the erosion and sediment transport are affected. Results indicate that a reduction of canopy size due to fire or logging affects the subsurface water table, runoff generation and bank storage. These hydrologic changes facilitate faster groundwater response in the subsequent rains and increase erosion rates by 12% to 15% for leaf area index changes of 50% in logging scenarios. Furthermore, results demonstrate that the affects of canopy size reduction are not homogeneous throughout the catchment. Taken together, the results from investigation of these three hypotheses show that variations in the subsurface flow field due to different climate or vegetation change scenarios are sufficiently large enough to influence both runoff generation on hill- slopes, and subsurface contributions to river discharge. The combined effects of canopy and evapotranspiration change, surface and top soil evaporation determine the amount of runoff and therefore control the erosion rates in the catchment.

Zusammenfassung

Die Untersuchung von Erosion ist motiviert durch die Vorhersage und Verhinderung von Bodenverlust auf landwirtschaftlichen Flächen, die Sanierung von Bergbau- und Altlaststandorten und um unser Verständnis der Reaktion der Erdoberfläche auf Veränderungen im Klima sowie in der anthropogenen Landnutzung zu verbessern. Diese Dissertation trägt zu unserem Verständnis der Erosion bei, indem sie die Auswirkungen der hydrologischen Prozesse in der ungesättigten Zone, der Niederschlagsverteilung und der Vegetation auf Erosion auf Einzugsgebietsskala untersucht. Die Methoden, die in dieser Studie verwendet werden, umfassen ein integriertes Grundwasser-Oberflächenwasser-Modell ergänzt um ein Sedimenttransportmodell für Flusssedimenttransport. Das hydrologische Modell löst die Diffusions-Wellengleichung auf der Oberfläche und die Richards-Gleichung im Boden, mit einem Wasseraustausch-Term, der Oberfläche und Boden koppelt. Sedimenttransport wird berechnet mit Hilfe der Wassertiefe auf der Oberfläche, die den Sedimenttransport mit den hydrologischen Prozessen koppelt. Diese Kopplung von Sedimenttransport und Hydrologie ermöglicht es, die Parameter zu untersuchen, die die hydrologische Reaktion des Einzugsgebietes bestimmen sowie deren Beziehung zur Erosion. Die Oberflächentopographie wird in kurzen regelmäßigen Abständen aktualisiert, so dass die Strömungsfelder die neue Topographie berücksichtigen und sich das System gemeinsam mit der Zeit entwickelt. Die Kopplung von Erosion und dem Wasserfluss an der Oberfläche ermöglicht eine genaue Vorhersage von Hang- und Flusserosion für die in dieser Studie untersuchten Szenarien. Die gekoppelten Hydrologie-Erosions-Modelle werden verwendet, um drei Hypothesen zu untersuchen. Die Auswirkungen von Schwankungen in den Niederschlagszeitreihen bei einer bestimmten jährlichen Niederschlagsmenge auf die Oberflächenerosion werden mit der ersten Hypothese untersucht. Die Ergebnisse zeigen einen großen Unterschied in den vorhergesagten Erosionsraten für Schwankungen in der Niederschlagsintensität, in der Niederschlagsdauer und in Trockenintervallen. Genauer gesagt kann die Erhöhung der mittleren Intensität um den Faktor zwei die Schubspannung im Flussbett um etwa 10% erhöhen. Es wird weiterhin gezeigt, dass die räumliche Verteilung der Erosion auch von Niederschlagsmustern abhängig ist. Ereignisse hoher Intensität und längerer Dauer bewirken Erosion im gesamten Einzugsgebiet. Ereignisse hoher Intensität und kurzer Dauer erzeugen große Schubspannung in den oberstromigen Bereichen, wo die Hänge steiler sind. Ereignisse von niedriger Intensität und längerer Dauer und kürzere Trockenintervalle erzeugen keine signifikante Menge an Bettschubspannung im Einzugsgebiet, weil der Niederschlag hauptsächlich verdunstet oder in den Boden infiltriert. Die zweite Hypothese untersucht die Auswirkungen der Vegetationsdecke und die Dauer der Vegetationsperiode auf die Erosion und den Sedimentaustrag aus dem Einzugsgebiet. Simulationen mit gleichen klimatischen und hydrologischen Bedingungen wurden mit verschiedenen Waldvegetationen durchgeführt, die sich im Wachstum, im Baumkronendach und in der Wurzeltiefe unterscheiden. Die untersuchten Waldarten werden klassifiziert in Wälder die hauptsächlich aus Laub-, Nadel- und Laubbäumen bestehen. Änderungen in der Dichte des Baumkronendachs beein-

flussen die Bodenalbedo und die potenzielle Evapotranspiration. Die Ergebnisse zeigen, dass die Höhe des Grundwasserspiegels variiert und unterschiedlich auf jeden Vegetationstyp reagiert. In der Wachstumsperiode ist der Grundwasserspiegel im Laubwald etwa 0,5 m tiefer als im Nadelwald. Die Transpiration der Pflanzen beeinflusst die Bodenhydrologie und der oberflächenabflussgenerierende Mechanismus ändert sich entsprechend. Es wird gezeigt, dass Laubwälder etwa 5% weniger Sediment als die Laub- oder Nadelwälder austragen. Die dritte Hypothese untersucht die Auswirkungen des Klimawandels und der anthropogen verursachten Verringerung der Vegetationsdichte auf Erosion. Diese Hypothese wird anhand von verringerter Baumkronendichte durch Buschbrände Abholzung ausgewertet. Die Reduzierung der Baumkronendichte ändert die hydrologische Reaktion des Einzugsgebietes und wirkt sich so auf Erosion und Sedimenttransport aus. Die Ergebnisse zeigen, dass sich eine Reduzierung der Baumkronendichte durch Brände oder Abholzung auf den Grundwasserspiegel, die Abflussbildung und die Uferspeicherung auswirkt. Diese hydrologischen Veränderungen begünstigen eine schnellere Reaktion des Grundwassers auf spätere Regenereignisse und erhöhen so die Erosionsraten um 12% bis 15% bei einer Veränderung des Blattflächenindex um 50% in Abholzungs-Szenarien. Darüber hinaus zeigen die Ergebnisse, dass die Auswirkungen reduzierten Baumkronendachdichte nicht homogen im Einzugsgebiet verteilt sind. Insgesamt zeigen die Ergebnisse aus den Untersuchungen dieser drei Hypothesen, dass die Variationen im Grundwasserströmungsfeld aufgrund der unterschiedlichen Klima- und Vegetationsszenarien ausreichend groß sind, um sowohl die Abflussbildung an Hängen zu beeinflussen als auch den unterirdischen Beitrag zum Abfluss im Fluss. Die kombinierten Effekte von Veränderungen in der Baumkronendichte, der Evapotranspiration und der Oberflächen- und Bodenverdunstung bestimmen die Höhe des Abflusses und steuern somit die Erosionsraten im Einzugsgebiet.

Contents

List of Figures

List of Tables

Chapter 1

Introduction

Geomorphology is the study of landforms and the processes that create them [1, 2]. Landforms result from interactions between tectonic processes that produce relief and climatic forces that redistribute mass through erosion and sediment transport. Quantitative study of the landforms involve modeling of tectonic uplift, hillslope processes that are assumed to behave like diffusion and fluvial erosion [3, 4, 5, 6, 7]. The uplift incorporates tectonic plate movements. Hill-slope processes are due to the tendency of loose soil and debris to go downward on a slope because of the gravitation pull of the Earth. Fluvial processes are considered as movement of sediments or riverbed erosion by moving waters on the surface of the landscape. Fluvial erosion is a complicated process, and links geomorphology and hydrology [2, 8]. After the mathematical formulation of the landscape evolution, in recent decades, numerical solution of the mathematical equations for the evolution of landforms and a quantitative understanding of these processes were made possible. The quantitative approach is shown to be useful in understanding the interactions between the three major mentioned processes. However, the quantitative approach in geodynamics simulation frameworks are based on simplifying assumptions on the fluvial processes which are computationally intensive. The simplifications involve calculation of erosion using peak or mean flow conditions [9, 10, 11, 12, 13, 12, 14]. Some of the fluvial processes such as secondary flow in river channels which is pivotal in meandering of rivers can not be incorporated in computational models of geologic time scale due to their computational cost. In these models, water discharge throughout the river network is calculated using upstream area as a surrogate variable. The usage of upstream area implies a steady-state flow condition for every precipitation event regardless of the duration and intensity of the event. Correlation coefficients are used to relate upstream area to water and sediment discharge, or bed erosion rates using the bed shear stress. The coefficients are heuristic and reflect the behavior of the sediment movement in the river on average for geologic times. Stream power concept is also used to investigate the equilibrium condition of a river. The simplified methods are convenient computationally as the time scales involved in geodynamics simulations range from thousands to millions of years. The interactions of the climate, vegetation and landforms are of interest to geomorphologists. The dependence of landforms and vegetation to climate are evident from observations of the distribution of the plants and biota in different parts of the planet such as low vegetation density and sand dune formations in dry deserts [15]. Attempts are made to understand the level of interaction between these processes using computational models [16]. Despite the complexity and the computational limitations of numerical simulation of landscapes, there is an urgent need to understand the interdependence of various processes to date, as one of the leading geomorphologists note [8]:

> Geomorphology is currently in a period of resurgence as we seek to explain the diversity, origins and dynamics of terrain on the Earth and other planets in an era of increased environmental awareness. Yet there is a great deal we still do not know about the physics and chemistry of the processes that weaken rock and transport mass across a planet's surface.

The interest also fueled by short term applications such as limiting the land surface erosion, soil loss and desertification [17, 18, 19, 20, 21]. Many traditional approaches to understand soil loss has provided little or insignificant results [22, 23]. One of the areas where there is lack of knowledge is the role of intricate hydrological processes and their interaction with landforms and landscape evolution. A better understanding of the a complex phenomena such as desertification and soil loss can only be achieved by a multidisciplinary approach that can take into account many feedback mechanism and long term interactive components in a regional or catchment scale. The short term and long term objectives of a multi-disciplinary approach is put forward by [24]:

> Recent cross-disciplinary enthusiasm to develop improved landscape evolution models is motivated by several factors, including: the need to predict changes in erosion and sedimentation rates in response to global warming scenarios; increased concern over soil loss; and to test the hypothesis that climate and tectonic processes are coupled through erosion and sedimentation

This study is a multidisciplinary attempt to bridge the geodynamics view of the sediment transport and hydrology using an state of the art hydrological simulation framework. Advances in computational sciences and technology, especially in the availability of faster hardware, makes it appealing to make distributed hydrological models in an scale that was not possible twenty years a go. Integrated hydrological models are becoming a reality after Freeze and Harlan [25] proposed the first blue print for such models in 1969. For many decades, the only major tool that was available to hydrologists was the unit hydrograph family of methods which is basically a linear approach with a strong stationarity assumption to estimate the discharge from precipitations in a catchment. Availability of distributed and coupled models, makes it possible to have a better view of the many processes and subprocesses such as infiltration, evaporation, transpiration and ponding which control the runoff generation leading to fluvial erosion. The blueprint proposed by Freeze and Harlan [25] is materialized by many coupled hydrological simulation frameworks [26]. The trend in the current models is to simulate the movement of the water in the surface by a diffusive wave approximation [27] and the movement of the water in the unsaturated zone and saturated zone with Richards equation and Darcy flow [28, 29] and couple these two flow fields with an exchange flux term [30]. These models are based on partial differential equations with mostly field measurable and physically meaningful parameters to minimize conceptual errors. The simplified two dimensional surface flow field used in the these models is shown to be a good approximation of the St. Venant equations [27]. This can act as computationally efficient solution in place of the costly Navier Stocks or the depth averaged St. Venant flow equations. The approach is more accurate compared with the methods used in the geodynamics simulation frameworks, but still limited due to its computational cost. However, the coupling of the integrated surface and subsurface hydrological model with a sediment transport equation can be helpful in gaining an accurate picture of the movement of the water on surface and subsurface and the erosion and transport of the sediment by water. In this study, the surface water depth and energy gradient is used to compute a distributed bed shear stress. The bed shear is then used to compute a sediment flux. The sediment flux therefore is affected by the topography and hydrological

parameters such as hydraulic conductivity of the soil, unsaturated flow field parameters, surface friction coefficients, vegetation density, precipitation and many other parameters that shape and from the hydrological response of the catchment. The coupled hydrological model allows for a controlled environment in order to isolate and study the effect of the a single parameter or a combination of parameters on the catchments hydrological and sediment transport response. The result of the coupling of erosion and hydrology has the potential to complement field studies to develop better field campaigns for monitoring of large or plot scale erosion. In this study, the emphasize is on the role of the precipitation patterns, role of vegetation and the effect of wild fires and logging (timber harvest) on erosion. The amount of increase in erosion rates is quantified and compared to the pristine conditions. The increase in heat wave induced mortality of the forests has been documented through out the globe [31]. The main hypothesis is that the subsurface hydrology has a key role in the emergence of the runoff generation mechanism when precipitation patterns or canopy size changes. Subsurface saturations and water table depth can be affected by precipitation patterns, vegetation density changes and climate which in turn affects the runoff generation and water discharge which influences fluvial erosion in the hill slopes, river banks and flood planes.

Simulation of the evolution of the catchment in geologic time scales with the proposed coupling of erosion and hydrology is not feasible due to computational costs. However, the approach strives to provide a detailed view of the linkage between erosion and hydrology in a year. The study of the mechanism and resulting dynamics can be a stepping stone in which a fully coupled erosion-hydrology simulation frame work can be built to simulate short term (decades to centuries) catchment evolutions. The goal is that insights gained here can help see the geodynamics modeling in a better light, resulting in understanding the limitations and advantages and the consequences of the assumptions made in setting up geodynamics models for densely vegetated areas and varying precipitation patterns. The insights can be helpful in interpretation of the results produced by simpler models as well.

In chapter two of this document, the research methods and equations that are solved including surface and subsurface coupling and computation of erosion is presented. The study area and model parameters along with boundary conditions are also introduced.

Chapter three of this document is the study of effects of precipitation patterns on the river bed shear as a proxy for erosion. A method of generating precipitation patterns is provided that produces precipitation patterns with the same posteriori and priori probability distribution parameters. These precipitation patterns are produced so that the annual precipitation is a prefixed total. Many geodynamics simulations are carried out on the basis of annual time steps. The hypothesis is that the precipitation patterns, which are defined by precipitation events intensity, duration and dry intervals can have a pronounced effect on the runoff generation and therefore on erosion rates.

Chapter four of this document explores the role vegetation plays in regulating the erosion rates by affecting the subsurface and surface flow fields. It is hypothesized that unsaturated zone and water table depth plays an important role in runoff generation and discharge in this catchment along the canopy storage. The role of water table elevation in catchment of study is analyzed for three different forest types. Keeping all the parameters constant except for the vegetation characteristic parameters such as Leaf Area Index (LAI), leaf stomatal conductivity, typical tree height and root depth, it is shown that canopy storage and plant transpiration regulate the water table depth. Therefore runoff generation is affected by plants in the forest. The level of runoff and erosion rate reduction is shown to be dependent to the plant characteristics.

Chapter five of this document is the study of the effects of the changes in canopy size on erosion. Canopy size can change due to logging (timber harvesting) and wild fires or anthropologically caused fires. Reducing forest canopy by logging and wild fires decreases potential evapotranspiration and canopy storage. The subsurface saturation levels, runoff generation and discharge in river streams are affected as a result. The dynamics of subsurface flow is studied in these scenarios and the rates in which the water table changes are shown to be the an important factor in increased runoff generation.

Chapter six synthesizes the results of previous chapters to conclude that subsurface flow and especially unsaturated zone flow dynamics is a key factor in controlling the fluvial erosion in the catchment of study. The role of the infiltration, bank storage and ground water mounds in producing the emergent erosion patterns are summarized and discussed.

Chapter 2

Methods and materials

Geomorphology can be viewed as the study of the displacement of the regolith and rock due to force of the gravity. Therefore the movement of the water in the landscape is an important part of geomorphology as an agent that moves sediment and regolith in the landscape. Many different models of the fluid movement (flow routing) could be used depending on the application or quantity of interest in geodynamics simulations. Flow routing is the solution of the conservation of mass and momentum for the fluid continuum over the landscape. Since the three dimensional Navier Stokes equations are too complex and time consuming to be solved in land surface evolution time scales, other simplified equations are used to estimate flow depth, or discharge on surface. One such simplification is the depth averaged equations namely St. Venant Shallow-water flow shown in equations 2.1 to 2.4.

$$\frac{\partial h}{\partial t} = q_{in} - (\frac{\partial uh}{\partial x} + \frac{\partial vh}{\partial y}) \tag{2.1}$$

$$\frac{\partial uh}{\partial t} + \frac{\partial hu^2}{\partial x} + \frac{\partial huv}{\partial y} + gh\frac{\partial \eta}{\partial x} + \frac{\tau_{bx}}{\rho} = 0 \tag{2.2}$$

$$\frac{\partial vh}{\partial t} + \frac{\partial hv^2}{\partial y} + \frac{\partial huv}{\partial x} + gh\frac{\partial \eta}{\partial y} + \frac{\tau_{by}}{\rho} = 0 \tag{2.3}$$

$$\tau_{bx} = C_f \rho u|u|, \tau_{by} = C_f \rho v|v| \tag{2.4}$$

where h is water depth $[L]$, t is time $[T]$, q_{in} is the distributed water flux to the surface $[LT^{-1}]$, u, v are flow velocity in x, y direction $[LT^{-1}]$, η is fluctuation of water depth from equilibrium $[L]$, g is the gravitational constant $[LT^{-2}]$, and τ_{bx} and τ_{by} are bed shear stress $[MLT^{-2}]$, C_f is the friction constant$[-]$ and ρ is water density $[ML^{-3}]$. The St. Venant equations can further be simplified into a one dimensional form. The numerical solution of the simplified form of St. Venant is still computationally too expensive for geologic time scales. In order to avoid the complexity of flow routing with these equations altogether, some researchers resorted to explicit rule based flow routing methods such as cellular automaton [32] to model the fluvial processes.

Runoff generation mechanisms used in geodynamics simulation frameworks are simple Hortonian, modified Oĺoughlin excess saturation or modified Topmodel approaches [33, 34] that are used in CHILD [11, 35]. These oversimplified models are simple yet useful approximations of runoff generation mechanisms. Variations of the simplified approach combined with other flow routing methods such as multi-

route flow [36] have been used in geomorphological simulation packages. In these models, simplifications are used to replace flow routing with approximation of flow passing through a river stream by using a surrogate variable like upstream drainage area [37, 38, 39, 8, 11].

An efficient formulation of the surface flow is diffusive wave equation which simplifies Saint-Venant equations in to one conservative equation and is shown to produce compatible water head compared with the numerical solutions of the original equation and analytic solutions [27]. A vital part of the flow simulation has also been the question of how and to what extent the subsurface flow interactions are important and what is the real extent of the contribution of the base flow in the river and stream discharge [40]. In order to address these questions, a simulation framework is needed that can simulate the coupled and integrated flow fields of surface and subsurface without any explicit assumption about the nature of runoff generation. In this study, an integrated surface and subsurface modeling framework called HydroGeoSphere is used in which most of the flow components has physics based and field measurable parameters.

HydroGeoSphere is a three dimensional fully coupled numerical software for the simulation of the surface and subsurface flow and solute transport. The developers of the HydroGeoSphere believe that it is an ideal tool for hydrological model building within watersheds in a realistic, physically-based manner. The program is reviewed in [41] and the basics of the numerical method is presented here [30, 42]. The Freeze and Harlan's original blueprint proposal has been criticized and an improved version is proposed by K. Beven [34]. Beven proposed an alternative blueprint with the emphasis on the role of the observables on the modeling of the hydrological systems. Many researchers have used HydroGeoSphere in the hydrological context [43, 29, 44, 45, 46] . HydroGeoSphere is used to address the importance of the bank storage for the river discharge production and the interaction of the river with the groundwater [40]. The application of the HydroGeoSphere in many different problems proved its versatility and usability. However, due to the complexity of the subsurface and surface interactions, there is not any analytic solution to verify the simulation frame work for the complex problems that are common place in real world applications. There has been a comparative study of the accuracy of similar models and they all show a reasonable level of agreement on problems being considered [26]. Due to the complexity of the simulation framework and the nonlinear interactions of the components, no comprehensive tests have been carried out to verify the accuracy and usability of the HydroGeoSphere. The consistency of the equations should be checked and the performance and behavior of each sub-processes have to be verified where parameters that are used belong to end member scenarios.

2.1 Subsurface flow modeling

HydroGeoSphere uses the mass balance equation for subsurface flow modeling. The equations 2.5 and 2.6 are a modified form of Richards equation [47] that are used to describe three-dimensional transient subsurface flow in a variably-saturated porous medium.

$$-\Delta.(w_m q) + \Sigma\Gamma_{ex} \pm Q = w_m \frac{\partial}{\partial t}(\theta_s S_w) \tag{2.5}$$

where w_m is a dimensionless volumetric fraction of the total porosity occupied by the porous medium (or primary continuum) $[-]$. t is time $[T]$, Γ_{ex} is the exchange flux between surface and subsurface, Q is the source or sink in the subsurface $[L^3L^{-3}T^{-1}]$, θ_s is the porous medium porosity $[-]$ and S_w is the

saturation level in the soil [−]. The fluid flux q $[LT^{-1}]$ is given by:

$$q = -K \cdot k_r \nabla(\psi + z) \tag{2.6}$$

where $k_r = k_r(Sw)$ represents the relative permeability of the medium [-] with respect to the degree of water saturation Sw [-], ψ is the pressure head $[L]$, z is the elevation head $[L]$ and θ_s is the dimensionless saturated water content, Q is source or sink term $[L^3L^{-2}T^{-1}]$, which is a volumetric fluid flux per unit volume representing a source (positive) or a sink (negative) to the porous medium.

Van Genuchten proposed a new and relatively simple equation for the soil-water content-pressure head curves, $\theta(h)$. Their proposed equation is described in this paper [48]. The particular form of the equation enables one to derive closed-form analytical expressions for the relative hydraulic conductivity, k_r, when substituted in the predictive conductivity models of N.T. Burdine or Y. Mualem. The resulting expressions for $k_r(h)$ contain three independent parameters which may be obtained by fitting the proposed soil-water retention model to experimental data or can be estimated by the use of the grain size distribution from the field.

2.2 Surface flow modeling

The surface flow equation solved by HydroGeoSphere is a simplified version of the St. Venant equations. This equation is shown to be a good approximation of the original equations [27]. The simplified form of equation is known as the diffusive wave equation are shown at equations 2.7, 2.8 and 2.9.

$$\frac{\partial \phi_\circ H_\circ}{\partial t} - \frac{\partial}{\partial x}(d_\circ K_{\circ x}\frac{\partial h_\circ}{\partial x}) - \frac{\partial}{\partial y}(d_\circ K_{\circ y}\frac{\partial h_\circ}{\partial y}) + d_\circ \Gamma_\circ \pm Q_\circ = 0 \tag{2.7}$$

$$K_{\circ x} = C_{\circ x} d^{1/2} \frac{1}{[\partial h_\circ / \partial s]^{1/2}} \tag{2.8}$$

$$K_{\circ y} = C_{\circ y} d^{1/2} \frac{1}{[\partial h_\circ / \partial s]^{1/2}} \tag{2.9}$$

where $\phi_\circ$ is a fraction of the surface that can be filled with water [−], H is water head in the surface $[L]$, t is time $[T]$, $d_\circ$ is water depth $[L]$, K_{ox}, K_{oy} are conductance terms $[L^3L^{-2}T^{-1}]$, $\Gamma_\circ$ is the exchange flux between surface and subsurface $[L^3L^{-3}T^{-1}]$, $Q_\circ$ is the source and sink term in the surface region and C_{ox}, C_{oy} are Chezy friction constants for the surface $[L^{\frac{1}{2}}T^{-1}]$. This representation of the St. Venant equation is very advantageous due to the transformation of three field variables namely h, u and v in to only one field variable H. At the other hand, since this equation is a diffusion or hyperbolic type, it can not capture hydraulic jumps and back and forth movement of the water when it hits an obstacle that may happen in the real world. The upstream scheme that employed by HydroGeoSphere ensures that water flows from higher elevation to the lower elevation in a monotonous pattern. Hidden in the form of the equation is the monotonic reduction of water head or energy heads which controls one way movement of the flow. Although the structure of the equation 2.7 resembles heat or diffusion partial differential equations, the boundary conditions are not exactly the same to the heat equation. The free fall or zero gradient boundary conditions as well as fixed water elevation can be applied in the boundary of the catchment for the surface flow. A major limitation of the depth averaged equations are that they are not capable of capturing the secondary flow patterns that are inherently three-dimensional and are responsible for the meandering rivers and dune and bar formations in fluvial systems. However, the

two-dimensional formulation that is implemented in HydroGeoSphere is a great improvement over the one dimensional formulation used in most of the geomorphological and hydraulics models. Though the current implementation is faster than solving St. Venant equations, it is not faster than simpler methods used currently in many geodynamics models and the time step is controlled to large extent by the size of the mesh used in the model. As the grid spacing is reduced, the time step should decrease to reduce the resulting error and keep the time integration stable according to Courant number stability criteria. In other words, the more accuracy demands are put on spatial domain, the smaller time steps will be needed and the computational cost in time for the model will increase. To couple the surface and subsurface no conservation of the momentum through the interface is needed as in general, flow through porous media is governed by conservation of mass and application of Darcy law. HydroGeoSphere also includes conceptualization of dual continuum, evaporation and transpiration, rill and obstruction storage effects facilitating a complex and physics based approach to hydrology. When coupling groundwater and surface water flow in one model, a common method is to utilize a first order coupling coefficient. It has been shown that this method is consistent with measurements [49].

2.3 Evaporation and transpiration modeling

HydroGeoSphere divides evapotranspiration into plant transpiration, direct evaporation from top soil and surface water bodies such as puddles, ponds, lakes and canopy evaporation. Transpiration by vegetation leads to water extraction from the plant root zone, which may be submerged partially into the water table and into the unsaturated zone. The rate of transpiration is estimated using equation 2.10 [50]:

$$T_p = f_1(LAI) \times f_2(\theta) \times RDF \times (E_p - E_{can}) \tag{2.10}$$

where T_p is the plant transpiration $[LT^{-1}]$, LAI is the leaf area index $[-]$, $f_1(LAI)$ is a function of the leaf area index $[-]$ as defined in equation (2.11), $f_2(\theta)$ is a function of the volumetric water content $\theta\,[-]$ as shown in equation (2.12), E_p is the potential evapotranspiration $[LT{-}1]$, E_{can} is the evaporation from canopy $[LT^{-1}]$ and RDF is the root distribution function defined $[-]$ in equation (2.13):

$$f_1(LAI) = max\{0, min[1, (C_2 + C_1 * LAI)]\} \tag{2.11}$$

$$RDF = \frac{\int_{z_1}^{z_2} r_F(z)\,dz}{\int_0^{L_r} r_F(z)\,dz} \tag{2.12}$$

$$f_2(\theta) = \left\{ \begin{array}{ll} 0 & \text{for } 0 \le \theta \le \theta_{up} \\ f_3(\theta) & \text{for } \theta_{up} \le \theta \le \theta_{fc} \\ 1 & \text{for } \theta_{fc} \le \theta \le \theta_o \\ f_4(\theta) & \text{for } \theta_o \le \theta \le \theta_{an} \\ 0 & \text{for } \theta_{an} \le \theta \end{array} \right\} \tag{2.13}$$

$$f_3(\theta) = 1 - \left(\frac{\theta_{fc} - \theta}{\theta_{fc} - \theta up} \right)^{c_3} \tag{2.14}$$

$$f_4(\theta) = 1 - \left(\frac{\theta_{an} - \theta}{\theta_{an} - \theta_o} \right)^{c_3} \tag{2.15}$$

in which C_1, C_2 and C_3 are dimensionless fitting parameters, $r_F(z)$ is the root distribution function

$[-]$, L_r is the rooting depth $[L]$, θ_{fc} is the moisture content at field capacity, whereas θ_{up}, θ_o and θ_{an} are the volumetric water contents of the soil at the wilting point, the oxic limit, and the anoxic limit, respectively.

Two models are available in HydroGeoSphere for calculation of evaporation. As a physics based model, having two methods of calculating one physical process is a dilemma in itself. The merits of each method is considered in more detail later on in this study. One approach assumes that evaporation occurs if the reference evapotranspiration E_p has not been removed by the mentioned canopy evaporation E_{can} and plant transpiration T_p. Therefore, evaporation from the surface water bodies and top soil is estimated in equation 2.16.

$$E_s = \alpha \times (E_p - E_{can} - T_p) \times EDF \tag{2.16}$$

where E_s is evaporation from the surface soil $[LT^{-1}]$, E_p, E_{can} and T_p are defined before and the parameter α is scaling factor that takes into account the water availability $[-]$. The other approach reduces the remaining PET by a reduction function as in equation 2.17.

$$E_s = \alpha \times (E_p - E_{can}) \times (1 - f_1(LAI)) \times EDF \tag{2.17}$$

in which the term EDF is the evaporation distribution function including the overland and subsurface and the rest of the symbols are defined in the previous equations domains [51].

In addition to evapotranspiration, HydroGeoSphere also accounts for storage of water due to both vegetation (obstruction storage) and micro-topography (rill storage) [42]. These two parameters control the movement of the water on the surface along with the surface resistance coefficient.

2.3.1 Potential evaporation form Thornthwaite equation(1948)

. Thornthwaite proposed an empirical method for the calculation of the potential evaporation from a region using a limited number of input variables. His method uses the daylight duration and mean of the temperature for the each month to give an approximate potential evaporation. Despite its empirical nature, it is widely used due to its simplicity and relatively accurate estimation of the potential evaporation.

$$PE = 16(\frac{T}{12})(\frac{N}{30})(\frac{10T_{air}}{I})^{\alpha} \tag{2.18}$$

where PE is the estimated potential evaporation in mm/month $[LT^{-1}]$, T_{air} is the average daily temperature $[^{\circ}C]$ and if it is a negative value, then zero must be used in its place. N is the number of days per month $[-]$ and T average length of the days in each month $[T]$. where I is dimensionless $[-]$ and defined as:

$$I = \sum_{1}^{12} (\frac{T_{air}}{5})^{1.514} \tag{2.19}$$

and α is defined as $[-]$:

$$\alpha = (6.75 \times 10^{-7})I^3 - (7.71 \times 10^{-5})I^2 + (1.792 \times 10^{-2})I + 0.49239 \tag{2.20}$$

This method is used here for the clear cutting scenario and as a check for the calculation of the potential evapotranspiration for the scenarios without transpiration.

2.3.2 Hourly potential evapotranspiration modeling

Penman-Monteith equation 2.21 is an expression of the conservation of energy [52, 53]. It calculates the energy availability to convert water in to water vapor. A daily and hourly version is proposed for the Penman-Monteith equation. The method originally was proposed to calculate daily evapotranspiration and has been successfully used in many regions. The transpiration of the plants contribute a term in the equation which varies among plants and climates and it is hard to estimate accurately [54]. Understanding the process of transpiration is still an ongoing area of research. In the calculation of daily PET, the plant conductivity is assumed to be a constant throughout the day and it give and average PET for each day. A newer version of the Penman-Monteith equation is proposed for the hourly calculation of the PET [52] . In this hourly version, the plant conductivity varies for day and night. The night time transpiration is assumed to be smaller than the day time transpiration. However, this assumption is not valid for the plants that grow in very dry and warm climates where most of the received daytime energy is stored in the leaf and photosynthesis is carried out at night. In effect, stomata are closed during the day and is open at night to release the byproducts of photosynthesis in warmer climates to prevent water loss. In order to calculate PET, hourly air and soil temperature, wind speed, relative humidity, cloud cover and solar radiation is used. Secondary parameters are calculated based on ambient temperature, such as Δ, c_p, γ and δe. Solar radiation is calculated using the distance and inclination of the sun.

$$PET = \frac{\Delta(R_n - G) + \rho_{air} c_p (\delta e) g_a}{(\Delta + \gamma(1 + \frac{g_a}{g_s}))L_v \rho_{water}} \tag{2.21}$$

$$g_a = \frac{\kappa^2 u}{[ln(\frac{z_m - z_d}{z_o})]^2} \tag{2.22}$$

$$g_s = C_{leaf} \times LAI \tag{2.23}$$

where PET is potential evapotranspiration rate $[L^3 L^{-2} T^{-1}]$, given that there is no water availability limit, Δ is the slope of saturation to temperature $[PaK^{-1}]$, R_n is net irradiation $[WL^{-2}]$, G is radiation from earth surface $[WL^{-2}]$, ρ_a is the air density $[ML^{-3}]$, c_p is specific heat capacity of air $[JM^{-1}K^{-1}]$, δe is vapor pressure deficit in the atmosphere $[ML^{-1}T^{-2}]$, g_a is the air conductivity $[LT^{-1}]$, γ is psychromatic constant $[PaK^{-1}]$, g_s is stomatal conductivity LT^{-1} and L_v is the latent heat of evaporation $[JL^{-3}]$, κ is the von Kármán constant $[-]$, u is the wind speed above the surface $[LT^{-1}]$, z_m is the elevation of the wind speed measurement $[L]$, z_d are zero displacement elevation, $Cleaf$ is the conductivity of the stomata $[T^{-1}]$ and LAI is the leaf area index $[-]$. The conductivity of atmosphere is calculated as in equation 2.22 which uses an exponential distribution for horizontal velocity changes and vegetation height and zero displacement height z_d. The canopy conductivity is calculated by the LAI and C_{leaf} which has different values for night and day for any given plant type.

Penman-Monteith equation is adopted by the Food and Agriculture Organization of the United Nations (FAO) for evaluating crop water requirements [52]. The *potential* refers to the fundamental assumption made in the derivation of the equation that there is not any lack of water limiting evapotranspiration. The surface is kept always wet and subsurface is always filled with water in a quantity that transpiration is not limited by anoxic and oxic limits. The measured or calculated evapotranspiration in these conditions is the maximum possible evapotranspiration. In order to get an actual evapotranspiration, the water availability should be considered in the catchment which is controlled by the flow movement equations.

In order to calculate hourly PET, data from Stuttgart synoptic weather station is used as it is close to the study region. The study region is introduced in section 2.8. The variations of the air temperature is shown in figure 2.1. The annual mean of temperature for this station is 10^oC. Temperature is a major factor for the calculation of PET. For areas that are shaded by trees, the sensible heat energy derived from ambient air help with the sublimation of ice or evaporation of water. At colder days, the drop in temperature will produce dew (liquid water droplets) on cold surfaces if atmosphere is humid and temperature is colder than dew point. Soil surface temperature is also shown in figure 2.1. Air temperature measured at two meters above ground and surface temperature measured at five centimeter below surface are strongly correlated (correlation coefficient of: 0.93 for this dataset). The soil surface temperature can be used to calculate the long wave radiation from the surface which is used in radiation energy input in PET calculation as shown in equation 2.21.

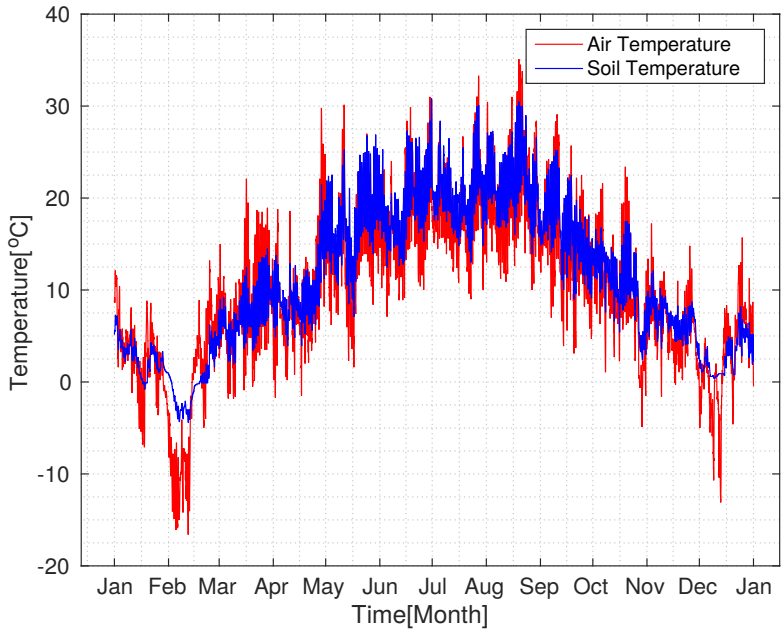

Figure 2.1: Temperature measurement at Stuttgart synaptic station for 2012. Annual Mean temperature is about 10^oC. Temperature is a major forcing in atmospheric demand for potential ET.

The relative humidity reported from the Stuttgart station is shown in figure 2.2. The deficit in partial vapor pressure is also an important factor in PET. The escape of water molecules from water surface to ambient air is more probable if the partial pressure of water vapor in atmosphere is low. PET scales directly with the vapor pressure deficit. Average relative humidity for this station is 75%. This shows that the area is very humid and this is a limiting factor for PET.

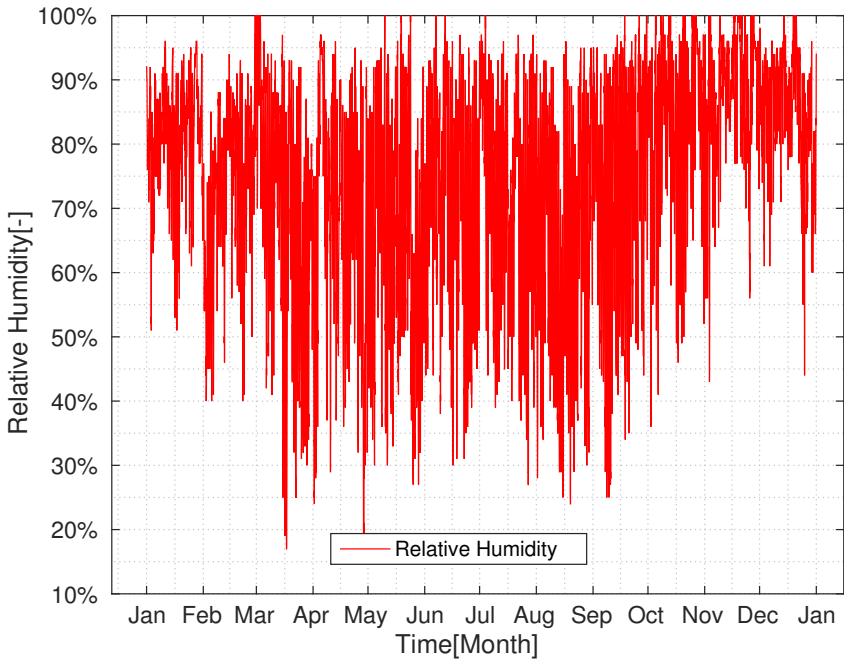

Figure 2.2: Relative Humidity measurement at Stuttgart synaptic station for 2012. Higher relative humidity is an indicator of wet climate. Mean annual humidity level is about 75%. The major control for potential evapotranspiration is transfered to the energy availability.

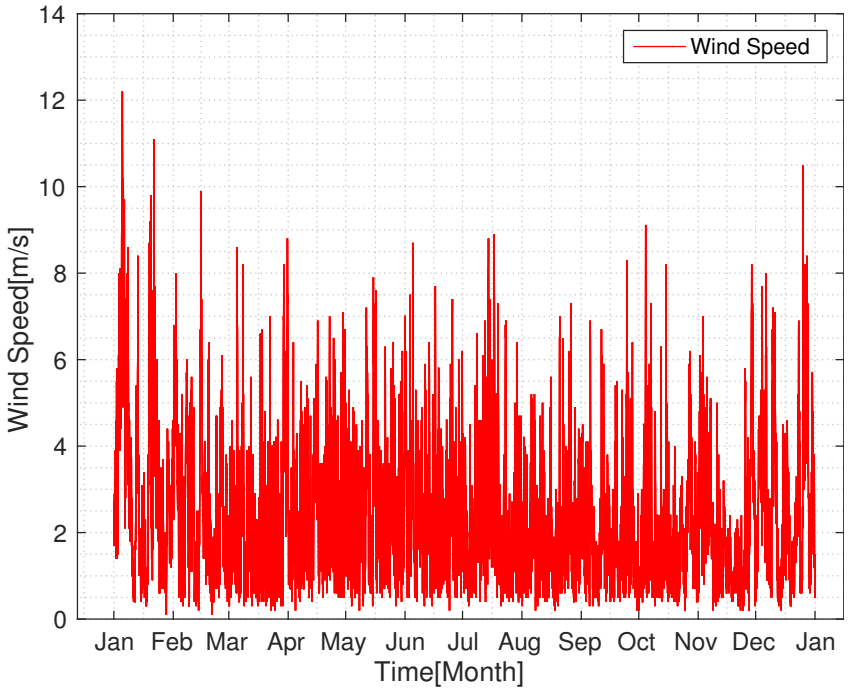

Figure 2.3: Wind speed as measurement at Stuttgart synaptic station for 2012. Annual mean wind speed is about 2.31 m/s. Wind is responsible for ascending of the lighter water vapor mixture by turbulent diffusion.

Wind speed is the other important factor in PET. The variations of wind speed is shown in figure 2.3. Average wind speed for this station is about $2.31\,m/s$. The air conductivity is directly proportional to wind speed. The von Kármán κ value is used to calculate the vertical component of the wind speed which takes away the water vapors from the surface by turbulent mixing.

2.4 Governing equations for the erosion and transport

The principal equation for the landscape evolution is the conservation of the mass as shown in equation 2.24 [10]. Increase or decrease of elevation due to tectonic forces and climatic factors could be formulated as a uplift source or sink term and the gradient of the sediment flux due to the fluvial or hillslope processes.

$$\frac{\partial z}{\partial t} = U - \nabla Q_s \tag{2.24}$$

where $z\,[L]$ is the height from a reference point far away from the region of study, t is time $[T]$, U is the is the tectonic uplift rate $[LT^{-1}]$ and Q_s $[L^2T^{-1}]$ is the fluvial sediment flux.

2.4.1 Hillslope processes

Hill-slope processes involve small agents like rain drops, grain salting, rodents and other animals that contribute to the short distance and gradual movement of the regolith on the surface [10, 11]. These constant movements involve many particles that result in many degrees of freedom. Traditionally, whenever many degrees of freedom exist in the system that are intractable as single entities, these effects are summed up into constants that reflect the over all behavior of these agents. In the case of hill-slope processes, the mathematical formulation resembles the diffusion process [55, 2]. Hill slope processes here are presented for the sake of completeness and as the time scale of the simulation carried out here is short, no hill-slope processes are included in the simulations.

Earlier numerical models [56] considered the possibility of using diffusion for the combined effects of the hill-slope processes and advection for the longer range movement of the material by water. It was shown that with diffusive hill-slope assumption, the parabolic shape of some of the hills can be explained and therefore this assumptions are adopted in to the mainstream geodynamics models. The movement of the particles from the hill-slopes for example, could be triggered by wind or by raindrops, insects or animals. Smaller particles can move larger particles (salting) and in time, these small movements accumulate to flattening of the hills. The overall behavior of these small disturbances is like the movement of the heat. Particles move from higher potential energy points to lower potential points in order to gain more stability. Since these small disturbances are so abundant and almost random, it is not possible to keep track of them as individuals. As in many physical problems with large number of similar particles, a diffusive formulation captures the movement of the regolith particles with reasonable accuracy. Effectively the mentioned processes are combined together in a constant in the form of a diffusion equation 2.25 in which the elevation of surface diffuses downhill.

$$\frac{\partial z}{\partial t} = -D_{iff}\nabla^2 z \tag{2.25}$$

where z is the surface elevation $[L]$, t is time $[T]$, D_{iff} is the elevation diffusivity $[L^2T^{-1}]$. The equation 2.25 predicts parabolic surfaces in the steady state. The system will reach steady state when gradient of elevation becomes zero. However, many observations show that most surfaces are linear when

the slope is larger than 20^o. The linear relationship does not hold for the larger slopes. To overcome this limitation, a new nonlinear relationship that has a limiting slope gradient as an extra parameter to control the rate of change of the slope as shown in equation 2.26 was suggested [57, 6]. It has been argued that though soil-mantled hill-slopes are typically convex near the crest, the slope increasingly becomes planar downhill, consistent with nonlinear, slope-dependent sediment transport models. In contrast to the widely used linear transport model in which sediment flux is proportional to slope angle, nonlinear models imply that sediment flux should increase rapidly as hill-slope gradient approaches a critical value. Furthermore some researchers [58] suggested that the local slope and transport relations may not be adequate in describing the hill-slope processes. They argued that some disturbance over the hill-slope may have longer range influences and may override the local slope relationship. Therefore, to extend the range of influence of the operation, they suggested a fractional differentiation operator.

$$\frac{\partial z}{\partial t} = \nabla \frac{-D_{iff} \nabla h}{1 - (\frac{\nabla z}{S_c})^2} \tag{2.26}$$

where S_c is the threshold hill-slope gradient [59, 6].

The movement of the soil and rock mass according to the equation 2.25 is limited by the availability of the detachable and movable particles called regolith. Regolith production, is due to the chemical or physical breaking and decomposition of the rocks that slowly emerge to the surface.

$$-\frac{\partial H_s}{\partial t} = \epsilon_0 e^{-\alpha H_s} \tag{2.27}$$

in which H_s is the regolith height $[LT^{-1}]$, ϵ_0 is the soil production rate constant $[LT^{-1}]$ and α is the weathering decay rate $[L^{-1}]$ [60, 59]. Availability of the material for the transport is determined by the rate of soil production according to the equation 2.27 . If there is not enough regolith or soil available for the transport, erosion will be a limited.

2.4.2 Fluvial processes

In this section, the mathematical formulation of the fluvial bed erosion is given. More comprehensive reviews could be found in [59, 38, 35]. Despite the short range material movement in the hill-slope processes, fluvial process can move regolith and rock for much longer distances. Regolith from the stream bed or soil washed from upstream of the river could move either as suspended load, wash load and bed load. Depending on the size and density of the sediments, some of the material will be deposited where the water in river slows down. When the water in river gains momentum, either due to the river channel shape or slope, it can excavate and cut through the river bed and move the excavated material along. Two major transport laws are proposed for the transport of the sediment by water in geodynamics literature that distinguish between two major fluvial processes. The transport limited law applies to rivers where there is no limit on the production of the regolith where as the detachment limited law applies for the rivers where the bed rock is exposed the supply of the regolith is limited. The bed erosion equation 2.28 formulation argues that if the catchment is detachment limited, then much more work should be done by river to erode and incise through the river bed which is enforced by a small k coefficient [61, 62, 63].

$$q_s = k(\tau - \tau_c)^n \tag{2.28}$$

where q_s is the sediment flux $[L^3T^{-1}]$, k and n are constants $[-]$, τ is the shear stress $[Pa]$ and τ_c is

the critical shear stress $[Pa]$.

For transport limited rivers, the limiting factor is the capacity of the river stream to move regolith out of the catchment. In these kind of scenarios the regolith generation in the catchment is faster than erosion rate. Equation 2.29 is used for transport limited catchments. The relationship between the flux of the water flowing in the river and the amount of the sedimentation as suspended load could be established empirically. These empirical relations are the basis for many models.

The equation 2.29 has theoretical basis and one empirically determined constant K_{br}. Equation 2.29 is used to relate the flux $Q\,[L^3/T]$, W channel width $[L]$ and channel slope $S\,[-]$ to the bed shear stress. Since the channel width is a function of flux, a smiler scaling law is used to find the corresponding width for a given flux.

$$\tau = K_t(\frac{Q}{W}^{M_b})S^{N_b} \tag{2.29}$$

where τ is the bed shear stress $[Pa]$, K_t is a constant $[PaTL^{-2}]$, W is the width of the channel $[L]$, S is the slope of the channel $[-]$ and M_b, N_b are dimensionless constants $[-]$.

The erosion in the river there for is formulated for the detachment limited case as:

$$D_c = K_{br}(\tau_0 - \tau_c)^{P_b} \tag{2.30}$$

where D_c is the sediment discharge $[L^3T^{-1}]$, K_{br}, P_b are dimensionless constants $[-]$. For the case of no limit on the production of regolith, the transport limited formulation is as equation 2.31.

$$Q_c = K_f W(\tau_0 - \tau_c)^{P_f} \tag{2.31}$$

where Q_c is the sediment discharge $[L^3T^{-1}]$, K_f, P_b are dimensionless constants $[-]$. A comprehensive study has been done on the nature of these laws by [64]. It is shown that these equations can be parameterized from field measurements and can be tested in physical models. The study confirms that these equations could be used a in a wide variety of geomorphological settings. Furthermore the limitations of these transport laws were discussed and the need to expand or include more subprocesses were acknowledged. Perron et al [65] focused on the relative effects of the diffusion and convection with the use of Peclet number which is a measure of the relative strength of advection to diffusion processes. Their results showed that the application of the current transport law will produce topography that resemble realistic topography qualitatively. They argued that even for the uniformly spaced valleys there is no quantitative framework for predicting valley spacing. Their work showed that there is a possibility of predicting the wavelength of the existing landscapes to the first degree by utilizing the mentioned transport laws. It was believed that fluvial processes are mostly detachment limited [66]. A recent work from Jon D. Pelletier [67] argues that the usage of both transport limited and detachment limited laws give a better match with the measurement if they are relatively weighted according to the relative abundance of the sand and rock to the clay and silt in the catchment.

The dynamic adjustment of the width of the channel W is an important factor in the morphological change of the river [68]. Attal and coworkers [68] emphasized the importance of channel width in controlling fluvial processes.

After establishing the proper form of the transport for sediments or regolith on the surface and river bed stream, the landform evolution can be calculated using the Exner equation 2.32.

$$\frac{\partial z}{\partial t} = -\frac{1}{1-\varepsilon}\overrightarrow{\nabla} \cdot \overrightarrow{q}_s \tag{2.32}$$

in which z is surface elevation $[L]$, ε is bed porosity $[-]$, q_s is the sediment flux $[L^3T^{-1}]$. In one dimensional elements like channels or river streams, where flow is specified as a scaler, the ∇ operator changes to differentiation along the length of the channel. The water flow equation 2.7 can be rewritten in a simple form by ignoring the source and sink terms as shown in equation 2.33:

$$\frac{\partial h_\circ}{\partial t} = \overrightarrow{\nabla} \cdot \overrightarrow{q}_w \tag{2.33}$$

where $h_\circ$ is the water depth $[L]$ and q_w is the water flux $[L^3T^{-1}]$ The coupling of the erosion and water flow is implicit in the sediment flux and water flux terms q_w, q_s as each flux is a function of both elevation of surface water head.

Most of the existing formulations for the Exner equation 2.32 is done for the one dimensional flow. The formulation usually has one or more empirically determined constant which makes them difficult to use in a two dimensional flow settings where the width of the channel is not explicitly specified. One such formulation as shown in equation 2.34 has a constant ϵ which is adjusted for one dimensional flow and the value of the constant for two dimensional flow is not known [69].

$$q_s = -\frac{8h_\circ^{\frac{1}{12}}}{\sqrt{(n)(R-1)}}\frac{\epsilon}{1+\epsilon}|q_w|\overrightarrow{\nabla}H \tag{2.34}$$

where $h_\circ$ is the water depth $[L]$, n is manning number $[TL^{\frac{-1}{3}}]$, R is the relative density of sediment to water $[-]$, ϵ is a dimensionless empirical constant and H is the energy head $[L]$. This equation explicitly couples water flux to the flux of sediment. However, the ϵ constant is not studied for the two dimensional flows so this form of the equation is not going to be used in this study.

In the current research, it is assumed the bedrock is well below the surface and there is an abundance of regolith available for transport. Therefore the transport limited approach is chosen to be implemented. In the transport limited approach, the bed shear is used to calculate the transport capacity as shown in equation 2.31. One way of calculating bed shear stress is by using equation 2.35:

$$\tau_b = \gamma(\frac{nq_w}{w})^{\frac{3}{5}}s^{\frac{7}{10}} \tag{2.35}$$

where τ_b is the bed shear stress $[Pa]$, γ is the specific weight of water $[ML^{-2}T^{-2}]$, n is manning number $[TL^{-\frac{1}{3}}]$, s is energy slope $[-]$ and w is the width of channel $[L]$. As with the previous equation, two dimensional form of the flow has never been reported in the geodynamics literature. However, there is not any empirical constants that need to be found in this form and the exponents have theoretical ground. In two dimensional case, the channel width w is assumed to be one or it can be assumed that the term $\frac{q_w}{w}$ is equal to the water flux per unit length. Therefore it is possible to rewrite the equation in a simpler form as shown in equation 2.36.

$$\tau_b = \gamma h_\circ s \tag{2.36}$$

where τ_b is the bed shear $[Pa]$, $h_\circ$ is the channel width $[L]$ and s the slope of the channel $[-]$. Once the bed shear is calculated, the sediment flux for the bed-load can be calculated empirically as shown in

equation 2.37 [70, 71].

$$q_s = k_f \rho_s (\frac{\tau_b}{(\rho_s - \rho_w) g D} - \tau_c)^{3/2} D^{3/2} \sqrt{\frac{(\rho_s - \rho_w) g}{\rho_w}} \tag{2.37}$$

where q_s is the sediment flux, k_f is an empirical constant $[-]$, τ_b, τ_c is the bed shear stress and critical shear stress $[Pa]$, ρ_s, ρ_w are sediment and water density respectively $[ML^{-3}]$, g is the gravitational constant of Earth $[LT^{-2}]$, D is the regolith diameter $[L]$ in order to calculate the energy slope s, energy slope in the x and y direction is calculated and sediment flux in the x and y direction is scaled according to the ration of the slopes in each direction to the total slope of th element as shown in equation 2.38.

$$s = \sqrt{(\frac{\partial H_\circ}{\partial x})^2 + (\frac{\partial H_\circ}{\partial y})^2} \tag{2.38}$$

where s is the energy slope of the water and $H_\circ$ is the water elevation $[L]$. Using the scaling of the flux according to the ration of the direction slopes to the total slope, sediment flux in each direction is calculated as shown in equation 2.39 and 2.40.

$$q_x = \frac{s_x}{s} q_s \tag{2.39}$$

$$q_y = \frac{s_y}{s} q_s \tag{2.40}$$

where s_x and s_y are directional slopes at x and y direction $[-]$ and q_s is the sediment flux $[L^3 T^{-1}]$.

2.5 Calculating erosion using control volume finite element

In order to solve the Exner equation 2.32, the formulation of the sediment flux is used according to equations 2.37, 2.39 and 2.40. To solve the transport equation on the catchment scale, a discretization scheme should be adopted. HydroGeoSphere models can work with triangular mesh which are suitable for irregular geometries like catchments. So here a triangular mesh is adopted for the domain discretization to solve the Exner equation numerically.

In traditional control volume approach, weather it is node or element centered, the solution domain is divided up to elements that have simple geometries like triangles, rectangles or cubes. Then conservation rules are applied to the variable of interest to get to a system of equations. In this system of equation, each node has one or multiple unknowns which represents the mean value of the unknown in the node or cell. This system of equations then can be solved to find the unknowns. If element centered control volume is used, the number of unknowns is the same as the number of elements, if a node centered approach is taken, then the number of unknowns are the same as the number of nodes in the system. The major draw back of this method is that the quantity of interest is approximated by a single value within the discretized cell. If derivatives of the unknown quantity is of interest, then the derivative can only be calculated at the interface of two cells. Despite this drawback, this method is simple to implement and locally conservative for linear steady state problems.

The control volume finite element method inherits many concepts from finite element method. The mesh or triangulation can be used as it is being used in finite element method. A major distinction is that in order to minimize the error residuals, no weighting (weighting function of unity) function is used.

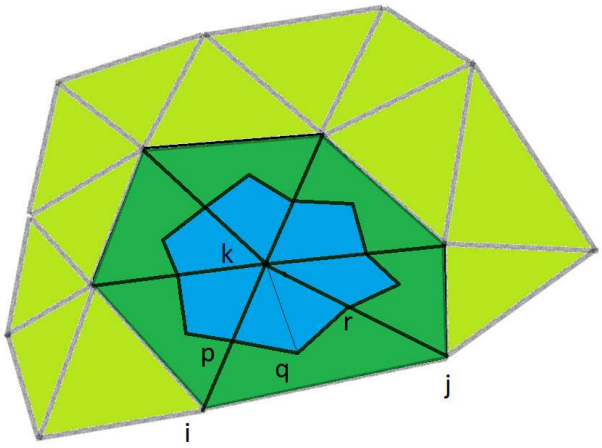

Figure 2.4: Control volume finite element discretization of the domain. The control volume is the blue area around the node labeled k. In control volume method, a single value is assigned for the entire control volume around node k. In control volume finite element method, the value is a linear combination of the basis function on each element, this provides a compact support on the element and differentiability within the element as long as the basis functions are differentiable.

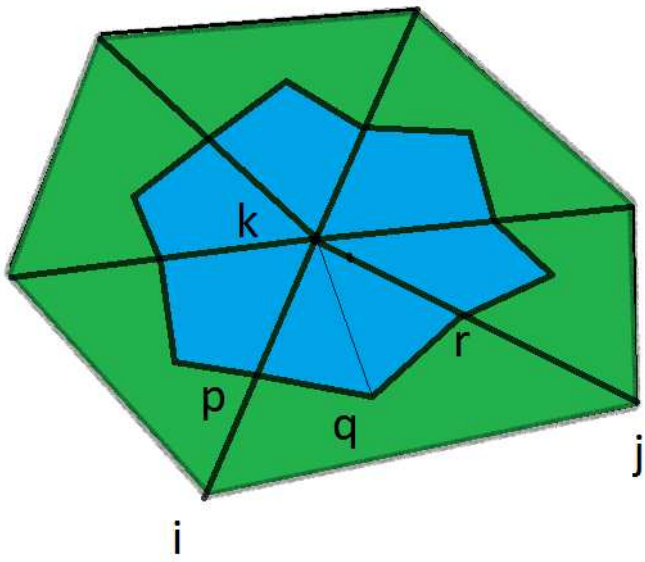

Figure 2.5: Control volume finite element integration on boundary of the node in control volume shown in blue. The conservation laws can be applied to any arbitrarily defined region. Here, the shaded area in blue is the control volume. The changes inside the region should cancel out with the in and out flux through the boundary. As the integration is a linear operator, the line integral at the boundary of the shaded region can be carried out piecewise and the result can be added to final flux at any desired order. This allows for the element wise computation of the fluxes per triangle.

In control volume finite element method, the state variables are expressed as linear combination of basis functions as in equation 2.41 where i loops over the degrees of freedom of the element and ϕ is the

shape function. Shape function for each node has a value of one at that node and zero at the other nodes. Within the element, the unknown parameter can vary according to form assigned to shape functions. The variables expressed as a linear combination of the basis function are differentiable as long as the basis functions are differentiable. The triangular discretization is shown in figure 2.4. The control volume is the shaded area and conservation of mass is applied for each control volume shown in blue. However, as integration is a linear function, one can divide the integration over each sub-triangles and evaluate the integration for each sub-triangle by processing the triangles and storing each sub-triangles results in its proper place in the stiffness or mass matrix according to the node id.

$$f(x,y) = \sum f_i \phi_i(x,y) \tag{2.41}$$

in which $f(x,y)$ is any given function, and ϕ is the linear hat or basis function $[-]$. These shape functions are usually linear. As the equation 2.41 shows, the variation in the spatial dimension of the function f is transfered to the variation in the shape function. The only unknowns that remain are the coefficients f_i if the problem is steady state. If there is time dependency in the problem, expressing the unknown can be different from the mentioned equation. A complete coverage of control volume finite element method is beyond the scope of this document.

As HydroGeoSphere solves the flow equations using control volume finite element method, A consistent node centered control volume is developed for the solution the Exner equation in this study.

To solve the Exner equation with control volume finite element method, all the distributed values are expressed in terms of basis function using equation 2.41 as shown in equation 2.42 and 2.43. As in finite element method, the mass matrix and flux vectors are calculated for each element. The only difference is that weighting function used is 1.

$$z(x,y,t) = \sum z_i(t) \phi_i(x,y) \tag{2.42}$$

$$q(x,y,t) = \sum q_i(t) \phi_i(x,y) \tag{2.43}$$

in which q is the sediment flux through the interface and other parameters are defined as before. Replacing the functions with the approximations made and integrating the equations over the part of the region near to each node the equation 2.44 is achieved:

$$\sum \frac{\partial z_i(t)}{\partial t} \iint \phi_i(x,y) \mathrm{d}x\mathrm{d}y = \sum \iint \nabla \cdot q_{is}(t) \phi_i(x,y) \mathrm{d}x\mathrm{d}y \tag{2.44}$$

where z_i is the elevation at point location i $[L]$, and q_{is} is the sediment flux $[L^3T^{-1}]$. With the application of the Guass's theorem, the integral at the right hand side of the equation 2.44 can be evaluated with a line integral as shown in equation 2.45.

$$\sum \iint \nabla \cdot q_{is}(t) \phi_i(x,y) \mathrm{d}x\mathrm{d}y = \sum \oint n \cdot q_{is}(t) \phi_i(x,y) \mathrm{d}s \tag{2.45}$$

in which the integration ($\oint$) is over the boundary of the control volume, n is the normal to the boundary and $\mathrm{d}s$ is the length element on boundary. As integration operator is linear, the integration around the boundary of the control volume carried out for each element separately and the results are added to complete the loop over the control volume as shown in figure 2.4. At the edges shared with two elements, there is no need to calculate fluxes as the normal from one element is the reverse of the normal from

the adjacent element and the results cancel each other out. The only remaining interfaces for the grayed area of interest for the node in the middle of figure 2.5 are pq and qr. To calculate the line integral, a five point quadrature integration method is used. since the integrand is nonlinear, a fifth order integration scheme ensures maximum accuracy.

The final system of equation 2.46 is a time dependent system where M is storage or mass matrix, Q_s is the input flux of sediments per node. This system of equations can be solved with simple time discretization shown in equation 2.47.

$$M\frac{\partial z}{\partial t} = Q_s(t) \tag{2.46}$$

Based on the discretization used, M can be a diagonal or a banded matrix where the elements of matrix are the relative capacity of the nodes to accumulate sediment. Q_s is the sediment flux $[L^3T^{-1}]$. The stability of the time stepping for the equation 2.46 is controlled by the eigen-values of mass matrix M. Refining the mesh will reduce the eigen-values and this in turn requires smaller time steps for the simulation remain stable. As with any transport equation, the

$$M(z(t+\Delta t) - z(t)] = \Delta t\frac{Q_s(t+\Delta t) + Q_s(t)}{2} \tag{2.47}$$

Although M is sparse and constant, making an inverse of this matrix will turn the inverse matrix non-sparse. Depending on the size of the problem, the multiplication of a full matrix can take longer than solution of the system of equations which are sparse. As no coupling is used here between elevation changes and hydrology due to the very small amount of elevation changes during the simulations, the solution proceeds with variable Δt until total simulation time is exhausted. An implementation of this approach can be found in the *hgsModel* class in the appendix section of this document.

2.6 Stream power for two dimensional transient flow

Stream power is the energy content of the flowing water in the surface per unit of time. It is a measure for the ability of streams to incise or erode the river bed [72, 73]. The stream power has been used extensively in rationalizing the fluvial erosion [74, 75, 76, 77, 73, 78]. The stream power used in literature is one dimensional. Here the concept of stream power is generalized to two dimensional surface flow. The specific power stream, which is the stream power per unit area of the stream is calculated for the two dimensional flow and later on is used to compare the resulting flow patterns for scenarios investigated in this study. Total stream power Ω is defined as the potential energy per time as in equation 2.48:

$$\Omega = \rho g Q S = \frac{\Delta P}{\Delta t} \tag{2.48}$$

where P is the potential energy which is defined as gmz where m is the water mass, g is the gravitational constant and z is the elevation component of the location of the mass in gravitational field.

A simple rational can be applied to argue that the stream power in 2d case can be the summation of stream power in both directions as shown in equation 2.52. Assuming a box of dimensions $L \times L \times h$ around the flowing water in river. The change in the potential energy per time is gives as:

$$\frac{\Delta P}{\Delta t} = g\rho LLh\frac{dz}{dt} = g\rho LLh(z_x u_x + z_y u_y) \tag{2.49}$$

where P is the potential energy of the differential element of water $[J]$, t is time $[T]$, g is the gravitational

constant $[LT^{-2}]$, z is surface elevation $[L]$, L is the width of the cube element $[L]$, u_x, u_y and are velocity components in x and y direction $[LT^{-1}]$, z_x, z_y are slopes in x and y direction $[-]$.

$$g\rho wwh(z_x u_x + z_y u_y) = g\rho w s_x Q_x + s_y Q_y \tag{2.50}$$

where Q_x, Q_y are water flux in x and y direction $[L^3T^{-1}]$. To get to the specific stream power, ω, dividing by the surface area of the element L^2, the specific stream power is derived:

$$g\rho(s_x q_x + s_y q_y) \tag{2.51}$$

where q_x, q_y are flow discharge per unit width of the across the cells $[L^3T^{-1}]$. the result is the specific stream power for a two dimensional flow that can be calculated for the scenarios in this case based on the flow velocity and elevation, and the slope of the surface in both directions.

$$\omega = \rho g(q_x s_x + q_y s_y) \tag{2.52}$$

ω is an scalar value $[W]$ which is the product of flow vector $(q_x,\ q_y)$ and energy gradient $(s_x,\ s_y)$.
A more rigorous derivation involves use of the Reynolds' transport theorem:

$$\frac{\Delta PE}{\Delta t} = \frac{D}{Dt}\iint_V g\rho z h\, dx\, dy \tag{2.53}$$

where ρ is the water density flowing on the landscape, z is the elevation of the surface $[L]$, h is the water depth $[L]$. The total derivative can be changed into local time derivative and convective derivative as shown in equation 2.54:

$$\frac{D}{Dt}\iint_A g\rho z h\, dx\, dy = \iint_A \frac{d}{dt}(g\rho z h)\, dx\, dy + \oint_P U_n.\nabla g\rho z h\, dw \tag{2.54}$$

where A is the area of the element projected on the surface $[L^2]$, P is the perimeter of the surface element $[L]$, dw is the differential element of perimeter $[L]$ and U_n is the velocity vector of the fluid normal to the boundary of the element $[LT^{-1}]$. The local derivative is small and can be ignored if the time change of elevation is small. The convective term can be written as equation 2.6:

$$\oint_S U_n.\nabla g\rho h z\, dS = \rho g \oint_S q_x s_x + q_y s_y\, dS \tag{2.55}$$

The flux term in equation is normal to the boundary. The resulting equation is the same formula shown in equation 2.51. The stream power calculated for each cell can be turned into the specific stream power by an inversion using the same mass matrix shown in equation 2.46.

2.7 Abdul catchment test case

Abdul catchment [79] has been used as a test bed for the development of the HydroGeoSphere simulation framework. The catchment covers about $15 \times 80m$ and the mesh that describes the geometry of it consists of 1374 nodes on surface and 2651 triangles. The small number of nodes and the special numbering of the nodes produces a narrowly banded stiffness and mass matrix which helps in faster solution of the problem. This makes it easier to test solution methods and carry out numerical tests on this catchment.

This catchment is only used as a test case in this study. The sediment transport for this catchment is shown at the end of this chapter.

2.7.1 Geometry

The mesh captures the catchment's layout with larger triangles at hill-slopes and smaller triangles in the stream channel. At the left of the catchment. The stream channel is completely horizontal from left to right. There is a small bend in the middle of the catchment which affects the flow field and sediment deposition and erosion. The hill slope at the right side of the catchment is slightly larger in the middle than the other side. So the small asymmetry can help in comparing the effect of slope on the amount of erosion. The slope at the each side is about is about 10%. In turn, it means that if surface soil reaches saturation on the hill-slope and water flows downward, the stream power can be large so that erosion on the hill-slopes can be expected.

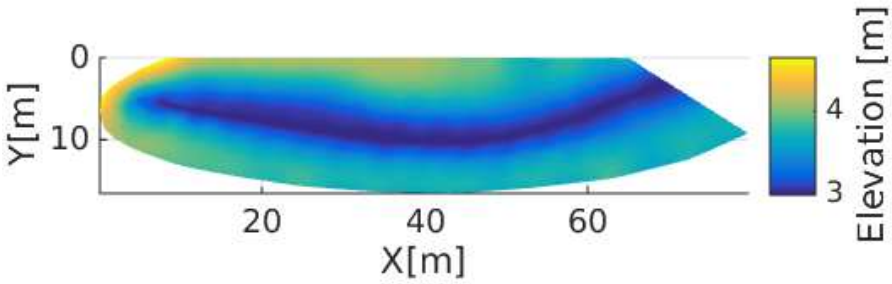

Figure 2.6: The Abdul catchment relief. A small catchment used to study the effects of unsaturated zone on the discharge generation [79]. This small catchment provides a test bed for simulating and testing new methods. In this study, this catchment is used to test the sediment transport.

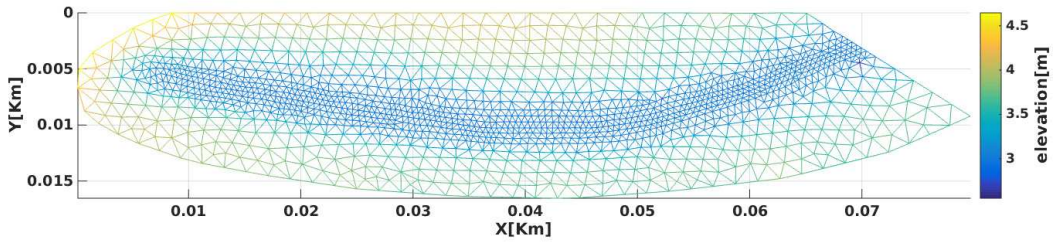

Figure 2.7: The Abdul catchment surface mesh. The river stream mesh is refined to better capture the water flow field on the surface.

2.7.2 Soil type and soil properties

The subsurface material in Abdul catchment is Borden sand [79]. The hydraulic conductivity with respect to pressure heads are shown in figure 2.8. The changes of hydraulic conductivity with respect

Table 2.1: Abdul model hill-slope properties

Manning number $[sm^{-\frac{1}{3}}]$	0.3
Obstruction storage height $[m]$	0.01
Rill storage height $[m]$	0.005
Coupling length $[m]$	0.2

Table 2.2: Abdul model channel properties

Manning number $[sm^{-\frac{1}{3}}]$	0.025
Obstruction storage height $[m]$	0
Rill storage height $[m]$	0
Coupling length $[m]$	0.5

to changes of saturation levels are smooth. This type of material is chosen so that the calculation of the flow field in unsaturated zone would be fast. The Abdul catchment has only one type of subsurface material. The data for soil properties of the Abdul soil type is provided in tabular format as model

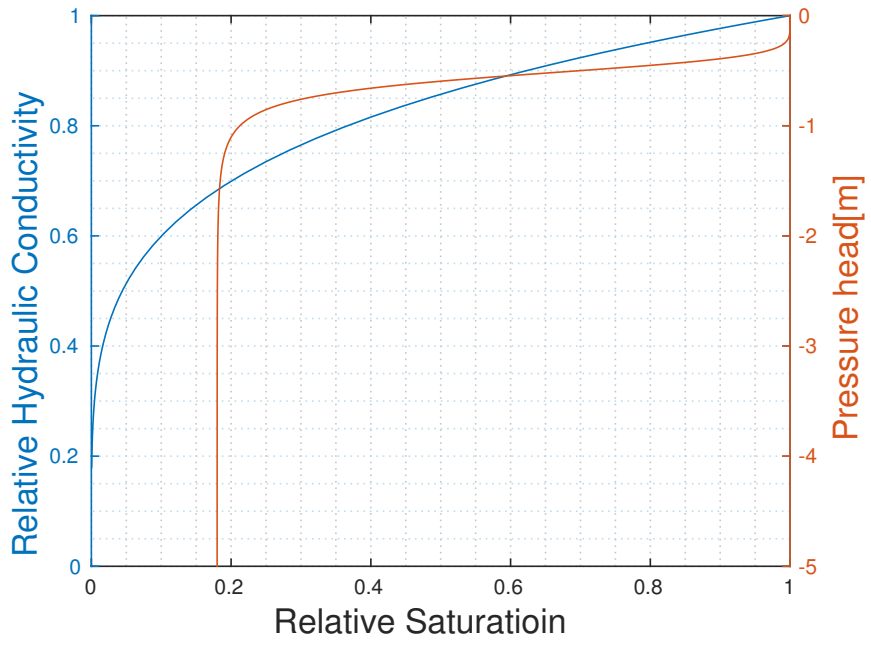

Figure 2.8: Soil properties for sand in the Abdul catchment. The dependence of water content to relative hydraulic conductivity and pressure head is shown here for the Borden sand [79]. There is a significant reduction in pressure head as this type of sand becomes unsaturated. The reduction in the hydraulic head is smooth.

input. For brevity, the data is not given here. The saturated hydraulic conductivity is 10^{-5} $[m/s]$. The other surface properties related to the flow of water and surface and subsurface interaction are shown in table 2.2 and 2.1. The stream channel is smoothed out due to the water flow and therefore it has a smaller friction resistance. The obstruction storage and rill storage account for the micro-topography and built up of the water depth so that water can start to move downhill.

2.7.3 Mesh properties

Mesh of the Abdul catchment is shown in figure 2.7. The mesh size controls the time step size which keeps the integration stable. As this catchment is very small, the size of each triangles in the mesh is also small. This makes the storage with in each cell and consequently the diagonal elements of the M matrix small. The output time steps for this example should be at the about 20 seconds to have a stable time integration for the calculation of the sediment transport. However, as this small catchment has been used as a suitable model for development of many module's in HydroGeoSphere, it is relatively fast and it has been used here as well to test and tweak the parameters of the sediment transport and development of the code.

2.8 Study area: Steinlach catchment

Steinlach catchment is located in the southwest of Germany in the state of Baden-würtemberg. Different layers of soil are identified in the region with a common three degree inclination toward south according to the geological maps. A simplified representation of structural formations in the catchment that are relevant for hydrological model are presented here [80] . The layers are used to define geologic structures with different parameters in the model as shown in figure 2.12. The middle layer is an aquitard. The top layer has a relatively large hydraulic conductivity. The boundary condition for the subsurface is chosen to be of free drainage type around the catchment. This does not affect the discharge as the flux is mostly toward the inside of the catchment except for the regions near the catchment outlet. Steinlach is one of the four catchments that is instrumented by the WESS group [81]. There has been one over flooding event in the Steinlach that rendered the instruments out of order in 2012. The vegetation cover is mostly forested as most of Europe is classified as Cfc under Köppen-Geiger classification system [82]. This indicates that the climate of the catchment is temperate, without any dry season and the summers are mild. The climate of the region excludes the possibility of having tundra or grass lands.

2.8.1 Geometry

Steinlach catchment spans about 25 km in latitude and 25 km in longitude as shown in figure 2.11. The largest part of relief is on the southern part of the catchment and as the river progresses toward the catchment outlet, the land becomes flat with smaller hills and slopes, indicating that the catchment is in the later stages of its evolution. The current land usage is agricultural, urban and forest land. This area was selected because a) it has topographic properties (e.g., size, relief, slopes) typical of many small- to medium-size catchments in southern Germany, b) discharge and precipitation measurements from neighboring station were available for use in this study, and c) the site has been used in other environmental studies [81, 83, 84]. The goal of this study is a sensitivity analysis and parameter study of the effects of precipitation, vegetation and unsaturated-zone processes on erosion rather than a prediction of the catchment's hydrology for management purposes. A simplified conceptual model and input parameters used for simulations are shown in tables 2.4, 2.3 and 2.5. The Steinlach catchment has a total relief of about 600m and a catchment area of 150km^2. Three nearby weather stations record hourly precipitation The digital elevation model (DEM) of the study area is shown in figure 2.10. The DEM is taken from the SRTM project which provides maps with 1 arc second ($\approx 90\ m$) resolution [85]. The catchment is delineated with the hydrological tools from the GRASS GIS software package [86, 87]. The depth of the

Figure 2.9: A measurement station utilized by WESS group. The small control structure is visible in the river. The goal of the small step is to detach downstream from the upstream to acquire a precise reading on the depth, which is turned into total discharge. Total discharge is used here to provide a calibrated catchment.

Table 2.3: Steinlach hill-slope properties

Manning number $[sm^{-\frac{1}{3}}]$	0.25
Obstruction storage height $[m]$	0.01
Rill storage height $[m]$	0.01
Coupling length $[m]$	0.5

model is limited to $100m$ at the catchment outlet with focus on unsaturated zone processes. The first part of this study dealing with effect of precipitation patterns is carried out on a the topography derived from a DEM with $90m$ grid spacing. the later parts require more detailed description of the topography, hence a DEM with a $25m$ grid spacing is employed [85] as shown in figure 2.11. The hydraulic and surface properties of the catchment is shown in tables 2.3 and 2.4.

The lateral boundaries of the model domain are located on the surface water drainage divide. The model initial conditions is a steady-state flow condition with a uniform yearly precipitation of 700 mm/yr (the approximate mean annual precipitation of the region). The triangular mesh generated for the Steinlach catchment is shown in figure 2.14. The river streams have a smaller mesh size in order to capture the flow generation and bank erosion better. An enlarged figure of the mesh for the lower part

Table 2.4: Steinlach channel properties

Manning number $[sm^{-\frac{1}{3}}]$	0.025
Obstruction storage height $[m]$	0.001
Rill storage height $[m]$	0.001
Coupling length $[m]$	0.5

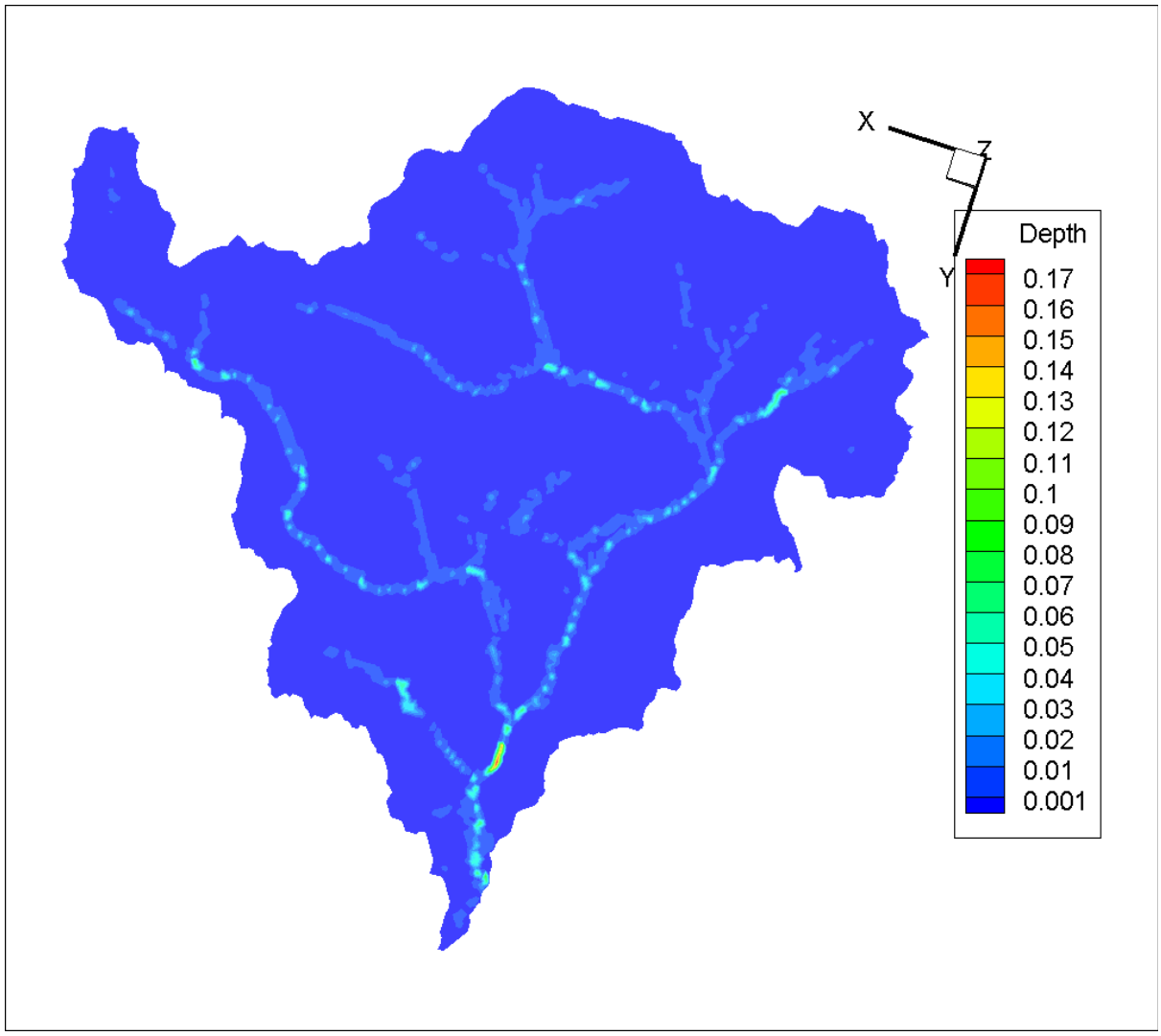

Figure 2.10: Water flow depth with $90m$ resolution. The $90m$ resolution is limited in highlighting the details of the catchment.

of the catchment is shown to give a better visualization of the relative mesh size in figure 2.15. The computational cost of the simulation increase as the mesh is more refined. The current mesh is chosen as a compromise between computationally effectiveness and minimum requirements of the mesh size for a faithful representation of the fluid flow in the rivers for models of this kind. With the mesh shown in figure 2.14, the simulation of the catchment for 1 year with hourly outputs takes about 48 hours on a machine quad core and dual thread machine with a central processing unit of 2.4 GHz and 8 giga byte of random access memory. Generally a mesh size much larger than this is used in order to facilitate faster hydrological simulation.

2.8.2 Lithology of the catchment

The three ornithological layers that are used in the model of Steinlach is summarized in table 2.5. Top layer is mostly sandstone (Lias α Rhät), the middle layer is marl (Knollenmergel) and the bottom layer is again sandstone (Stubensandstein). Although many geologic layers are identified in the region, Only

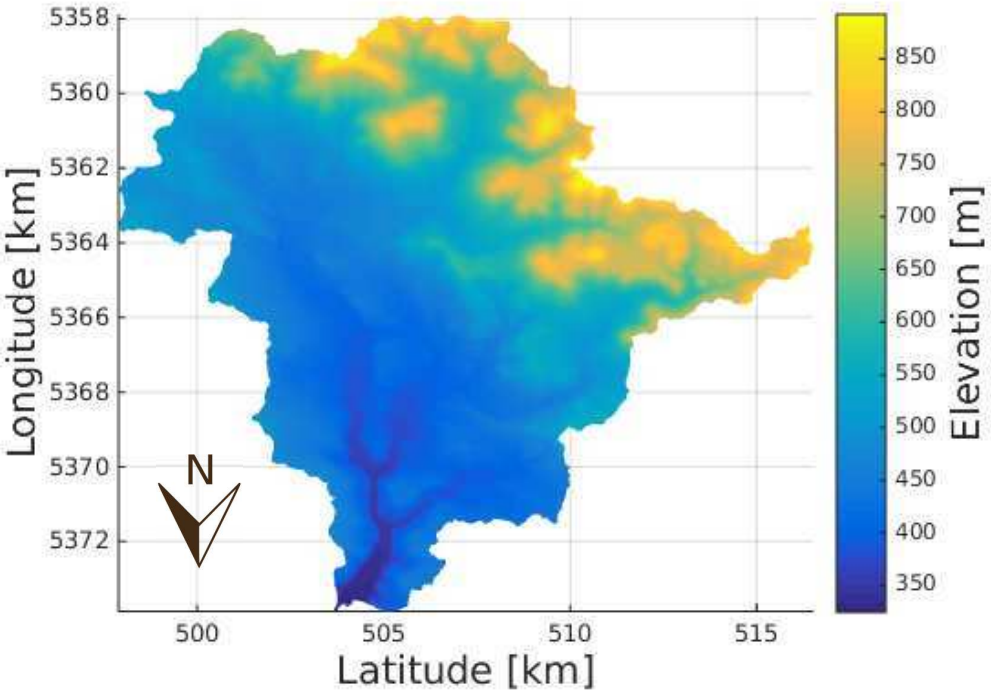

Figure 2.11: The Steinlach catchment relief based on $25m$ resolution of the DEM. The relief is mostly at concentrated to the top of the catchment. The rest of the catchment is relatively flat. This allows the study of sediment production, transport and deposition through various slopes and upstream areas.

three hydraulically distinct layers are used in this model. These layers are named top, middle and bottom layers. Steinlach is a well developed catchment. The relief is mostly concentrated at the south of the catchment. The slopes are steep at the mountainous region and the rest of the catchment has smaller slopes. The mesh is very limited in representing the details of the river channel due to the limitations in computational cost. There is a 3^o of inclination of the layers toward south. The real extent of the subsurface catchment of Steinlach is not known. The free boundary discharge assumptions are made in the boundary.

Table 2.5: Steinlach soil types

Property	Top layer	Middle layer	Bottom layer
Hydraulic conductivity $[m/s]$	$1E^{-5}$	$3E^{-8}$	$1E^{-6}$
Specific storage $[-]$	0.21	0.12	0.21
Porosity $[-]$	0.05	0.41	0.18
Von Genuchten α $[-]$	4.5	4.5	8.7
Von Genuchten n $[-]$	1.3	1.3	1.6
Residual saturation $[-]$	0.1	0.1	0.05
Minimum relative permeability $[m/s]$	$1E^{-19}$	$1E^{-19}$	$1E^{-19}$

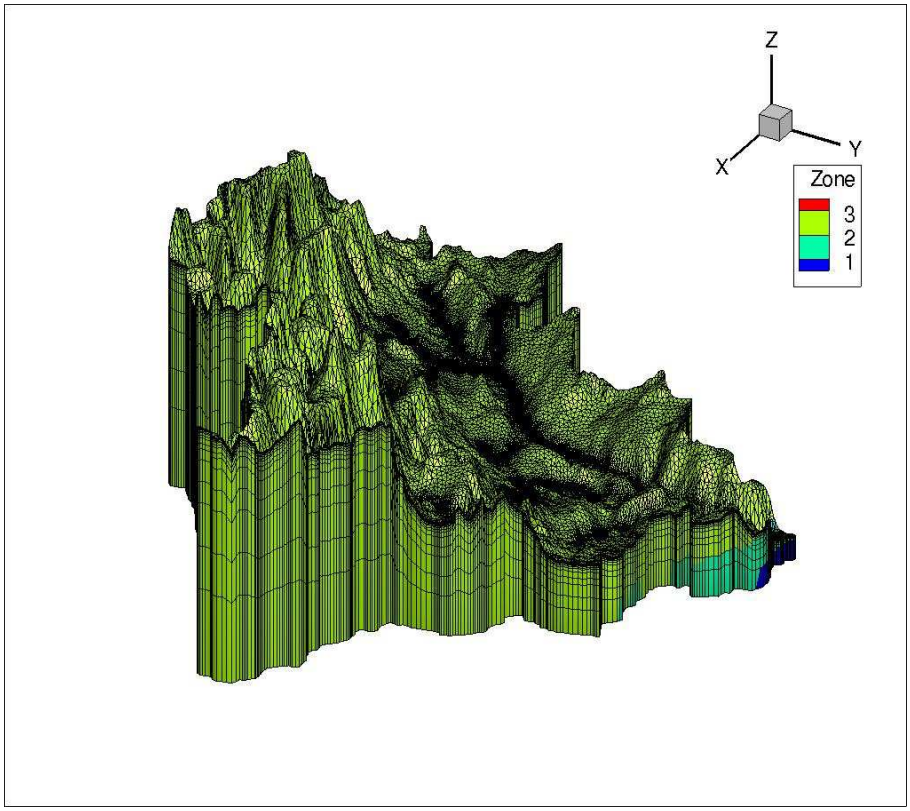

Figure 2.12: The Steinlach catchment subsurface layers (not in scale). The subsurface is divided to 3 layers. The layers are dipping by about 3 degrees to the left of figure. The second layer is an aquitard (low hydraulic conductivity). There are many layers present int the catchment but the hydraulic behaviors are assumed to be presented by one layer in this study.

2.8.3 Hydraulic head monitoring in observation wells

In order to monitor the changes of the water table in the catchment, many observation points are defined in the model as shown in figure 2.16. The wells are placed at hill-slopes and near river streams to see how different parts of the catchment's subsurface react in different scenarios.

2.9 Calibration and data availability

As the current study is focused on study of different parameters, an accurate calibration of the model is not required. The parameters within the physical models define the behavior of the system. In this study, only a **plausible** model is required. Base flow is important as it shows how the surface and subsurface are linked and how they interact to produce the flow in river both during and after a rainfall as shown in figure 2.18. The climate of the region is classified as temperate and the monthly average variation is shown in figure 2.17. Precipitation increases at the summer. Winter and autumn precipitation is slightly less than summer precipitation. This can have implications for the response of the erosion driven under the effect of vegetation and climate change.

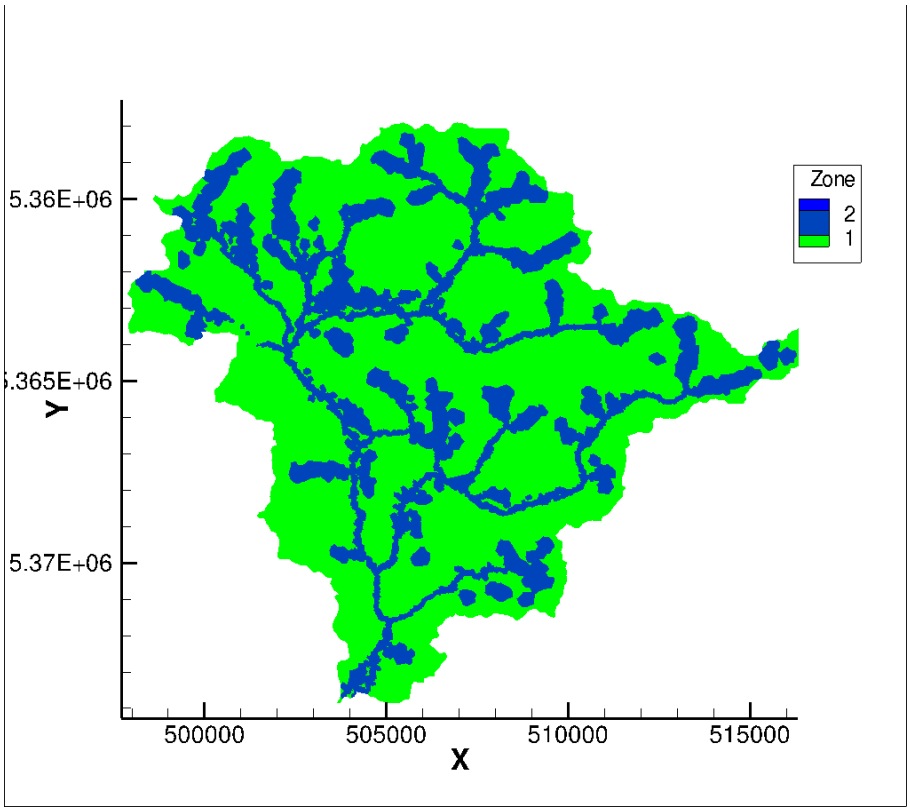

Figure 2.13: Vegetated and river channel networks. Surface of the catchment is divided to vegetated lands where forests grow and a river and flood plane, with no vegetation. The physical properties such as manning number are different for these stream channels and vegetated areas.

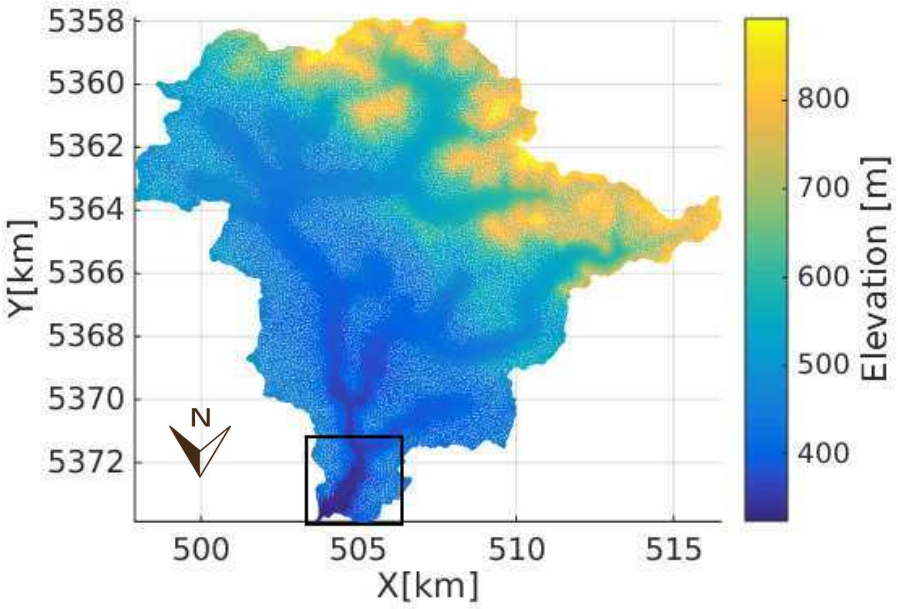

Figure 2.14: The Steinlach mesh. The river streams are refined to give a better view of the riparian flow and exchange process as well as erosion in the river banks. Mesh is produced by GMSH, the gnu mesh generator. An magnified part of the mesh in the black box is also shown at figure 2.15

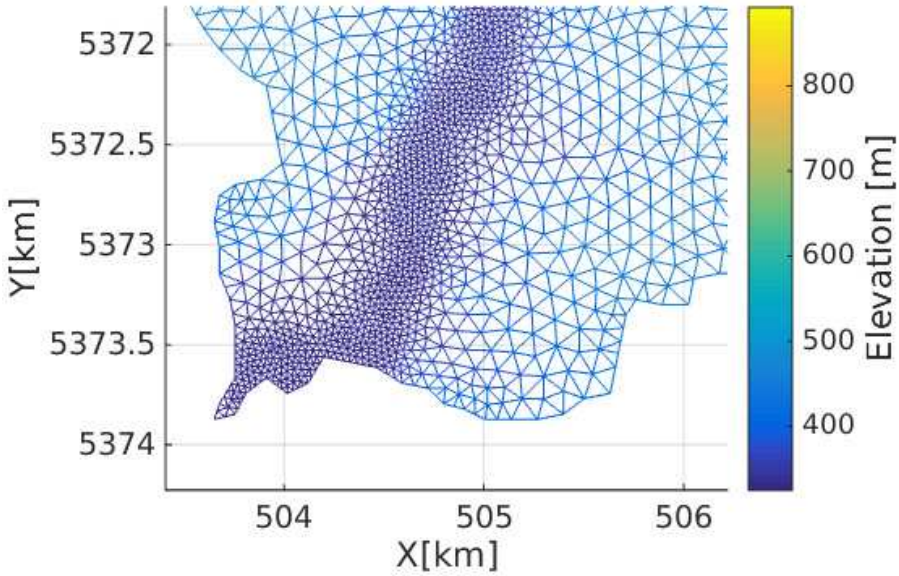

Figure 2.15: The Steinlach mesh at outlet. The outlet part of the mesh showing the mesh refinement. It is essential to keep the number of unknowns to minimum to facilitate lower computational cost

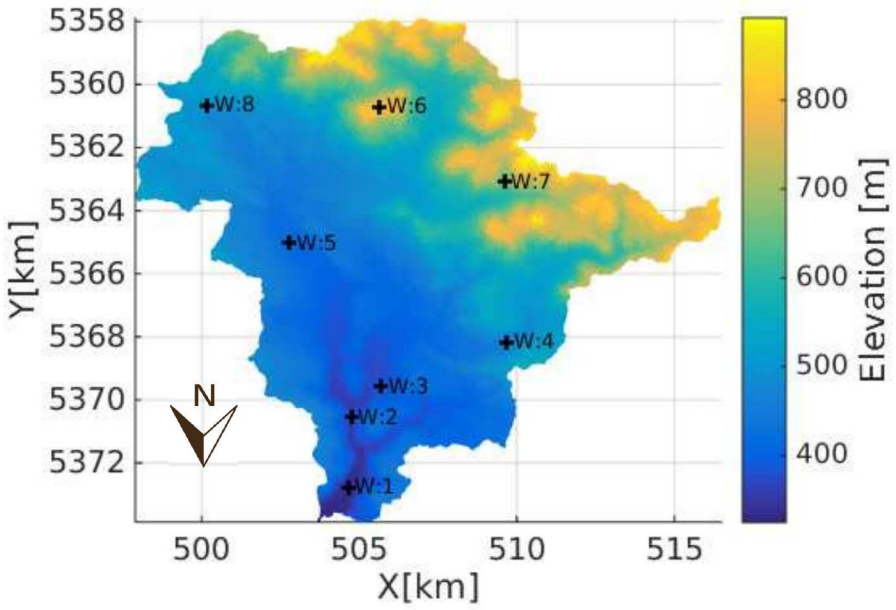

Figure 2.16: Position of observation wells in Steinlach Catchment. Observation wells are placed throughout the catchment ranging from top of the hills, head waters, flood planes and catchment outlets. These provide a glimpse on the subsurface water table fluctuations for the simulations

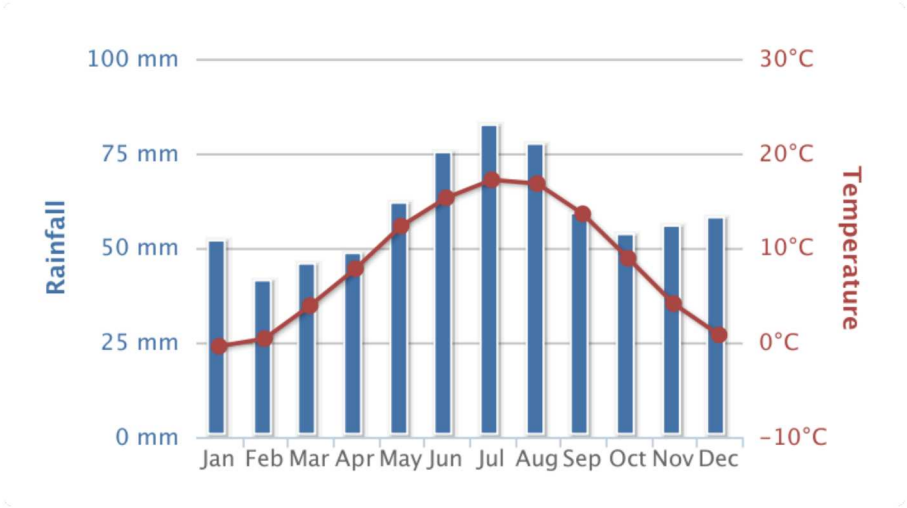

Figure 2.17: Monthly precipitation and temperature for the region from 1900 to 2012. The climate of the region is temperate and there is an all year around precipitation. There is also an increase in the precipitation levels at summer. On average, temperature fluctuates and rarely becomes less than zero.

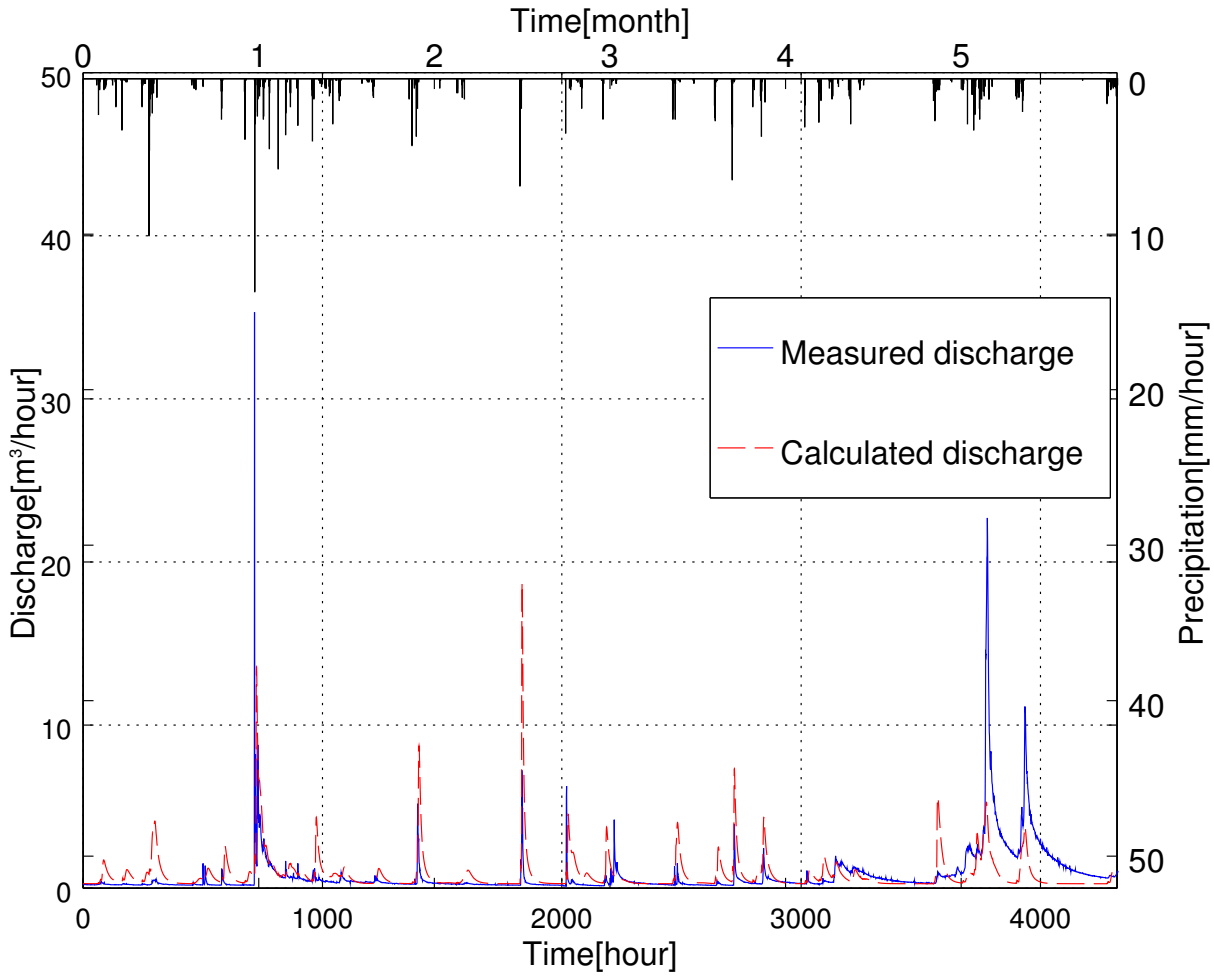

Figure 2.18: The Steinlach calibration is meant to add a layer of confidence to the plausibility of the model used here as the study is mostly based on the effects of many different hydrological parameters on erosion rather than the study of a single catchment.

Table 2.6: Parameters for the erosion in Abdul catchment

Gravitational constant $[m/s^2]$	9.81
Sediment density $[kg/m^3]$	2650
Water density $[kg/m^3]$	1000
Sheilds critical stress $[Pa]$	0.0496
Sediment porosity $[-]$	0.2
Mean sediment diameter $[m]$	0.0005
Empirical parameter (Ks) $[-]$	0.397

Calibrating a complex physical based model is not trivial. As the goal of this study is to have an acceptable model for parameter studies, calibration is carried out on the basis of reproducing main features of the discharge. HydroGeoSphere is used mostly for problems where LAI value is lower than 2. This also reflects that it has been used mostly for much larger scales. The densely vegetated models are rarely reported in literature [28]. A review of the parameters used for the evapotranspiration and leaf interception can be found in [28].

Hourly precipitation data of the three nearest weather stations were used from the German weather service (DWD) to provide a starting point for the analysis of the effects of precipitation patterns on erosion.

2.10 A small test case: erosion on Abdul catchment

There is no analytical solution to be used as verification for the sediment transport process due to its nonlinear structure of sediment transport equation. A simple catchment such as Abdul provides a suitable test bed to run multiple simulations and test to see if the computation's are reasonable. A suit of parameters that are used to calculate Abdul catchment erosion and deposition, with formulation presented at equation 2.35 to equation 2.46 is shown in table 2.6. By trial and error, a suitable time step established for the time stepping and HydroGeoSphere is set to output water heads for the given time step. The output is then used to calculate the erosion and deposition in the catchment as shown in figure 2.19 for every 15 seconds. Erosion in Abdul catchment shows a good qualitative representation of how water flow affects and erodes small catchments. Region encircled as A in figure 2.19 shows the largest sediment deposition. Point A is the start of the stream flow and therefore it does not have enough flow discharge to move the sediment. From both sides of point A, bank erosion brings sediments in to the region and the material stays there. Regions similar to point B show hill-slope processes and smaller amount of erosion compared to similar points located at the opposite side of the stream labeled as C. At the bank with smaller slope, the amount of erosion and deposition are the same. At regions located at the points labeled with C, there is a larger amount of erosion and gullying that can be observed. The length of the stream labeled as E does not show any deposition as this part of the stream transports the regolith due to higher discharge contributions. Hill-slope process are enhanced due to larger slope at sides labeled with C. At the start of the reach of stream labeled as F, channel has a slight bend and this slows down water flow and deposition is enhanced at the bend. Reach F also shows some deposition of sediment. The emergent erosion and deposition pattern is the result of 7200 seconds of simulation with 15 output intervals.

The water depth envelop for the duration of the simulation is shown in figure 2.20. Maximum water depth of $12cm$ in the stream channel is observed for the duration of the simulation. The sharp decrease

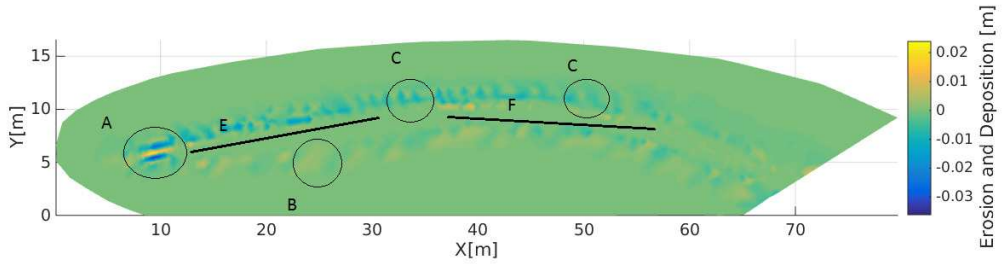

Figure 2.19: Erosion and deposition patterns in Abdul catchment show gullying and transport and deposition. The effect of slope can be seen by comparing the erosion in two sides of the channel.

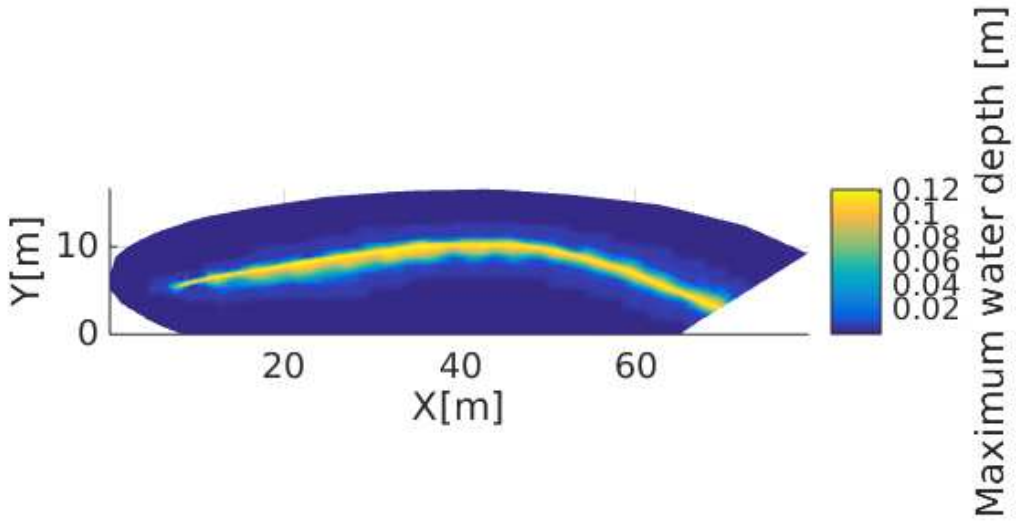

Figure 2.20: Maximum water depth envelop for Abdul catchment. Water depth and slope define the stream power which produce the erosive force.

of water depth at the right bank shows that it is steeper than left bank. Water depth recorded at the hill-slopes are a small fraction of the largest water depth, but combined with a slope of 10%, it is possible for the flow to erode the hill-slopes and the make visible gullies as shown in figure 2.19.

Chapter 3

Effects of precipitation patterns on erosion

Controls on topographic development such as tectonic uplift, hillslope processes, fluvial, glacial and eolian forces have been widely studied. The field has revitalized over recent years because of the potential coupling of erosion and atmospheric, biologic, and lithospheric processes [88, 89, 90, 24, 3, 71, 91, 92, 93, 94]. A potentially significant factor influencing catchment erosion is the frequency and magnitude of precipitation events [95, 96, 97]. However, the current knowledge is lacking in how climate change and short-term distribution of precipitation events affect fluvial erosion, considering the infiltration and response of subsurface storage. Isolating the effects of different precipitation patterns and its effect on the long term evolution of the catchment has been studied with various methods [38, 97, 98, 88, 99]. In this study, previous contributions are complemented by quantifying the transient unsaturated-zone response to different precipitation distributions to show how the coupled surface and subsurface flow influence runoff generation, river discharge and ultimately shear stresses river stream bed.

Previous studies document how climate and topography influence catchment runoff and river discharge, as well as the shape of hydrograph [100, 101, 9]. Recent work has demonstrated that the spatial distribution of precipitation plays a less important role on hydrograph peaks than does the temporal distribution of precipitation [102, 103]. Peaks in river discharge are influenced by the antecedent subsurface saturation levels [104, 105]. It is observed that saturated regions in the catchment enhance runoff production, hence it is suggested that unsaturated zone flow in the subsurface is important for quantifying how temporal variations in precipitation can influence runoff and subsequently erosion [102]. This part of the current study is focused on the precipitation patterns and frequency of rain events effect on activating fluvial erosion considering the subsurface and surface interactions. Any precipitation pattern can be characterized with its intensity, duration and dry period before the event. These characteristics has shown to have exponential probability distributions *pdf* [106] and has been shown to be a good estimator for short-term precipitation time series of up to five years. The mean values of these characteristics are shown in table 3.1. The surrounding weather stations exhibit similar precipitation pattern records as shown in table 3.1. The effects of the climate change on the precipitation patterns are regional. At many temperate regions, the total change in precipitation is very small, however, there will be an increase in intensity and duration at some seasons and a decrease at some other seasons[107]. Intensity duration curves will be reshaped without the total annual precipitation changing extensively as shown in figure

Table 3.1: Precipitation statistics of the three recording stations nearest to the catchment.

	Herrenburg	Metzingen	Rottenburg
Mean duration [hour]	3.14	3.21	3.12
Total precipitation [mm]	574	527	697
Mean intensity [mm/hour]	0.86	0.76	0.92
Mean dry intervals [hour]	21.09	20.46	19.81
Number of events	211	216	223

3.1.

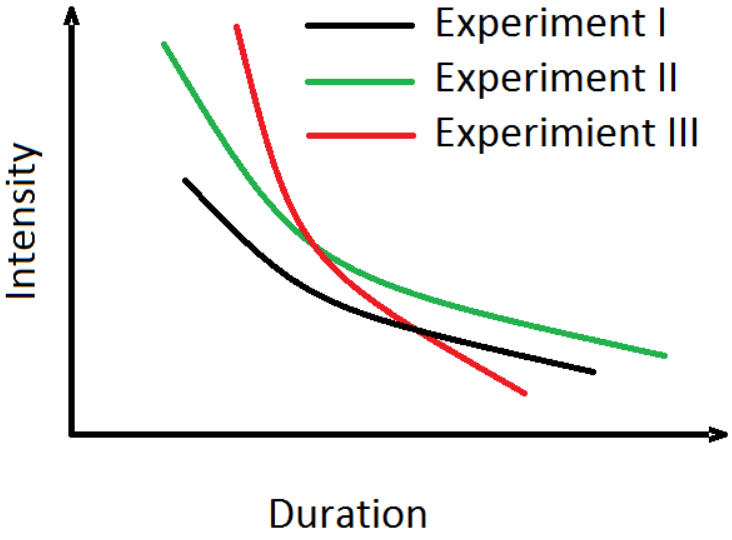

Figure 3.1: A conceptual graph of enforced IDF properties on generated precipitation patterns. A method is developed to produce a fixed total annual precipitation

3.1 Generation of different precipitation patterns

Synthetic time series of precipitation events were generated by modifying the characteristics of the probability distribution functions of the observed measurements. The total amount of yearly precipitation is fixed to 700 mm. Three exponential *pdf*s are used to characterize the precipitation events: one for the intensity P $[LT^{-1}]$ of the individual precipitation events, one for the duration D $[T]$ of these events, and one for the time intervals I $[T]$ between individual events. These three precipitation elements (intensity, duration, and interval) are the basis for the simulations for the quantification of the effects of precipitation patterns on erosion.

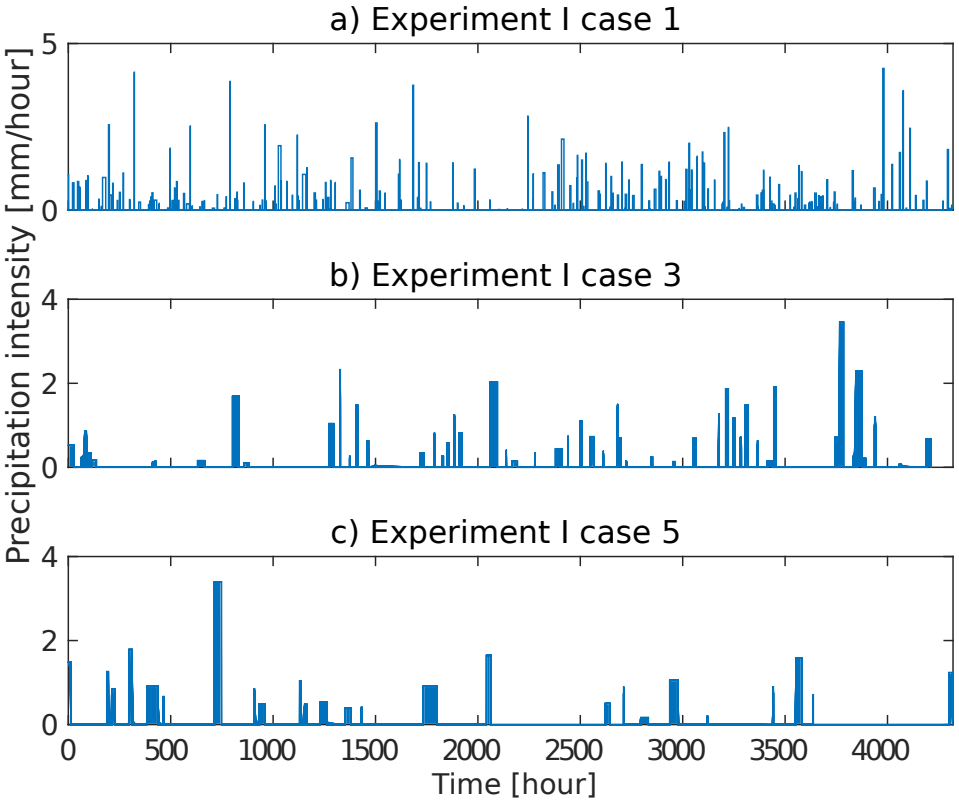

Figure 3.2: Example precipitation distributions used in simulations and produced from the exponential distribution (see text and Table 3, 4, 5 for explanation). Only case 1, 3 and 5 for experiment I are shown here for brevity. The increase of dry intervals and the increase in duration can be seen in case 3 and case 5. The mean precipitation intensity is constant in the experiments. Thus, the precipitation events adds up to the same total amount, but the precipitation characteristics are different for each case and experiment.

$$\begin{aligned} f(P) &= \frac{1}{\overline{P}} \exp\left(-\frac{P}{\overline{P}}\right) \\ f(D) &= \frac{1}{\overline{D}} \exp\left(-\frac{D}{\overline{D}}\right) \\ f(I) &= \frac{1}{\overline{I}} \exp\left(-\frac{I}{\overline{I}}\right) \end{aligned} \tag{3.1}$$

The exponential *pdf* requires only a single parameter, namely the mean value of the observations, indicated in equation 3.1. The exponential distribution function is the maxentropic distribution for a semi-infinite variable characterized by a single parameter; it describes events that become less frequent as the magnitude of the event increases. This function is used in many weather generators [108, 109] and also in the CHILD landscape evolution model [10, 11] to generate precipitation events. The parameters needed for the generation of rainfall events were derived from measurements at the three weather stations closest to the catchment. Using these parameters, many precipitation realizations are produced to act

as the base case for the catchment. This method restricts the precipitation events to cases with identical total precipitation volume V_{fixed} over the fixed time period T_{fixed} of six months, leading to the following conditions:

$$\begin{aligned} \sum_{i=1}^{n} P_i D_i &= V_{fixed} \\ \sum_{i=1}^{n} D_i + I_i &= T_{fixed} \end{aligned} \tag{3.2}$$

Because P, D, and I are exponential distributions, the following expected values $E[\bullet]$ are known:

$$\begin{aligned} E\left[\sum_{i=1}^{n} P_i D_i\right] &= n\bar{P}\,\bar{D} \\ E\left[\sum_{i=1}^{n} D_i + I_i\right] &= n\left(\bar{D} + \bar{I}\right) \end{aligned} \tag{3.3}$$

From above expressions, it can be seen that out of the four parameters that define the precipitation pattern, n, $\bar{P}$, $\bar{D}$, $\bar{I}$, only two can be changed independently. Depending on the parameter being changed in each experiment, the number of events or one of the other event characteristics can be calculated as a dependent variable. Since the artificially generated precipitation events are drawn from random distributions, the likelihood of exactly meeting the conditions of equations 3.3 and 3.2 is low. Therefore the conditions are relaxed by introducing relative tolerance criteria ε_i:

$$\left\| \sum_{i=1}^{n} (P_i D_i) - V_{fixed} \right\|_2 < \varepsilon_1 V_{fixed} \tag{3.4}$$

$$\left\| \sum_{i=1}^{n} (D_i + I_i) - T_{fixed} \right\|_2 < \varepsilon_2 T_{fixed} \tag{3.5}$$

In order to obtain precipitation time series with the correct mean, two error margins are introduced to cover a rectangular area of the probability space as shown in equations 3.4 and 3.5. The values for ε_1 and ε_2 are taken to be half a percent for both total duration and total precipitation. Making the error margins too small would causes a high fraction of rejected realizations for the tolerance criteria. A reasonable choice of the error margins can be as high as one percent, since the variation in the precipitation from year to year is larger than one percent of the mean precipitation in general. The values of these error margins is low enough that the variations in discharge or shear stress can be attributed only to the changes in the patterns of the precipitation. It is possible to also treat the number of events as a random variable with a normal distribution. This requires further data to establish the standard deviation and mean. However, treating the number of events as an extra random variable will add an extra degree of freedom to the parameters without changing the results significantly. Therefore n is calculated and taken as a constant for each case in each experiment. By rejecting the realizations that don't fall into the error margin, the posterior statistics of the accepted realizations are guaranteed to meet the desired statistics. An example realization of a precipitation time series is shown in figure 3.2.

Table 3.2: Precipitation metrics for experiment I with uniform mean precipitation intensity and total precipitation of 700 mm/year.

	case 1	case 2	case 3	case 4	case 5
Intensity (mm/hour)	0.76	0.76	0.76	0.76	0.76
Duration (hour)	3.21	6.24	12.84	19.26	25.68
Intervals (hour)	16.78	33.58	67.16	100.74	134.32
Number of events	216	108	54	36	27

Table 3.3: Precipitation metrics for experiment II with uniform mean precipitation duration and total precipitation of 700 mm/year.

	case 1	case 2	case 3	case 4	case 5
Intensity (mm/hour)	0.76	1.52	3.04	4.56	6.08
Duration (hour)	3.21	3.21	3.21	3.21	3.21
Intervals (hour)	16.79	36.79	76.79	116.79	156.79
Number of events	216	108	54	36	27

Using the sample and reject method developed here, 300 time series of precipitation events are generated for the three different experiments: keeping the mean precipitation intensity (experiment I), the mean precipitation duration (experiment II), respectively the mean number of events (experiment III) constant. Total precipitation was 700 mm/year in all realizations. Each experiment is subdivided into five cases of twenty realizations each. The cases differ in the mean of the two remaining variables characterizing the precipitation events. In addition to the previous stochastic realizations, regular precipitation events were simulated , in which the mean values of precipitation intensity, precipitation duration, and dry intervals were taken to be constant. These simulations are denoted as "regular precipitation". Tables 3.2, 3.4 list the metrics of all cases considered in the study.

3.2 How is discharge affected by precipitation patterns?

Figure 3.3 shows the hydrographs at the catchment outlet for the regular precipitation events. For each experiment (i.e., I, II, and III), the output hydrograph for cases 1 to 5 are color coded. The vertical axis is the discharge from the catchment in m^3/s and the horizontal axis is limited to about seven days of the simulation period. The subplot (a) in figure 3.3 is the hydrographs of experiment I with the inputs as shown in table 3.2. The (b) and (c) subplots correspond to the experiment II and III as shown in tables 3.3 and 3.4. For experiment I and II, the interaction of the base flow and the surface runoff can be seen. In the subplot (c) of this figure, for the experiment III, the baseflow disappears as the precipitation events are close to each other and the dry intervals are small.

Table 3.4: Precipitation metrics for experiment III with uniform mean number of events and total precipitation of 700 mm/year.

	case 1	case 2	case 3	case 4	case 5
Intensity (mm/hour)	0.76	1.52	3.04	4.56	6.08
Duration (hour)	3.21	1.60	0.80	0.53	0.40
Intervals (hour)	16.79	18.39	19.19	19.46	19.59
Number of events	216	216	216	216	216

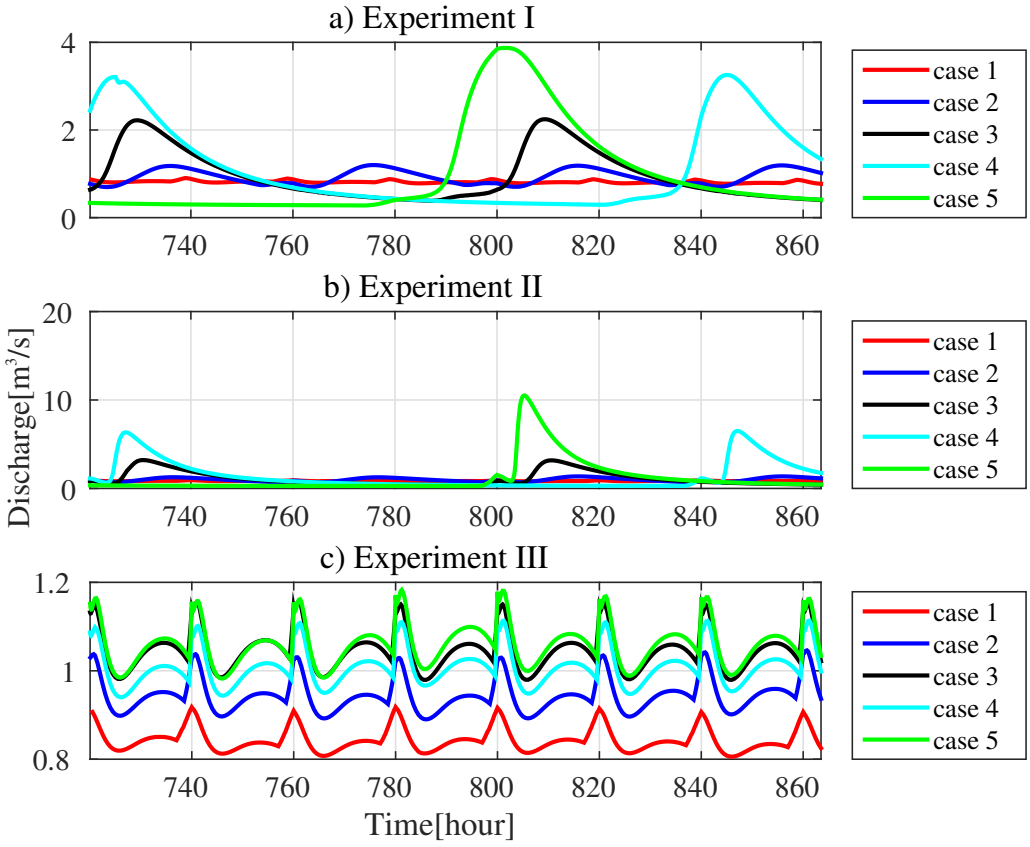

Figure 3.3: Hydrographs for regular precipitation events $[m^3/s]$. As the duration and dry interval increase, the hydrograph peaks become larger and base flow becomes smaller for experiment I. For experiment II, the peaks are at largest with the increase of intensity and dry intervals. Experiment III shows how the base flow changes and how the hydrograph shifts upward with the increase of intensity and decrease of duration for a constant dry interval.

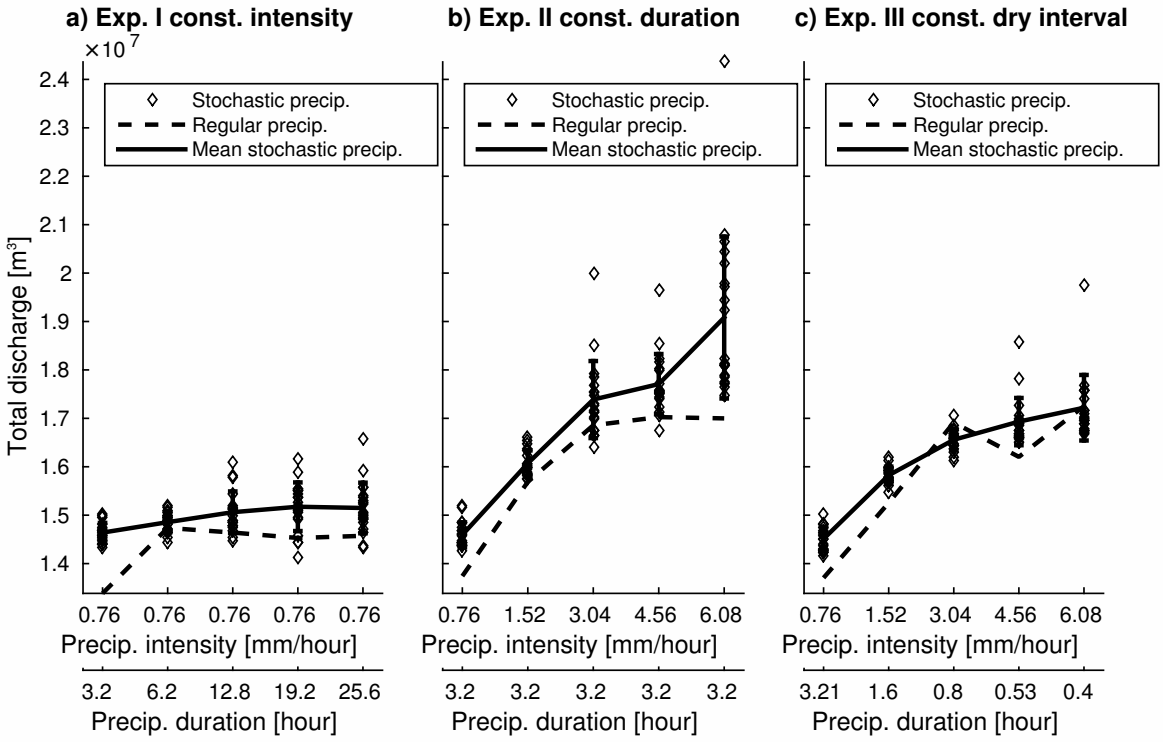

Figure 3.4: Total discharge for regular and stochastic precipitation events $[Pa]$. Instantaneous discharge is summed up over the simulation period to produce total discharge. Regular and stochastic precipitations cases (tables: 3.2, 3.3 and 3.4) produce similar discharge. The largest discharges are associated with large intensities of precipitation in experiment II (b) and III (c). Constant mean duration (experiment II) produce larger discharge rather than smaller durations (b). The error bars indicate one standard deviation for the stochastic precipitations.

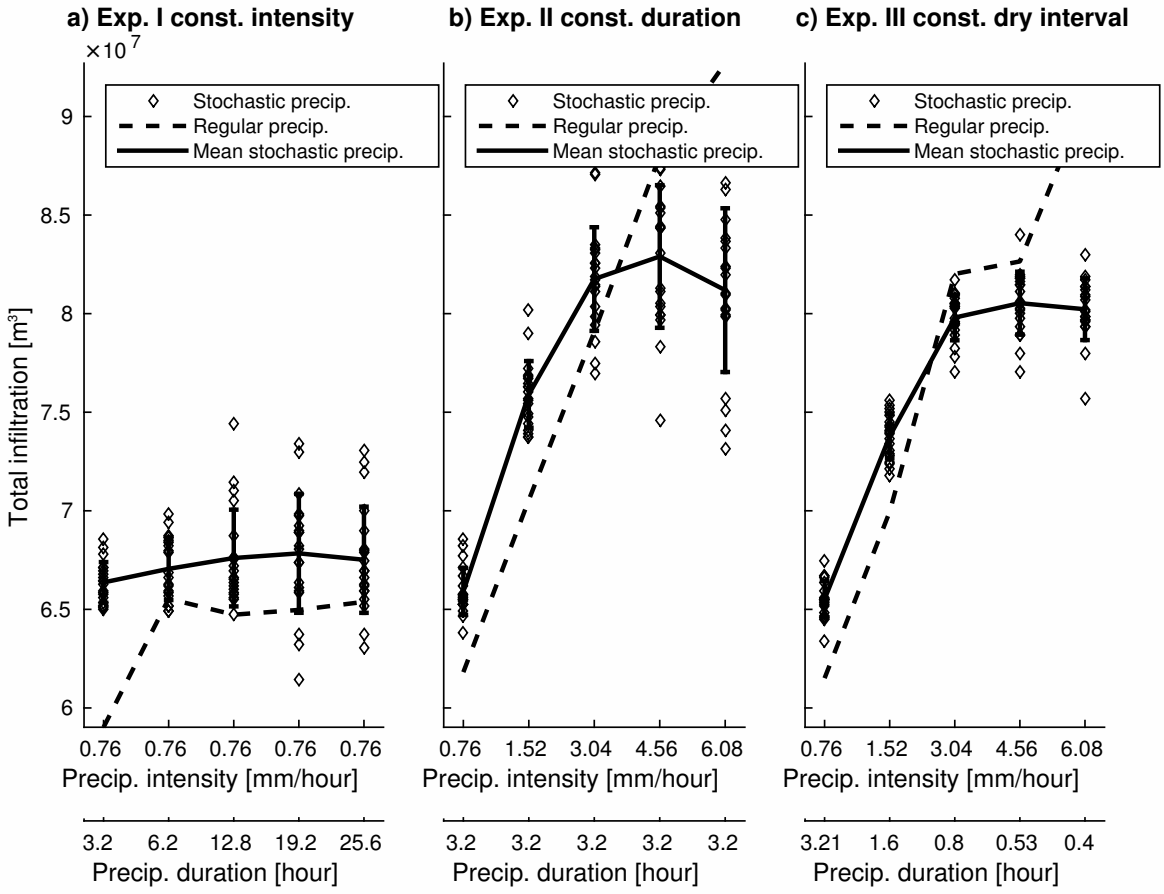

Figure 3.5: Total infiltration for experiments $[m^3]$. Regular and stochastic cases follow the same trend except for the extreme intensities in experiment II (b) and III (c). The infiltration rates for experiment I is constant as the mean intensity is constant for this experiment (a). With the increase of intensity in experiment II and III (b and c), the infiltration increase and then decreases. The decrease happens when the surface layer becomes fully saturated and limits the infiltration. The error bars indicate one standard deviation for the stochastic precipitations.

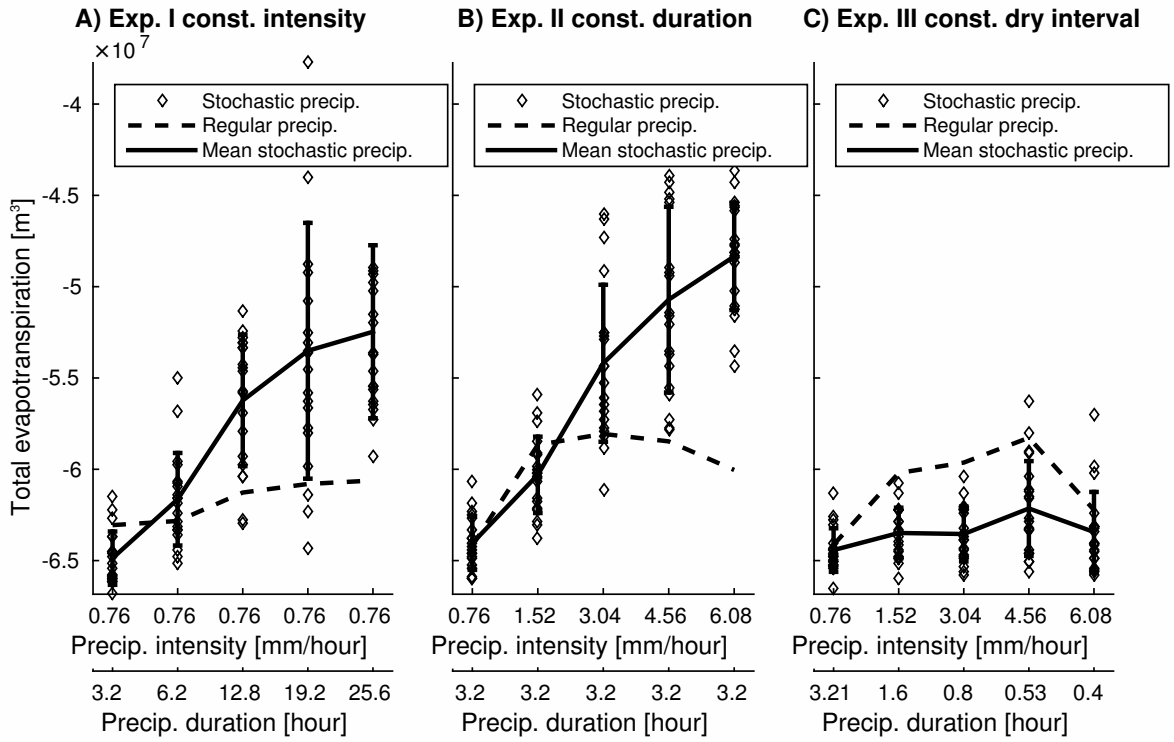

Figure 3.6: Total evapotranspiration for experiments $[m^3]$. Evapotranspiration removes water from the catchment such that the values are negative. Experiment I and II show a reduction in evapotranspiration as the number of events decrease (a, b). The dry intervals increase so the surface water availability decreases. For experiment III (c), the surface water availability is constant as the dry intervals are short and the number of precipitation events are more than experiments I and II. The error bars indicate one standard deviation for the stochastic precipitations.

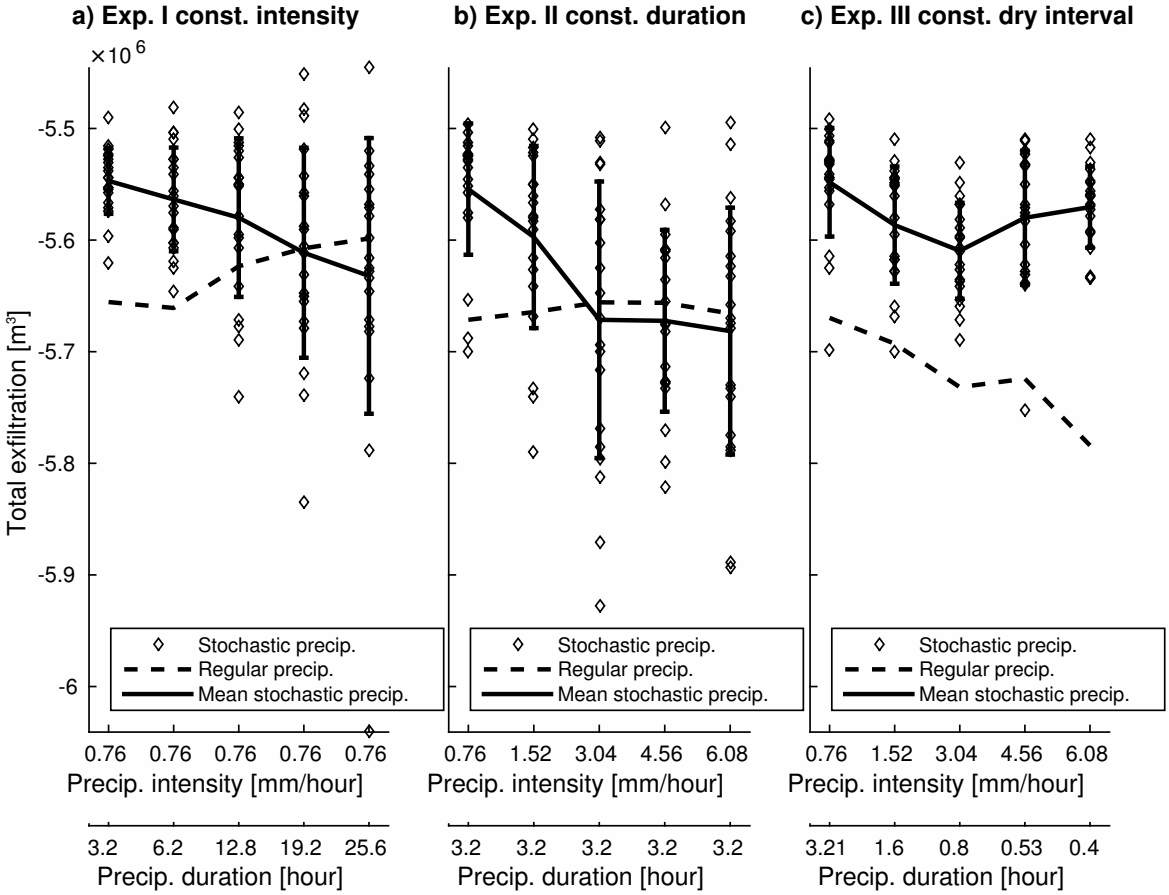

Figure 3.7: Total exfiltration (cross flow to the river) $[m^3]$. Exfiltration or cross flow is water sourced from that subsurface that feeds the river. The total exfiltration is small compared to infiltration or evapotranspiration. The overall variation in the exfiltration is also small compared to variations in other variables. The error bars indicate one standard deviation for the stochastic precipitations.

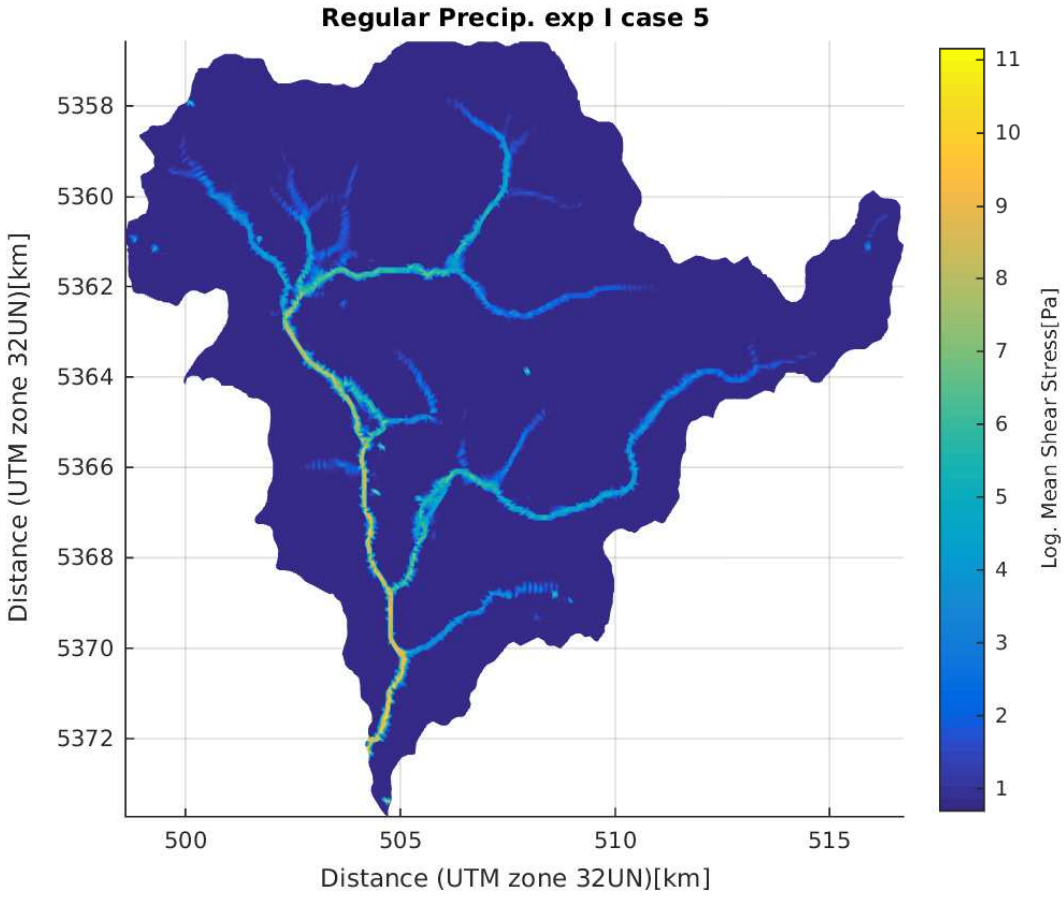

Figure 3.8: Spatial distribution of the shear stress over the river network $[Pa]$. This simulation acts as the basis for comparison between the three experiments. The spatial distribution of the regular precipitation pattern for experiment I, case 5 (table 3.2) is shown here. The values are in logarithmic scale to show the smaller variations. The increase of shear as the tributaries add discharge to the channel can be seen.

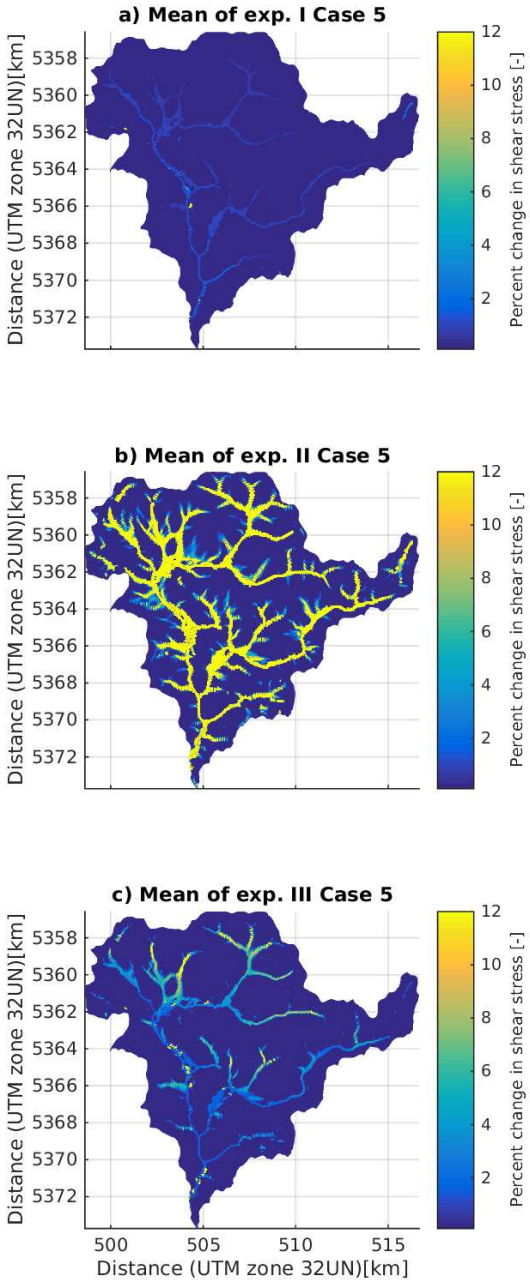

Figure 3.9: The percent changes of spatial distribution of the shear stress over the river network [Pa]. Changes in mean shear stress distribution over the river stream for experiment I,II and III case number 5 of 20 simulations for each experiment respectively shown here in a,b and c. There is a large difference in the shear stress magnitude for experiment II (b) where the intensity is high and duration is relative long. Experiment I (a) and Experiment III (c) have similar ranges of levels of shear stress. The drainage network is well defined in experiment II(b) even in head water regions. Experiment I and III are most likely to be dominated by hillslope processes and produce a smooth landscape.

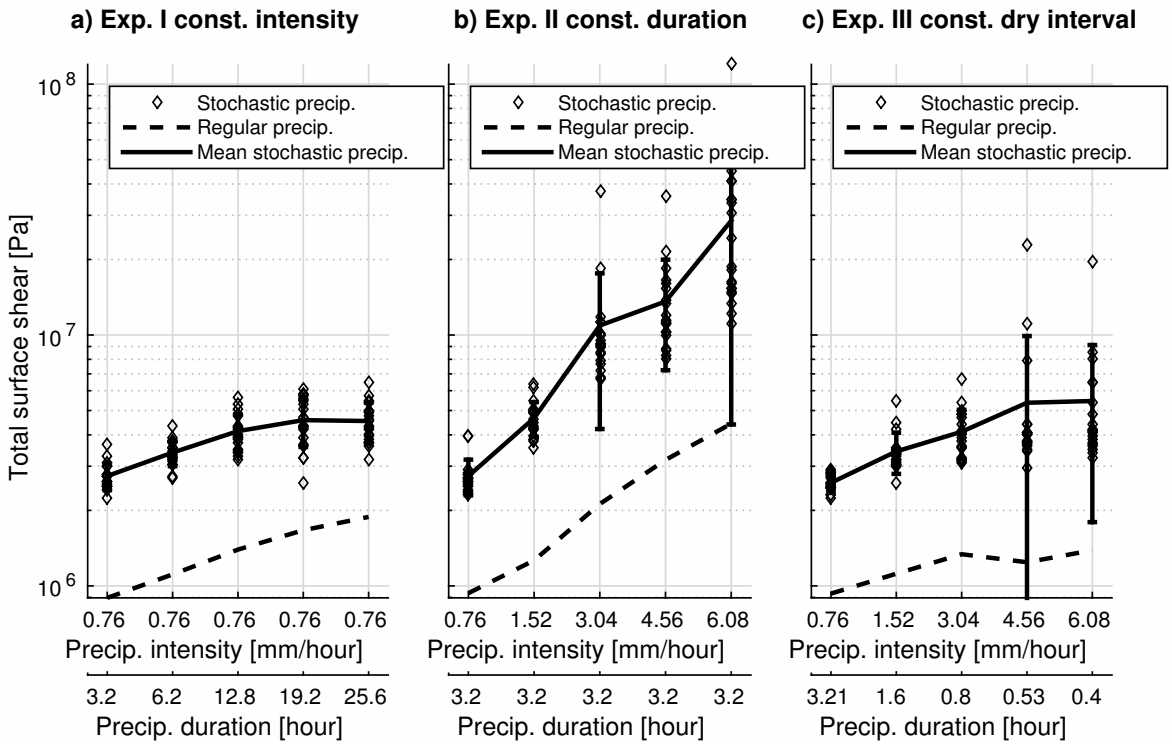

Figure 3.10: Total shear stress for regular and stochastic precipitation events [Pa]. The distributed shear stress is integrated over the catchment surface for the entire simulation period to give a single number representing the erosion potential of moving water in the river channel. The trends in shear stress is different from the total discharge. Shear stress for experiment II(b) follows the discharge trend, which indicates a strong correlation, but for the experiment III(c), where the intensity is the same as experiment II(b), the shear stress is almost constant while the total discharge increases. The one standard deviation is small for experiments I and III(c). Experiment II(b) is more sensitive to the precipitation patterns. The error bars indicate one standard deviation for the stochastic precipitations.

Figure 3.4 shows the total discharge at the catchment outlet, for all cases of the three experiments. The regular precipitation discharge is shown with dashed lines, whereas the continuous lines show the stochastic precipitation discharges. The error bars centered about the mean value for stochastic precipitations indicate ± one standard deviation. The largest discharge is observed in experiment II (figure 3.4b) where the intensities are larger and the mean duration is constant. The second largest discharge occurs in the experiment III (figure 3.4c), where the precipitation intensity increases as the durations decrease. From experiment II and III, it is possible to conclude that total discharge can increase if the mean of intensities increase. However, the increase is asymptotic as the total volume of precipitation is limited. In experiments II and III, the increase in total discharge from case 1 to case 5 is about 25%. In experiment I, where the mean intensity is constant and precipitation durations and dry intervals increase, the total discharge is almost constant. The precipitation is partitioned to infiltration, exfiltration, and evapotranspiration within the HydroGeoSphere model according to conceptual understanding and modeling of the hydrological cycle. This partitioning depends on the duration and intensity of precipitation events and the duration of dry periods. Figure 3.5 shows the total amount of infiltrated water in each experiment. For experiment II and III (figure 3.5b, 3.5c), where the precipitation intensities increase, the infiltration increases and becomes constant. The increasing trend of discharge in experiment II and III are the same, despite the differences in the precipitations characteristics for these experiments. Infiltration capacity is the maximum volumetric water that can flow into subsurface per unit of area in time. Figure 3.5b and 3.5c show that with the increase of precipitation intensity, total infiltration increases in the catchment until the precipitation intensity reaches to about $4mm/hour$. The increase of infiltration stops at the mentioned value regardless of the duration of the events. It can be deduced that a tentative value for the infiltration capacity of the catchment is $4mm/hour$. The increase of the infiltration in the experiment II and III is about 12%. For experiment I (figure 3.5a), the infiltration is constant as the infiltration capacity is never reached since the intensity of the precipitation is small. Figure 3.6 shows the total evapotranspiration from the surface and subsurface. For experiments I and II (Figure 3.6a, 3.6b), the evapotranspiration decreases, and for experiment III, the evapotranspiration remains constant and high. Experiment I and II have larger dry intervals and as the dry intervals become larger, the availability of the water for evapotranspiration decreases. Experiment III is composed of many precipitation events with short dry intervals. This allows for the surface and upper layers of the subsurface to store water which facilitates evapotranspiration. The decrease in evapotranspiration in experiments I and II from case 1 to 5 is about 30%.

Figure 3.7 shows the contribution of the groundwater table and bank storage to the river discharge. The infiltrated part of the precipitation that is stored in the porous medium and enters the river is the base flow of the river. The exfiltration is negative according to the conventions of Hydrogesphere as it leaves the porous medium. The total variation in exfiltration is one order of magnitude smaller than other partitioned components. Since flow in porous media is governed by potential difference and governed by Darcy flow in this scale, the exfiltration rates to the river are almost at the same scale.

3.3 Shear stress at the riverbanks and riverbed

Figure 3.10 shows the total integrated shear stress calculated on the surface of the catchment. The total shear stress in the catchment is computed using equation 2.35, integrated over the entire surface flow area and the total 6 month simulation duration. The plot is in semi-log scale in the vertical axis to make

small values visible. Experiments I and III (Figure 3.10a, 3.10c) show a small increase of total shear stress for the corresponding changes in the precipitation characteristics, whereas changes in experiment II is about one order of magnitude larger. While the total discharge from the catchment has the same trend with increasing precipitation intensity in experiments II and III (Figure 3.10b, 3.10c), the trends in shear stress do not follow the increasing trends in the precipitation intensities. The total surface shear increases with the increase of precipitation intensity as shown in figure 3.10b. In figure 3.10c the increase of total surface shear is about 30% of the experiment II and the shear stress do not increase from case 4 to case 5. This exemplifies that the most effective shear stress is on the surface flow, and thus the largest erosive power, occurs in cases in which the intensity is high and the duration is long enough to achieve cumulative large discharge from all sub-catchments into the main stream.

3.4 Results

3.4.1 Experiment I: Constant Mean Intensity

In this experiment, the mean precipitation intensity is kept constant and the mean duration of precipitation events and dry intervals increase by a factor of two from cases 1 to 5. To keep the total precipitation constant, the number of events decreases for cases 1 to 5 as listed in table 3.2. This kind of climate can be seen in rainy seasons of semi-arid or wet areas. The regular precipitation events are introduced first.

The regular experiment hydrographs, in figure 3.3a shows that with increasing the duration of precipitation events and dry intervals, the peak flow increases and the base flow decreases. With the increase of mean duration in the stochastic precipitation simulations, the total discharge (dashed line in figure 3.4a) shows a slight increase at first and remains almost constant with longer durations. The total infiltration (solid line in figure 3.5a) remains constant as well.

The stochastic realizations have the same mean values as the corresponding regular case (see table 3.2). but the parameters the define them are realizations from exponential *pdf*s. Applying the exponential *pdf*, smaller values of the precipitation and dry-interval durations are more frequent than larger values. As shown in figure 3.4a, the regular case provides the lower limit for the stochastic discharge, whereas the total shear stress hardly differs between the regular and stochastic results (see solid and dashed lines in figure 3.10a).

For experiment I , the evapotranspiration decreases and exfiltration slightly increases as shown by figures 3.6a and 3.7a. Total shear stress over the surface remains almost constant with increasing duration of precipitation events and dry intervals (dashed line in figure 3.10a). In these simulations the shear stress required to exceed the critical shear stress for sediment mobilization is low enough that base flow conditions would not contribute to erosion. In comparison to the experiment II (figure 3.10b), the total shear stress is relatively small in experiment I and significant impact on catchment erosion is not anticipated.

In experiment I, the intensity of precipitation does not exceed the infiltration capacity of the soil, so that infiltration can act as sink for surface flow throughout the precipitation events. This is illustrated by the lines of figure 3.5a. Furthermore, storing the water in the shallow subsurface facilitates extended evapotranspiration, which increases with the duration of dry intervals (figure 3.6a). Total Exfiltration into the rivers, plotted in figure 3.7a does not show a strong dependence on the duration of precipitation events and dry intervals; in fact it only slightly differs between the different experiments.

3.4.2 Experiment II: Constant Mean Duration

In this experiment, the mean duration is constant, whereas the intensity of precipitation events and the duration of the dry intervals increases from cases 1 to 5 (see table 3.3). This distribution of precipitation implies that the total number of events decrease to keep the total precipitation constant. In this experiment, the peaks of the hydrographs are larger and narrower than in experiment I, which can be seen in figure 3.3b.

The base flow decreases with the increase of the peak flow. The peak discharge is approximately twice as large as in the corresponding cases in experiment I (figure 3.4a, 3.4b). With the increase of intensity, the total discharge increases for the stochastic and regular precipitations as shown in figure 3.4b, respectively. The infiltration increases until the precipitation intensity reaches the maximum infiltration capacity of the soil as shown in figure 3.5b (solid line). The evapotranspiration decreases as shown in figure 3.6b (solid line). Evaporation decreases because with few precipitation events the near surface layer becomes dryer and less water is available for evapotranspiration. There is a notable difference between regular and stochastic simulations for the total evapotranspiration as shown in Figure 3.6b (solid line for stochastic and dashed line for regular precipitations): In the stochastic simulations, a few large events produce most of the precipitation over a short duration. This water does not reside at the surface or in the shallow subsurface long enough to facilitate extended evapotranspiration.

As shown in Figure 3.7b (solid line), the total exfiltration in experiment II is almost constant regardless of intensity of precipitation. Though the overall variation in the exfiltration between experiments are small, this experiment shows the largest exfiltration to the river.

Figure 3.10b (solid line) shows that the total shear stress for this experiment. The shear stress increases with an increase in precipitation intensity, following the same trend of the total discharge. The mean increase in total shear stress is about 22% from one case to the subsequent case and in total a mean increase of almost 90% from cases 1 to 5 in experiment II. The variations in the observed shear stress per case is also much larger than in the other experiments. This shows that the shear stress is much more sensitive to larger mean precipitation intensities when the precipitation durations are adequately long.

3.4.3 Experiment III: Constant Mean Duration of Dry Intervals

In this experiment (see Table 3.4 for parameters), increasing the intensity of precipitation events goes along with decreasing the duration. The mean duration of the dry intervals remain almost constant and the number of events is also constant for each case. This kind of precipitation distribution can be found in very wet climates. The hydrographs for this experiment with regular precipitation are shown in the Figure 3.3c. Since the duration of the dry intervals is shorter than the residence time of the catchment, no return to true base flow is observed in regular precipitations (Figure 3.3c). The solid lines of Figure 3.4c show that the discharge increases with increasing precipitation intensity. This trend is similar to that of experiment II. The infiltration capacity of the top soil responds to the increase in intensity, and total infiltration is reduced with increasing intensity as shown in Figure 3.5c (solid line). Figure 3.6c illustrates that mean is almost constant, regardless of the precipitation intensity. This is explained by high number of events keeping the shallow subsurface and surface wet. Exfiltration to the rivers is also almost constant as shown in Figure 3.7c but, as already stated, the difference compared to the other experiments is small.

In experiment II, the surface shear stress increases slightly with increasing precipitation intensity and approaches an asymptomatic value (see solid line in Figure 3.10b). In this experiment, shorter durations

of the precipitation events prevent addition of flow to the main channel, thus leading to less total shear stress, and since the base flow almost disappears and is replaced with the discharge from precipitations, the total discharge is also increasing as shown in Figure 3.4c. The variations in the shear stress for each case is smaller than the corresponding case to experiment II, indicating that the duration of precipitations events exerts a strong control in the resulting total shear stress in the catchment.

3.5 Conclusions

The main objective of this study was to show how unsaturated-zone processes influence the potential for fluvial erosion when precipitation patterns change in a catchment. As the model used in this study is more accurate in routing the flow both on the surface and in the subsurface, the shear force distribution on the surface of the catchment is more accurate than those produced by static routing used in current geologic time landscape evolution and sediment transport models such as CHILD [110] and tRIBS [111]. There fore the results of the simulations carried out here can represent the hydrologic behavior of the catchment more accurately than the methods generally used in geodynamics discussed in chapter two. Though the shear stress is used as a surrogate to erosion, it is expected that the dependence of erosion on the bed shear stress would result in similar patterns as the shear stress.

Effects of storm duration on erosion have been considered by scaling the total flow passing through any point of the catchment with the ratio of the precipitation-event duration to the residence time [38]. It is shown that this scaling of the peak discharge with duration of the precipitation events, impacts the geomorphology of the catchment over geologic times. Based on the results of this study, it is possible that climatic variations can result in different catchment morphology. The simulation results show that shear stress pattern response of the catchment is not the same for the changes in precipitation intensity and event duration. An average shear stress of about $100Pa$ is distributed throughout the river stream in the catchment for the increasing precipitation intensities with a fixed mean duration. At the other hand, the same value of shear stress is spatially limited to the larger slopes in the mountainous regions for the increasing precipitation events with decreasing durations. The fixed mean intensity events do not produce the same level of shear stress distributions the shear stress of about $10Pa$ is observed in the river stream. The long term evolution of a landscape is the accumulation of the smaller changes and disturbances that occur in time. The simulation period in this part of the study is limited to six month. However, the spatial distribution of the shear stress patterns are different. The difference reaches up to one order of magnitude. It is logical to assume that the differences in shear stress predicted here for the six month will accumulate over geological times to result in a different landscapes. The computational cost of these simulations do not allow a geologic time scale simulation, however as shown by the use of less costly computational models [38], the expectation of having different looking landscape is not beyond reason.

The experiments II and III can be seen as an special case of variations in precipitation duration where a strict total precipitation is applied as a constraint. To compare the spatial distribution of shear stress over the catchment, the regular precipitation of the experiment I, case 5 is chosen as a base (table 3.2). Case 5 is chosen because it is an extreme case for all of the three experiments and the differences is more pronounced. The base case is shown from figure 3.8. The logarithmic changes in the variations in spatial distribution of the shear stress for case 5 of the experiments I, II and III are shown in figure (3.9). Subplot a, b and c correspond with the experiment I, II and III. As it is also shown in figure 3.10, the

shear stress for the experiment II is one order of magnitude larger on average. Shear stress in experiment I and III (figure 3.9a and 3.9c) are the same order of magnitude and have the same spatial extent. For the experiment II (figure 3.9b), the faster erosion rates in the river stream can trigger larger amounts of sediment from the hillslope processes and the amount of the sediment transport rate can be estimated to be higher than the other two experiments. The shear stress for experiment II (figure 3.9b) is larger in the head water regions of the watershed as well is there are a stronger shear stress in the floodplains compared to experiment I and III. The shear stress in experiment I and III is not only smaller, but mostly limited to river channels with the exception of the headwaters in the experiment III as can be seen from figure 3.9c. The differences in drainage density is also significant between experiment II and experiments I and III. Though, in some respects, experiment I and III look similar, the long term evolution of these two systems are not certain to be similar. The experiment III has more erosive potential in head waters and hills compared to experiment I (figure 3.9a and 3.9c). It can be interpreted that the higher elevations can be consumed more rapidly in experiment III where the intensity is higher than experiment I. It is also argued that climatic driven incision can be hard to be distinguished from tectonic driven patterns even when there are distinctive patterns in the landscape that hint to the climatic driven incision [90]. The results of experiments show that the various patterns of climatic change can have a variety of erosional powers which can make the distinction of climatic and tectonic driven erosion even more challenging. For example, distinguishing patterns in experiment I and III can be difficult as they produce almost the same magnitude of shear stress as shown in figure 3.9a and 3.9c.

Chapter 4

Effects of vegetation type on hydrology and erosion

The interaction of climate and geomorphology has been studied extensively [37, 63, 89, 112]. Though it is still computationally prohibitive to keep track of subsurface soil saturation and its movement accurately for geological time scales, many simplifications make it possible to have conceptual and physical models that can illuminate the role of subsurface and its interaction with vegetation in landscape evolution dynamics. With accounting for transpiration and keeping track of the subsurface soil saturation levels, it has been shown that climate and vegetation are linked and co-evolve to produce different aspects in southern and northern hemispheres due to the solar irradiation [113, 40, 16, 114]. Apart from the long term evolution of the catchment that can take millions of years, short term phenomena like soil loss and desertification are also a motive for understanding how vegetation affects fluvial erosion. This can show us how planting trees and reforestation can be made more effective in reducing erosion rates [22, 23, 22, 115].

Adding sediment transport to the integrated hydrological model is shown to be computationally challenging [117, 118]. It is argued that the runoff generation can be better understood if the role of the subsurface flow field is taken into account [119, 120, 121, 120, 121]. Lague et al. [119] argue that a physics based understanding of the hydrology can be a solid foundation for quantification of the interactions between biology and geomorphology. As argued in chapter two, the physics based hydrological models capture the surface and subsurface interactions. The importance of the interaction between surface and subsurface can vary depending on the conditions of the catchments. As a measure of linkage between surface and subsurface, a dimensionless number is proposed by Gleeson [122]. This number quantifies the importance of the linkage between the subsurface water levels and the surface topography, showing that climate can act as a long term control on the evolution or stability of the surface. Topographically controlled water tables indicate a lower recharge rate or higher aridity. At humid climates with higher recharge rates, the water table is usually near surface and has a strong influence on the runoff generation, bank storage activation and discharge to the river streams.
The large scale control of vegetation on erosion rates are established by observations made in sediment transported in large rivers by Langbein [123]. It is shown that the highest rates of erosion are in the regions where vegetation density is low with adequate precipitation to mobilize the regolith. The semi arid lands therefore are at the largest risk of the erosion and soil loss.

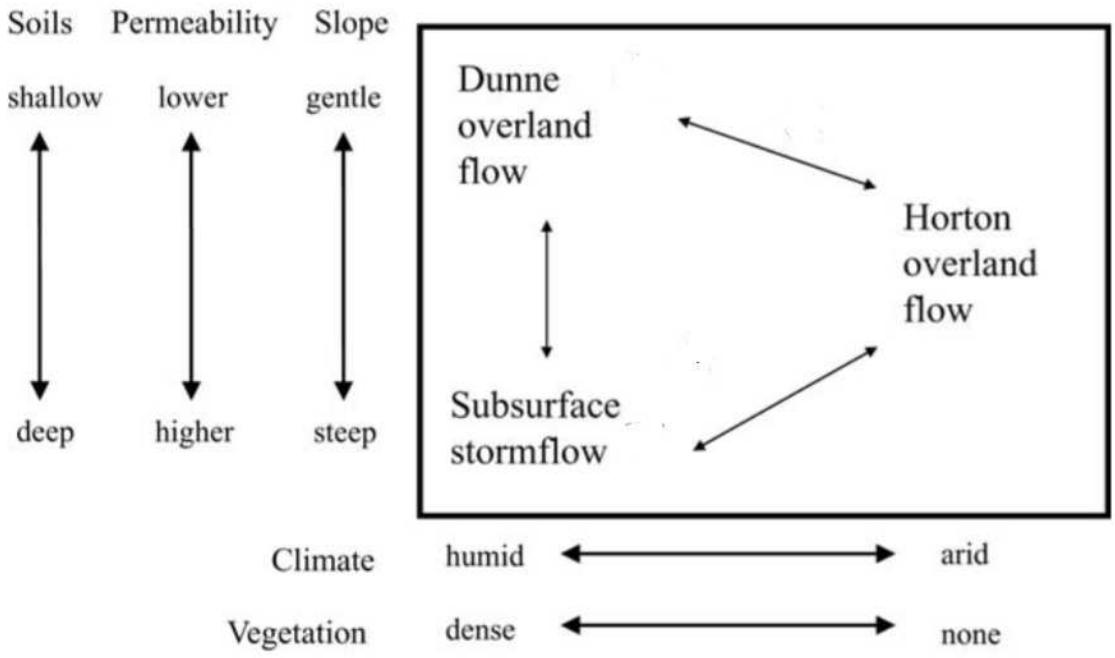

Figure 4.1: Dunne diagram identifies three different ways that a catchment can respond to precipitation. The precipitation can infiltrate in to the subsurface in its entirety. Runoff can be generated where there is a saturation excess or runoff can be generated where there is an infiltration excess. These three types of runoff generation are controlled by vegetation, topography, precipitation and soil properties [116].

The accumulation of knowledge on how various parameters control runoff are conceptualized by Dunne [116, 124, 120, 125]. The Dunne diagram identifies the hydrologic, topographic and biologic factors that control the runoff generation and provides a conceptual map for understanding the response of a catchment. The Dunne diagram is shown in figure 4.1. Large catchments are not limited to one type of behavior as delineated by the Dunne. The distribution of the slopes for example, can be variable in middle aged catchments, where part of the catchment has eroded away and is relatively flat. It is possible to use Dunne diagram as an initial guide to probable runoff generation mechanisms. It can act as a map for identification of the controlling parameters in sub-catchments of a large catchment that have one or more of the identified features in the Dunne diagram.

Vegetation density can affect the hydrological response of a catchment. The natural vegetation of the Steinlach region is temperate forest according to Kottek [126]. Forests show various characteristics depending on the species of the trees growing in them. The growth of the trees in forests need water. The water is captured by the roots of the trees and is transfered by the xylem to the leaves to be used in photosynthesis process. The water transported through the tree trunk is called sap flow. The sap flow measurements show that transpiration is a major part of actual evaporation in forests [127]. The canopy evaporation also is important in forested areas and is studied by various field measurements in Pine forests [128, 129].

The utility of numerical hydrological simulations are demonstrated in the modeling of the forested areas to show the importance of the boundary conditions and grid spacing [130]. It is also shown that vegetation can act as a barrier for the sediment movement and provide protection against erosion [131].

In this research, a different approach for coupling of the erosion and hydrological cycle is taken which has its roots in geomorphological formulation of the surface evolution [8]. This approach relates the sediment flux to the bed shear. Topographic evolution results from the movement of the regolith by water according to Exner equation as explained in chapter two. The bed shear is calculated from the flow which is controlled by the hydrological parameters. HydroGeoSphere allows us to examine the effects of variations in potential evapotranspiration and root depth due to tree types with the use of various input parameters. The input parameters to the model can specify potential evapotranspiration, root depth, canopy size and canopy storage capacity, rill storage and surface manning number. This provides a virtual lab for identification of the first order controls on erosion and sediment transport. In this chapter, the main focus is the study of the effects of canopy size, controlled by the length and extent of the growth season. The goal is to quantify the role of the subsurface and especially the unsaturated zone flow which is regulated by the plant transpiration. The choice of plant type are limited as each climate controls vegetation density. Given a fixed annual precipitation and evaporation, each catchment can support a limited amount of vegetation as the plants will compete for the resources in natural settings [15]. It is established that mean annual temperature and the ratio of evapotranspiration to precipitation known as aridity index control the vegetation type and density. The location of Steinlach catchment with mean annual temperature of about $10\,^oC$ and aridity index of about 0.8 to 1.2 hints toward temperate rain forests or temperate forests. Grasslands, shrubs, tropical forests and other forms of vegetation are not possible in this location. With human interference (logging, land use change, human caused fires) the vegetation density can change and therefore the erosion in the catchment can change which will be addressed in the next chapter.

An important boundary condition in HydroGeoSphere model is the potential evapotranspiration. The actual evapotranspiration amounts to about 64% of the precipitation world wide. As two methods are provided in HydroGeoSphere for the evapotranspiration processes, the question arises which one is the most suitable for the simulation of the forests where there is a large amount of variation in leaf area index (LAI). In the following section, the drawbacks of each of the methods are explored and a proper choice is made based on modeling results and experimental observations made by Food and Agricultural Organization (FAO) [52] and other field studies.

The precipitation patterns are assumed to be the same for all the forest types. Forests of different species can have various temporal distributions of leaves and canopy size throughout the year. With fixing environmental controls such as precipitation, the controlled catchment is studied by the hydrological simulation framework and sediment discharge and erosion rates are determined. This is helpful in understanding a forests response to precipitations based on the tree types and the duration of the growth season. More specifically the effects of the canopy size and root depth on the erosion are studied in this chapter.

4.1 Evapotranspiration modeling for catchments with large variations in LAI

A major draw back of the distributed models is that there is the possibility of over parameterization. As the number of parameters grow, the equations can fit any observation with an acceptable accuracy where some parts of the model can compensate for the behavior of the other parts. This kind of problems are difficult to detect if the models behavior is not studied for the full range of possible parameters. In the

case of HydroGeoSphere, the governing equations are highly nonlinear and the global behavior of the system is not well understood. As the integrated fully coupled models become more prevalent, the need for accuracy in these models increase as researchers want to study minute changes in the hydrological system due to small changes in parameters such as water retention capacity of soils [132, 133]. The difficulty is multiplied when there is no agreed upon method of measuring transpiration and evaporation and all measurement methods do not produce the same results [129, 134]. However, the basic and physically acceptable picture can be put together from physical principals and observations [135, 136]. Furthermore using sensitivity analysis techniques, it has been shown that spatial distribution of potential evapotranspiration have a significant role in the catchments behavior [137].
HydroGeoSphere divides total evapotranspiration into four parts. However, estimates of potential evapotranspiration usually produce one total rate as shown in the calculation of the evapotranspiration in chapter two. Here, the Penman-Monteith equation is used to estimate the potential evapotranspiration. The formulation of Penman-Monteith presented in chapter two and further details can be obtained from [52].

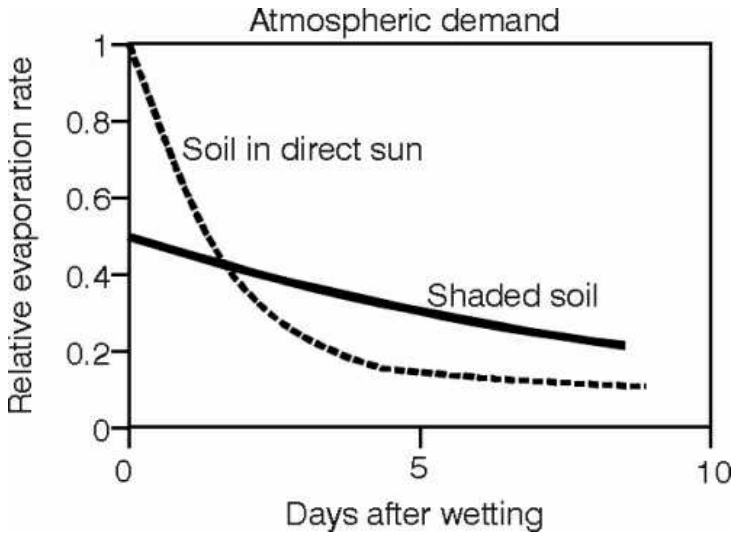

Figure 4.2: Relative evaporation rates for shaded and soil exposed to solar radiation. This experiment is reported in FAO56. The strong dependence of the evaporation on the water availability and atmospheric demand rather than solar radiation alone is observed. Solar radiation contributes energy to the evapotranspiration. The sensible heat energy also drives the evaporation in the shaded region. The ratio of shaded to solar evaporation can be different depending on the latitude and time of the year [52].

HydroGeoSphere proposes two methods for the calculation of the evapotranspiration. In a physics based formulation of the hydrological process, having two ways of computing a physical process poses a problem as only one of them can be grounded on physical principals. Both of these methods, break up evapotranspiration to four parts. Each of these parts are deducted from the potential evapotranspiration starting with canopy interception. The plant transpiration is calculated as a function of root distribution and LAI as shown equation 2.11, 2.12 and 2.13.

The first method of calculating evaporation from surface and top soil, referred here as the original

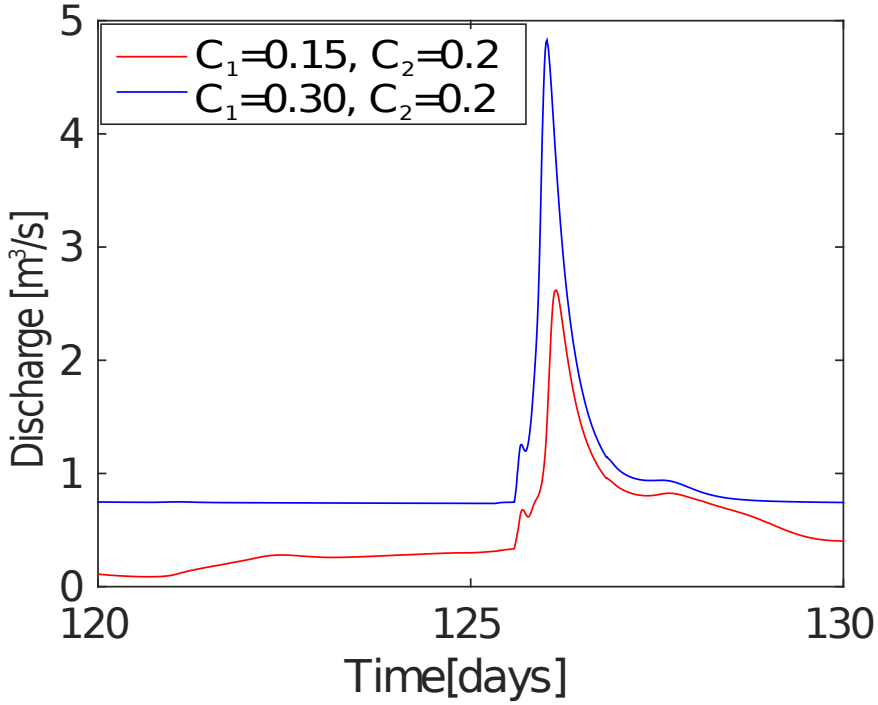

Figure 4.3: Hydrograph for two sets of f_1 function constants. The constants for model in blue line result in larger value of f_1 function and therefore should produce a smaller hydrograph due to larger transpiration. However, since $1 - f_1$ becomes zero, the river discharge shown in hydrograph is larger. This experiment is designed to show the problem of having two evapotranspiration methods just by changing the constants inf f_1 and keeping the LAI parameter constant.

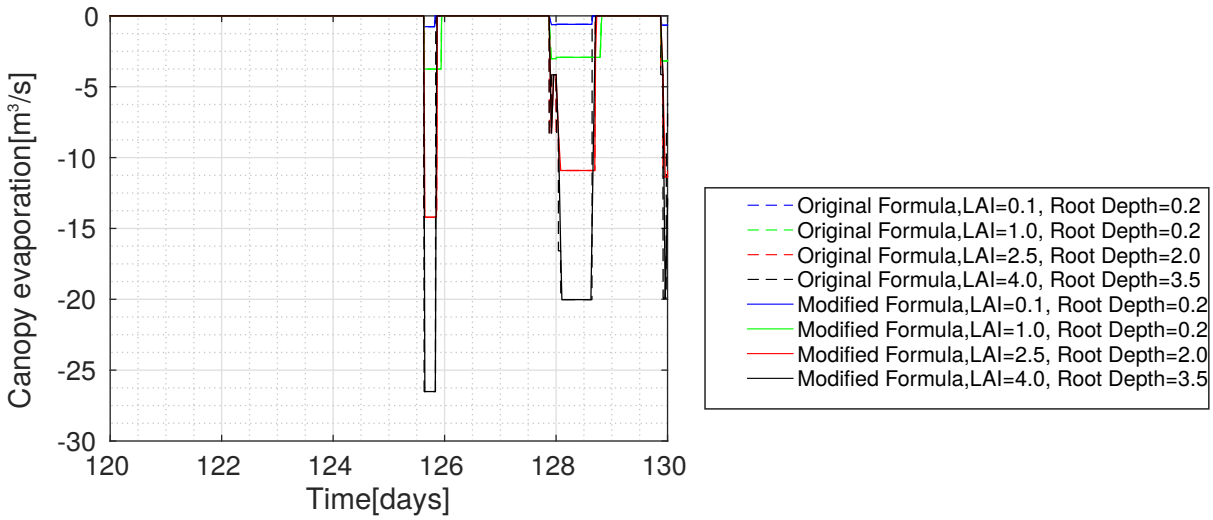

Figure 4.4: Canopy evaporation for original and modified model. Canopy evaporation is the same for both methods as it only incorporate LAI and an storage coefficient.

method are shown in equation 2.16 is fully compatible with the original definition of potential evapotranspiration. This approach don't apply any reduction factors to the residual potential evapotranspiration.

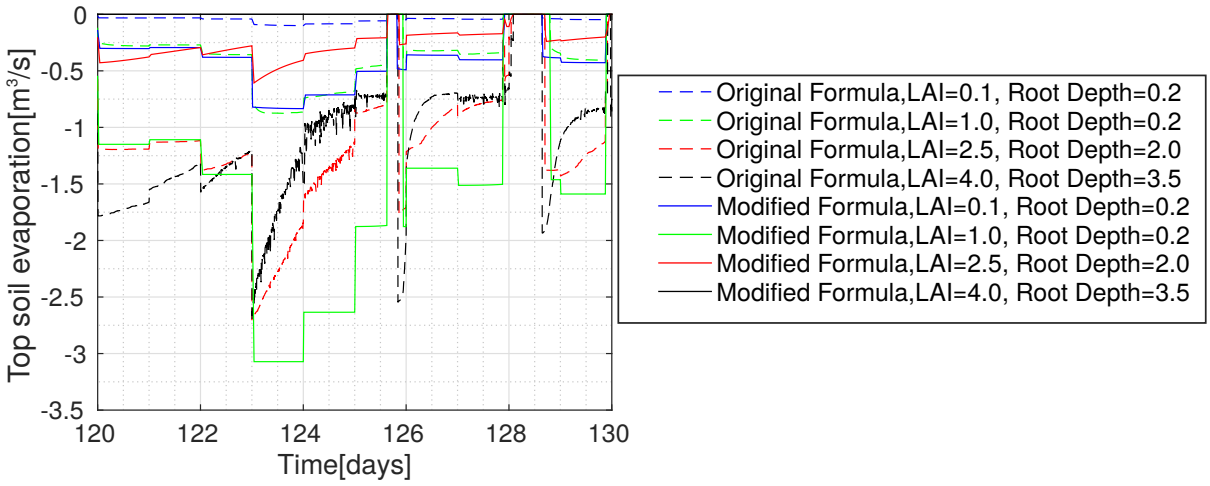

Figure 4.5: Porous media surface evaporation for original and modified model. The evaporation from the subsurface soil is driven to zero in the modified method (LAI of 4.0), while it is nonzero and significant in the original formulation. For the smaller LAI values, the original and modified formulations are also different. The reduction can be attributed to the shading effect by vegetation. However, as shown in figure 4.2, the shaded soil is also capable of evaporation due to atmospheric demands.

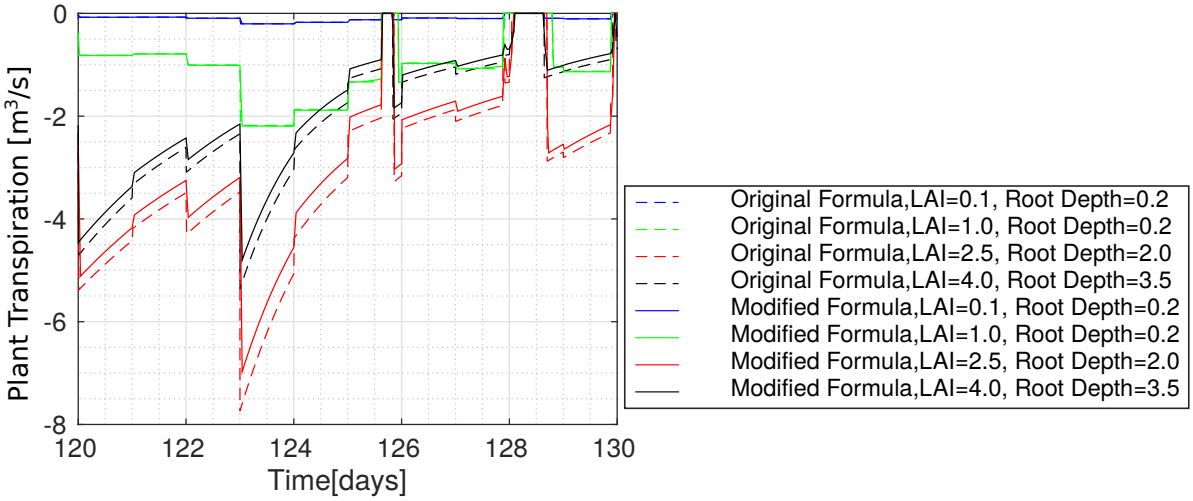

Figure 4.6: Plant transpiration for original and modified model. Plant transpiration for each of the methods of calculation is similar. Original method in general produces larger transpiration. The root depth is also an important factor. The plant transpiration is affected by soil properties such as field capacity and residual water saturation. The same level of transpiration is observed for both models, indicating that water availability in the soil is at the same level. The same water availability indicates of water shows that the remaining water on the surface should evaporate or turn to runoff.

The second formulation here refereed to as the modified method reduces the evapotranspiration potential by a factor of $1 - f_1(LAI)$. The reasoning is that shading due to the canopy reduces the potential evaporation from the surface. Though it seems to be a good reason to reduce the potential evapotranspiration, it should be noted that what is calculated as a potential evapotranspiration is the combination of evaporation and transpiration. This reduction can only be applied to the evaporation caused by direct

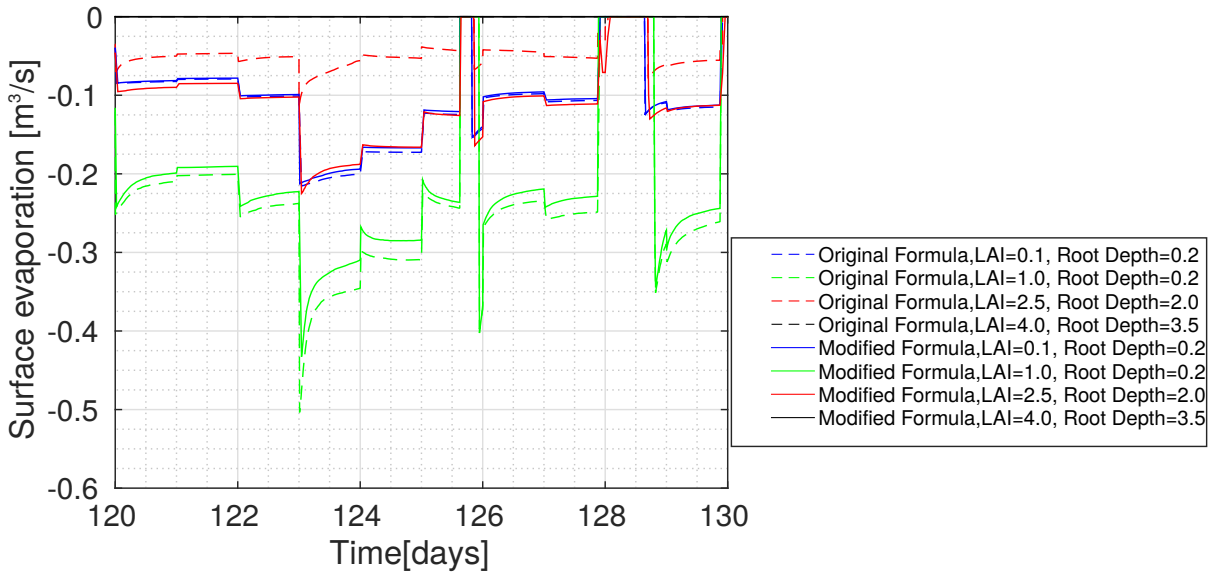

Figure 4.7: Surface evaporation for original and modified model. Surface evaporation is the same as the subsurface evaporation. The same formulation is used to calculate evaporation from the surface. The difference between surface evaporation becomes significant as the LAI becomes larger.

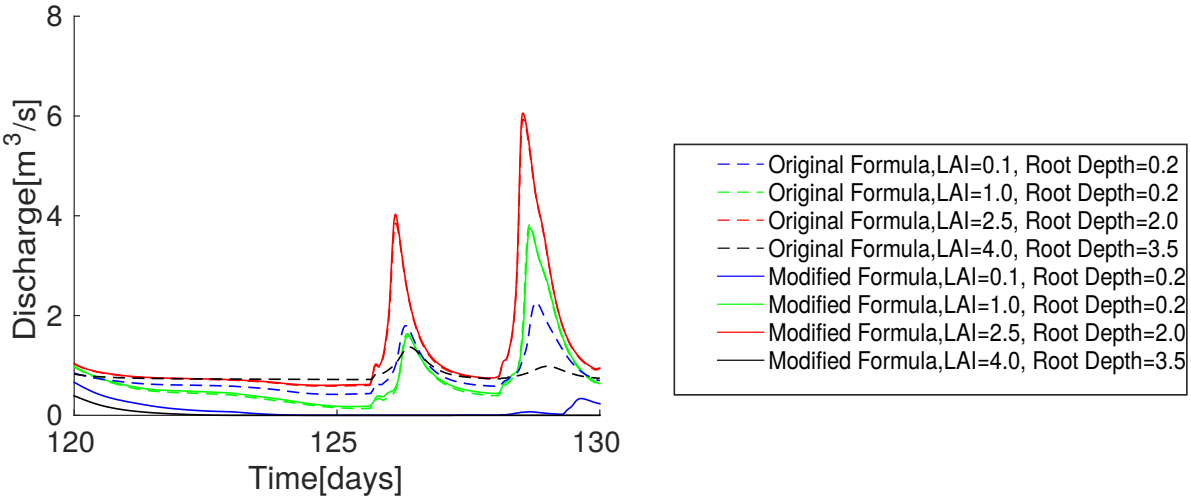

Figure 4.8: The hydrograph shows when using the (solid lines), the hydrograph is lowered as the is expected. The dashed lines have the surface evaporation reduced significantly. In the case of LAI = 4, the transpiration is forced to zero. This effectively removes a large sink and the water that should have been evaporated, turns into runoff and ends up in the river stream. The base flow for small LAI and large LAI are closee to each other. The solid lines show a systematic reduction of base flow with increasing LAI.

solar radiation and not the total value of potential evapotranspiration. Furthermore, the f_1 function is a linear function which is defined by two constants c_1 and c_2. This function can become equal to one for the widely used values of the constants in the equation and make the reduction factor of $1 - f_1(LAI)$ equal to zero for some values of leaf area index. This in effect means that there will be no surface

evaporation in the HydroGeoSphere model for as long as f_1 function is above or equal to one. It may be argued that the choice of c_1 and c_2 should be made so that the reduction factor does not become zero. Though this gives an extra level of control, the primary goal of f_1 function is to control the actual transpiration of the plants, and it has been shown that for leaf area index below two, proper values of c_1 and c_2 are 0.2 and 0.3 [138]. Assuming that f_1 should increase with the increase of LAI, it is not logical to choose smaller c_1 and c_2 values for larger LAI values. As a simple test, two sets of the c_1 and c_2 values are used in two simulations and part of the resulted hydrographs are shown in figure 4.3. These two models are different only in the parameter values of c_1 and c_2. The modified method of calculating evapotranspiration is selected in HydroGeoSphere. The logical expectation is that discharge for smaller f_1 value should be larger. However, the simulation shows that the discharge is larger for the larger f_1 function. In this test, the constants c_1 and c_2 are chosen so that the one set of them makes f_1 function equal to one. Therefore the surface evaporation and top soil evaporation is turned off. The actual evaporation is limited to the transpiration from the plants. This leads to an excess of the surface water on the surface and top soil which leads to the increase of the discharge from the hydrograph. The choice of the surface evaporation method in HydroGeoSphere becomes important as reducing evaporation to zero, affects the surface saturation, infiltration rates, total evapotranspiration and runoff generation and discharge. Simulations conducted to show the effect of each of these methods on hydrograph and surface and top soil evaporation. The results of the top soil evaporation, surface evaporation, canopy evaporation and plant transpiration for multiple sets of LAI and root depth are shown in figures 4.4, 4.5, 4.6, 4.7 and 4.8. From the results of these simulations, using the original methods seems to better reflected the overall behavior of the catchment.

Experimental evidence also supports the choice of the evapotranspiration model as shown in figure 4.2 as reported by FAO56 [52]. The shading reduces the rate of evaporation at the start of the experiment, however, the potential evaporation is not totally hindered as the ambient heat can transfer energy to water and cause evaporation. It should be noted that there is also many measurements from various forests that show the existence of a surface evaporation component ranging from 20%, to 15% of actual evapotranspiration [139, 140, 141].

A closer look at the formulation of these two approaches show that the equation used in the modified version 4.1 does not take into account the availability and distribution of the water in root zone. The surface evaporation in the modified form is computed using equation 4.1.

$$E_s = \alpha \times (E_p - E_{can}) \times (1 - f_1(LAI)) \times EDF \tag{4.1}$$

in which E_s is the evaporation from the surface $[LT^{-1}]$, α is the scaling function $[-]$, E_p, E_{can} are potential evapotranspiration and canopy evaporation $[LT^{-1}]$, f_1 is the a function of leaf area index $[-]$ and EDF is the evaporation depth function $[-]$. The reduction of the surface evaporation according to equation 2.16 and 2.17 produce similar results if constants c_1 and c_2 are chosen so that the f_1 function does not become equal to one. In this case the constants in the evapotranspiration are treated solely as degrees of freedom in the model, so that a suitable water extraction by plants can be achieved. The choice of the constants in f_1 should reflect the effectiveness of the plant is in transpiration.

The problem with 4.1 can be also explored by simple assumptions about the state of evaporation. By assuming zero canopy evaporation, the equation is simplified to the form shown in equation 4.2. The transpiration formula also reduce the to the equation 4.3 and the evaporation from the original method is simplified into equation 4.4. If T_p is replaced from equation 4.3 into the equation 4.4, the result is

equation 4.5.

$$E_s = \alpha \times (E_p) \times (1 - f_1(LAI)) \times EDF \tag{4.2}$$

$$T_p = f_1(LAI) \times f_2(\theta) \times RDF \times (E_p) \tag{4.3}$$

$$E_s = \alpha \times (E_p - T_p) \times EDF \tag{4.4}$$

$$E_s = \alpha \times E_p \times (1 - f_1(LAI) \times f_2(\theta) \times RDF) \times EDF \tag{4.5}$$

The parameters in the equations are defined same as before. Comparing the equation 4.5 and 4.2 with the assumption of no water availability limits, where the α is equal to one and $f_2(\theta)$ is the maximum value possible, shows that these equations produce the same value. However, when the surface is partially wet and the potential evapotranspiration conditions do not apply these equations will have different values. The difference results from the way transpiration works in the equation 4.5. In this equation, there is a term RDF which is the contribution of the water availability in the root zone at given depth and the $f_2(\theta)$ function that takes into account the behavior of the vegetation with respect to water availability. Therefore, at the times that the transpiration is limited due to various constraints, the $E_p - T_p$ term is not zero. However, in the equation 4.3, when f_1 is equal to one due to large values of LAI, the surface transpiration stops regardless of the amount of transpiration. This formula basically ignores the most important control on evapotranspiration namely the availability of water. Replacing actual transpiration by plants and using the $1 - f_1$ function to reduce the amount of surface evaporation basically assumes that plants are transpirating at maximum rate (in potential transpiration).

4.2 Base line model: Sparse vegetation

In order to compare each experiment with a base line, a model with no vegetation or clearcut scenario is defined here. The clearcut scenario has a different albedo value and therefore the evaporation is smaller than total evapotranspiration. The evaporation is also limited to the surface and the top soil as there is no transpiration from the plants. This in turn reduces the actual evapotranspiration.

4.2.1 Potential evapotranspiration

Potential evapotranspiration for the base line is calculated with albedo of 0.159 and no vegetation. Important parameters that affect the clearcut potential evaporation are albedo, lack of vegetation and wind speed profile. Wind profile depends on the topography and the catchments orientation.

The amount of change in evaporation with the introduction of small amount of vegetation depends largely on the species and the age of vegetation. To validate the clear cut evaporation potential calculated using Penman-Montieth equation, the Thronthwaite equation is also used to estimate the potential evaporation. The two methods give similar total annual evaporation rates.

4.3 Experiment I: Deciduous Forest

Deciduous forests have trees that loose their leaves at autumn when the weather starts to get colder. The variations in the LAI is documented by [142]. The total reduction of the LAI exposes the soil and

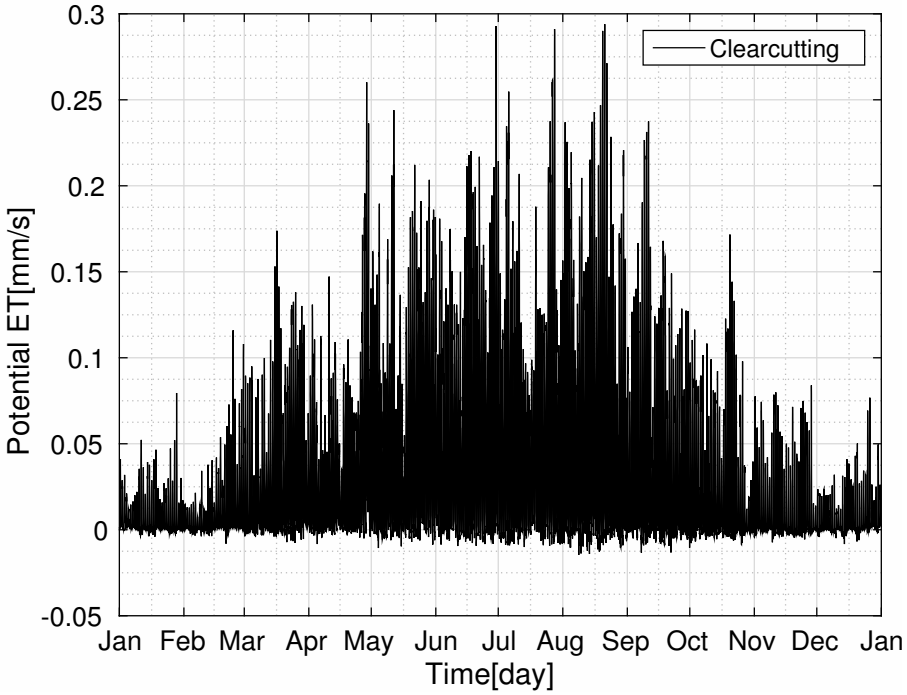

Figure 4.9: Computed clearcut evaporation. The albedo increases due to the lack of vegetation. There is also the lack of vegetation which affects the total evapotranspiration. The wind speed over the catchment also will be different. No feed back between clear cutting and the atmosphere is assumed. Part of the energy that would have been used by photosynthesis and also shading will warm up the land and the soil surface will be warmer. There micro-climates which reduce the temperature locally and shade the surface of the soil is also not present here.

the albedo changes from the albedo of the forests to the albedo of bare ground. The calculation of the potential evapotranspiration should include this change of albedo to correctly reflect the boundary conditions of the catchment. This changes the amount of the solar energy reflected back to atmosphere from the catchment. The energy budget of the surface changes as a result. The root depth of the of these types of forests are estimated to be about 4.7m [143].

4.3.1 Annual LAI variation

The idealized LAI for Deciduous forests start with a zero transpirational vegetation (LAI = 0.0) for the winter and early spring. As the growth season approaches, a rapid increase of LAI to 4 occurs. With the onset of autumn, the trees starts to loose their leaves. The LAI is reduced to zero again at late August. The distribution of the LAI affects the hydrological response of the deciduous forest. The canopy interception is highest in the summer and lowest for the spring and winter precipitations. The transpiration follows the LAI so the subsurface is affected by the plants only in the growth season. The root depth suitable for this kind of forests can be variable. Variation of LAI for this kind of forest is shown in figure 4.11.

4.3.2 Evapotranspiration

Evapotranspiration is regulated by the leaf stomatal resistance and the canopy density, vegetation height and albedo. The stomatal resistance is chosen to be $50s/m, 200s/m$ for day and night time respectively. Since there is not any wind measurements available, the $2m$ wind measurement is used for all the forests. It is important to note that each forest will have it's own micro-climate throughout the year. There will be also an aspect control on the amount of energy received by plants. The resulting evapotranspiration is shown in figure 4.12.

4.4 Experiment II: Pine Forest

Pine forests or coniferous forests have needle shaped leaves. This type of trees can grow tall and they don't loose their leaves in winter. Pine forests also known as temperate needle leaf forests. These forests can usually be found in the higher latitudes of northern hemisphere [128].

4.4.1 Annual LAI variation

The idealized LAI for the winter and early spring is around 2 and there is an increase in the LAI in the growth season to 3. The LAI variation for a year is shown in figure 4.13.

4.4.2 Evapotranspiration

Stomatal resistance for this kind of forests are relatively larger than Deciduous forests. The needles are better in preserving the water and withstanding the colder temperatures. For Pine forests, the proposed nightly and daily stomatal resistance are $200s/m$ and $67s/m$ [128].

4.5 Experiment III: Hardwood Forest

Hardwood forests are a combination of different plants and trees. They may include undergrowth shrubs, pine trees, broad leaves and Deciduous plants. This kind of combination of the plants are observed in the Schönbuch forest where the Steinlach catchment is located.

4.5.1 Annual LAI variation

The LAI variation for the Hardwood forest has both the character of the Deciduous and coniferous forests. Part of the trees in these Hardwood forests don't loose their leaves. So the winter LAI is about 0.5. At the growth season LAI reaches to the value of 4 and similar to the Deciduous forest, by the end of the growth season, the LAI is reduced [142]. The LAI variation is shown in figure 4.15.

4.5.2 Evapotranspiration

The stomatal resistance proposed for this type of forest is $50s/m$ and $200s/m$ for daytime and night time. A potential evapotranspiration for this forest is shown in figure 4.16.

4.6 Summery of forest parameters

A tabular summery of the parameters presented at table 4.1. Albedo changes the amount of sun energy input to the surface. Part of the this energy is spent in warming up the earth surface, and part of it is consumed for photosynthesis. Surfaces with smaller albedo values increases the energy input to the surface and therefore potential evapotranspiration is increased. The Deciduous forests have the largest of the root depth and LAI. The stomatal resistance is smaller compared to Pine forests which makes them efficient in transpiration. The Hardwood forest has large LAI and intermediate root depth. The albedo for the clearcut vegetation is that of bare land. The rest of the parameters are the same for all models. Climate parameters such as wind speed, relative humidity, pressure, surface and subsurface temperature and solar radiation are the same for the simulation period for all of the models.

Table 4.1: Parameters used for forests types in the experiments

	clear cut	Hardwood	Deciduous	Pine
Root depth[m]	-	3.48	4.7	2
Maximum LAI[-]	-	4	4	3
Minimum LAI[-]	-	0.5	0.0	2
Stomatal resistance night[s/m]	-	200	200	200
Stomatal resistance day[s/m]	-	55	50	67
Albedo	0.159	0.091	0.092	0.062
Canopy storage $[m/m^2]$	-	0.0005	0.0005	0.0003

4.7 Results

The precipitation is partitioned in to different components for the Steinlach catchment. The partitioning values are shown in table 4.2 and figure 4.17. The values are turned in to the equivalent depth of precipitation for the entire catchment. The first row in 4.2 is the infiltration. As it is shown by the values in the table, the total infiltration rates are almost equal. The infiltration is controlled by top soil saturation, rill storage and obstruction storage parameter. The rill storage and obstruction storage height are chosen to be $0.001m, 0.002m$ respectively in HydroGeoSphere [41, 144]. The role of these parameters are to simulate the effect of micro-topography and depression storage or reduction of the velocity of water due to obstructions. Infiltration is an internal exchange flux between surface and subsurface and it does not produce any flow in or out of the catchment. The infiltration for Deciduous forest is slightly larger (about one percent) as the Deciduous forest has only large canopy size in the growth season. As the catchment is in equilibrium annually, the infiltrated water transfered out of the catchment eventually by transpiration or river discharge. The next row in the table 4.2 is the exfiltration out of the subsurface and into the surface. Exfiltration for the clear cut scenario, is about twice as large as the forested experiments. The deficit in the exfiltration for the forests can be attributed to the plants transpiration which takes water

Table 4.2: Water cycle components for forests and base model

	clear cut (small undergrowth)	Hardwood	Deciduous	Pine
Infiltration[cm]	49.7985	46.5537	49.6803	45.2940
Exfiltration[cm]	4.6477	1.8019	2.3653	1.4913
Canopy ET[cm]	1.7186	14.8829	10.3601	15.2339
Surface ET[cm]	11.7411	26.8923	25.9285	27.6204
Plant Transpiration[cm]	0.7084	20.1728	19.6535	12.0649
River Discharge[cm]	20.4496	7.9715	9.9677	8.3220

directly from the root depth and does not allow the water to reach to the surface. Canopy evaporation for Deciduous forest is about 30% less than Hardwood and Pine forests. The transpiration component is the same for Hardwood and Deciduous forests. This is due to the larger root depth in Deciduous forest compared with Hardwood forests. River discharge is at the same order of magnitude for the forests. The potential evapotranspiration is higher at the growth season, where Hardwood and Deciduous forests have almost the same amount of LAI. The higher stomatal resistance and smaller root depth reduces the efficiency of the Pine forest for transpiration.

The Surface evapotranspiration for the forests is twice as large as the clear cut scenario. Evapotranspiration is most effective when there is water available for evaporation. For the case of clearcut scenario, a larger portion of the precipitation exits the catchment as discharge from the river as the bank storage readily activated due to higher water table depth. For the forests, the lower water table provides more storage and therefore water is stored in the catchment and some part of the stored water contributes to the surface evaporation. Plant transpiration is also a major sink in the forested catchment simulations. Pine forest transpiration is less than the other forests as Pine leafs (mostly needles) have higher stomatal resistance and shorter root depth. Hardwood and Deciduous forests transpire the same amount of water. The discharge for forests in the last column is controlled by when the LAI is large and when it is small. Besides transpiration, the canopy storage also important in flow generation. The discharge for the clear cut model is twice as large as the forested simulations. This is mostly due to the larger activation of the bank storage and groundwater storage as is shown in the exfiltration column and lack of other storage buckets such as canopy and transpiration.

The emergent behavior of the subsurface and interaction with the surface is of importance here as HydroGeoSphere allows us to peer into the dynamics of how different elements such as vegetation, bank storage and groundwater change in time.

4.7.1 Analysis of hydraulic heads in observation well

A suitable way of looking at the variation in groundwater levels is to place observation wells over the catchment. Eight observation wells are placed in different places in the model as shown in figure 2.16. Observation wells and points show the variation of hydraulic head in surface and subsurface due to the various forcing and boundary conditions. The changes in water levels on the surface and subsurface are recorded for each computational time by HydroGeoSphere. Observation point one is located in the flood plane. It is the nearest point to the outlet. The free flux boundary condition and the impermeable middle layer near the outlet control the water table elevation throughout the catchment. The divergence of hydraulic head between forest simulations are larger compared to the other points.

Observation point number tow is located at a beginning of a small narrow valley. For the clearcut model, this point is inside the river stream as the surface hydraulic head is higher than the elevation of the observation well. The river stream goes dry for the forested simulations. The coupling is much tighter between surface and subsurface flow and the subsurface hydraulic head responds to most of the precipitation event.

Observation well number three is located further away from the river and is located between two river streams. The hydraulic head are monotonically rising for the time period in the figure. This shows that the steady state hydraulic head was lower than the dynamic steady state but the same patterns are present as well for different forests. Also the daily fluctuations of the plants breathing are not present in the forested catchment showing weaker linkage between this part of the catchment to the global dynamics of the rest of the catchment. This shows that there are parts of the catchment that are not influenced to large extent by small fluctuations of the surface and the hydraulic heads are controlled by topography alone.
The trends in observation well number four are the same as observation point number five. Except that it is further away from the river stream as well as having more upslope area.
Observation point number five is located at the flood plane near the river. The clearcut model at this point is a recharging point. The subsurface hydraulic head is above the surface head. Water table is close to the surface. The upstream area of the point is much larger and therefore the activation of the subsurface is much larger and more significant. The linkage between surface and subsurface is larger. The rate of change of subsurface is larger if the subsurface is lower as shown in figure 4.22.
The surface head shows a large fluctuations with the precipitation. The point is part of the river for clearcut model and part of the flood plane for the forested simulations. As the upslope area increase, the cumulative effect of bank storage and groundwater activation to the precipitation events are more pronounced

Observation well number six is located at a the peak of a local hill. The subsurface hydraulic head is about $12m$ below the surface. For all the simulation cases, the water tables have the same height. There is not any water accumulation on the surface as well. This shows that the surface is dry and therefore all of the precipitation infiltrates into the subsurface or moves downstream as the slope is large. The head variation for this point is shown in figure 4.23.

Observation point number seven is located downstream a small valley. As it can be seen from the relief map as shown in figure 2.11, the upslope area is small. There is a small amount of fluctuation for the surface hydraulic head. The subsurface hydraulic head for the clearcut model is close to the surface elevation. The subsurface hydraulic head is higher for the Pine forest compared to the Deciduous and Hardwood forest as shown in figure 4.24.

Observation well number eight is located at the elevation of $493.825m$. The variations in subsurface and surface hydraulic head is shown at figure 4.25. In the subsurface hydraulic head variation for the forests follow a similar pattern. The clearcut model has a higher water level. The difference between the clearcut scenario hydraulic head and forests hydraulic head is due to transpiration. In this observation well, the surface water levels do not change as much as the subsurface. As this point is near to the catchment boundary to the south, there is not any flow accumulation on the surface.

All the observation points have similar trends. For the time period shown in the figures, the Deciduous forest lowers the water table more than the other two forest type. The difference between water table elevation have spatial and temporal dependence. The difference between hydraulic head in the growth season can be as large as $5m$. At the start of the growth season, the water table elevations are close to each other and then rapidly each water table diverge from other scenarios based on the root depth and LAI. Water table for the Hardwood forest is lower than Pine forest water table as the root depth and LAI is larger than Pine. The Pine forest is not very efficient in transpiration because the canopy size is about 2/3 of the Deciduous and Hardwood canopy. The root depth is about 1/2 of the Deciduous and Hardwood root depth.

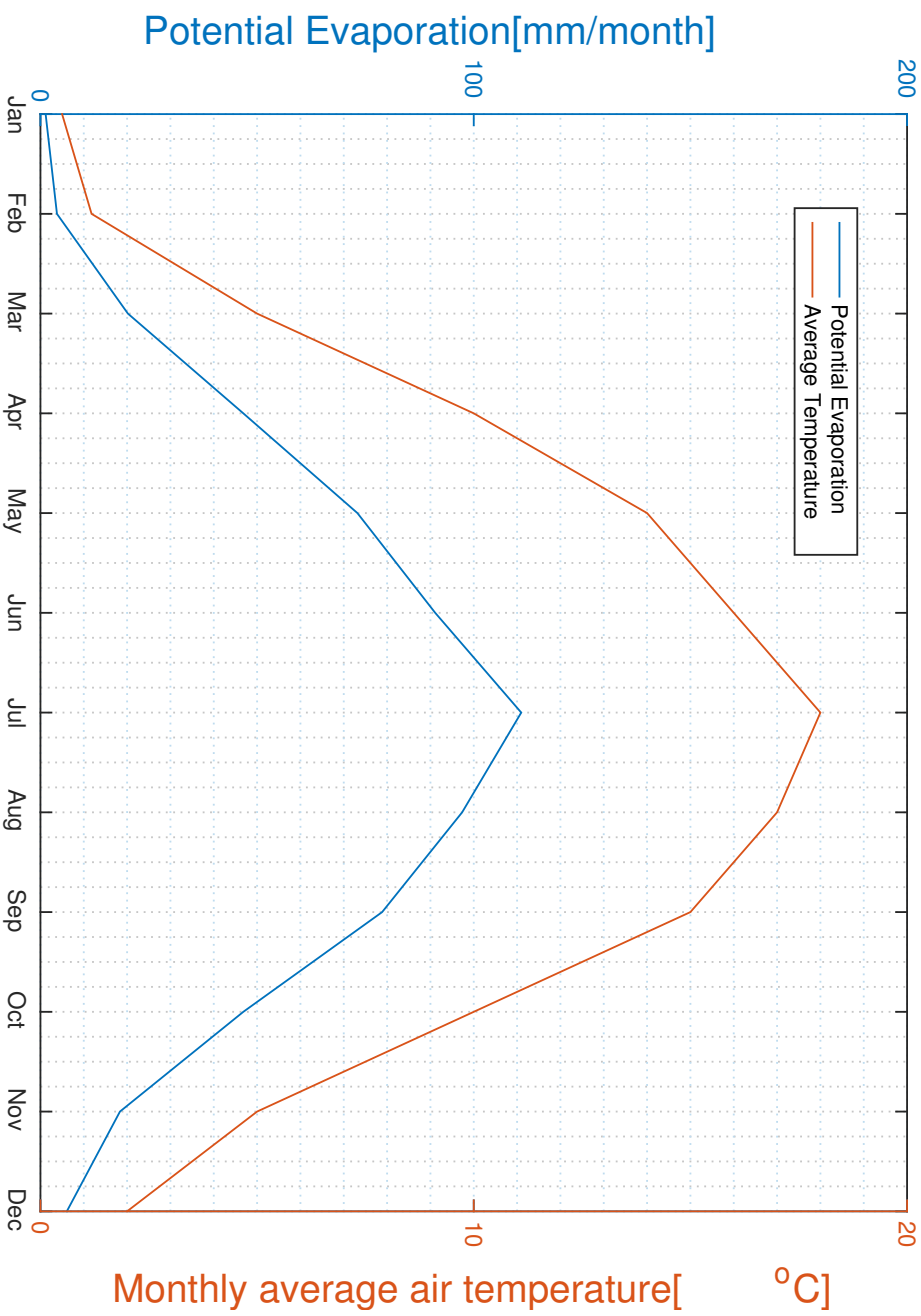

Figure 4.10: Thornthwaite potential evaporation for clearcut scenario. The empirical equation of the Thornthwaite is used to estimate potential evaporation for the clearcut case. The result are in good agreement with the Penman-Montieth equation.

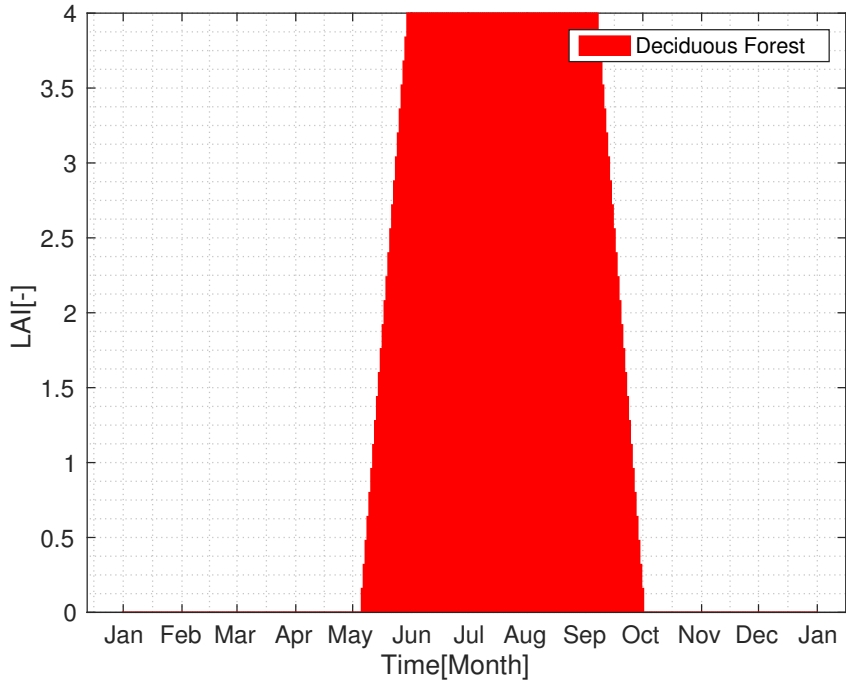

Figure 4.11: Annual variation of LAI for Deciduous forest. Deciduous forests are characterized by loosing their leaves when the weather becomes colder in autumn. In the growth season, they produce a large canopy with higher efficiency in transpiration compared to the Pine forests. The LAI values are fitted and simplified to reflect the measured trends [142].

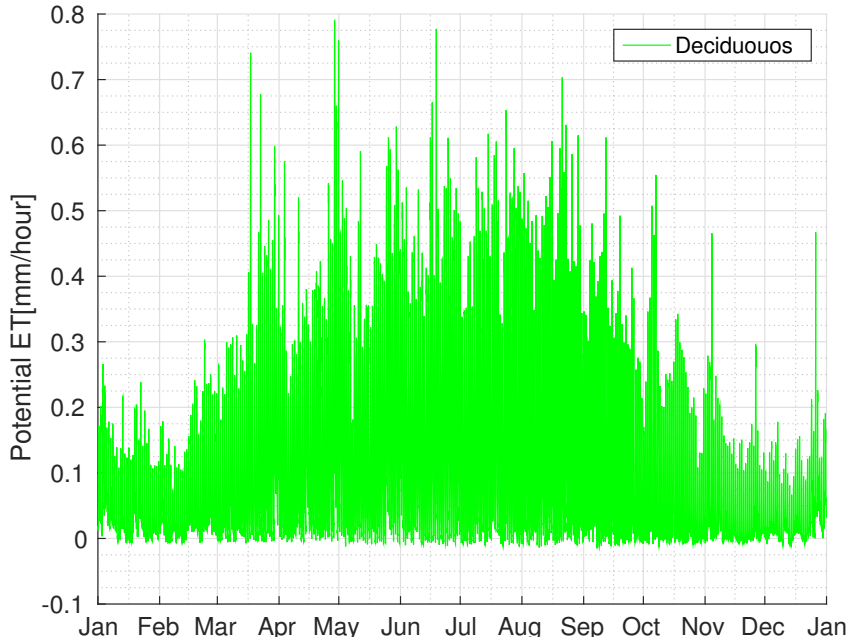

Figure 4.12: Evapotranspiration computed for Deciduous forest. The evapotranspiration in this case is largely controlled by the LAI, albedo, and stomatal resistance of the tree types. PET is strongly influenced by the LAI increase in the growth season and decreases as the LAI is reduced.

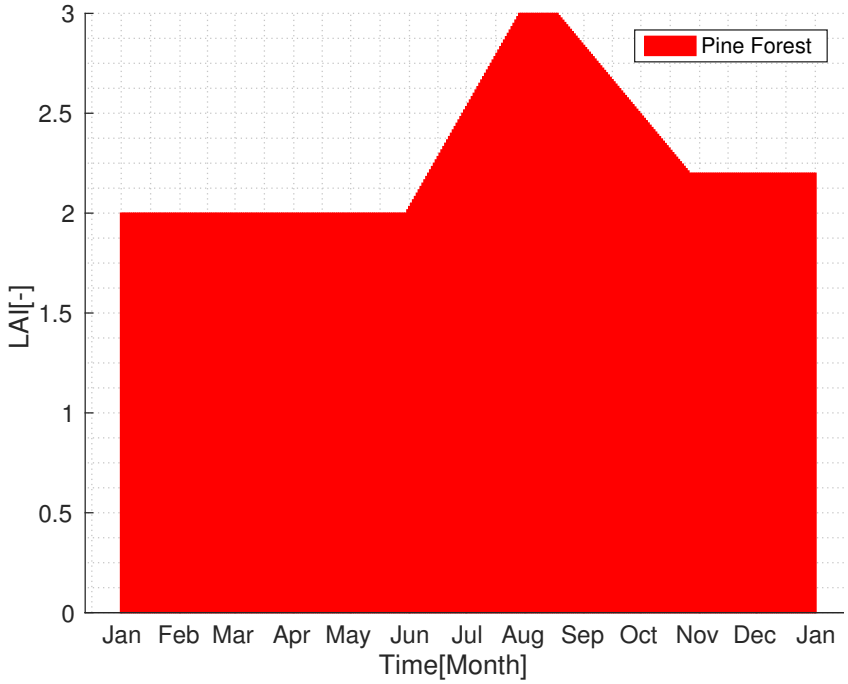

Figure 4.13: Annual variation of LAI for Pine forest. Pine forests have needle shaped leaves and they keep these needles all the year around. They mostly grow in colder climates and are more resistant to harsh weather systems. The stomatal resistance is high, which makes them relatively inefficient in transpiration. The LAI values shown in this figure are fitted and simplified to reflect the measured trends [128].

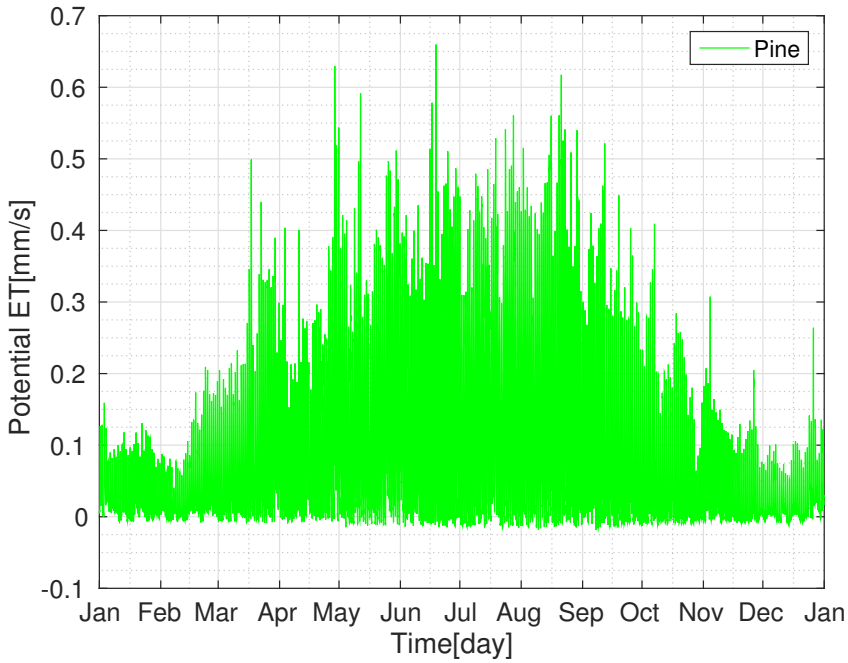

Figure 4.14: Evapotranspiration computed in Pine forest. As Pine forests do not lose their leaves throughout the year, the potential et predicted for Pine forest is also largely affected by existence of transpiration of the Pine leaves(needles).

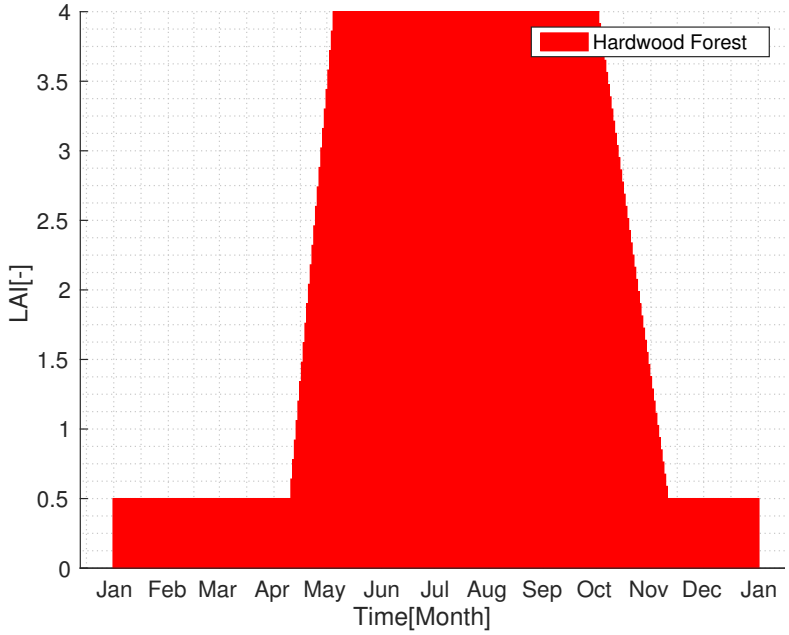

Figure 4.15: Annual variation of LAI for Hardwood forest. Hardwood forests are a mixture of Deciduous and Coniferous forests. This kind of forests are also suited for harsh environments and can grow a large canopy. The LAI values are fitted and simplified to reflect the measured trends [142].

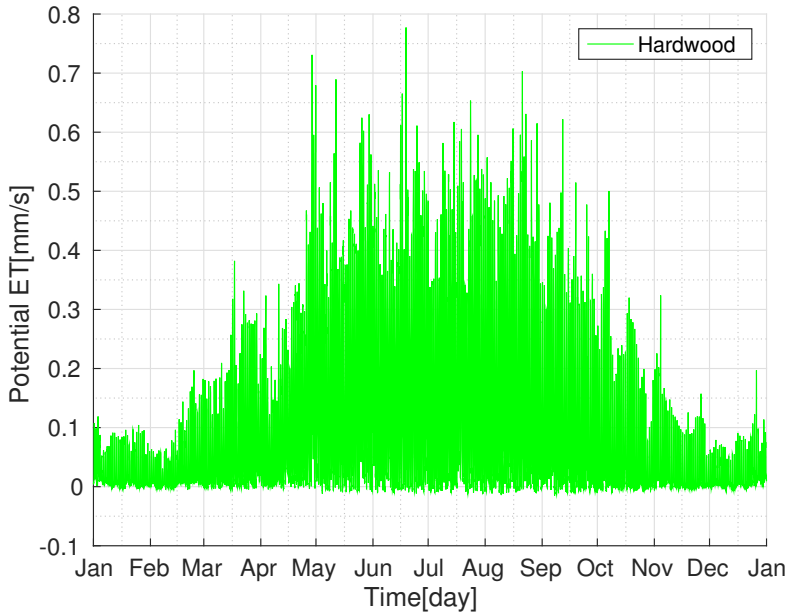

Figure 4.16: Evapotranspiration for Hardwood forest. The Hardwood forest mostly consist of Deciduous trees with an addition of ever green trees. The stomatal resistance of Deciduous plants is used for the computation of the PET in this kind of forest.

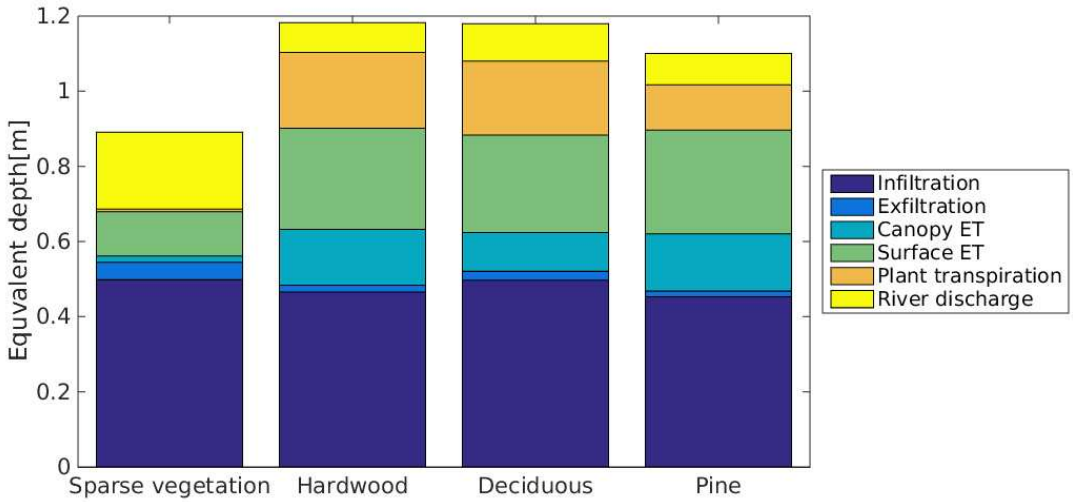

Figure 4.17: Equivalent water depth of components of water cycle for each forest and base model. The infiltration and exfiltration happen inside the catchment and do not change the total balance in and out of the catchment. The values do not sum up to a conservative value as a result of exchange fluxes between surface and subsurface. There is also an storage component in the surface and subsurface which is assumed to be small for the annual simulation.

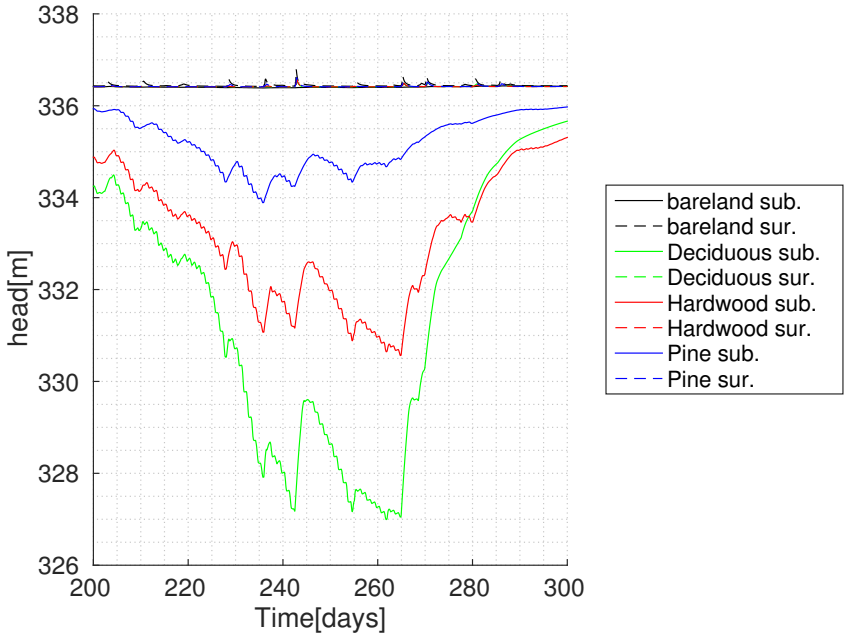

Figure 4.18: Surface and subsurface hydraulic head for observation point one. The water table depth show an average coupling to the surface and the water tables diverge with a greater rate.

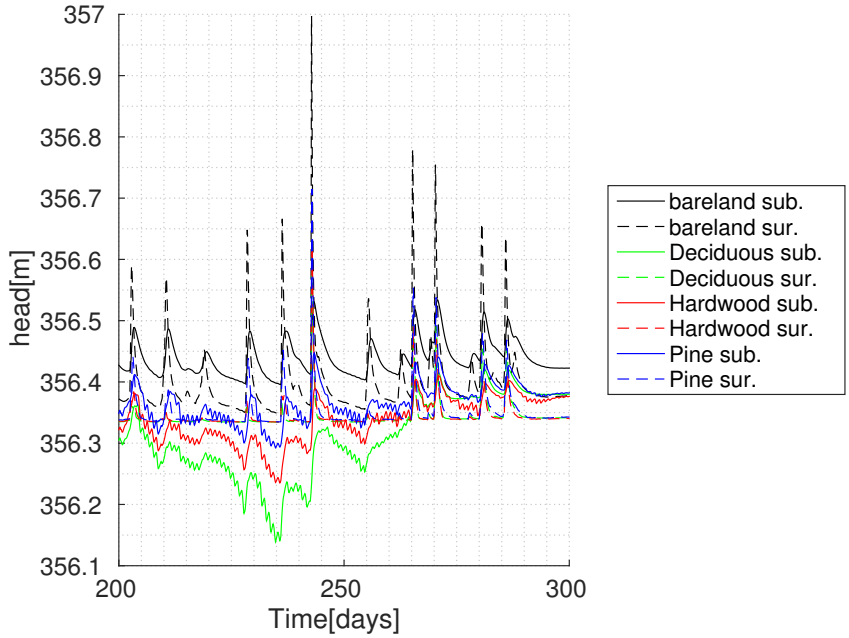

Figure 4.19: Surface and subsurface hydraulic head for observation point two. This point is located on the river bed. The coupling is very strong and subsurface hydraulic head is largely above surface head, which acts as a recharge point for the river.

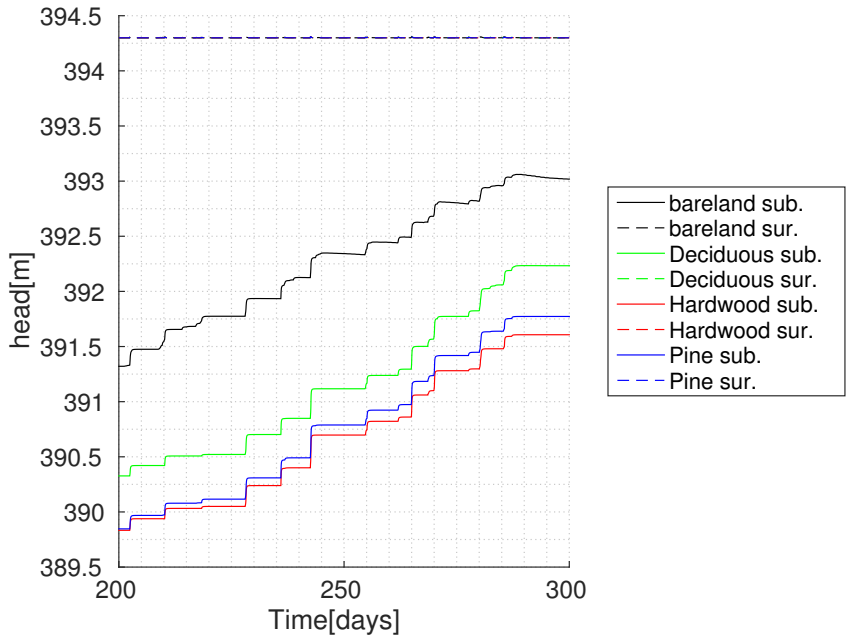

Figure 4.20: Surface and subsurface hydraulic head for observation point 3. The subsurface hydraulic head rises as the surface head stays zero. There is not any sign of the daily fluctuations of subsurface hydraulic head, indicating a topographical control on this part of the catchment.

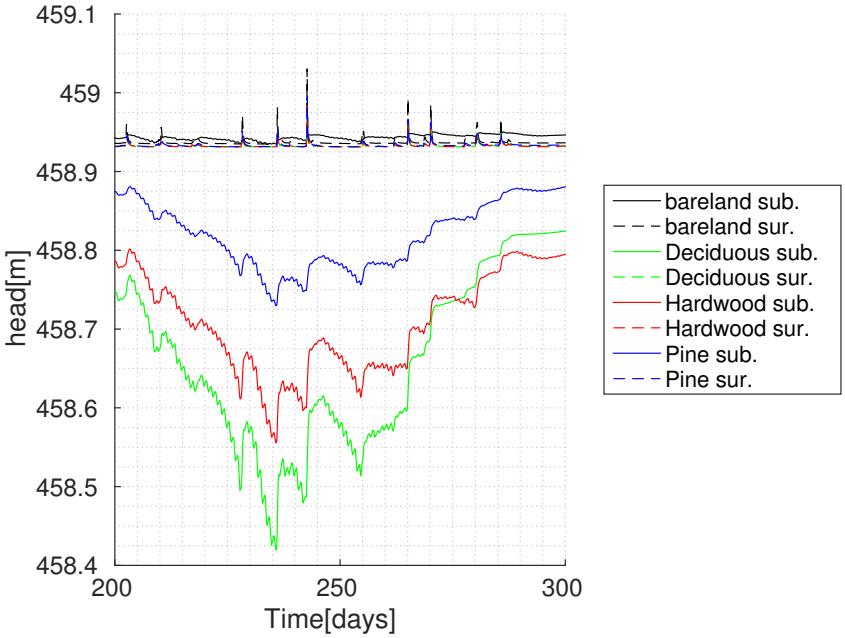

Figure 4.21: Surface and subsurface hydraulic head for observation point four. This point shows a tighter coupling between surface and subsurface. For the clearcut simulation, it acts as a recharge point.

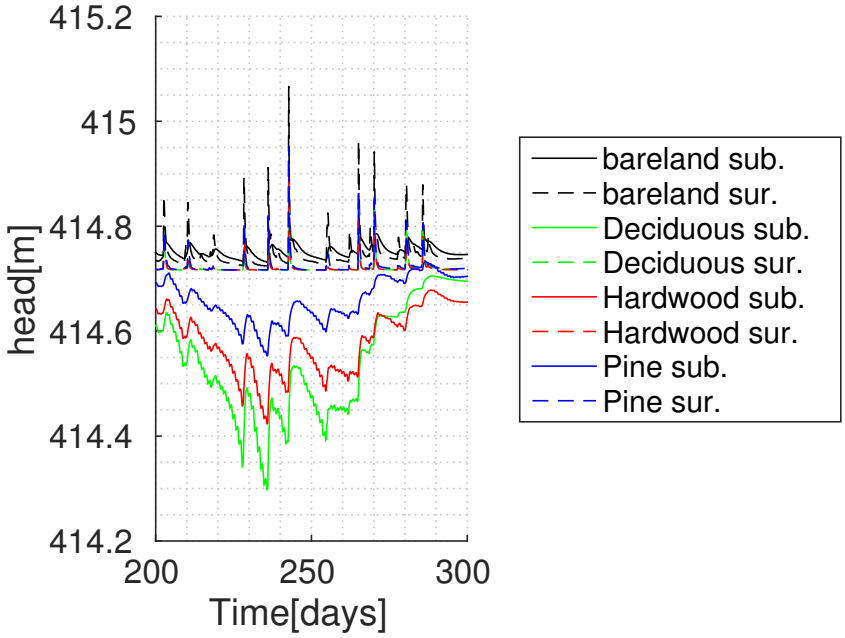

Figure 4.22: Surface and subsurface hydraulic head for observation point five. Water table for clearcut model is always above the surface water head. For forested simulations, this point gets water from the river.

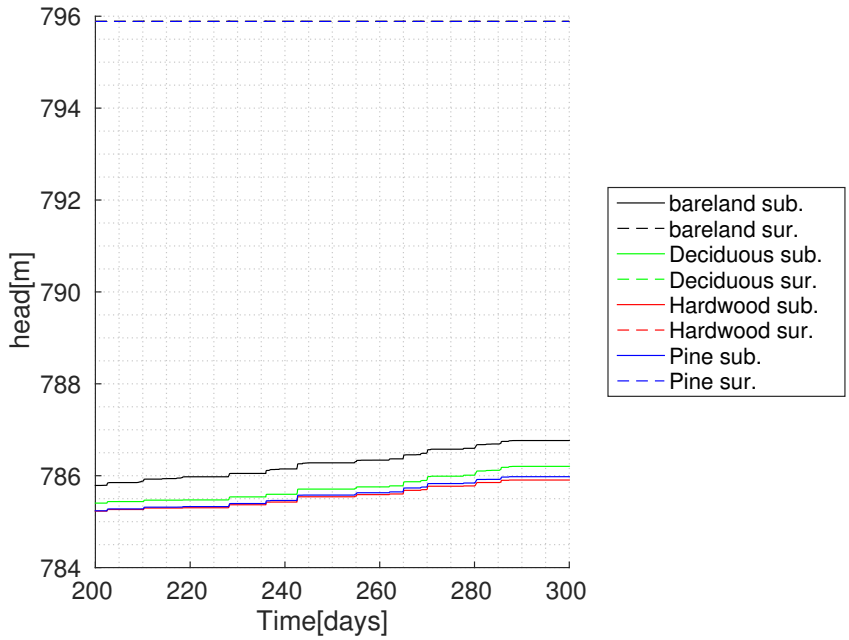

Figure 4.23: Surface and subsurface hydraulic head for observation point six. This point located at the hillslope with a small upslope area with steep slopes. Surface water shows small magnitude fluctuations as subsurface water table is also affected.

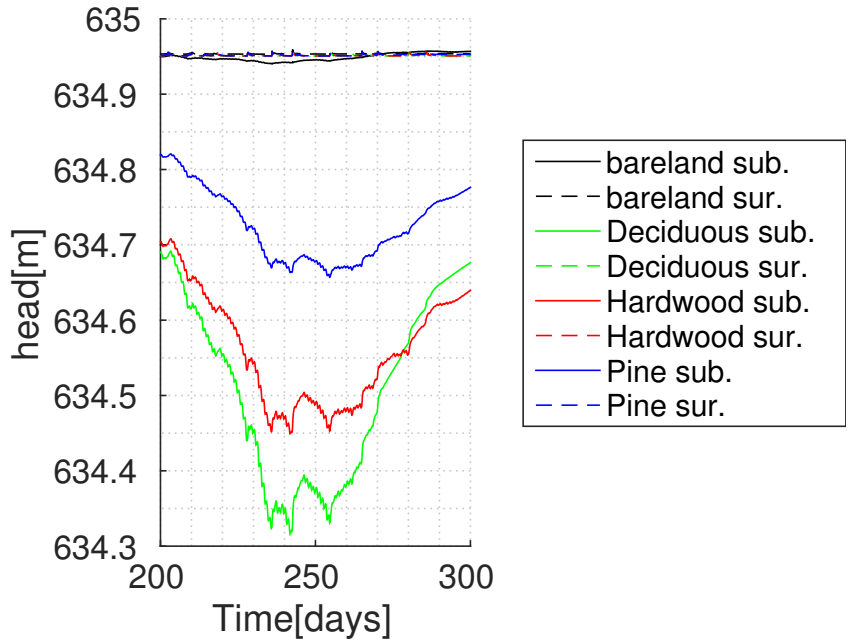

Figure 4.24: Surface and subsurface hydraulic head for observation point seven. The water table is distanced from the surface and there is not a significant amount of coupling between surface and subsurface. This point is located on the mountainous southern part of the catchment.

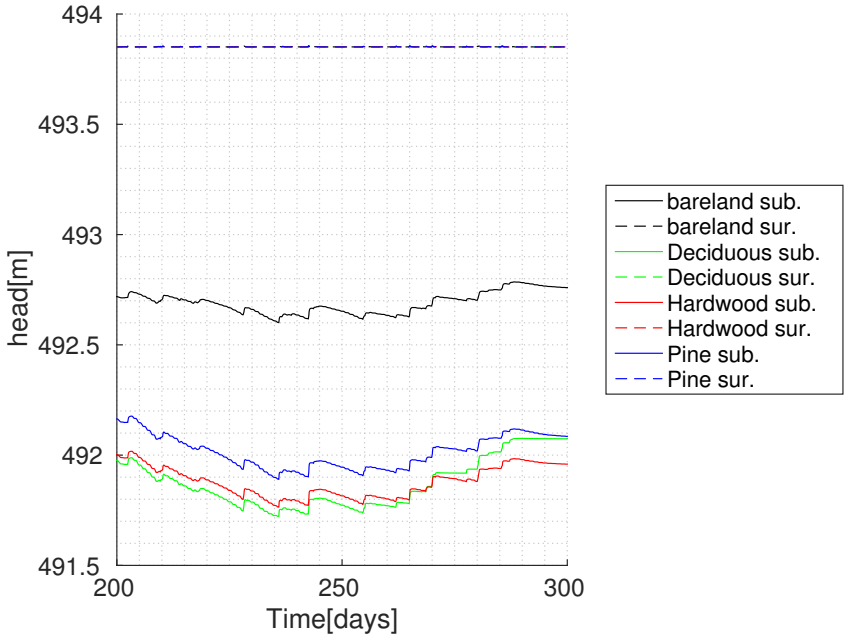

Figure 4.25: Surface and subsurface hydraulic head for observation point eight. This point is located near the boundary of the catchment. The subsurface shows small decrease and recover for all simulations while the surface head is not largely affected by precipitation events

4.7.2 Analysis of seasonal evapotranspiration

Total actual evapotranspiration for the Deciduous forest is shown in figure 4.26. Plant transpiration for the catchment is shown in figure 4.27. Total actual evapotranspiration is strongly influenced by the transpiration. The largest transpiration occurs at early May to late August.

Surface evaporation is due to the evaporation from the topsoil and surface water bodies, river stream or puddles. Surface evaporation is highest where subsurface water feeds into the surfaces near the river stream network. As discussed before in this chapter, the choice of evaporation formula affects the base flow and peaks for the catchment. Using the f_1 function to reduce the surface evaporation, would have turned the evaporation from the surface to zero when LAI becomes large. This in turn allows the surfaced water to reach the river stream and contribute to the base flow. At the other hand, calculating the surface evaporation using transpiration component allows for the evaporation demands to be met.

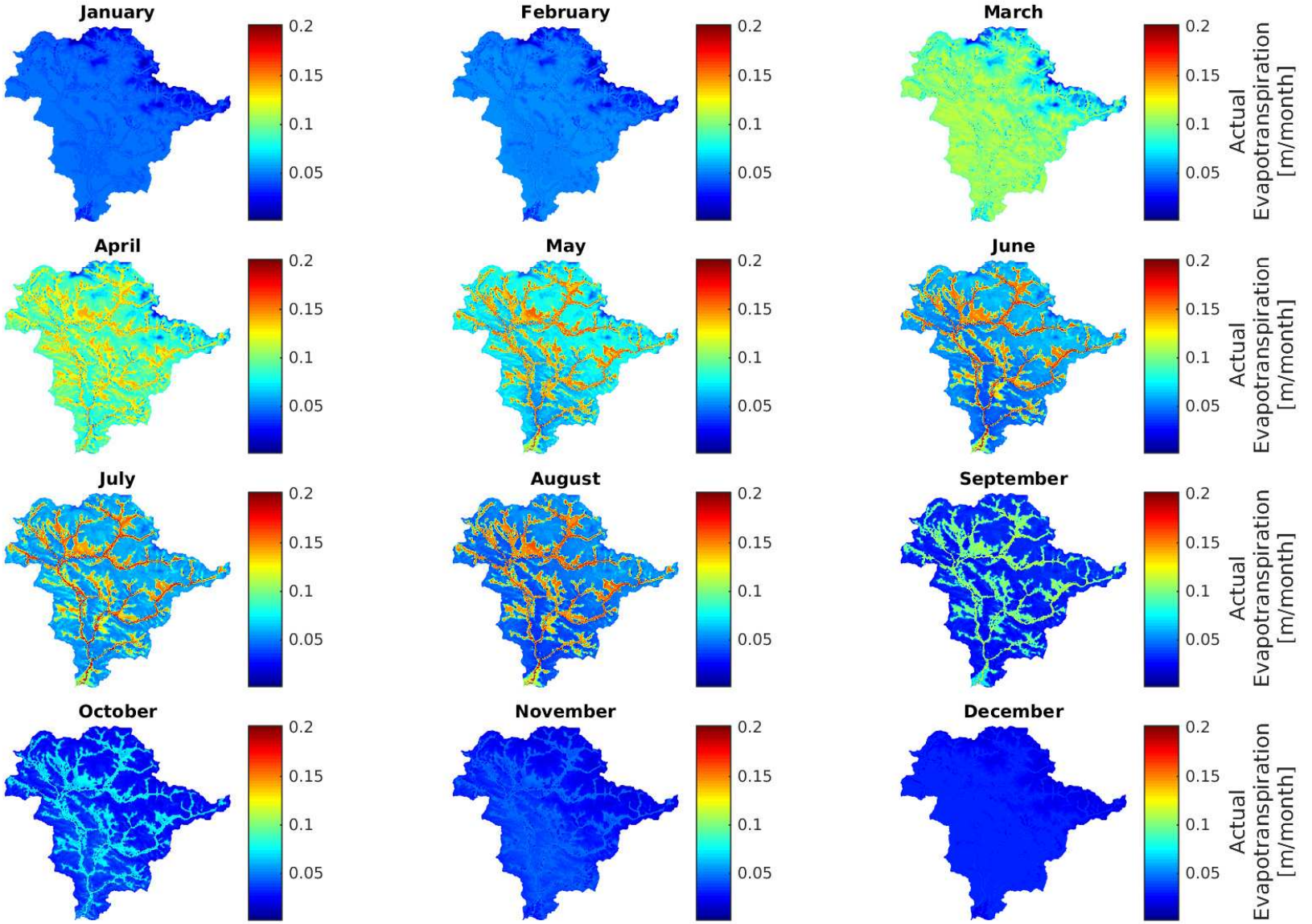

Figure 4.26: Deciduous forest actual evapotranspiration. Evaporation is reduced due to existence of small amount of transpirational leaves in non-growth season. Winter and autumn have the smallest amount of evapotranspiration. The availability of the water and movement of water from various parts are strongly influenced by ET.

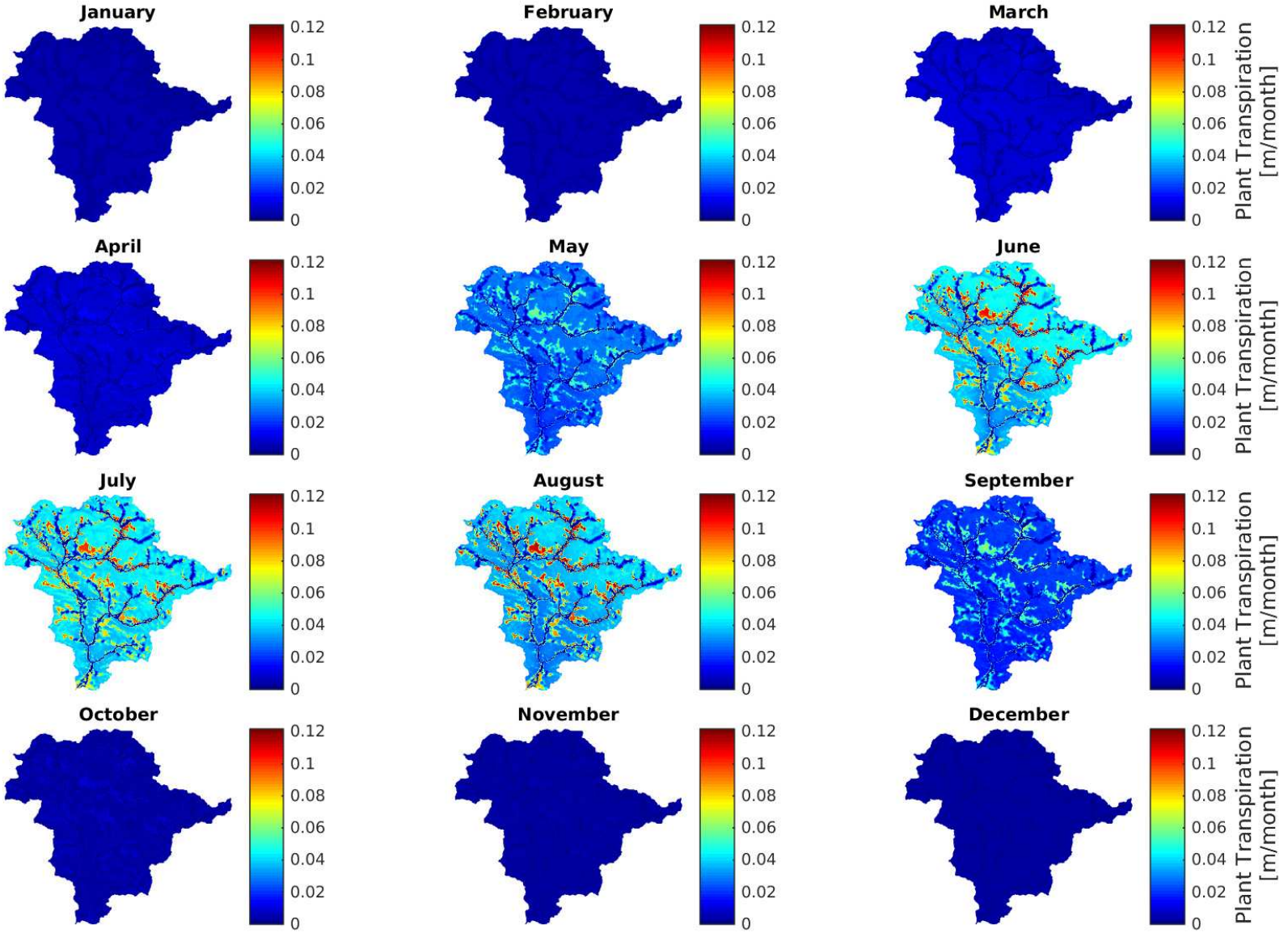

Figure 4.27: Transpiration from Deciduous forest. Part of the infiltrated flow is transpired by plants mostly in the growth season (summer), effectively lowering the water table which in turn increases infiltration rate for the overall catchment. Plant transpiration is significantly reduced in non-growth seasons. Allowing for the recovery of the water table.

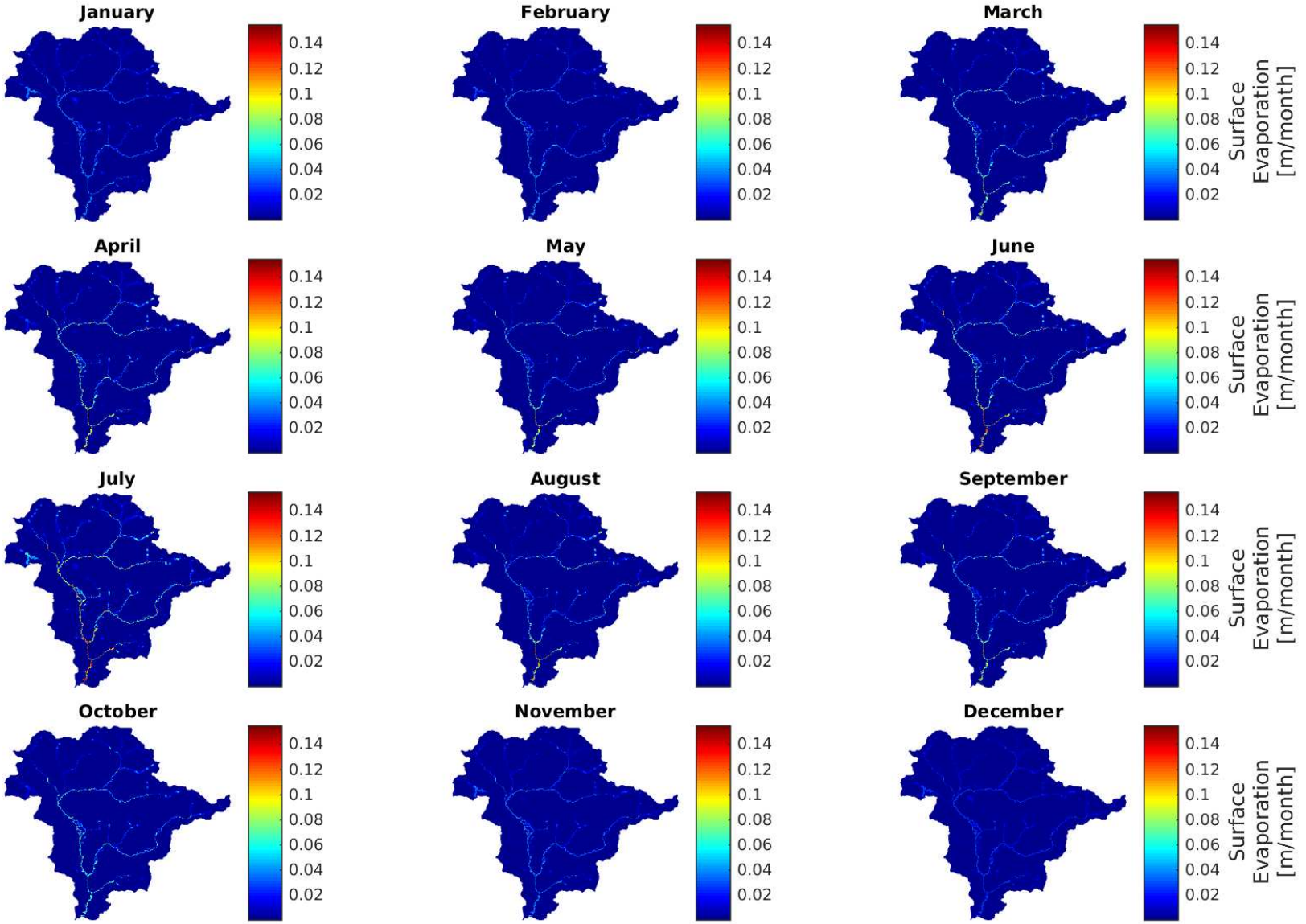

Figure 4.28: Surface evaporation from top soil in Deciduous forest. The evaporation from the top soil and the lakes and puddles on the surface make up the surface evaporation. The surface evaporation and transpiration make up the actual evaporation. Surface evaporation reaches the maximum at late spring and most of the summer.

4.7.3 Analysis seasonal of exchange flux

Exchange flux between surface and subsurface depend on the head difference of the respective flow fields. For parts of the catchment with deep water table, the exchange flux is always toward the subsurface. As the water table nears to the surface and becomes larger than the surface water hydraulic head, an exfiltration flux feeds water to the surface. As an extreme case of the fluctuation of LAI, deciduous forest's exchange flux is shown in figure 4.29. The Hardwood and Pine forest exchange flux show the same trends but with smaller variations.

The monthly variations show that the state of the water table changes as the growth season start and the transpiration by plants lower the water table and moisture content of the root zone. As the subsurface moisture content becomes low at July, August and September, the average exchange flux is feeding the subsurface. At winter and early spring and late autumn, where there is not a large transpirational LAI in the catchment, the water table recovers to its highest level and the river stream start to gain water from the subsurface. The spatial distribution of the exchange flux is also important and catchment topography plays an important role in how the surface and subsurface interact.

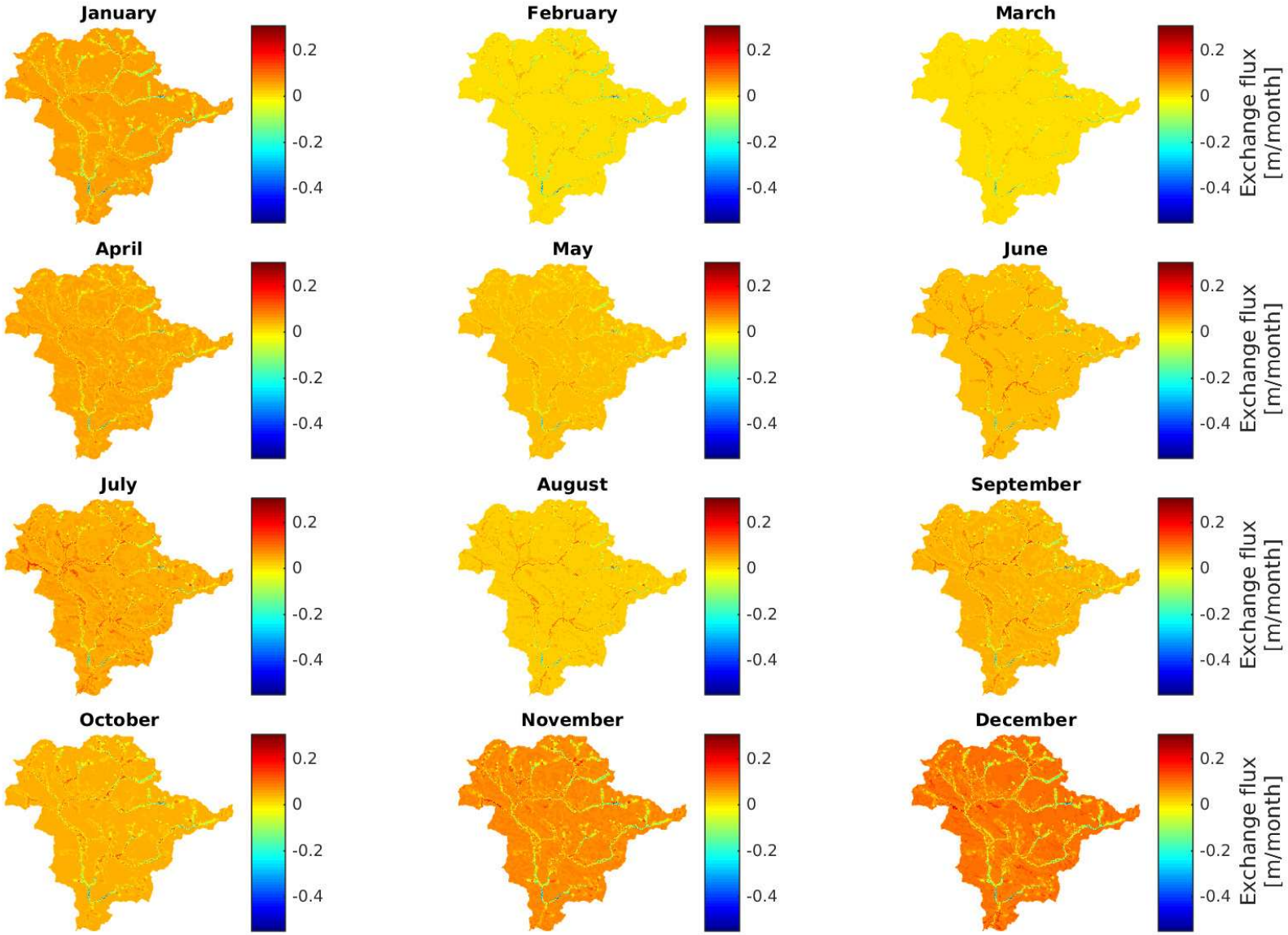

Figure 4.29: Deciduous forest exchange flux. The spatial and temporal distribution of the surface and subsurface exchange flux is shown for the catchment. At winter and early spring, the water table is high and the subsurface water is mostly exfiltrated to the surface near the river stream networks. The river is mostly in a gaining mode. The trend changes at the start of the growth season as the forest canopy starts transpiration, the exchange flux is reversed in river network. The water table elevation declines and more water is infiltrated to the subsurface. At the end of growth season, the recharge of the water table is facilitated by the decline of plant transpiration as the water table rises. The rise of the water table restarts the exfiltration of the subsurface water to the surface especially in the flood plains.

4.7.4 Analysis of hydrographs

Hydrograph fluctuations emerge as a result of interaction between various process in the catchment. Parts of the hydrograph for the experiments are shown in figure 4.30 and 4.31. The discharge from the catchment is regulated by the size of the canopy to a large extent. The clearcut scenario has the largest peaks, followed by Deciduous forest, Hardwood forest and Pine forest.
As hydrograph is an emergent single value variable in time for the entire catchment. The contribution of the subsurface discharge requires modeling of the age of a water or a tracer compound. 4.2.

Although the hydrographs look very similar for the forests, there are subtle differences in the peaks and over all behavior due to the canopy size. The precipitation intensities larger than about 3 to 4 mm/hour do not produce a flood event hydrograph as the precipitation is mostly absorbed by the various sinks in the catchment. Deciduous forest and Hardwood forest peaks are very close to each other at the end growth season. The Pine forest produces the largest peak at the beginning of the growth season.

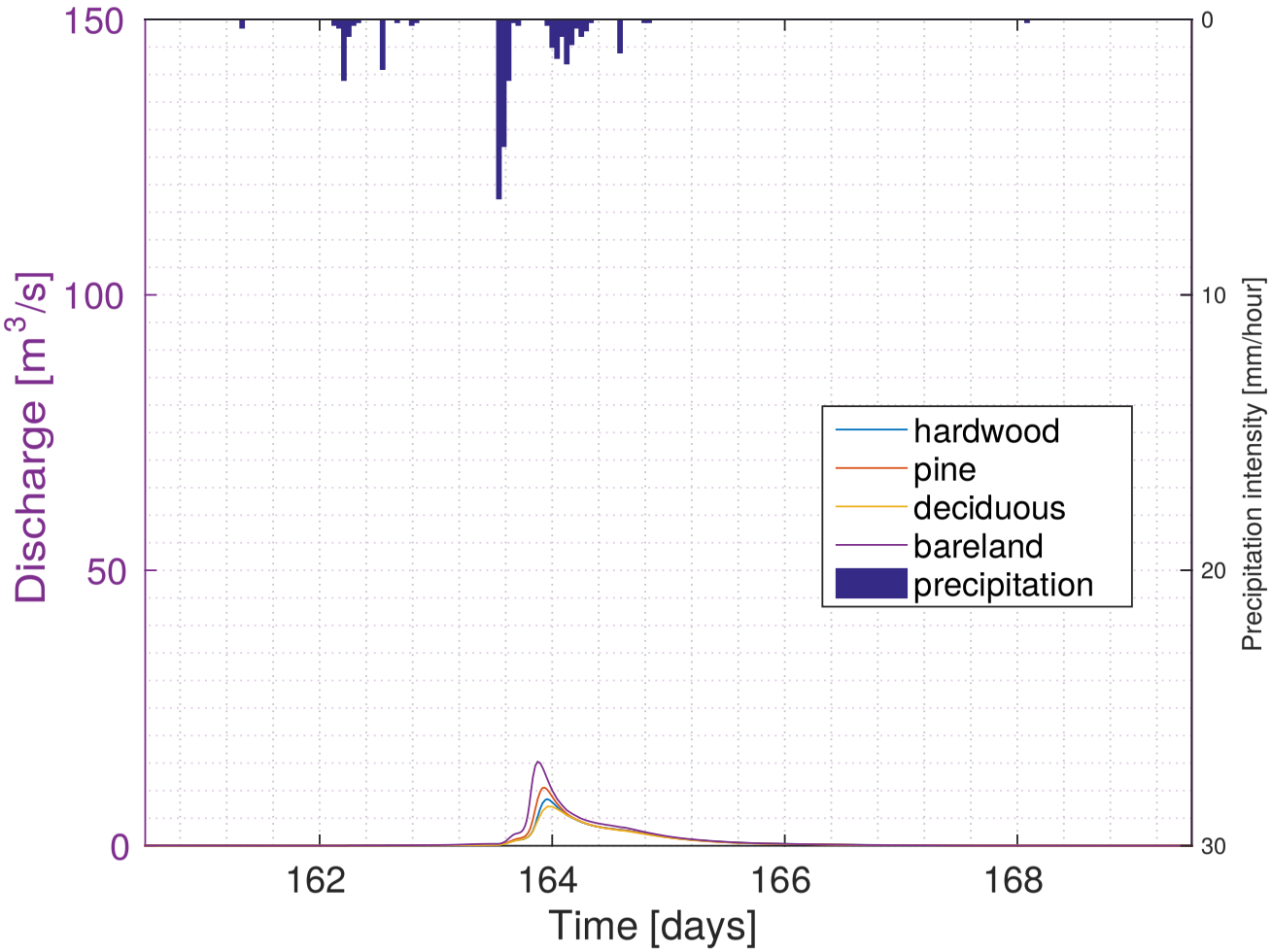

Figure 4.30: Annual discharge for the forests at the beginning of the growth season. The largest peaks are in the clearcut scenario followed by Deciduous forest, Hardwood and Pine forest. Precipitation intensities smaller than $4mm/hour$ are absorbed by various sinks like canopy and infiltration to subsurface. For intensities larger than $4mm/hour$, the canopy storage and subsurface storage are overrun and discharge occurs which causes erosion.

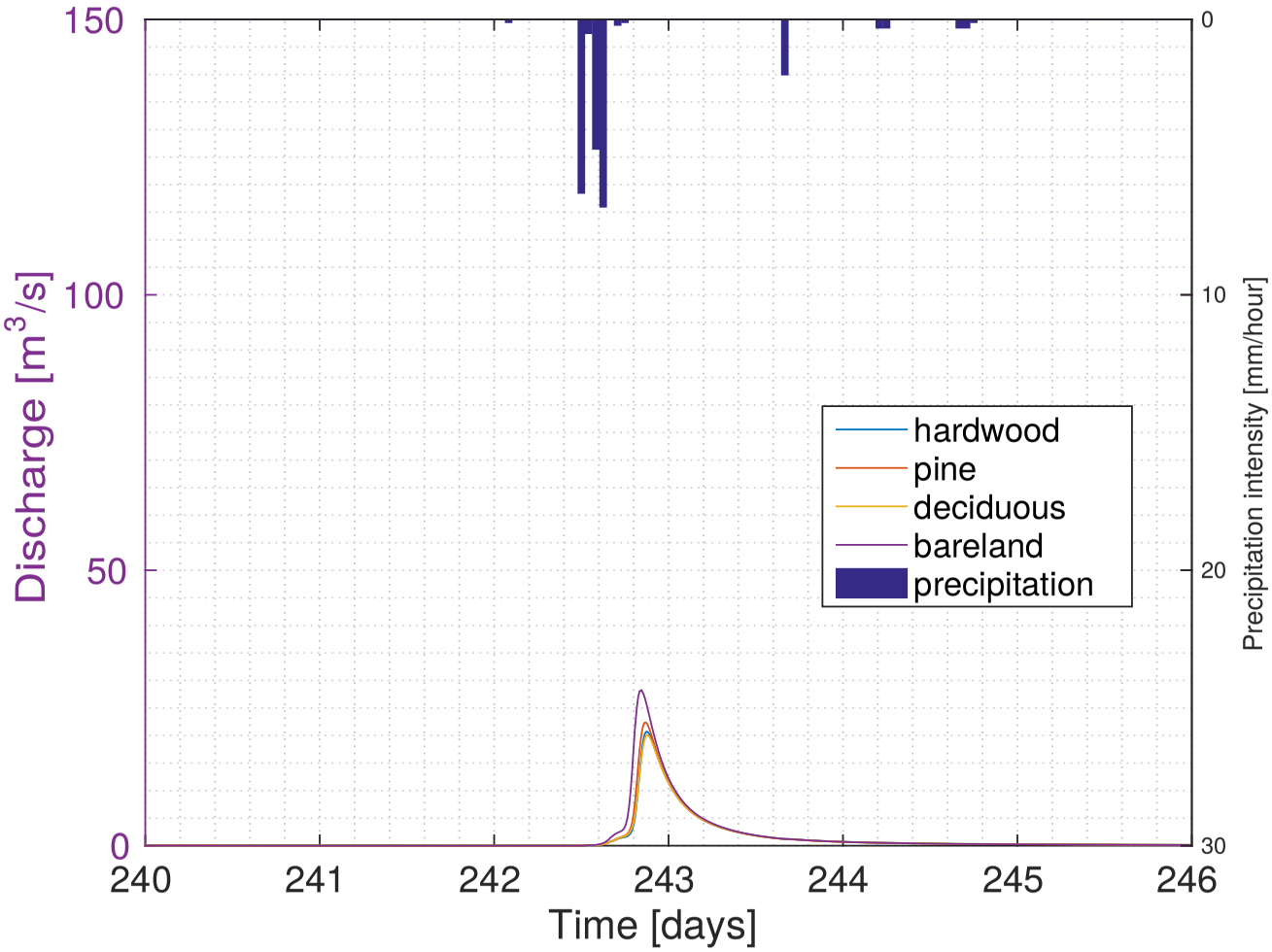

Figure 4.31: Annual discharge for the forests at the end of growth season. The clearcut scenario produces the largest peak after the growth season. The flow discharge from forests are close to each other and the difference between canopy size is attenuated by the diffusion processes in the river flow. However, the Pine forest's peak is larger than the Deciduous and Hardwood forest.

4.7.5 Analysis of specific stream power

Stream power is an effective measure for quantifying the ability of stream to erode the bedrock or transport sediments throughout the catchment. Stream power is the product of stream slope and water flux flowing for a given reach or river network. In mountainous headwater regions, the steeper slope (about 20% to 10%) compensates for smaller water flux and therefore sediment and regolith can be moved downstream. At flat regions, the flux is larger (catchment dependent) and the slope is very small (about 3% to 0.1%). As a result, the river stream is at dynamic equilibrium and mostly transports the regolith produced at the upstream. Here specific stream power for the forests and the clearcut simulations are analyzed .
The two dimensional transient surface flow allows us to study the actual erosive power associated with the river bed and flood bank erosion. Stream power, does not depend on the regolith or soil properties. Therefore it can be seen as a parameter that can act as a bridge between hydrology and geodynamics. This makes it a good criteria for the comparison of the potential erosion in the catchment and its relation to hydrological processes without an explicit knowledge of the river bed material hardness or the availability of the regolith.

The mean stream power for the forests are similar. Here the maximum of the mean stream power for the Deciduous forest is discussed. Envelop of maximum values per node for each month for the Deciduous forest are shown in figure 4.32. The envelope is made up of the maximum value of the specific stream power at each node for each month. Stream power travels as a wave for each event. Various factors, such as temporal variation of the precipitation and canopy size and evapotranspiration control the stream power and therefore erosion in a catchment. The overall trend is that for most of the precipitation events, the stream power is largest in winter and late autumn. However, large intensity precipitation events can produce significantly large stream power in the stream network in the growth season.

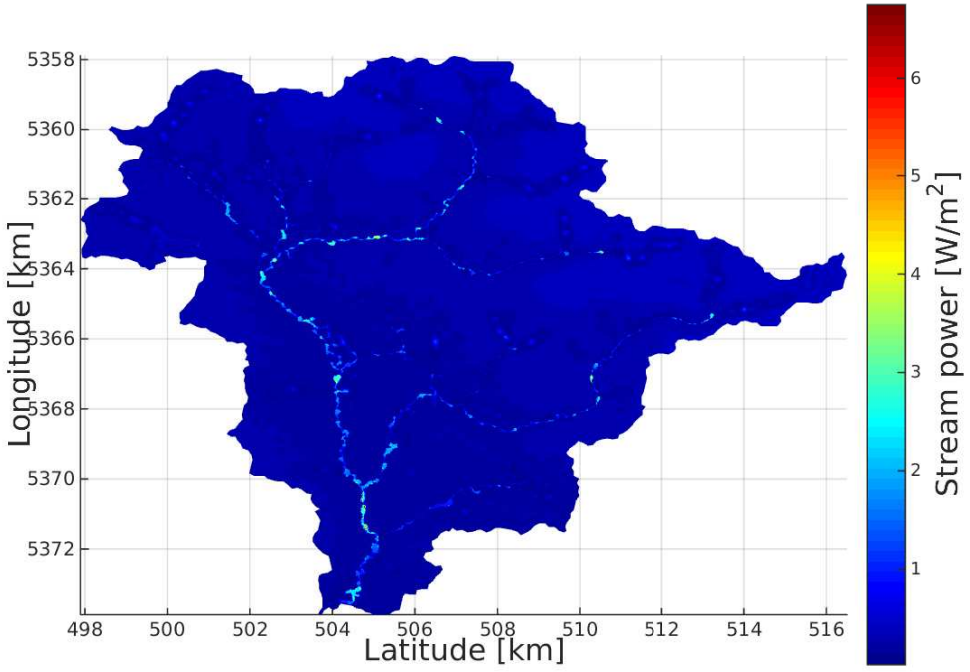

Figure 4.32: Average specific stream power for clearcut scenario]. Average of the specific stream power in the river stream. Stream power travels as a wave for each event. The annual average here shows specific hot spots of erosion. the hotspots arise due to the higher local velocities due to the geometry of the river at that point.

4.7.6 Analysis of erosion patterns.

Erosion for the forests is calculated according the formulation presented in chapter two and the results are presented here. According to the diffusive wave equation, water flux is proportional to the $h^{\frac{5}{3}}$ and erosion is proportional $h^{\frac{2}{3}}$ where h is the depth $[L]$ of the water in the river if the critical shear is ignored. The rate of increase of sediment is slower than the rate of increase of water flux as the water depth increase. With the increase of the discharge, the wet perimeter of the river also increase and therefore the water depth does not increase proportionally with the discharge. The filling of the flood banks limit the increase of the water depth according to the river channel topography.

The erosion rates is controlled by the number of the precipitation events that can overcome canopy storage, infiltration capacity and evapotranspiration rates to produce an increase in the river discharge. when the river bed shear stress becomes larger than critical shear stress on the river bed, the movement of the regolith starts. At winter and early spring, when the evapotranspiration demand is low and water table elevation is recovering from the growth season depletion, the smaller precipitation events are more likely to elicit larger discharge peaks and therefore more energy is available for the transport of regolith. The higher water table causes a steady rate of exfiltration that supplies the base flow, expediting more runoff and river stream interception. The storage of precipitation in the subsurface and slow release of the of water dampens the precipitation events to large extent in the summer where transpiration and evaporation demand is high throughout the catchment. Monthly erosion patterns for Hardwood forest and clearcut scenario is shown in figure 4.33, and 4.34. The spatial distribution of the erosion pattern in the forests are similar. This is due to the limitations of the mesh size. the with the increase of the water discharge, the river width increase and therefore the water depth does not increase as much to reflect the increase in the river bed shear stress.

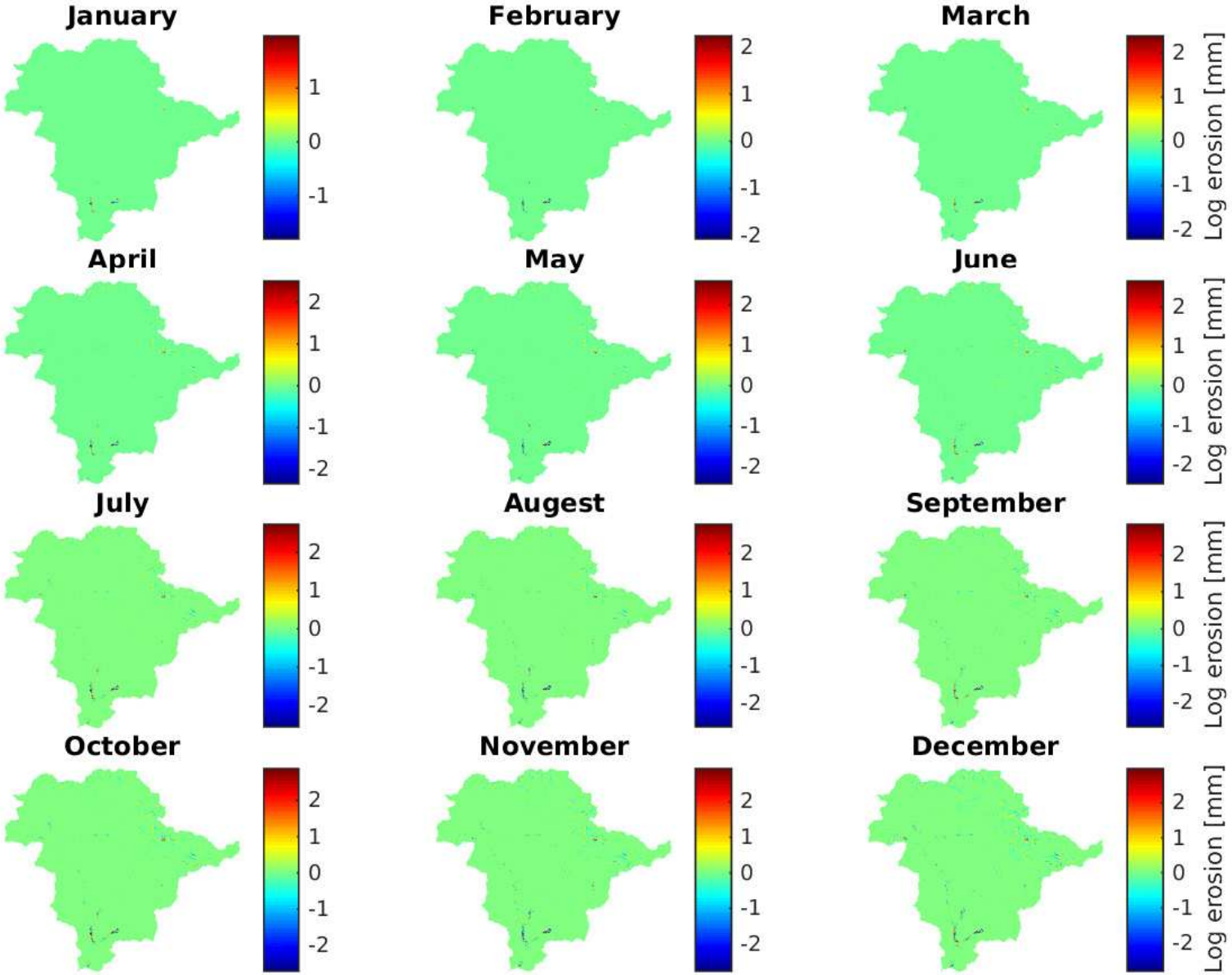

Figure 4.33: Monthly erosion patterns for Hardwood forest. The spatial distribution of the erosion in forests are similar. Erosion rate is larger in the outlet as the amoun t of water flux is larger near the outlet. The headwater and hillslope erosion rates are much smaller than the main channel erosion rates.

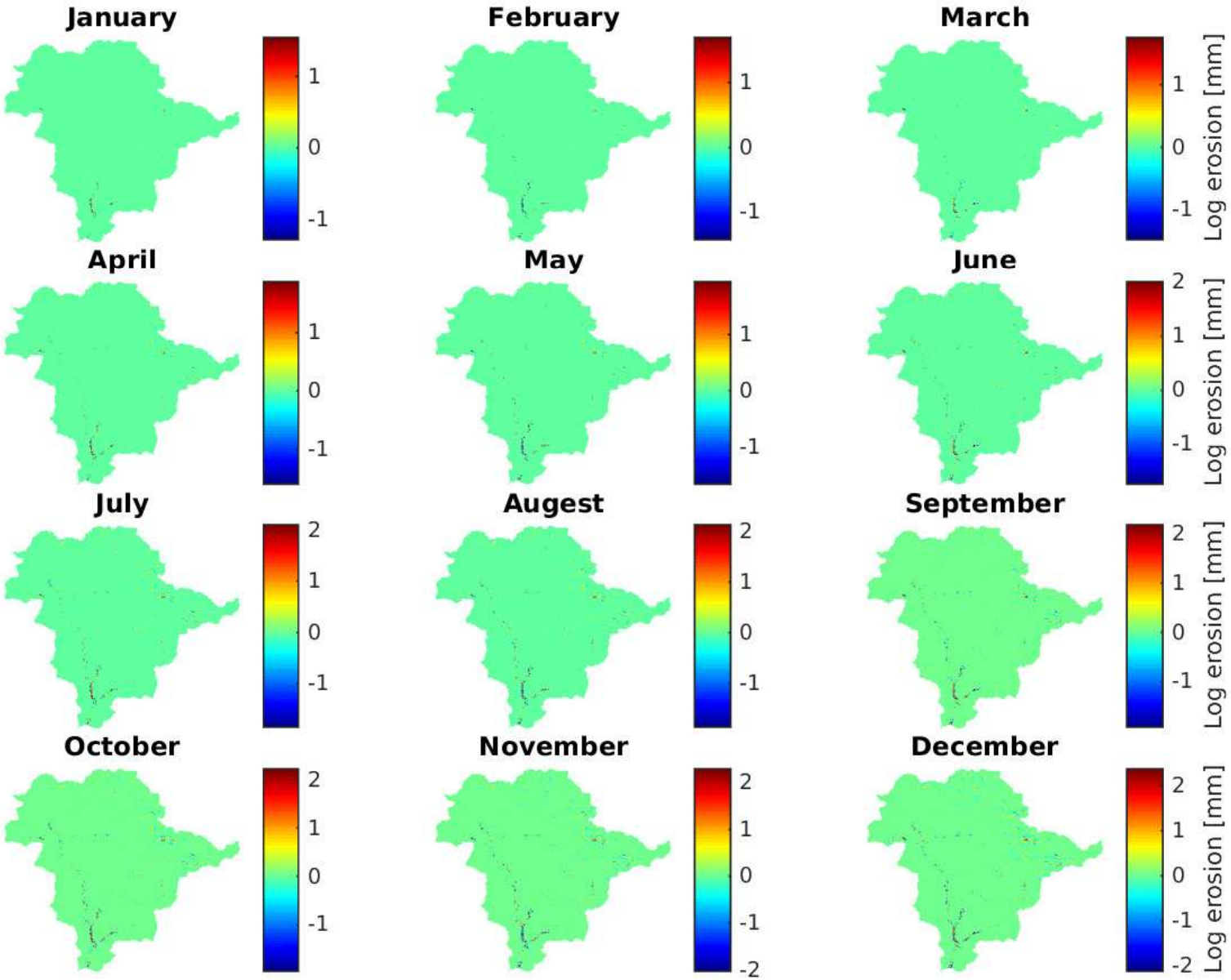

Figure 4.34: Monthly erosion patterns for clearcut scenario. An increase in the intensity of the erosion and the spatial extent of erosion is seen for the clearcut scenario. The spread of the flow over larger area limits the increase of the erosion. An accurate representation of the topography and river bed geometry is a major drawback of the current approach.

The spatial distribution of the erosion patterns are important for how the bank and floodplain erosion work. The cumulative bed load sediment flux discharge out of catchment is shown in figure 4.35. The discharge shows how erosion is effected by various parameters on a catchment level scale. Deciduous forest has the largest sediment discharge followed by Pine and Hardwood forests. With the start of the growth season, The Deciduous forest canopy starts to be more effective both as canopy interception and subsurface transpiration. This lowers the erosion rate in the Deciduous forest at the growth season. Deciduous sediment flux is about 5% more than Pine and Hardwood forests. The response of the forests in the beginning and end of the year are much more pronounced. The increase of the discharge for the events at the beginning and end of the year is larger compared for the precipitation events despite the increase of the intensity of the events in the summer. The representation of the geometry of the catchment is a controlling factor as the depth of the water does not increase significantly with the increase of discharge.

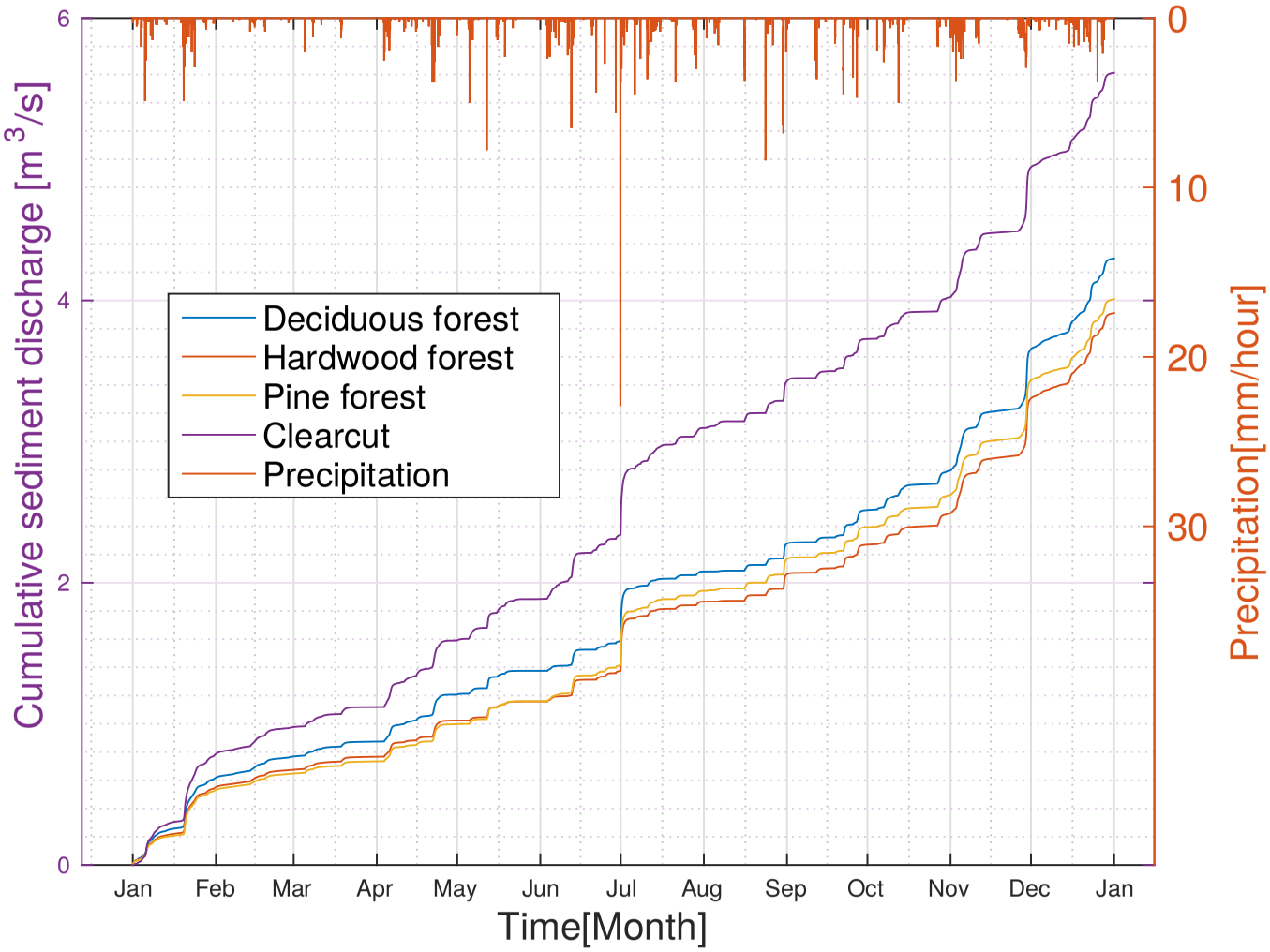

Figure 4.35: Sediment flux for forest scenarios. Deciduous forest's winter response to the precipitation is larger due to the lack of canopy before and after the growth season. Starting with growth season, canopy interception and subsurface transpiration is activated in the Deciduous forest which reduces the rate of the sediment discharge, At the end of growth season, the sediment flux increase again as the canopy interception goes to zero and transpiration from subsurface also vanishes. The sediment discharge from Pine forests is less than Hardwood and Deciduous forests before the growth season as it has a larger canopy size. With the onset of the growth season, the hardwood canopy size increase and the discharge from the hardwood decrease faster than the pine forest. The Pine forest sediment discharge overtakes the sediment discharge from the Hardwood forest. The clearcut scenario produces about 150% more sediment than the forests.

4.8 Conclusions

The hydrological simulations show that the ground water table depth is controlled by plant transpiration. The canopy interception becomes important when the potential evapotranspiration is significant at summer. The water table is controlled by recharge in mountainous regions of the catchment rather than topography. The forest types studied here can be viewed as perturbations of the existing forests in the region. The existing forest composition is mostly of the Deciduous type interwoven with conifers. The three forests show a general trend in the erosion but there is also a variation in their response to the precipitation as a hydrological driver. It is noteworthy that these hydrological forest simulations do not intend to capture all the pertinent mechanisms and dynamics of the catchment. The effects of macro-pores, raindrop disturbance of the hill-slopes, details in top soil variations are not included here. The models are also limited in the mesh size, having implications both for the hydrology and erosion. The spread of the river stream is larger than in reality which in effect increases the exchange width with subsurface, increases the interception surface of the river channel and hydraulic radius of river. The conceptualization of the runoff generation mechanisms (Dunne diagram) [119, 120, 145] provide a simple starting point for understating the response of the forests. However, the catchment studied here has many variable features than a single point in the Dunne conceptual model can not be used successfully for the characterization of the runoff generation. The Catchment can not be categorized as one of the saturation excess, infiltration excess or Hortonian runoff system. The water table at the hilltops at the south of the catchment are deeper than rest of the catchment. the slopes are much higher at the mountainous region and vegetation density varies from month to month. So a dynamic transition between runoff generation mechanisms are expected. The advantage of the formulation and solution of the partial differential equations that govern the flow of water in the surface and subsurface does not require for any explicit assumption on the part of the modeler about the nature of the runoff. Although having a conceptual model of how the transitions and possibilities can develop are helpful. The transition from saturation excess to infiltration excess happens within the domain where the physics of system dictates as the drivers or boundary conditions change.

The climate input for the simulations presented in chapter two indicate a year around precipitation pattern with an slight increase of precipitation intensity in summer. Evapotranspiration demand is also highest in the summer and lowest in winter. According to the Penman-Monteith equation [52], smaller vegetation densities limit the evapotranspiration. Evapotranspiration reaches the evaporation limit when the LAI increases. However, the increase in not linear a saturation level is reached with the increase of LAI. Assuming that the evaporation from the surface is according to the formulation presented in the beginning of this chapter [26, 146, 42], and the potential evapotranspiration is according to the Penman-Monteith [52], each forest's response can be studied in to 3 phases.

The first phase starting from January to the beginning of the growth season, is characterized by the lower evapotranspiration demand due to lower solar declination. The mean precipitation intensity is also about 10% lower than maximum precipitation intensity that occurs at summer. The canopy size is zero for Deciduous forest. The Hardwood forests canopy size is 12.5% of the maximum canopy size and the Pine forest canopy size is about 67% of the it's maximum canopy size. As the potential evapotranspiration is smaller at this phase, the existance or lack of the canopy do not influence the erosion rates in a significant way. The trends are similar for the forests. The difference in water flux and sediment flux is also small (2 to 5 percent). Hardwood forest produces slightly more sediment discharge than Pine

forest as its canopy size is smaller. The transpiration of the plants in the Pine and Hardwood forest do not impact the subsurface water table in a significant way. At this stage, the water table elevation is recovered from the summer evapotranspiration.

The second phase can be roughly identified with the start of the growth season from June to end of growth season at September. At this phase, the precipitation intensities increase by 20%. Potential evapotranspiration increase significantly (about 150% to 200%). The canopy size increase based on the type of the trees in each forest. The water table is continuously lowered by transpiration based on root depth and canopy size. The lowering of the water table is more pronounced in the Deciduous forest in the growth season as the root depth is larger and the canopy grows rapidly to the lai value of four. Despite the increased intensity of the precipitation events, most of the events do not produce runoffs and the precipitated water infiltrates into the subsurface or evaporated from the canopy. A limited number of precipitation events with high intensities or longer durations produce runoff and cause erosion on this phase. The increase in Potential evapotranspiration and increase in canopy counter the increase in precipitation intensity and a strong control on the amount of erosion is observed for the forests.

The third phase starts at end of growth season at late September until January. At this phase, the depleted water table starts onto the recovery path while the lower declination of the sun reduces the evapotranspiration demand again, and there is a reduction in the intensity of the precipitation events. The decrease of canopy and lesser evapotranspiration demand shows an increase in the erosion rate. Part of the precipitation infiltrates to the subsurface and base flow recovers due to the increase of water table elevation. Average stream power for this phase is also higher due to the existence of base flow. The runoff and stream flow at this phase are more active even with lower intensity events and therefore erosion rates increase slightly. the increase of the LAI in Hardwood forest at the growth season reduces the sediment flux.

The sediment discharge from the catchment is controlled by various factors. The catchment seems to have a long term memory that exceeds the antecedent precipitation time scales. The reduction of the rate of sediment discharge in the Deciduous and Hardwood forest in growth season shows the effectiveness of the canopy interception. Canopy interception proves to be less important when the evapotranspiration demand is low. Though the patterns of growth in the Hardwood and Pine forest are different, the over all sediment discharge from these forests are close. On the other hand, the Deciduous forest produces about 5% more sediment discharge. This can be attributed to canopy size variation and lower canopy interception in total. The combination of the Leaf Area variations, root depth and canopy interception provides a distinguished dynamics for each of these forests. The clearcut scenario has a discharge of about 150% of the discharge from forested scenarios. All of the scenarios assume the same value for the erodibility of the soil. It is possible that a clear cutting of a forest may loosen and disturb the top soil and make the soil more susceptible for erosion.

Chapter 5

Effects of wild fires and timber harvest on erosion

Drought induced tree mortality has become more frequent and severe in the past two decades world wide [31]. Observations in reoccurring seasonal droughts in woodland/conifer, temperate, broadleaved and tropical forests are systematically higher than expected normal levels of seasonal droughts. At the same time multi-year drought index of observed drought index is not higher than expected levels. This shows that temporal and seasonal variations in the rainfall due to climate change can reduce or wipe out entire forested areas as it happened in some parts of the world [147, 148, 149, 150]. The observed trend is consistent with the projections of IPCC [107] that the temperature variations in regional scale will be much larger than the global fluctuations. The current climate change will cause a higher temperature rise in some regions of the world. Therefore, regional changes will be more important than global temperature rise. The impacts of fire on different settings has already been studied and knowledge gaps has been identified [151, 152, 153]. Intentional burning of the forests and croplands in order to increase farming lands or clean up the farms after harvest for the next cultivation season are wide spread practices around the world. It is argued that fire changes the soil chemistry, affects biology and hydrology of the watersheds. Some studies report an increase in the ash and regolith supply after a fire in the forests which leads to an increase in erosion rates [17]. In order to control and limit the erosion rates, mulching and stabilization as an alternative is considered and a modeling scheme is proposed to reduce the erosion rates [154, 155]. The effects of the wild fires can be diverse, for example fire affects the chemical composition of the peatlands leading to an increase in the water repellency. This in turn enhances runoff generation and therefore increase flow discharge [156, 20, 157]. Regional studies on the effects of wild fires on catchment hydrology also indicate that the catchment hydrology responds immediately after the burn and the long term (five years) water availability also changes [158]. The average annual stream flow reported is twice as high compared to the unburned forest in some regional small watersheds. It is also shown that the severity and level of the burn on the forest controls the runoff and inter-rill erosion rates [159]. The loss of protective cover by fire is studied in western Montana and it is concluded that the erosion is stimulated by the lack of cover more than the change in water repellency [21]. A controlled hydrologic simulation on two plots with various burn levels show that the erosion rates increase after fire and recommends rehabilitation of the land to control erosion [160].

Timber harvesting is another major factor in reducing the forest density and vegetation levels. Forests and vegetation in general always seen as a controlling factor for erosion. A reduced or selective logging has been studied in order to rehabilitate forests in different regions [161, 162] in order to reduce the adverse affects of deforesting. Large scale harvesting of forests can alter the hydrology of a catchment, causing larger annual and season discharges in the precipitation season [163]. It is reported that the effect of selective logging is species despondent [164]. Some species are more vulnerable and therefore logging can have ecological consequences as well as geomorphological and hydrological effects. Clear cutting of the forest also increases the snow accumulation in colder catchments and faster meltdown and increase in the peak flow. Logging after a fire burned the forest is also a common practice. It is argued that post fire logging does not disturb the under-story vegetation in a catchment studied in northeastern United States [165].

In forested regions, the first order control on runoff is the canopy size. The canopy also acts as a sink in the subsurface due to the transpiration by leaves. Plant transpiration changes the energy balance on the surface as part of the energy is used in photosynthesis, the temperature around the plants is lower due to shading and the photosynthesis. Therefore any changes in the vegetation density in forests can have an effect of water cycle and consequently on erosion. Our goal in this part of the study is to complement the ongoing research in understanding the first order changes in the response of the catchment erosion due to effects of wild fire and timber harvest or logging. The distributed hydrological simulation framework can help us to get a comprehensive picture of the mechanisms and possible changes in the runoff generation mechanisms. The simulations conducted here focus on the major controlling parameters. It is assumed that the changes in the scale of the catchment does not change the climate of the region. The changes in the LAI due to logging and fire only changes the micro-climate of the catchment which in turn these changes are reflected on the potential evapotranspiration. The tree species of forest that are studied here provide a picture on how various parameters interact and produce an emergent erosion pattern that ultimately shape the geomorphologic response of the catchment. The major hypothesis is that the reduction of LAI leads to a shift from low runoff producing mechanisms to a more productive runoff mechanisms. It is postulated that the runoff in higher slopes should shift toward a saturation excess or Dunne runoff mechanisms and in lower or steeper slopes, the runoff should shift toward a Hortonian overland flow as the vegetation density decreases in some parts of the catchment.

5.1 Logging caused enhancement of erosion as an anthropogenic disturbance

Logging reduces the canopy size in forests. Therefore the potential and actual evapotranspiration is reduced. This is considered here as a first order parameter that is going to have to most observable effect in hydraulic head distribution in the forests. The harvesting practice varies regionally, including harvesting a small amount of timber with no impact on ecology of the forests to industrial scale harvesting that can clear the forest or using a harvest rate of 2/3 [164, 161, 162]. The logging scenario assumed to be happening at a harvesting rate of 50% of available trees. The LAI therefore is reduced by 50%. The question is how this harvest rate is going to change the hydrological response of the catchment and how the erosion rates will be affected. Figure 5.1 shows the variations in the logging forest LAI. The potential evapotranspiration for the logging scenarios are shown in figure 5.2, 5.4 and 5.3. The potential evapotranspiration is reduced due to the smaller value of the canopy size. However, the reduction

is not significant due to the way the Penman-Monteith equation is setup. The canopy size becomes less important as the LAI becomes larger. In this case, the reduction of LAI reduces the potential evapotranspiration by about 10% of the full canopy evapotranspiration.

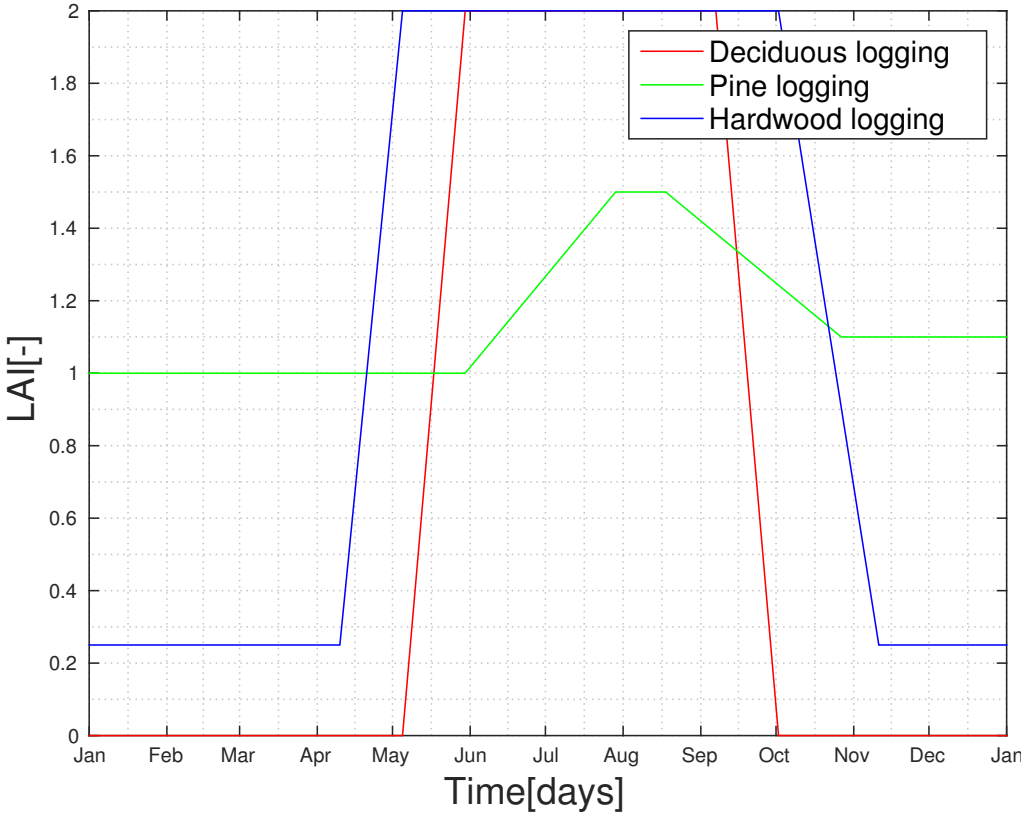

Figure 5.1: LAI for logging scenario in the forests. There are various approaches in timber harvest ranging from harvesting a very small amount of timber or harvesting in an economic scale. Here, the timber harvesting is assumed to be 50% of the available trees. This reduces the transpirational leaves by half, effectively reducing the plant transpiration and canopy interception. Potential evapotranspiration is also influenced by the amount of harvest.

5.2 Wildfire caused enhancement of erosion due to climate change

It is estimated that climate change will bring in periods of longer droughts at some regions [31]. The longer drought periods make forests more vulnerable to wild fires. The fire break outs have two observable effects. Depending on the spatial extent of the wildfire and duration of it, all the transpirational leaves can burn out in the current growing season. The absence of leaves reduce or halt plant transpiration from forest canopy or undergrowth. The extraction of the moisture from the root depth halts and therefore the ground water level should rise in the burned regions. The overall expected effect is an increase in runoff generation and therefore an increase in sediment discharge. The simulations here focus on the effect of the elimination of the canopy alone. Other effects are not included in the simulations. For example, it is reported that wild fires decrease top soil hydraulic conductivity up to 30%. This can cause a further increase in runoff generation. The increase in the frequency of wildfires in the forested landscapes therefor

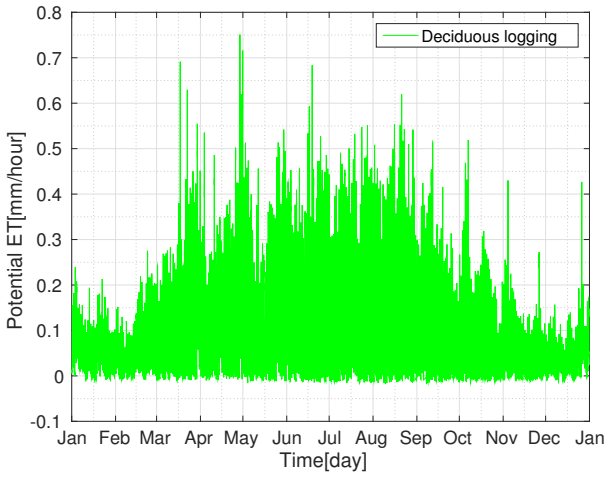

Figure 5.2: Potential evapotranspiration in Deciduous forest. Deciduous forests lose their leaves at colder season of the year. When the canopy size is zero, the potential evapotranspiration becomes the potential evaporation from the surface. Based on the albedo of the soil and climatic condition, Potential evaporation can be larger or smaller than potential evapotranspiration.

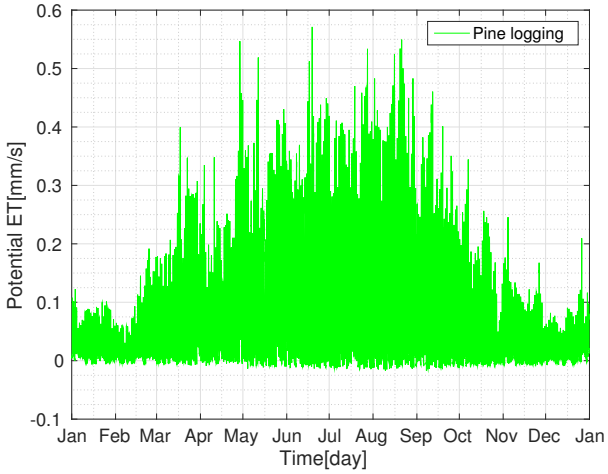

Figure 5.3: Evapotranspiration in Pine forest. Pine forests have a significant transpirational canopy throughout the year. The effect of plant transpiration is small in the colder season as the evapotranspiration is limited by the availability of energy.

is expected to increase sediment discharge. Understanding the hydrology and mechanics of the wildfire can be helpful in implementing remedies or identifying problematic zones after a fire break out. The reduction of LAI due to fire is shown in figure 5.5. The corresponding potential evapotranspiration for the forests are shown in figure 5.6, 5.7 and 5.8.

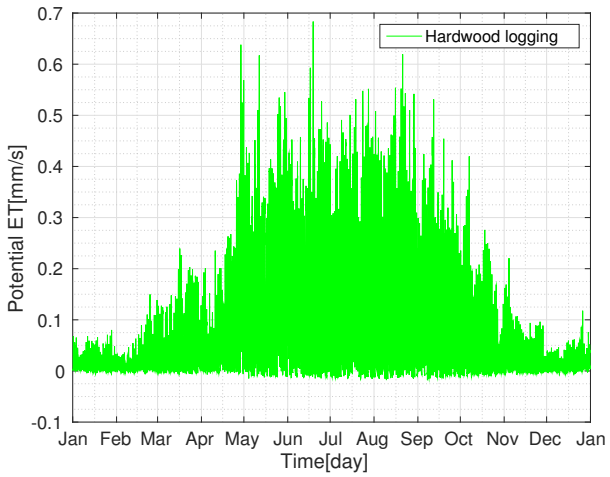

Figure 5.4: Potential evapotranspiration in hardwood forest. The Hardwood forest is a mixture of Coniferous and Deciduous trees. It has the characteristic of both forest types. In the colder seasons, the potential evapotranspiration is reduced due to the energy constraint.

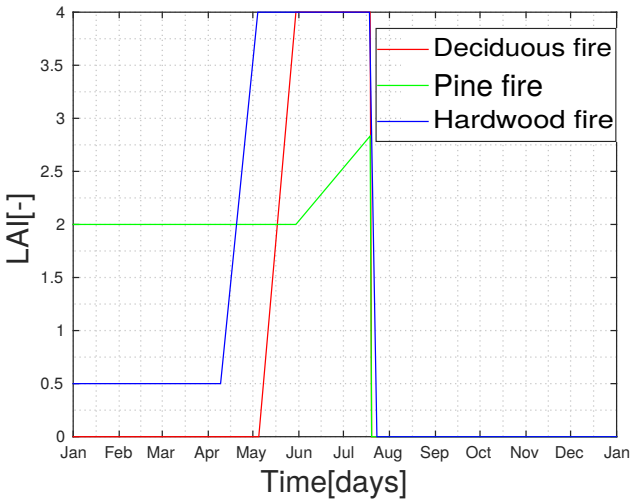

Figure 5.5: LAI reduction in fire scenarios for the forests. The sudden reduction of the LAI to zero due to fire break out removes the canopy interception. As there is no leaf left in the catchment, the potential evapotranspiration is also affected.

Table 5.1: Annual potential evapotranspiration for forest scenarios using Penman-Montheith.

Forest	in tact forest	logging	fire
Deciduous $[m]$	1.3504	1.1599	1.2221
Hardwood $[m]$	1.0461	0.94522	1.0937
Pine $[m]$	1.0923	0.96988	1.1523
Thornthwaite method $[m]$	0.5946	-	-
Clear cutting $[m]$	0.6764	-	-

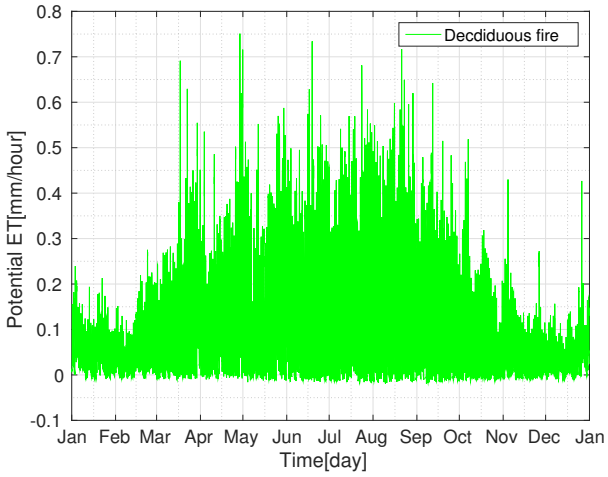

Figure 5.6: Evapotranspiration in Deciduous forest fire scenario. The onset of the fire causes the canopy size to become zero, which affects the potential evapotranspiration.

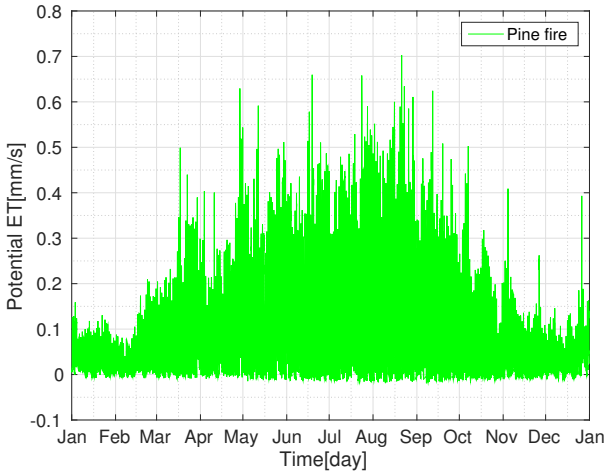

Figure 5.7: Evapotranspiration in Pine forest fire scenario.

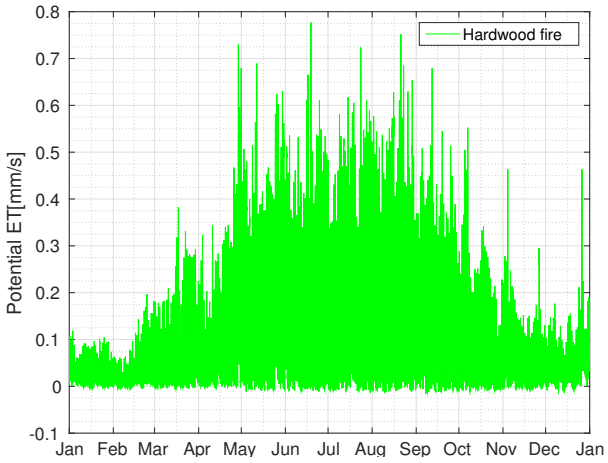

Figure 5.8: Evapotranspiration in Hardwood forest fire scenario.

The annual potential evapotranspiration for different scenarios are summarized in table 5.1. The clear cutting scenario has the smallest annual evapotranspiration according to the Penman-Monteith and Thornthwaite method. The Thornthwaite and Penman-Montheith are in good agreement with each other for the potential evaporation. It should be noted that the penetration of the light to the bottom of canopy is reduces exponentially and the evaporation from the surface can never only become zero if the atmospheric saturation level is 100%. The evaporation from the undergrowth or the surface below the canopy is controlled by the ambient temperature and water vapor deficit. The convective flux of air removes the water vapor from the canopy and facilitates evaporation from the top soil and surface waters below the canopy in the forests.

5.3 Results

This section is the discussion and analysis of the results for logging and fire scenarios in the forests. The hydraulic head in the observation wells, actual evapotranspiration and spatial top soil saturation levels are discussed which are the control variables in the runoff generation mechanisms. The sediment discharge in each forest for the logging and fire scenario is analyzed as the result of changes in the hydrology of the catchment.

5.3.1 Analysis of observation well head fluctuations

Fluctuations of the groundwater hydraulic head is a function of the net recharge. The hydraulic head variations at surface and subsurface are shown in figures 5.9 to 5.16. The fluctuations of the water table and surface water are linked when the water table is closer to surface as discussed in the analysis of the observation wells in chapter four. In general the hydraulic head in the subsurface for the logging scenario with a smaller canopy size and lower potential evapotranspiration is higher groundwater table elevation. The fire scenario eliminates canopy and transpiration at the middle of the growth season. Therefore the water table recovers to the clearcut scenario in about two month time. The rate of recovery is related to the upstream area of the point. Some observation points like point 6 and 8 are not as strongly linked to the surface as other points. Observation points 1 and 5 are strongly linked to the surface as these points lie close to the river stream or located at the floodplain. Though the evapotranspiration is not drastically decreased in the growth season for the logging scenario, the reduction of the canopy storage causes larger water availability as throughfall. The top soil surface receives more precipitation and therefore has higher saturation level for the canopy and after the fire. This in turn cause slightly larger runoff generation throughout the catchment for the logging scenario.

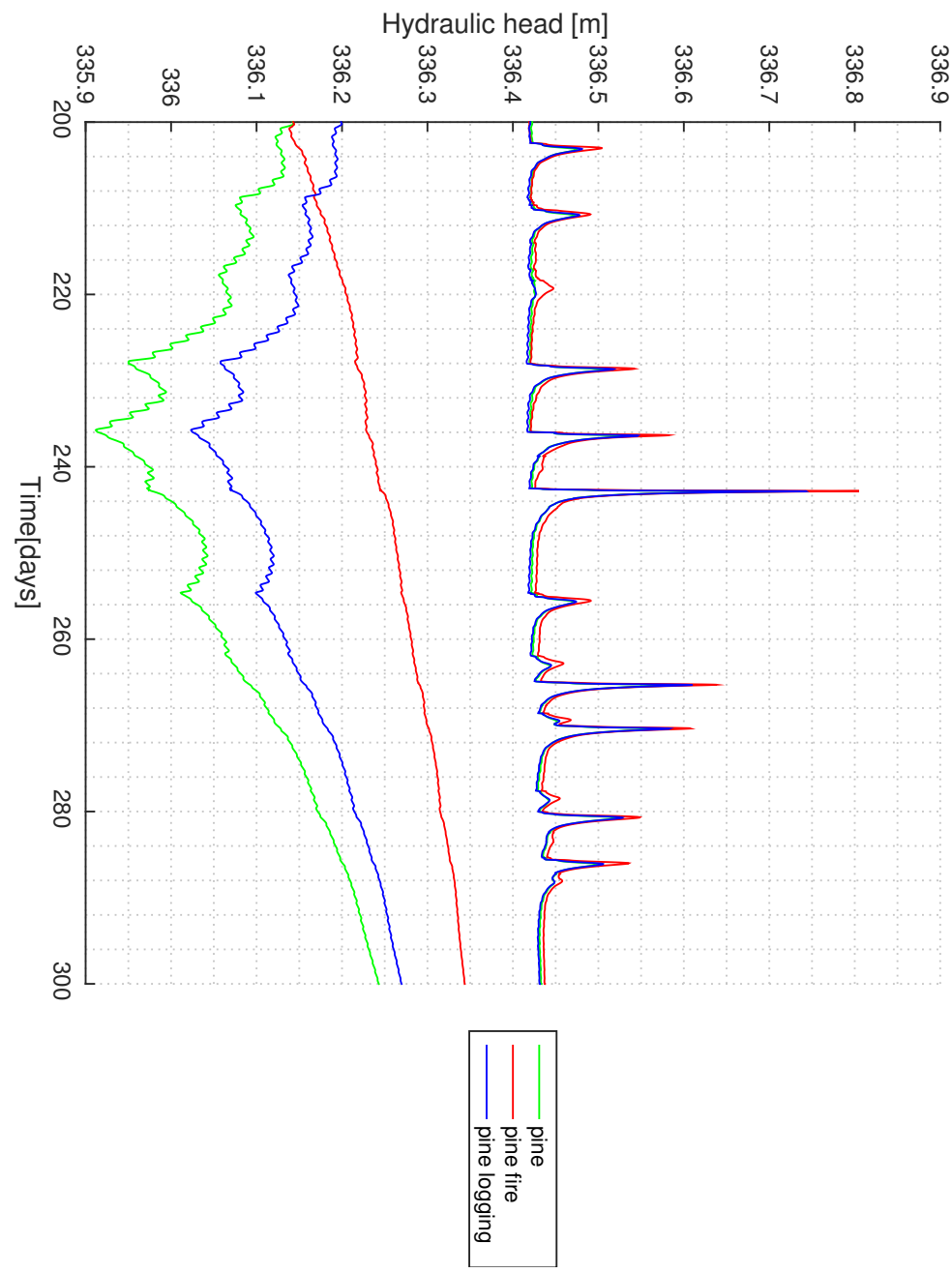

Figure 5.9: Surface and subsurface hydraulic head variations for Pine forest scenarios at obs. point 1. The Pine forest subsurface fluctuations are larger than the fire and logging scenarios. The response of the fire scenario does not have any daily or seasonal spiked response. Logging scenario subsurface hydraulic head is higher due to lower transpiration.

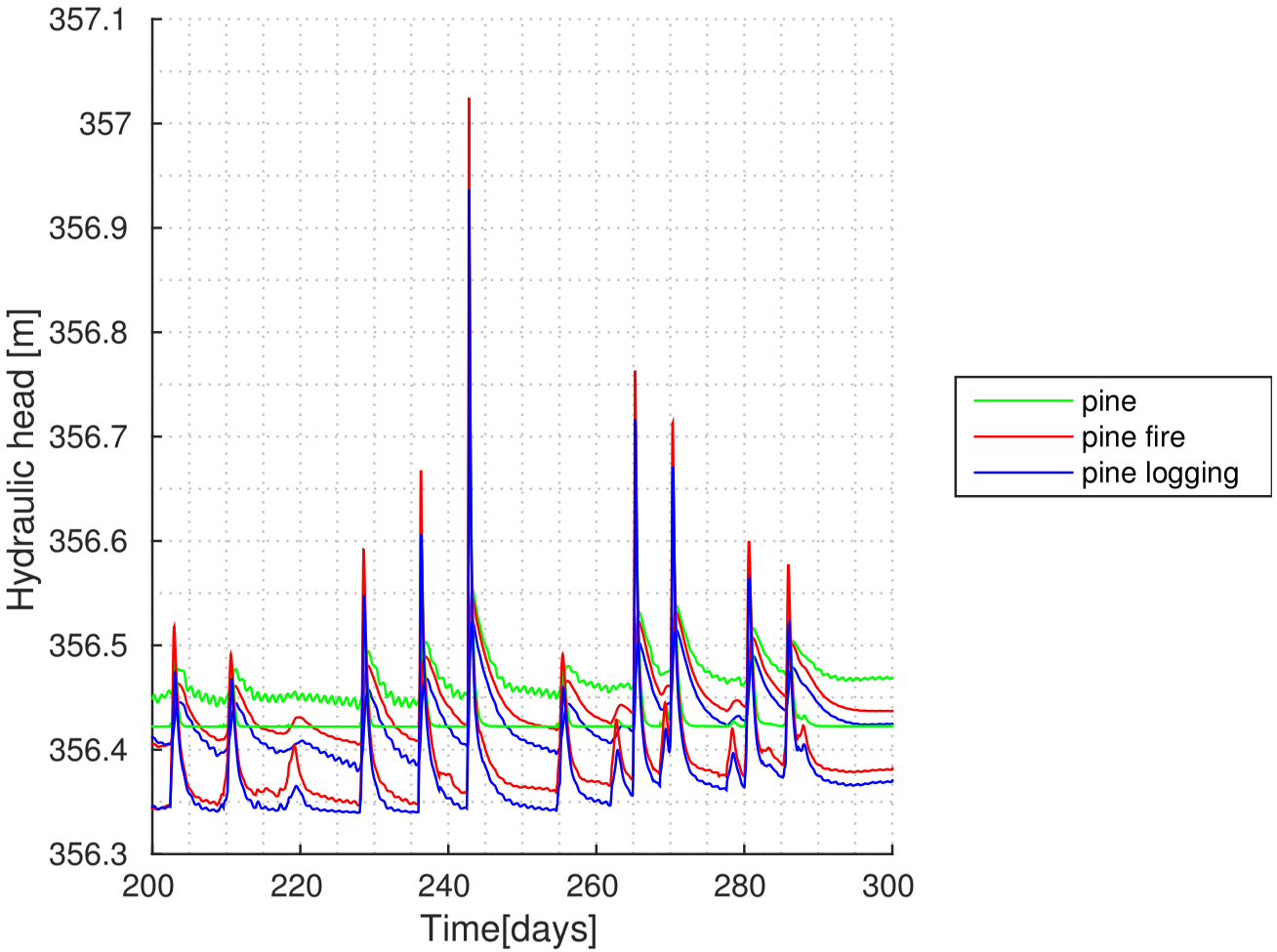

Figure 5.10: Surface and subsurface hydraulic head variations for Pine forest scenarios at obs. point 2. This point is located within the floodplain and becomes part of the river for fire and logging scenarios. Subsurface head is in general above the elevation and this point is always a recharge point for river. The difference between fire and logging and Pine forest scenarios are not pronounced. the daily subsurface hydraulic head fluctuations due to plant transpiration are still observable in the growth season. Increase in the peak of the river is inversely proportional to the leaf area index.

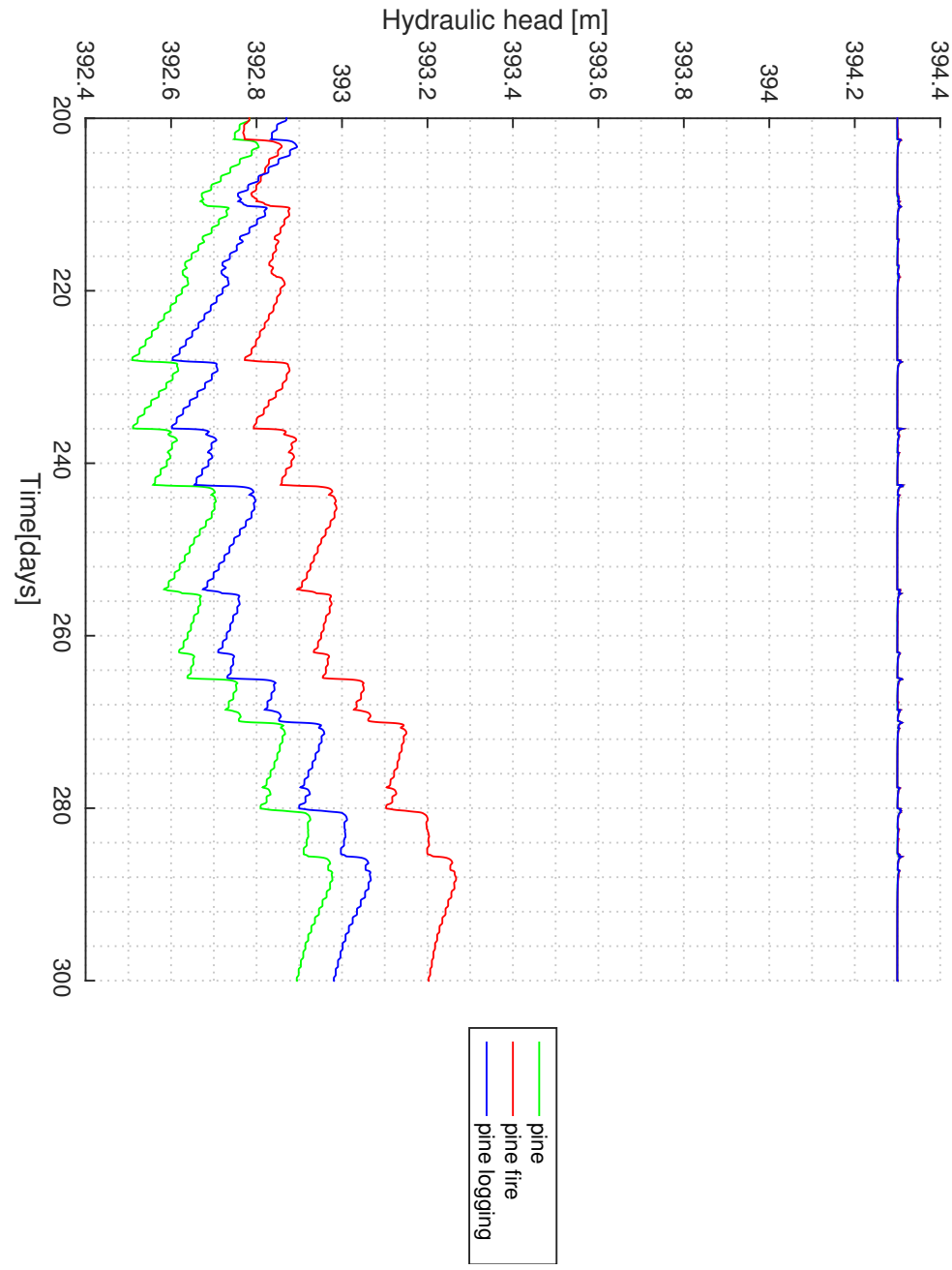

Figure 5.11: Surface and subsurface hydraulic head variations for Pine forest scenarios at obs. point 3. This observation point is not largely affected by the surface processes. The water table depth is around 3.5m and it is likely the water table here is regulated by the topography rather than recharge. The fire scenario water table is affected by removing the transpiration and the water table recovers slowly to the clearcut scenario.

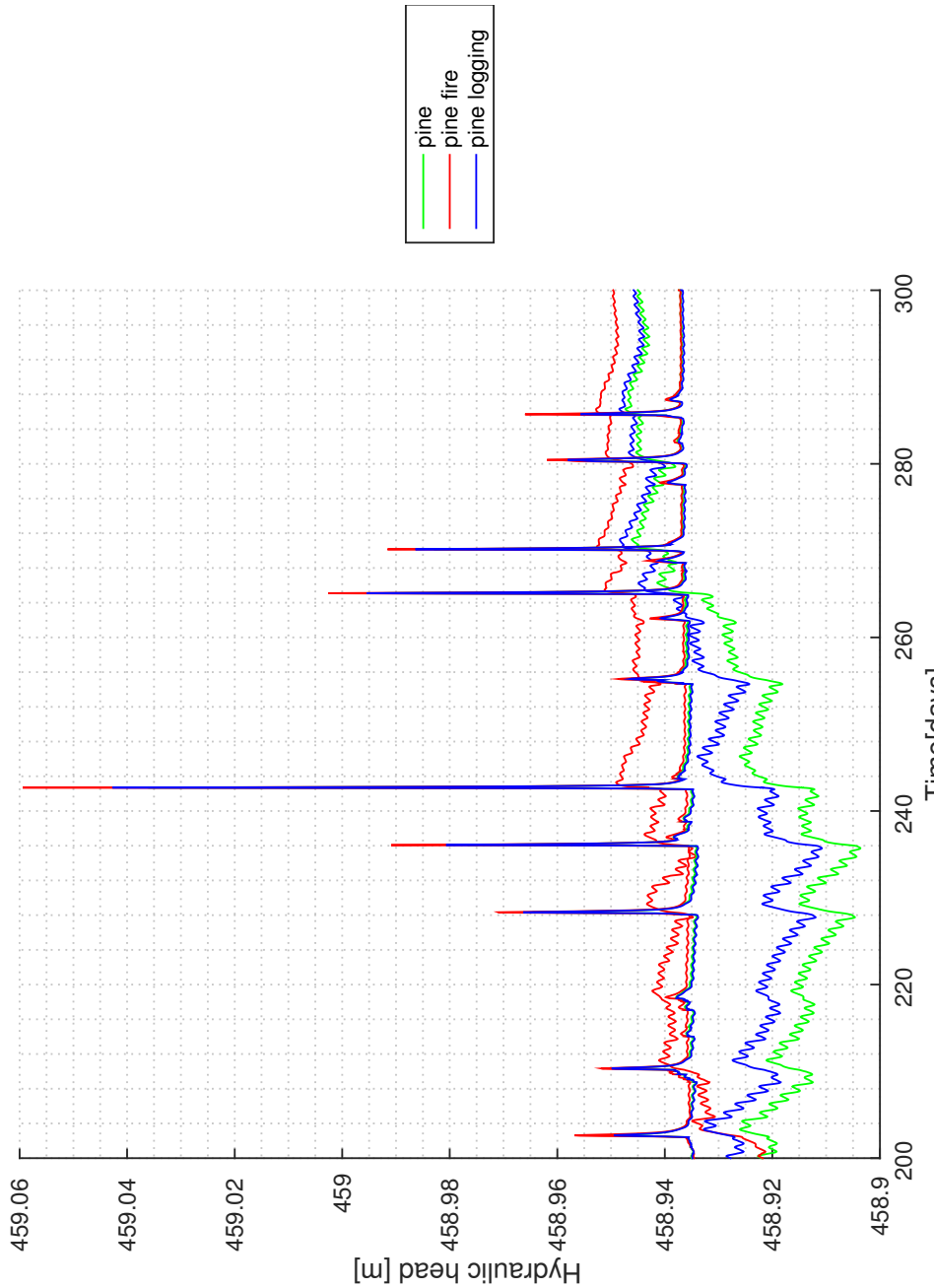

Figure 5.12: Surface and subsurface hydraulic head variations for Pine forest scenarios at obs. point 4. This point is near the river stream network. For the Pine forest scenario, the water table is about 1m below the surface. For the logging case, at the end of growth season this point becomes a recharge point to the river and river starts to gain water. The recovery of the water table in the fire scenario is fast as this point is downstream of multiple sub-catchments. The peaks produced by fire scenario becomes the second largest in a short period after the LAI reduction.

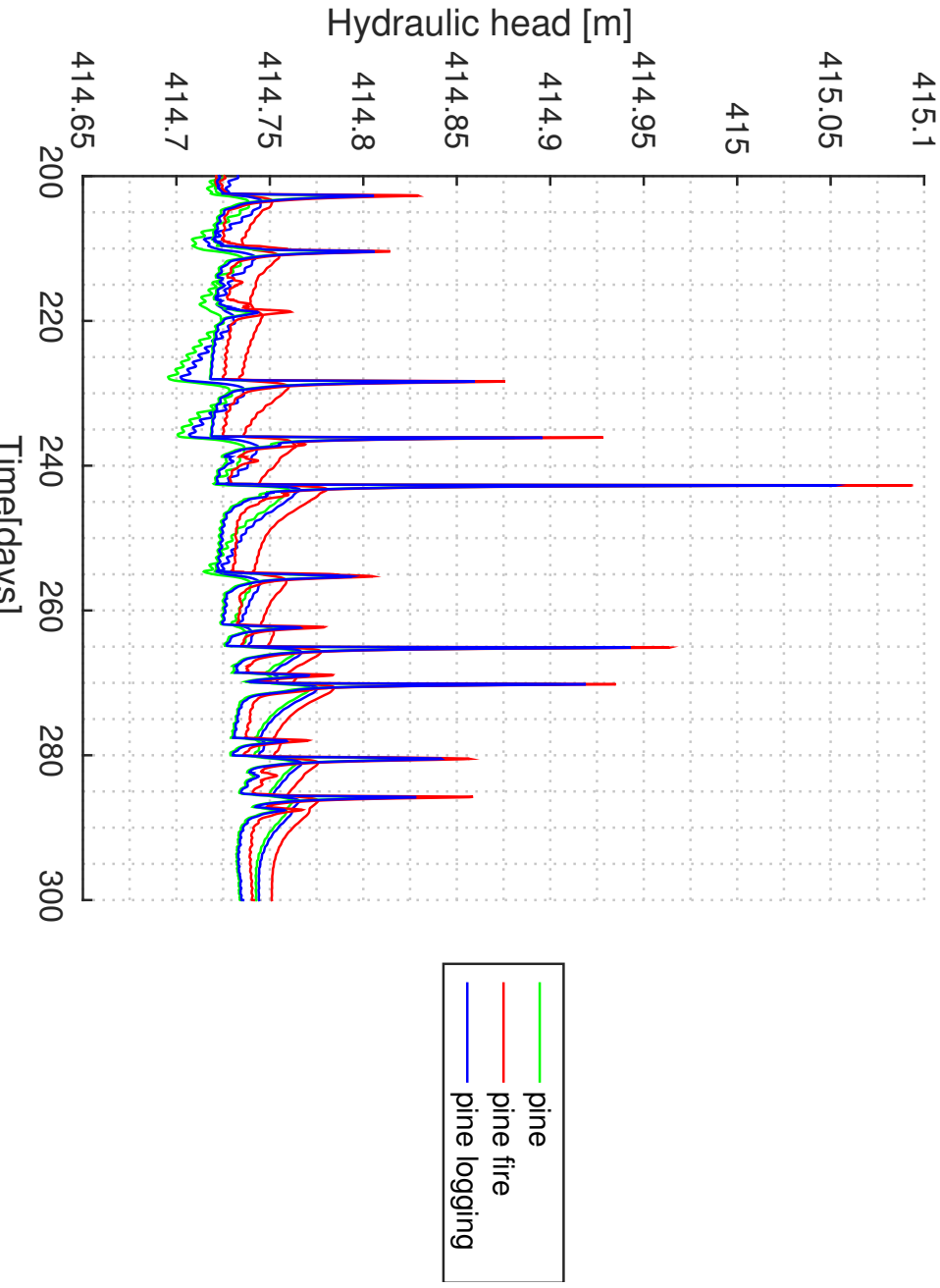

Figure 5.13: Surface and subsurface hydraulic head variations for Pine forest scenarios at obs. point 5. This point is in the floodplain of the river network in the middle of the catchment. The water table is close to the surface and saturation is slightly reduced due in forest scenario. The recovery of head to clearcut case is relatively fast. This point is a recharge point for the river except for a limited time in the growth season for the fire and logging scenarios.

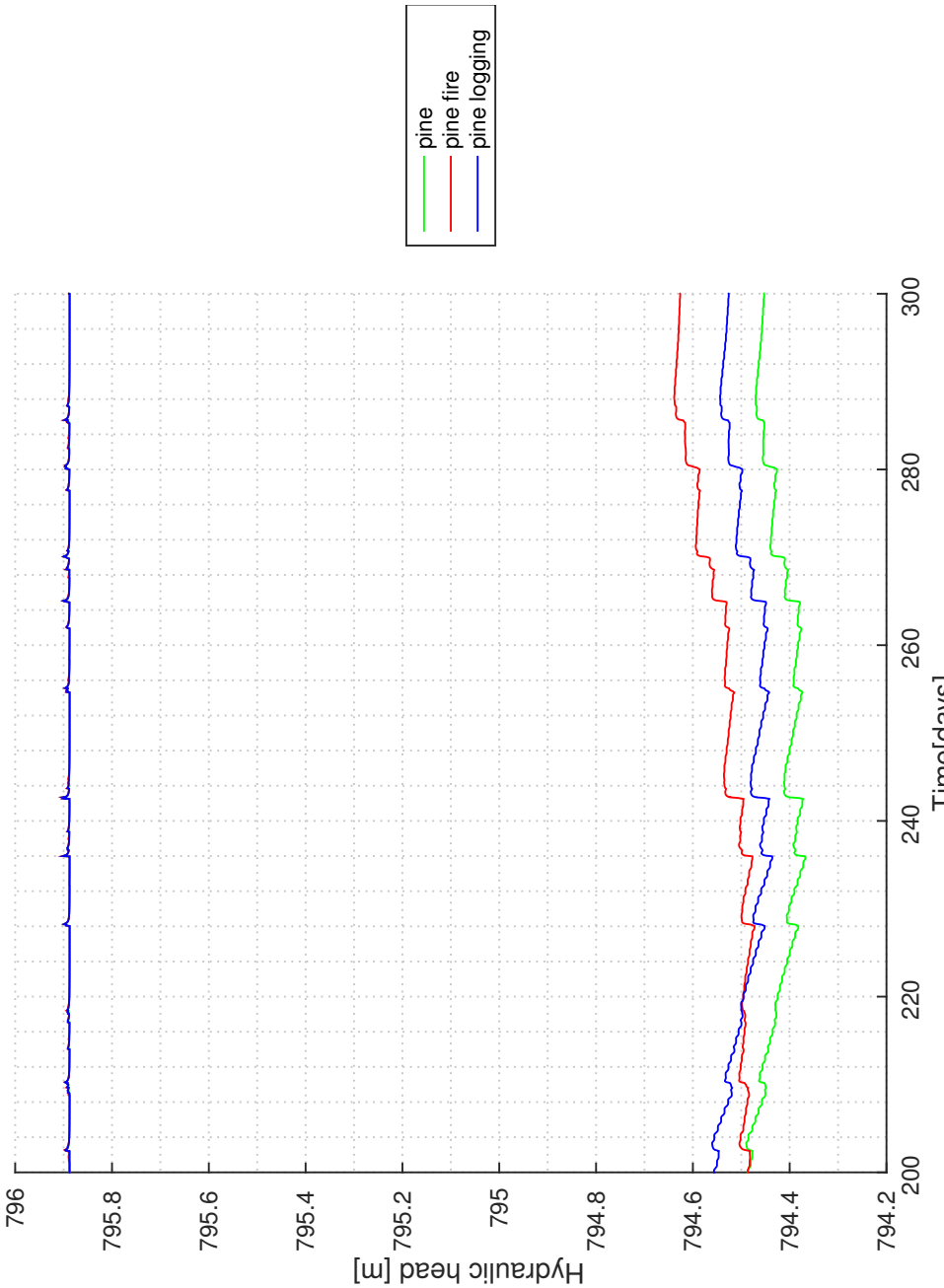

Figure 5.14: Surface and subsurface hydraulic head variations for Pine forest scenarios at obs. point 6. This point is the at peak of the mountain inside the catchment. The water table depth is about 10 meters below the surface. This point is not affected by the precipitation events and water table is largely controlled by recharge. The daily transpiration of the plants does not effect the subsurface due to the depth of water table.

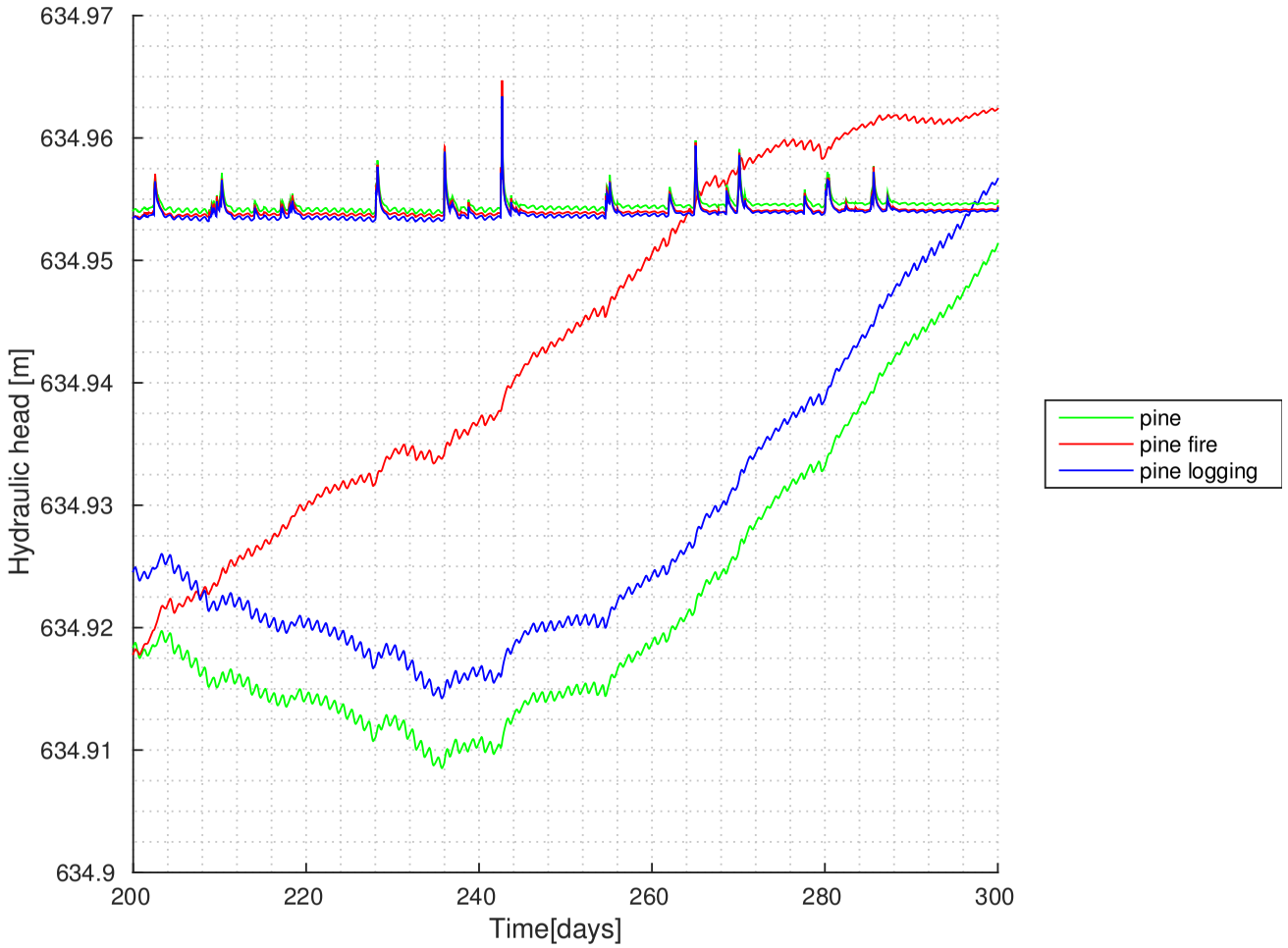

Figure 5.15: Surface and subsurface hydraulic head variations for Pine forest scenarios at obs. point 7. This point is located downstream a smaller upstream area near to the border of the catchment. The difference between scenarios are with in the $30cm$ head fluctuation of the subsurface. as the upstream is smaller. The recovery of water table in the fire scenario is also slower than other points with larger upstream area. This point is at the headwater region where the river stream is starting to form. The erosion at these points are important as these points are in the interface between hillslope processes and fluvial processes. The regolith produced by the hillslope transport mechanisms are moved downstream into the river by smaller flux, higher slope stream power generated here.

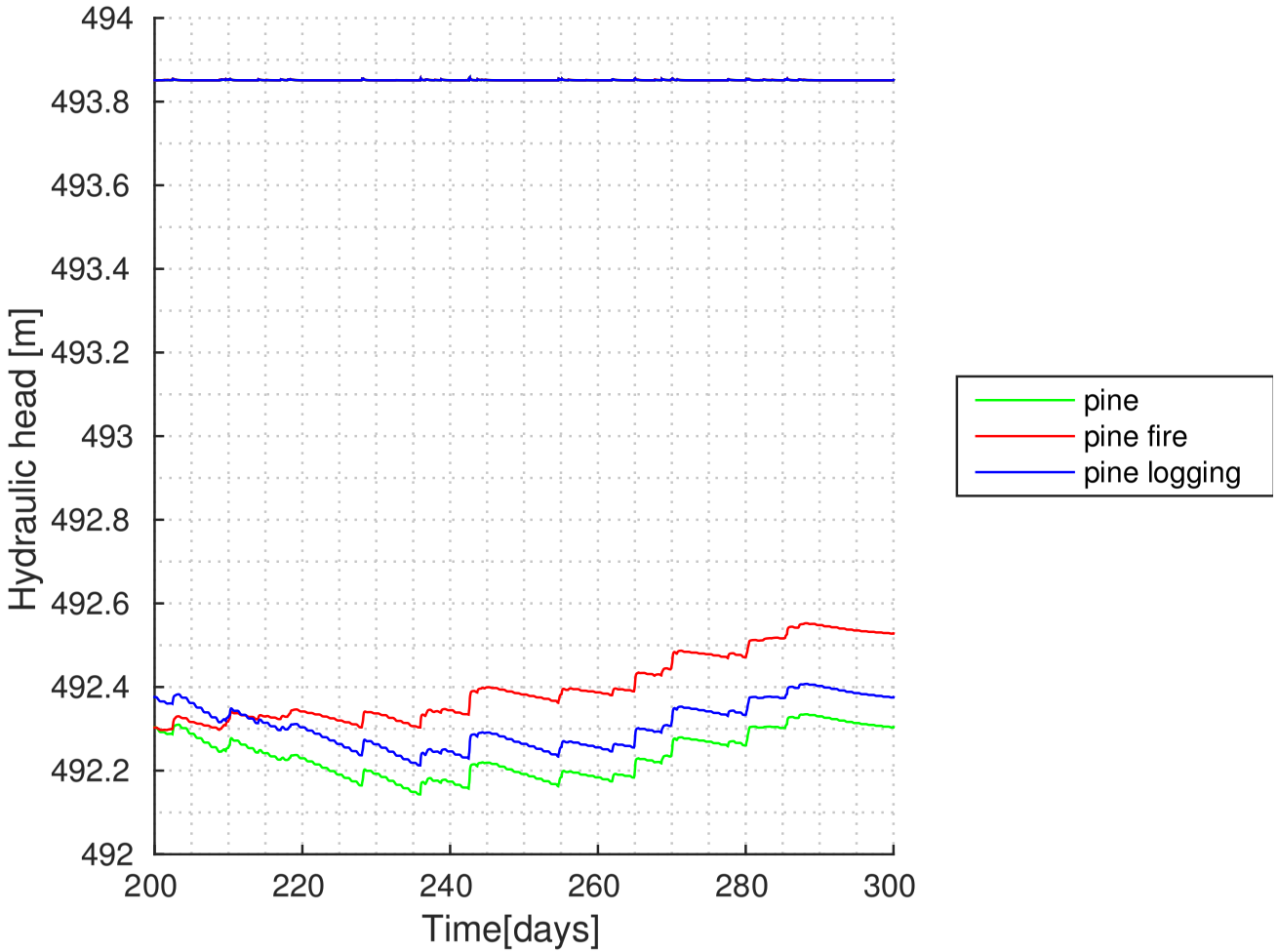

Figure 5.16: Surface and subsurface hydraulic head variations for Pine forest scenarios at obs. point 8. This observation point is at the floodplain of the river stream network, downstream of a small sub-catchment. The water table depth is about $2m$ below the surface and surface water level fluctuates in small magnitude after precipitation events. This is an indicator of a saturation excess flow generation mechanism on the surface. As in observation point 7, in places with larger slopes the stream power is due to higher slope rather than higher discharge in the stream network. The subsurface water level recovery for the fire scenario is slow. The surface head fluctuations are small for all scenarios as opposed to the difference in water table head.

5.3.2 Analysis of seasonal actual evapotranspiration

The reduction of canopy size by fire or logging reduces potential evapotranspiration according to Penman-Montieth. However, the change of the potential evaporation is not significant for the logging scenario. The decrease is about 10% of the pristine forest for the logging scenario and about 20% for the fire scenario. The actual evaporation changes significantly as a result of reducing the canopy by half in logging and zero in the fire case. The reduction of the canopy storage changes the water availability below the canopy for the logging scenario. The response of the catchment for the increased water availability is different in colder and warmer month of the year. In the colder month of the year, the evaporation is limited by the energy. Therefore the transpiration is also reduced in the logging scenario from January to April. With the onset of the growing season the limiting factor in evapotranspiration is the availability of the water. Therefore, the month of May to August have an increase in total evaporation. From August to December, there is again an overall decrease in actual evapotranspiration. The actual evapotranspiration for the Hardwood forest is shown in figure 5.17. The monthly ratio of actual evapotranspiration for the fire and logging scenario is shown in figure 5.18 and 5.19.

The logging scenario has half of the original LAI for the forests. The reduction of LAI reduces the potential evapotranspiration. The maximum monthly transpiration is reduced by more than half. With the decrease of canopy cover as well as reduction in transpiration, water availability for surface evaporation, infiltration or runoff increase. This is in accordance with the subsurface water levels where a higher subsurface level is seen for the logging scenario. Surface evaporation is also reduced. This can be due to the increase in water availability which enhances water accumulation and higher velocities that can move water out of the catchment faster. Therefore the large availability of water combined with large evapotranspiration demand causes a larger evaporation and transpiration. Combined with the lower evapotranspiration demand in winter and autumn produces a larger base flow in winter and autumn. Logging in general produces lower surface evaporation and transpiration.

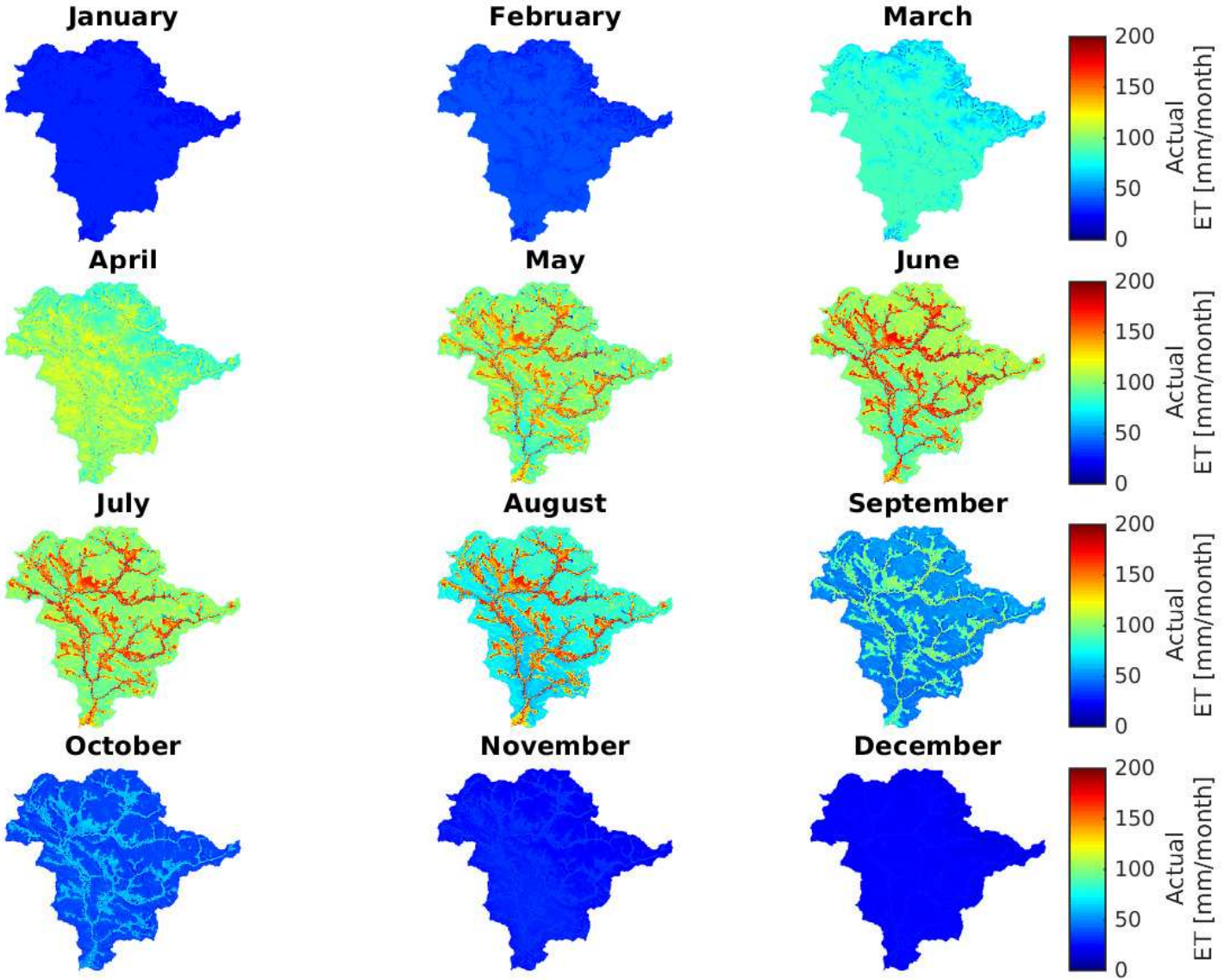

Figure 5.17: Total evapotranspiration for the Hardwood forest. Total evapotranspiration is controlled by availability of energy in colder months of the year and availability of water in the warmer months of the year. The surface evaporation is homogeneous throughout the catchment in the colder season. The largest evapotranspiration occurs at the floodplains or the foothills of the mountains where the infiltrated water from the hills is pushed out by slab flow or mounding mechanism.

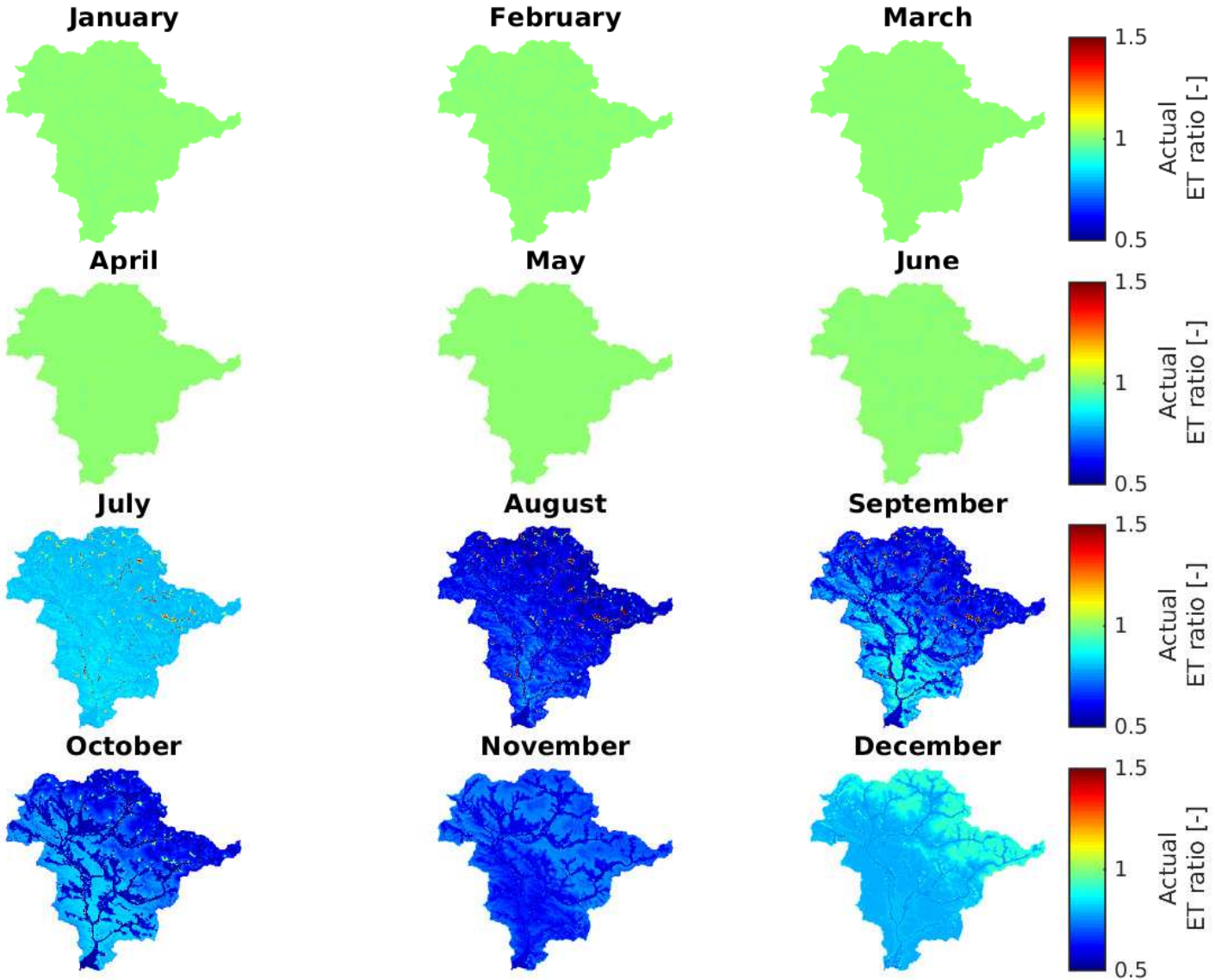

Figure 5.18: Total evapotranspiration ratio for Hardwood fire scenario. The January to middle of July are the same as the pristine condition of the Hardwood forest. There is a rapid reduction of evapotranspiration due to the reduction of the canopy to zero by fire. The total evapotranspiration in month of August to November is about 50%. The reduction in month of December is about 75%. The decline of total evapotranspiration is due to the lack of transpiration and canopy storage.

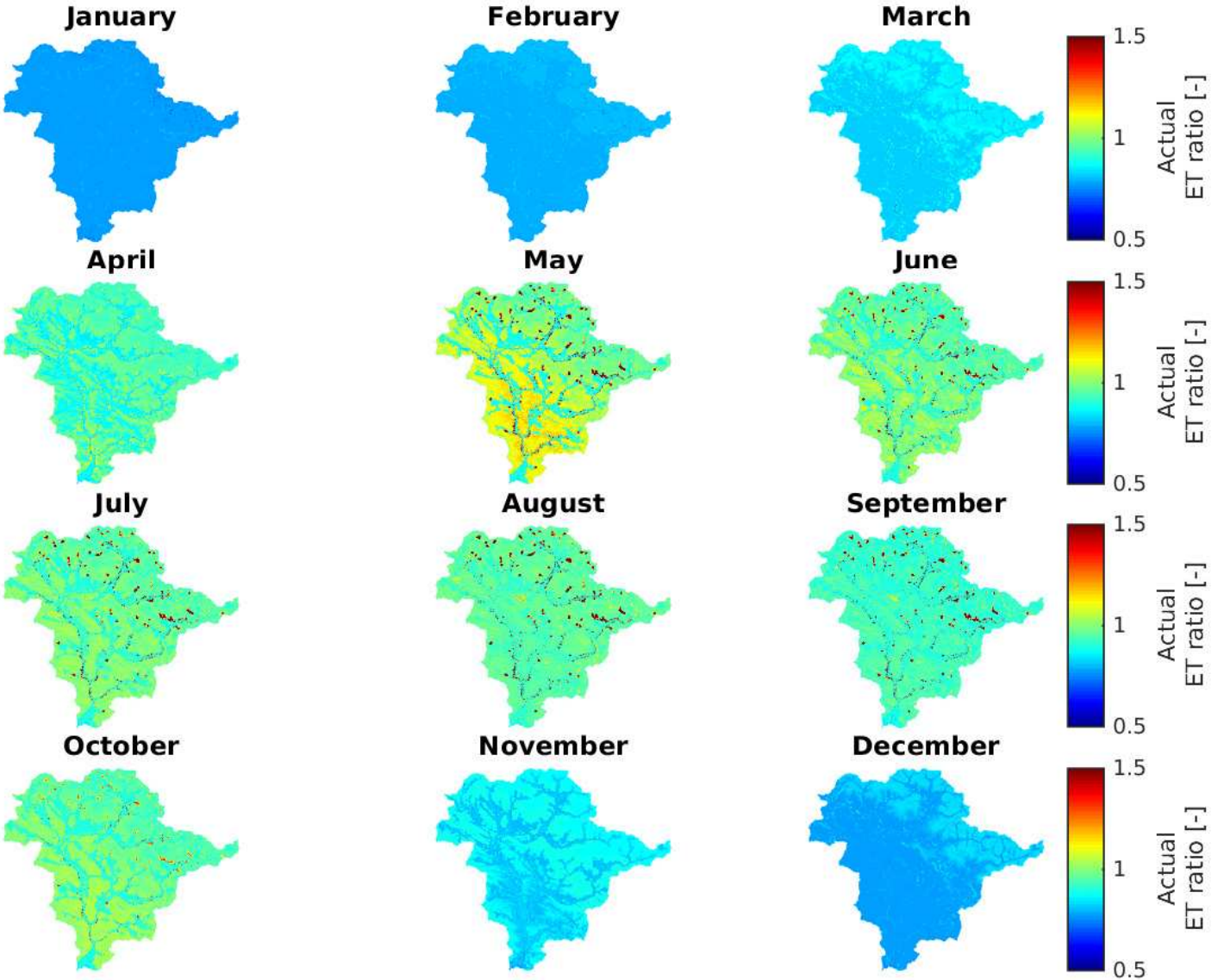

Figure 5.19: Actual evapotranspiration for the Hardwood logging scenario. In the colder month of the year (January, February, March, November and December) the decrease in total evapotranspiration is about 70%. This is due to the energy limited nature of evapotranspiration. In the warmer month of the year, there is an increase in total evapotranspiration throughout the catchment. the increase is about 5% to 10% in most of the regions in the catchment.

5.3.3 Analysis of top soil saturation

The top soil saturation changes for the fire and logging scenario is the one of the effects of the changing in transpiration and canopy storage. Here the changes of the top soil saturation level for the Pine forest, Pine forest fire and Pine forest logging are analyzed. As shown in analysis of the observation wells, the water table responds differently in flat and mountainous parts of the catchment. The response of the observation wells are due to the changes on the top soil saturation levels for the catchment. The monthly top soil saturation levels for the pine forest are shown in figure 5.20. The pattern is the depletion of the soil moisture by evaporation and transpiration in the growth season, and increase of soil moisture in the colder month of the year. For the fire scenario, the top soil saturation ratio to the Pine forest saturation is shown in figure 5.21. In the month of August, the top soil saturation starts to increase in the flat region of the catchment. For the next month, the increase of top soil saturation is about 10% and at the month of December, the increase of top soil saturation is about 20%. The the top soil saturation level increase in the mountainous region are smaller in general. The increase of saturation starts in the flood plains and propagates to distant areas from the river network. The saturation ratio for the Pine forest logging to the Pine forest is shown in figure 5.22. The increase of the saturation levels are largely at the March, April and May. The increase is limited to the flat region of the catchment. With the increase of the potential evapotranspiration at the growth season the difference of the saturation levels become smaller. This shows that the actual transpiration by plants is not directly proportional to the canopy size.

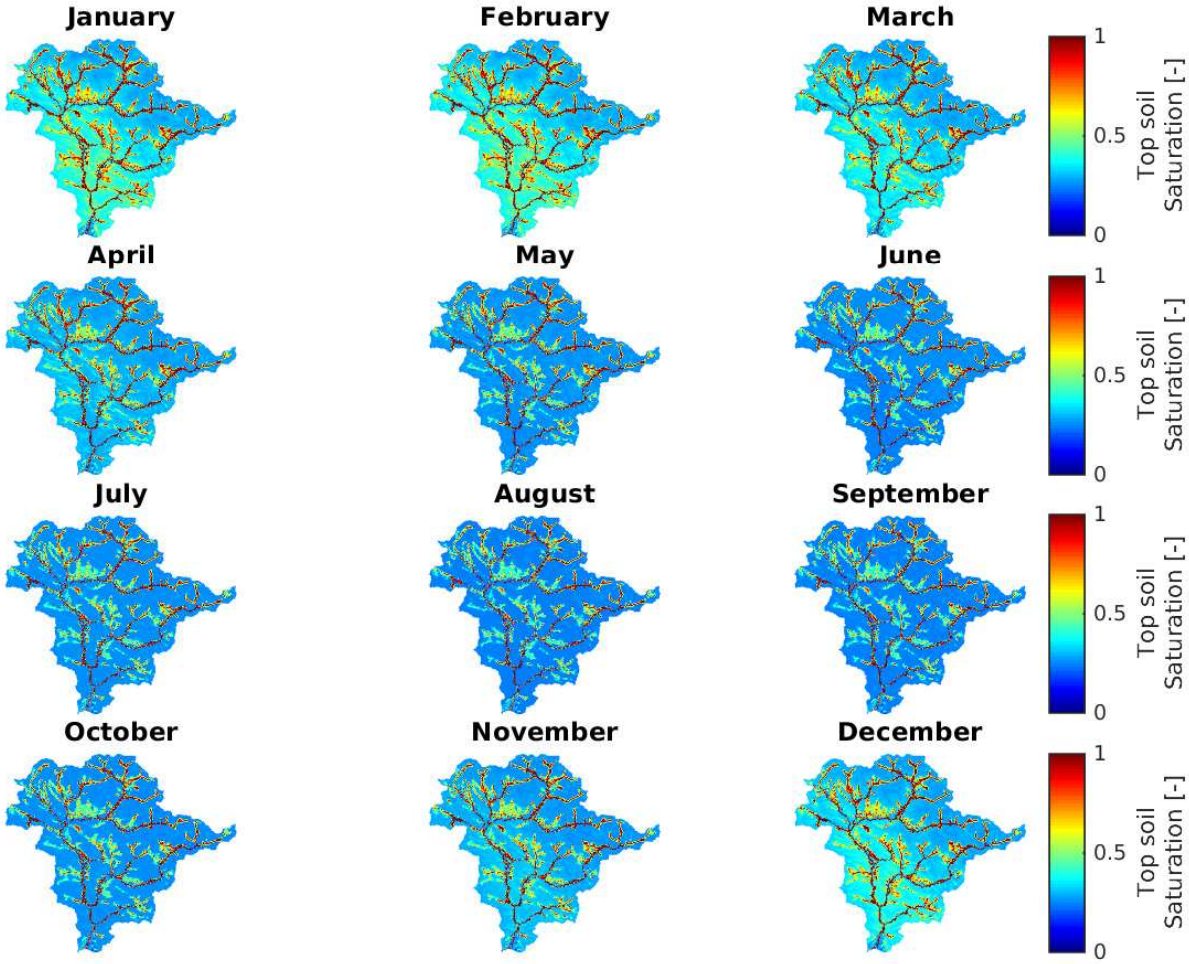

Figure 5.20: Top soil saturation level for pine forest. The January to March is characterized by a higher saturation levels in the flat region of the catchment. With the increase of the potential evapotranspiration, the saturation levels drop from April to late October. The water table recovery starts from November and continues until the January.

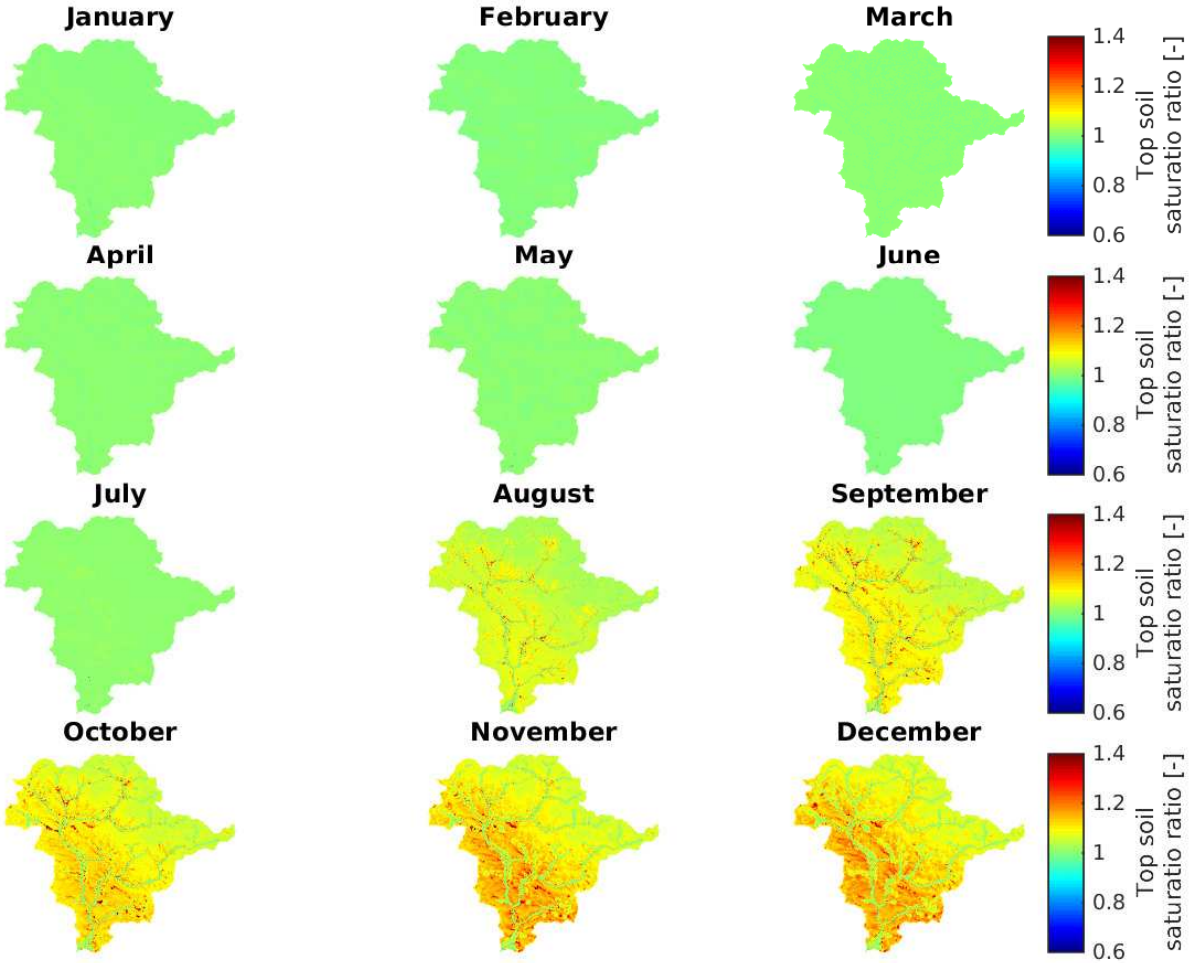

Figure 5.21: Top soil saturation level for pine forest fire scenario. The saturations levels are the same as the Pine forest until the fire break out time. The saturation levels increase after the fire. The increase in saturation level in flat region of the catchment is about 30%, The increase of saturation levels in the mountainous region is about 10%.

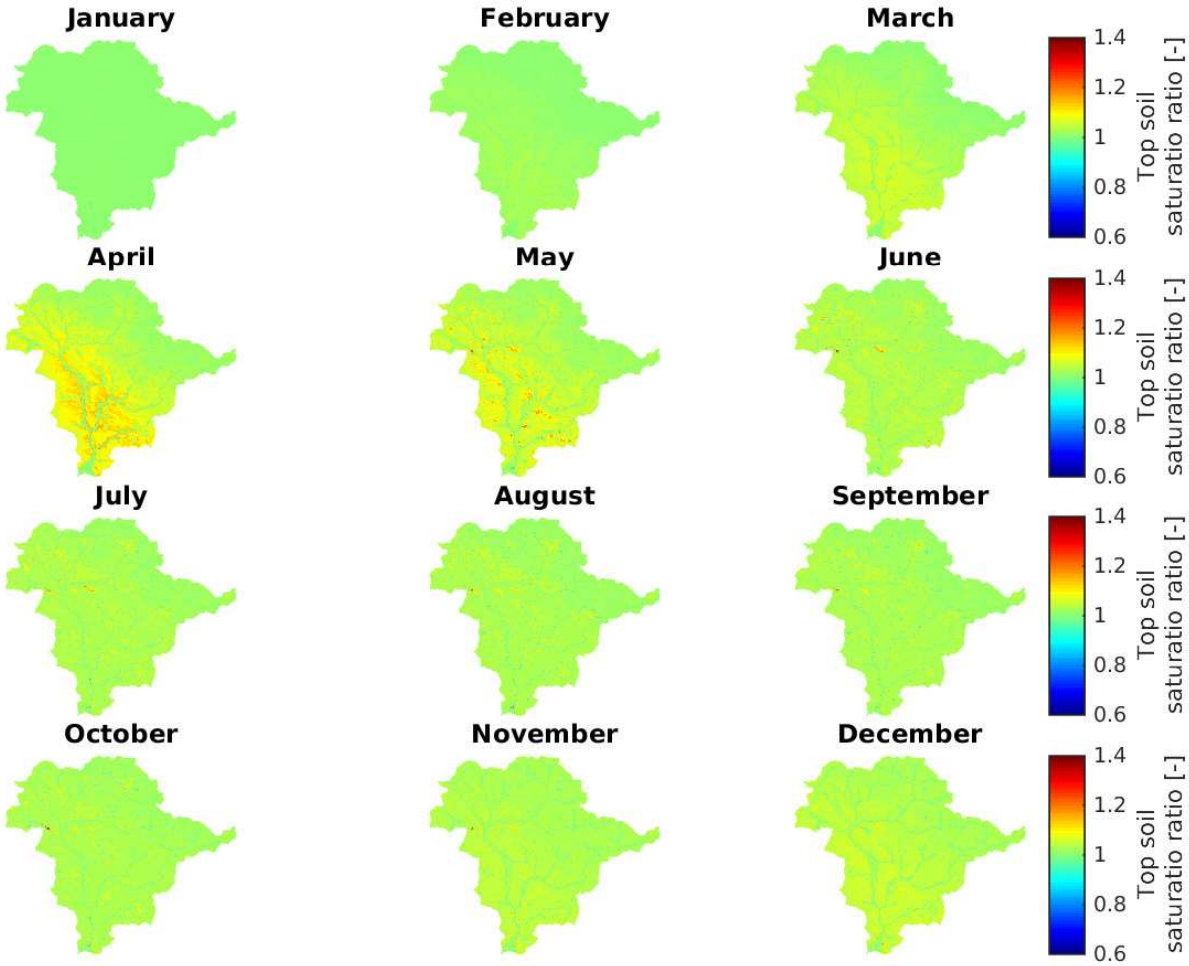

Figure 5.22: Top soil saturation level for pine forest logging scenario. The logging scenario shows a slight increase in the top soil saturation levels. The increase is more pronounced in March, April and May. The saturation levels are not affected in the mountainous part of the catchment. At the growth season, the increase of the saturation level is about 10%.

5.3.4 Analysis of surface erosion patterns

The regions of the catchment susceptible to erosion is the same as the Deciduous, Pine and Hardwood scenarios. The disturbance of the canopy by fire and logging changes the hydrological cycle. The decrease in transpiration, affects the surface and subsurface flow dynamics. However, as the river channel is not accurately presented in the model due to computational limitations, the flow spreads over a larger area with the increase of discharge. Therefore, the spatial distribution of the erosion does not change significantly. The sediment discharge from the catchment however is affected by the fire and logging disturbances. The cumulative sediment discharge is for Deciduous forests is shown in figure 5.23. The sediment discharge for the Deciduous forest is about twice as large in the colder season compared to the growth season. The large canopy size and transpiration acts as an strong control on the sediment discharge. With the fire event at late July, the canopy is removed and the transpiration is eliminated. This reduction of the canopy, reduces the actual evapotranspiration. The total sediment flux for fire scenario increase and at the end of the simulation period, the erosion from the fire scenario is about 15% larger than the pristine Deciduous forest. For the logging scenario, the increase of the sediment flux starts from the beginning of the simulation. The response of the Deciduous logging scenario is slightly larger than the Deciduous forest for all of the precipitation events. At the end of the simulation, the increase in the sediment discharge is about 12%. The total sediment flux from the fire scenario is smaller than the logging scenario until middle of the October. From middle of October to the end of simulation, the fire scenario produces larger sediment discharge. At the end of the year, fire scenario sediment discharge is about 5% more than logging scenario. The reduction of the canopy size by 50% does not increase the sediment discharge significantly. The clearcut case cumulative sediment discharge is about 150% of undisturbed Deciduous forest. The fire scenario reduces the canopy size to zero. The subsurface is much strongly affected and the rate of the subsurface water table recovery is much faster. Therefore, the erosion rate increase faster than the logging case. The trends of the sediment discharge in the Pine and Hardwood forest logging and fire scenario show the same rate of change as in Deciduous forest. However, the canopy exists for the Pine and Hardwood throughout the year, while Deciduous forest canopy size is zero at the beginning and end of the year.

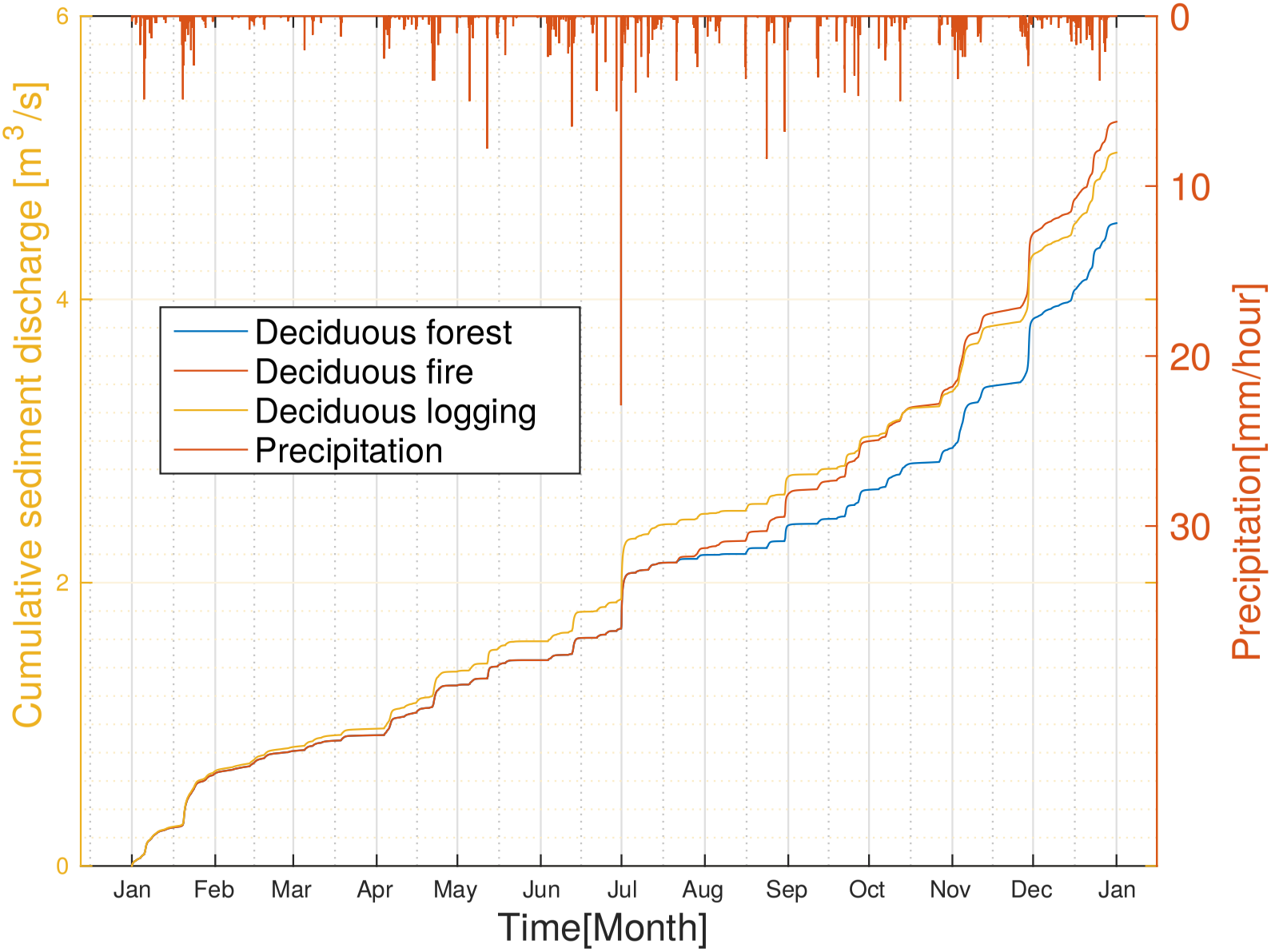

Figure 5.23: Cumulative sediment discharge for Deciduous scenario. The sediment flux is affected by reduction of the canopy (logging) and wild fire. The reduction of the canopy by 50% in the logging scenario increase the sediment discharge from the catchment by about 15%. The fire scenario increase the sediment discharge by about 12%. The contrast between logging and fire highlights the extent of the effect of the subsurface.

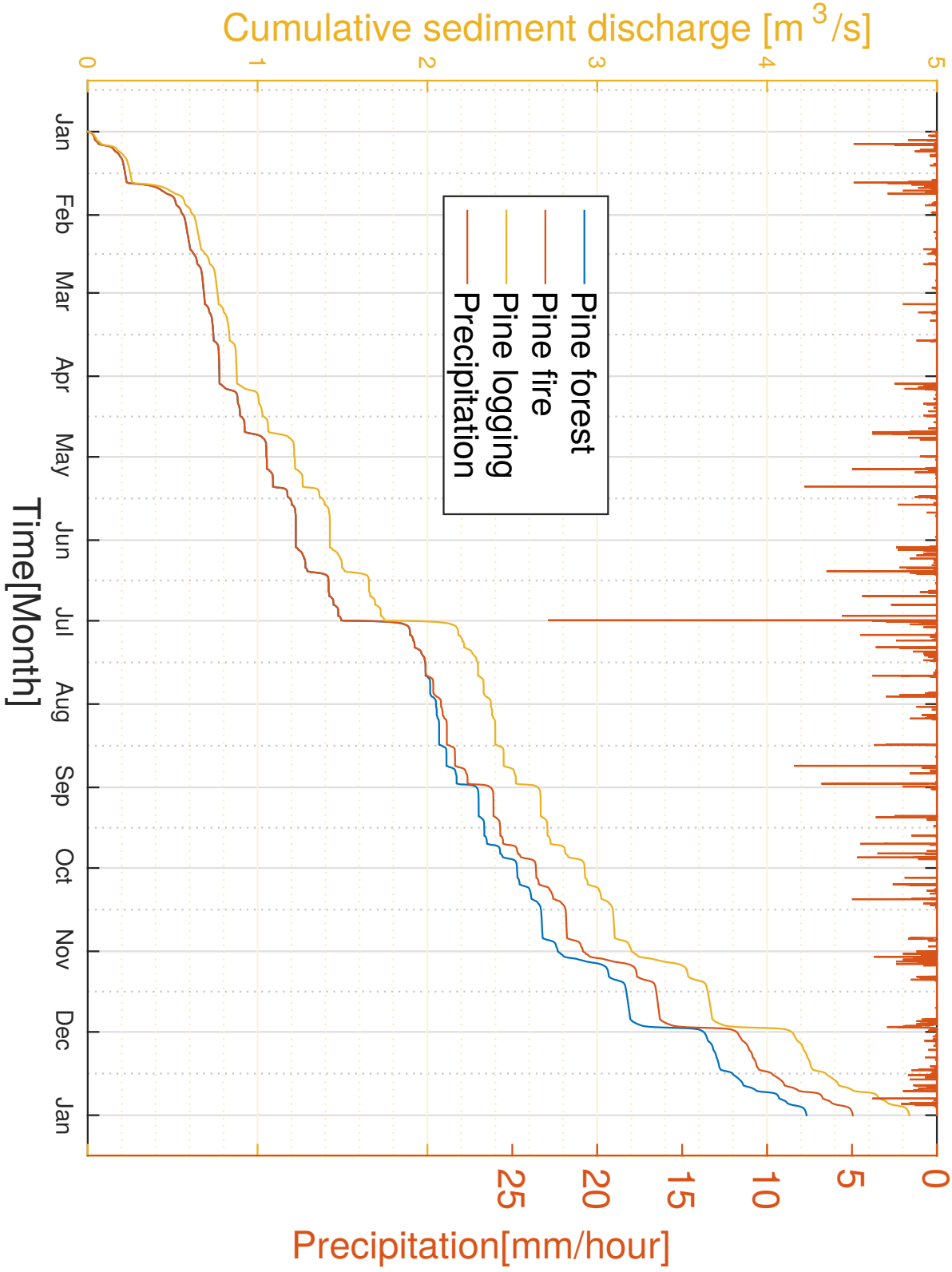

Figure 5.24: Cumulative sediment discharge for Pine scenario. The fire and logging scenario produce more sediment discharge than the pristine Pine forest. The rate of the increase sediment discharge is larger for the fire case which reduces the canopy size to zero. The annual increase for logging scenario is about 12%. The annual rate of increase of sediment discharge is about 20% for fire scenario.

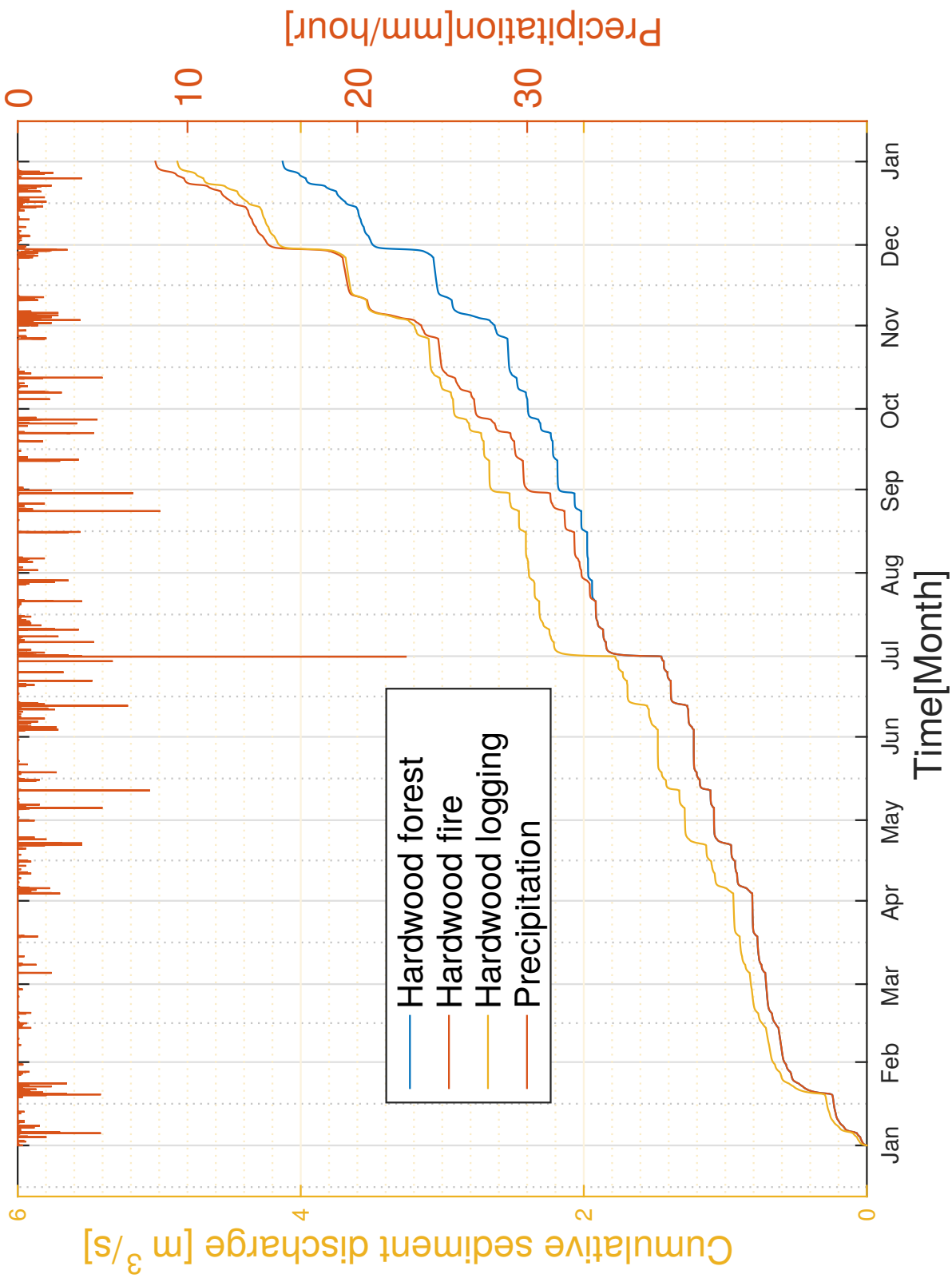

Figure 5.25: Cumulative sediment discharge for Hardwood scenario. The logging scenario produces about 11% more sediment discharge than Hardwood forest. The fire scenario produces about 15% more sediment discharge. The fire scenario discharges about 4% more than logging scenario by the end of the simulation period.

5.4 Conclusions

Naturally occurring or human caused fires are very common in the arid areas of the world. The changing climate makes many forests susceptible to fire break outs as well. The deforestation of the land by burning is practiced in many countries [31]. The burning of the topsoil vegetation is usually done by farmers to help the soil for the next cultivation season. These fires sometimes get out of control and burn the nearby forests which results in unintended consequences. The scenarios considered here for the Deciduous, Hardwood and Pine forests with the climate forcing derived from the synoptic weather station of Stuttgart show similar behaviors. Fire eliminates the transpiration and canopy storage. Therefore the ground water level recovers rapidly to the clearcut situation. An increase in sediment discharge is observed from the simulations both for the fire and logging scenario. The sediment discharge is a function of the material and lithology as well as hydrological conditions in the catchment. The erosion coefficient chosen for the regolith in the catchment is one order of magnitude less than loose sand. The erosion rate after the fire increase with a faster rate. The annual total sediment flux increase at the end of the simulation period is about 15% to 20%. The way a catchment responds to a fire depends on the timing of the fire event and the climatic factors. However, for the catchment studied here, fires occurring before the growth season can have larger sediment discharges. It should be noted that parameters that are affected in fire are not limited to the canopy size and transpiration [151, 17, 18]. There are other parameters such as top soil hydraulic conductivity that change as a result of the fire. This can increase sediment discharge by reducing infiltration to the subsurface. The level of the burn of the vegetation and canopy also can be a control on the erosion. Some forest burns reported in forests that are superficial and the trees come back to life and start to grow in the next growing season. The climatic forcing in the catchment is the spatial and temporal precipitation pattern and evapotranspiration demand. For the Mediterranean climates, the increase of erosion due to fire can be larger as the precipitation occurs mostly in non growth season. In the geodynamics simulation, the recovery of the system and the frequency of the forest fires can have an important effect the evolution of the landscape. If the fire events are frequent, the periodic fires increase the erosion in a catchment. The sediment discharge at the end of the simulation is about 15% to 20% for the fire scenarios. The Hardwood and Pine forests are affected by a fire scenario about 5% more than the Deciduous forest.

Logging or harvesting timber from forests is practiced around the globe with different harvest rates [161, 162]. Logging after a fire is popular to salvage the burned logs and trees [164, 165]. The logging scenario studied here is the harvest of timber with a 50% rate. There is a range of values reported for the increase of sediment discharge from forests that had timber harvesting in place. The impact of logging is reported to be variable based on the relative location of the harvested trees relative to each other and the stream network. The sediment discharge increase about 10% on average for all the forests studied here. The largest increase is in the hardwood forest. The subsurface saturation levels for the growth season change at the order of about 5% to 10%. The changes in the subsurface saturation are spatially limited to the flat region of the catchment. The response of the catchment is strongly controlled by climate and the temporal distribution of the rain events. In case the majority of the precipitation events were to occur at the colder month of the year (Mediterranean climate) rather than throughout the year as is the case here, the increase in sediment discharge would have been significantly different. Two major vegetation controls of the transpiration and canopy act on the catchment. The transpiration is largely active during the growth season when the canopy is largest and the potential evapotranspiration is also significant. At the colder month of the year at winter and late autumn, the canopy storage has a small

impact. The topography of the catchment needs to be accurately reflected with the mesh specially in the river stream network in order to study these disturbances in more detail. The increase of sediment discharge for Deciduous forest at the end of one year of simulation for fire and logging scenario is about 12%. The discharge from fire scenario increase with a larger slope and overtakes the sediment discharge from logging scenario. The slow down of the erosion discharge depends on the rate of the recovery of the plants in the catchment in the fire scenario. The Pine forest fire and logging scenario is about 15%. The fire scenario sediment discharge is larger than the logging case. The same pattern is present in the Hardwood scenario. The behavior of the subsurface water level is controlled by the root depth and canopy size. For the Pine and Deciduous forest, the fire scenario discharge rate is faster than the discharge rate increase of the Hardwood forest. The Hardwood forest has a larger canopy and a comparable root depth to Deciduous forest. The all year around canopy of the Pine forest balances the smaller root depth it. Therefore the trends of the sediment discharge are similar in the forests and fire and logging scenarios.

Chapter 6

Synthesizes of results and conclusions

Fluvial erosion is a key driver in the evolution of the semi-arid and wet climates. It activates and controls hill slope processes, and river bed erosion. In the headwater of the catchment, the river carves into the hills and regolith produced by hillslope processes is moved downstream. The energy required for the transport of the regolith is provided by the stream power which is the product of stream bed slope and the water flux passing through the river network [2]. Traditionally in the geodynamics modeling frameworks, a surrogate parameter such as upstream area is used for calculation of flow accumulation and water flux through the landscape [10, 166, 69]. In order to capture as much of the hydrology of the system under study, various methods have been used that deal with how the runoff is generated. Hortonian or infiltration excess runoff generation assumes that a fixed amount of water can infiltrate into the subsurface regardless of duration or intensity of the precipitation event. The rest of the precipitation becomes runoff [167]. In this approach, the duration of the precipitation event is neglected and the intensity and infiltration rates determine the amount of runoff. Bucket runoff model assumes that various features of the catchment like canopy size, micro-topography, and evaporation has a fixed amount of capacity to absorb the precipitation. Any precipitation event that exceeds this volume will produce a runoff. Another approach is the O'loughlin saturation excess runoff model. In this method, precipitation is divided into the overland and subsurface flow. The hydraulic conductivity of the subsurface determines how fast the subsurface water moves. The movement down the energy gradient allows for the method to simulate the dynamics of the runoff generation according to whether the top soil is saturated or not. The last method used in the geodynamics simulations is the TOPMODEL approach [168] which is similar to the O'lougphlin method without the return flow to the river. These methods try to include the dynamics of the water movement through subsurface and surface in a computationally feasible manner, ignoring many subtle features of the hydrological systems. A well known feature of nonlinear systems is that if the system starts from two similar initial conditions in two simulations, the system can diverge into totally different states ultimately. The equations that govern the evolution of the landscape are too complex as they are linked to the topography and hydrology of a given catchment. The stationary points of the governing equations are not known except for the trivial case of flat surfaces with no disturbance. This is a major limitation in long term simulations with crude tools because it is not clear if the assumptions that make up the model are valid through out the evolution of the catchment. If the system at one point

in time turns from infiltration excess to saturation excess runoff generation mechanism due to change of the soil properties as the material from the surface is moved away, the amount of the runoff generated will be different and the erosion rates will change accordingly. This may have a great impact on the evolution of the surface topography. In this study, the goal is to understand hydrology as it relates to the erosion process in a forested catchment without any explicit assumptions on the nature of the infiltration and runoff generation. The runoff generation mechanisms are conceptualized in the Dunne diagram [116, 145]. The runoff generation according to the Dunne depends on the depth to the bedrock, hydraulic properties of the subsurface, slope, vegetation cover and aridity index of the catchment. The catchment erosion also incorporates the lithology of the surface material. Whether the catchment erosion is detachment or transport controlled or there are tools available for the erosion and abrasion of the bed. The combination of these parameters can force parts of the catchment to have different response to the precipitation events. Hortonian flow occurs mostly in arid catchments with no or little vegetation. The air entry pressure for the soil or topsoil is also large so that the wetting front does not move fast enough into the subsurface. In humid areas with dense vegetation, saturation excess surface runoff or subsurface storm flow can occur. Saturation occurs when the depth to bedrock is small or hydraulic permeability is small with mild slopes. The flow is most likely infiltrates in the subsurface where the soils are deep with steeper slopes and higher hydraulic conductivity. Each of these runoff generation mechanisms can produce different stream power and erosion potential in a given catchment. Moreover, if the catchment is large enough, all of these mechanisms can be present and the simplifications used in the traditional geodynamics models are not adequate for the accurate simulation of the catchment. Attempts has been made to incorporate various hydrological concepts into the geodynamics models. Correcting for the travel time within the catchment, for various precipitation durations, is shown to produce significantly different outcomes of in the evolution of hypothetical catchment [38].

The rigorous hydrological approach used in study incorporates many parameters such as precipitation characteristics, vegetation type and vegetation density, timber harvesting and fire break outs in the forest. This simulation package and similar ones are due to paradigm shifting proposal initially set forward by Freeze and Harlan [25] and later realized by many simulation packages that followed [26]. The main advantage of this framework is that there is no explicit assumptions made on the nature of the runoff generation mechanism. The system can turn from Hortonian infiltration excess to subsurface flow as dictated by the properties of the media and forcing in the catchment. The response of the catchment is determined depending on the state variables at any location and time. This captures the true dynamics of the evolution of the system. The coupling of the climate and erosion has been an interesting topic in geodynamics [37, 38, 110, 90, 169]. There has been field studies that link erosion to the annual precipitation globally [123]. It is argued that with the increase of the annual precipitation, the erosion rates increase and then reaches a peak which trailed by a decline in sediment production. The physical reason for the mentioned outcome is that with the increase in annual precipitation, the hydrology and ecology of the catchments, namely vegetation density changes, causing a reduction in the runoff and fluvial erosion and sediment transport out of the catchment. In the first part of this research, the effect of the precipitation patterns with a fixed total precipitation are analyzed. Due to the computational limits, the shortest hydrological cycle (a year) is chosen for the simulations of vegetation type and density. For the precipitation patterns effect a simulation time of 6 month is used. The effectiveness of the events for the erosion is measured in how much total bed shear is produced by the flowing discharge in the river. A method is developed to produce precipitation patterns that respect the limitations posed on the

total annual precipitation and simulation duration. The posteriori and priori means of the parameters that define the precipitation patterns are kept with in small error margins so that the effects can be attributed to the variations in the patterns and not to the changes in the volume of precipitation. The results show that for longer duration events with small intensities, the runoff generation is limited and the runoff generated is very limited. The precipitation infiltrates to the subsurface and subsurface flow delivers water as the base flow to the river streams. The base flow is not very effective in producing large bed shear stress. For the events with medium durations and larger intensities, the saturation excess infiltration reaches for the sand type used in the catchment. The amount of the runoff produced over the catchment produces a larger amount of bed shear stress on the river streams. For the events with higher density and shorter duration, the runoff generation becomes more active in the headwaters where the slope is higher. In this case, the bed shear stress is only effective in larger slops which limits erosion to the mountainous part of the catchment. With the simulations carried out, it is shown that there is strong dependence between the spatial distribution of the bed shear stress and temporal distribution of the precipitation events.

Another major hydrological and ecological control on the erosion is the vegetation density which is controlled by the availability of water or more precisely by the aridity index which is the ratio of potential evaporation to precipitation. Forests and croplands increase the potential evapotranspiration. The extraction of water from root zone dries up the root zone soil and produces an extra storage in the lower layers of soil and affects the movement of water through the subsurface. At the same, the availability of water in the subsurface controls the existence of the vegetation. The interaction of vegetation and water flow requires time scales that are beyond the computationally feasible ranges for the current computational facilities with the detailed models that are used in this study. Simplified approaches that allow for long time simulations show a strong link between erosion, vegetation and water flow [170, 113, 37, 171]. Without the use of the interaction of water availability and vegetation water demand which shapes and forms the vegetation density in a catchment, a limited type of vegetation is suitable to be used for the location of the Steinlach catchment [15]. The climate (mean annual temperature) and availability of the water (annual precipitation) favors tropical forests as natural vegetation types. In this part of the study, three forests are used to investigate the effects tree species on the hydrological and fluvial erosion of the catchment. These tree types of forests, Deciduous, Hardwood and Pine forests have different characters like Albedo, stomatal resistance, root depth and canopy interception. The annual leaf area index variation are also different in these forests. Deciduous forests loose their leaves except for the part of the year and Pine forests are mostly ever green. The Hardwood forest is a mixture of evergreen and Deciduous type. As the Deciduous forests loose their leaves, the soil becomes bare and the albedo of the soil changes, as well as a small portion of the sunlight that was being absorbed for photosynthesis can be spent on latent heat of evaporation or heat up the surface. The change of albedo can affect the potential evaporation. Therefore the ration of aridity changes. However, at the other hand, the canopy storage is also reduced and and root zone consumption of water is also halted. How the forests respond to precipitations of average intensity is largely influenced by these changes.

The climate change is going to affect the distribution of the vegetation in most of parts of the world by changing the availability of the water [107, 172, 169]. Forests create their own micro-climate by using part of the sunlight for photosynthesis, shading the surface soil and keeping it cool. However, the heat waves has been observed that cause massive damages in the forests worldwide [31]. An increase in the heat induced mortality and forest fires have been observed worldwide. The intentional burning of the

croplands and forests to clear the way for agriculture or clean the land for the next cultivation season is an ongoing practice in many parts of the world. Naturally occurring fires also have become more frequent in forests [31]. Various parameters of the forest system and catchment are affected by fires such as water repelling capacity and hydraulic conductivity of the top soil [151, 152, 173, 158, 174, 175]. Harvesting of the timber and logging also reduce the forest density and understanding the effects on erosion and hydrology are important [163, 164, 161, 162]. The effects of fire and logging are investigated on the hydrology of the catchment and later on the stream power and erosion rates from these forests by defining one fire scenario and one logging scenario on the Deciduous, Hardwood and Pine forests. The fire occurs in the beginning of the growth season and wipes out all the transpirational leaf. The albedo changes from the forest albedo to the bare ground albedo and therefore the evaporation potential is changed. The response of the catchment after the fire scenario is studied in detail and how the erosion rate changes respectively is shown to increase in forests types that are studied. The increase in runoff is due to the disappearing of the extra storage caused by the transpiration of the plants. The recovery of the water table depth to the clearcut scenario causes the runoff generation mechanism to shift toward saturation excess and more runoff increases the erosion rates. However, the increase in not linear as the topology and stream geometer controls the water depth and therefore the shear stress on the river bed does not increase linearly with discharge. The logging scenario introduces a harvest rate of 50% of trees and therefore reducing the canopy without the change of albedo in general. This affects the total amount of transpiration and canopy storage and affects the hydrology, saturation levels, water table and runoff generation mechanisms. The amount of increase in erosion also is nonlinear and reflects the changes in hydrology.

The simulations show that catchment behaves distinctly in the mountainous regions and flat regions. The lower water tables combined with the transpiration in the mountains region causes lower saturation levels on the top soil. the flow is mostly subsurface flow regime except for higher intensity events which can produce infiltration excess in some parts and cause erosion in the headwaters. At the flat regions, the water table is generally higher and saturation is lowered by transpiration in the growth season. The higher intensity events are less effective in producing larger peaks in the discharge due to canopy interception, larger subsurface storage and larger evaporation. At the cooler month of the year, the water table starts to recover and saturation excess runoff increases, causing more erosion. Transpiration is a major control on the subsurface and how part of the precipitation is infiltrated in the topsoil is largely affected by the plants. The way vegetation functions as a control on the runoff and fluvial erosion is topographic dependent. In the higher regions where the water table is lower, only the canopy storage is a control parameter. At lower and more flat regions, the water table is higher and the water table is lowered by transpiration in the growth season and therefore an extra storage is created. the effectiveness of this extra storage is a function on the unsaturated soil properties of the top soil. The higher air entry pressure, and lower conductivity will produce higher runoff and higher erosion and lower air entry pressure with higher hydraulic conductivity will have a larger portion in infiltration. The amount of infiltration also will depend on the temporal distribution of the precipitation throughout the year. This shows the importance of the ground water table and the unsaturated zone in regulating and controlling the runoff generation mechanism. The ground water table in the forests are controlled by the canopy and root depth. The Pine forest for example has larger canopy size (large LAI) but smaller root depth and the needles are not efficient in transpiration. At the other hand, the Deciduous forest has a large canopy only in the growth season and the root depth is also large but active only when the canopy size is none

zero. These tow parameters limit the response of the catchment in different ways. The Deciduous forest ground water table elevation is lowered rapidly in the growth season, and after the end of the growth season, the water table recovers rapidly tot he clear cut ground water table elevation. The fire and logging scenario also exert control on the ground water table. The elevation of the ground water table acts as a memory for the catchment. The memory extends to about a year in the pristine conditions. The state of the catchment or the memory of the system is polluted by the fire and the response of the catchment changes accordingly. The response of the system is controlled by the topography of the system as well as the vegetation and lithology.

This work is limited in its presentation of the various physical features of the catchment due to the computational limitations (computational cost of the simulation of catchment) and it is intended to be a hypothetical catchment study. The simplifications are made so that the observations can be attributed to the changes in input variables with in the controlled environment of the simulation framework.

The complex and computationally expensive simulation framework chosen here for the experiments provides us with the insight on how a catchment in its entirety responds and changes according to various input parameters such as precipitation, vegetation, topography and soil types. The insight can be helpful in choosing the right type of the runoff generation mechanism, and possibly development of the tools that can incorporate more than one type of runoff generation system in a single catchment.

Appendices

Mathematical notation

Symbol	Meaning	Dimension
α	scaling factor	[-]
C_f	friction coefficient	[-]
c_p	heat capacity of air	$[JM^{-1}K^{-1}]$
$d_\circ$	water depth	[L]
Δ	slope of saturation curve	$[PaK^{-1}]$
D_{iff}	hillslope diffusion constant	$[L^2T{-}1]$
D	mean sediment diameter	$[L]$
E_{can}	canopy evaporation	$[LT^{-1}]$
EDF	evaporation distribution function	[-]
Ep	potential evapotranspiration	$[LT^{-1}]$
$\epsilon_\circ$	soil production rate	$[LT^{-1}]$
E_s	surface evaporation	$[LT^{-1}]$
η	water depth	[L]
f_1	function of LAI	[-]
$f_2,\ f_3,\ f_4$	function of	θ [-]
g_a	air conductivity	$[LT^{-1}]$
γ	lapse rate	$[PaK^{-1}]$
γ	specific weight of water	$[-]$
g	gravitational constant	$[LT^{-2}]$
g_s	canopy conductivity	$[LT^{-1}]$
G	short wave irradiation of soil	$[WL^{-2}]$
$H_\circ$	energy head	[L]
H_s	regolith depth	$[L]$
H_s	regolith depth	$[L]$
h	water depth	[L]
κ	Von Karman constant	[-]
k_f	empirical constant	$[-]$
K	hydraulic conductivity	$[LT^{-1}]$
$K_{ox},\ K_{oy}$	hydraulic conductance	$[LT^{-1}]$
k_r	relative permeability	[-]
LAI	leaf area index	[-]
L_v	latent heat of evaporation	$[JL^{-3}]$

Symbol	Meaning	Dimension
$M_b,\ N_b$	constants	$[-]$
M	mass matrix	
∇	gradient operator	$[L^{-1}]$
N	days in each month	[-]
n	manning number	$[TL^{\frac{-1}{3}}]$
ω_m	porosity	[-]
$\Omega,\ \omega$	stream power	$[-]$
ϕ	shape function	$[-]$
ψ	hydraulic head	[L]
q_{in}	rain flux	$[LT^{-1}]$
q_s	sediment flux	$[L^3T^{-1}]$
Q_s	sediment flux	$[LT^{-1}]$
Q	water flux	$[LT^{-1}]$
RDF	root distribution function	[-]
ρ_{air}	air density	$[ML^{-3}]$
$\rho,\ \rho_w$	water density	$[ML^{-3}]$
ρ_s	sediment density	$[ML^{-3}]$
R_n	net solar irradiation	$[WL^{-2}]$
R	relative density of sediment	$[-]$
S_c	critical slope	$[-]$
S	channel slope	$[L]$
s	distance	[L]
S_w	soil saturation	[-]
$s_x,\ s_y$	energy gradient in x and y direction	[-]
T_{air}	air temperature	$[^\circ C]$
$\tau_{bx},\ \tau_{by}$	shear stress	$[MLT^{-2}]$
$\tau,\ \tau_c$	bed shear, critical shear	$[Pa]$
T	day length	[T]
θ_{an}	anoxic saturation limit	[-]
$\theta_\circ$	residual saturation	[-]
θ_{fc}	field capacity saturation	[-]
θ_{ox}	oxic saturation limit	[-]
θ_s	porosity	[-]
Tp	plant transpiration	$[LT^{-1}]$
t	time	[T]
U	tectonic uplift	$[LT^{-1}]$
u, v	velocity	$[LT^{-1}]$
u	wind speed	$[LT^{-1}]$
Γ	exchange flux	$[L^3L^{-2}T^{-1}]$
W	channel width	$[L]$
x, y, z	Cartesian coordinates	$[L]$
$z_m,\ z_d,\ z_o$	distance	[L]

hgsModel class object

```
classdef hgsModel < handle
   properties
       % erosion parameters....
       g  % gravitational constant
       D  % diameter of the sediments
       Rs % reletive wieght of sediments
       Rw % relative weight of water
       Manning_n %manning number, may be unused.
       Tc  % critical shear stress
       porosity % porosity of the sediments
       gamma % g*Rw
       Ks % erodibility
       Kb % erodibility of the bed
       beta % ration of bed load to total load
       teta % porosity.
       % segment element(Finite Element)
       SelectedNodes;  % used in export and import
       SelectedElements;
       verbos = 0; % level of verbosity
       % project directory
       RootDir % root dir of the project used to read and write
       BaseName % the name of the model
       % mesh and points data
       tri % surface triangulation
       x % x coordinate (surface)
       y % y coordinate (surface)
       z % z coordinate (surface)
       %
       H   % head
       Henv
       h   % water depth in surface
       Z   % elevation of the surface
       n % number of nodes
       m % number of Triangles.
       t % current time.
       Hpm % subsurface head
       i   % index of the file read (integer)
       xyz % coordinates of all the nodes
       prisim % prisim element connectivity
       PmSat  % porouse media saturation
       PlantTranspiration  % transpiration by plants
       %%% finite voluem data
       MassMatrix   %
       MassU   % ULP decomposition of the mass matrix done in
           CalcMassMatrix
       MassL
       MassP
       vA  % vertex area
       w   % interface width
       nx  % normal vector for the sediment flux interface in xdirection
       ny  % normal vector for the sediment flux interface in ydirection
```

```
51          L   % distance from node i to node j
52          tA  % area of the elements
53          segment
54          bnd_nodes   % nodes to enforce zero boundary conditions
55      end
56      methods
57          function obj = hgsModel(ModelPath,ModelName)
58              %create model from the model directory and the model prefix
59              obj.RootDir = ModelPath;
60              obj.BaseName = ModelName;
61              prefix = strcat(obj.RootDir,obj.BaseName);
62              filename = strcat(prefix,'o.coordinates_pm');
63              % read the node coordinates
64              obj.xyz = ReadCoordinates(filename);
65              filename = strcat(prefix,'o.coordinates_olf');
66              % read the indes of the nodes
67              [index,obj.n]=ReadIndexOlf(filename); % index in to coordines ,
                    number of nodes.
68              filename = strcat(prefix,'o.elements_olf');
69              % read the surface elements (triangles)
70              obj.tri = ReadElementsOlf(filename);
71              filename = strcat(prefix,'o.elements_pm');
72              % read the porous media elements (prisims)
73              obj.prisim = ReadElementsPM(filename);
74              %MassMatrix = sparse(length(obj.xyz),length(obj.xyz);
75
76              %%%%%%%%%%%%%%%%%%%%%%%%%%
77              %extract surface triangulation points and nodes from 3d
78              %representation
79              id=1:length(obj.xyz);
80              id(index) = 1:length(index);  % map the indexes to id.
81              obj.tri = id(obj.tri);
82              obj.x = obj.xyz(index,1);
83              obj.y = obj.xyz(index,2);
84              obj.z = obj.xyz(index,3);
85              % initialize to elevation
86              obj.Henv = obj.z;
87              obj.t = 0;      % set current time to zero
88              % Allocate memeory for the massmatrix, this is used only in
                    control volume
89              % finite element method.
90              obj.MassMatrix = sparse(length(obj.x),length(obj.x));
91              % Allocate memeory for triangle areas
92              obj.tA = zeros(length(obj.tri),1);
93              %%% set erosion parameters...
94              obj.g = 9.81;  %gravitational constant
95
96          end
97          function obj = StartCluster(obj,n) % set and start cluster with n
                nodes
98              obj.pool = parpool(n); % request n processes
99          end
100         function [PmSat,t] = ReadPmSat(obj,i)
101             % this function reads saturation levels in the porous media
```

```
102             % calls ReadPmVaraiable function
103             filename = strcat(obj.RootDir,obj.BaseName,'o.sat_pm.',pad(i),
                    num2str(i));
104             if exist(filename,'file') % if header file exists
105              % if file does not exist, quit quitly.
106                  if obj.verbos
107                      disp(['Reading: ',filename]);
108                  end
109             [PmSat,t] = ReadPmVariable(filename,length(obj.xyz));
110             obj.i = i;
111             else
112                 disp(['File does not exist:',filename]);
113             end
114             if length(PmSat) ~= length(obj.xyz)
115                 error('Reading failed, wrong number of s');
116             end
117
118         end
119         function obj = ReadHeadOlf(obj,i)
120             %this function reads Overland flow Head
121             % calls ReadHeadOlf
122             OlfHead = strcat(obj.RootDir,obj.BaseName,'o.head_olf.',pad(i),
                    num2str(i));
123             if exist(OlfHead,'file') % if header file exists
124              % if file does not exist, quit quitly.
125                  if obj.verbos
126                      disp(['Reading: ',OlfHead]);
127                  end
128             [obj.H,obj.t] = ReadHeadOlf(OlfHead,obj.n);
129              obj.h = obj.H -obj.z;
130              obj.i = i;
131             else
132                 obj.i = 0; % failed to .
133             end
134         end
135         function [data,t] = ReadExchFlux(obj,i)
136             %this function reads Exchange flux output
137             % calls readOlfProp function
138             filename = strcat(obj.RootDir,obj.BaseName,'o.ExchFlux_olf.',pad
                    (i),num2str(i));
139             if exist( filename ,'file') % if header file exists
140              % if file does not exist, quit quitly.
141                  if obj.verbos
142                      disp(['Reading: ',filename ]);
143                  end
144             [data ] = ReadOlfProp( filename);
145              obj.i = i;
146              t = obj.t;
147             else
148                 obj.i = 0; % failed to .
149                 disp('can not ');
150             end
151         end
152         function [data,t] = ReadPlantTranspiration(obj,i)
```

```
153             % this function reads Plant Transpiration
154             % Cals the same function as ReadHeadOlf buth with the proper
155             % file name as input.
156             PlantTranspiration = strcat(obj.RootDir,obj.BaseName,'o.
                    ETPmTranspire_olf.',pad(i),num2str(i));
157             if exist( PlantTranspiration ,'file') % if header file exists
158              % if file does not exist, quit quitly.
159                  if obj.verbos
160                      disp(['Reading: ',PlantTranspiration ]);
161                  end
162             [data ,obj.t] = ReadHeadOlf( PlantTranspiration ,obj.n);
163              obj.i = i;
164              t = obj.t;
165             else
166                 obj.i = 0; % failed to .
167                 disp('can not ');
168             end
169         end
170         function [data,t] = ReadTotalET(obj,i)
171             % this function reads Total ET
172             file = strcat(obj.RootDir,obj.BaseName,'o.ETTotal_olf.',pad(i),
                    num2str(i));
173             if exist( file ,'file') % if header file exists
174              % if file does not exist, quit quitly.
175                  if obj.verbos
176                      disp(['Reading: ', file ]);
177                  end
178
179              [data ,obj.t] = ReadHeadOlf( file ,obj.n);
180              obj.i = i;
181              t = obj.t;
182             else
183                 obj.i = 0; % failed to .
184                 disp('can not ');
185             end
186         end
187         function [data,t] = ReadPmEvap(obj,i)
188             % this function reads porous media evaporation or evaporation
189             % from top soil.
190             file = strcat(obj.RootDir,obj.BaseName,'o.ETPmEvap_olf.',pad(i),
                    num2str(i));
191             if exist( file ,'file') % if header file exists
192              % if file does not exist, quit quitly.
193                  if obj.verbos
194                      disp(['Reading: ', file ]);
195                  end
196
197              [data ,obj.t] = ReadHeadOlf( file ,obj.n);
198              obj.i = i;
199              t = obj.t;
200             else
201                 obj.i = 0; % failed to .
202                 disp('can not ');
203             end
```

```
204         end
205         function [data,t] = ReadETEvap(obj,i)
206             %this function reads surface evaporation
207             %
208             file = strcat(obj.RootDir,obj.BaseName,'o.ETEvap_olf.',pad(i),
                    num2str(i));
209             if exist( file ,'file') % if header file exists
210              % if file does not exist, quit quitly.
211                  if obj.verbos
212                      disp(['Reading: ', file ]);
213                  end
214
215              [data ,obj.t] = ReadHeadOlf( file ,obj.n);
216              obj.i = i;
217              t = obj.t;
218             else
219                 obj.i = 0; % failed to .
220                 disp('can not ');
221             end
222         end
223         function data = ReadOlfProperty(obj,filename)
224             % a generic function for reading Overland flow output
225             if exist(filename,'file')
226                 data=ReadOlfProp(filename);
227             else
228                 data = 0;
229             end
230         end
231         function obj = ReadHeadPm(obj,i)
232             % this function reads Porous media Head
233             PmHead = strcat(obj.RootDir,obj.BaseName,'o.head_pm.',pad(i),
                    num2str(i));
234             if exist(PmHead,'file') % if header file exists
235              % if file does not exist, quit quitly.
236                  if obj.verbos
237                      disp(['Reading: ',PmHead]);
238                  end
239             [obj.Hpm,obj.t] = ReadHeadPm(PmHead,length(obj.xyz));
240              obj.i = i;
241             else
242                 disp(['File does not exist:',PmHead]);
243             end
244         end
245 %         function obj = surf(obj)
246 %             trisurf( obj.tri, obj.x, obj.y, obj.h, 'edgecolor','none');
247 %             colorbar;set(gca,'YDir','reverse'); axis equal;view(0,90)
248 %         end
249         function obj = plotHydrograph(obj, withprecip,tmin,tmax)
250             %this function reads and plots the hydrography.
251             %It can also read the precipitation file and limit the axis to
252             %tmin to tmax if provided.
253             [t,q]=ReadHydrograph(strcat(obj.RootDir,obj.BaseName,'o.
                    hydrograph.hydrograph_nodes.dat'));
254             %tmin = 6*30;
```

```
255             %tmax = 190;
256             if ~withprecip
257             plot(t/3600/24,q,'linewidth', 1);set(gca,'fontsize',18,'
                    linewidth',.5);
258             xlabel('Time[days]');
259             ylabel('Discharge[M^3/s]');
260             %title('Hydrograph')
261             if nargin >2
262             xlim([tmin tmax]);
263             end
264             else
265             %hold on;
266             % plot the precipitation as well.
267             rain = load(strcat(obj.RootDir,'/precip.txt'));
268
269             [AX,H1,H2] = plotyy(t/3600/24,q, rain(:,1)/3600/24,rain(:,2)
                    *3600*1000, 'plot', 'bar','linewidth',.5);
270
271              grid on
272              %set bar graph properties
273              set(get(AX(1),'Ylabel'),'String','Discharge[M^3/s]', 'FontSize'
                     ,16)
274              %set(AX(1), 'XTick', 0:2:22);
275              %set(AX(1), 'TickLength', [0 0]);
276              set(AX(1), 'Xlim', [0 max(t)/3600/24] );
277              set(AX(1), 'Ylim', [0 2.1*max((q)+0.0001)]);
278              set(AX(2), 'XTickLabel', []);
279              %set(AX(1), 'Xgrid', 'on');
280              set(AX(1), 'Ygrid', 'off');
281              %set(AX(1), 'Ylim', [0 (1 + max(x1) * 1.1)]);
282              % set(AX(1), 'YTickLabel', []);
283              set(AX(1), 'FontSize',14);
284
285              %set line plot properties
286              set(get(AX(2),'Ylabel'),'String','Precipitatioin[mm/hour]', '
                     FontSize', 16)
287              %set(AX(2), 'XTickLabel', []);
288              set(AX(2), 'Xlim', [0 max(t)/3600/24] );
289              set(AX(2), 'Ylim', [0 2*max(rain(:,2))*1000*3600+.000000001] );
290              %set(AX(2), 'Xgrid', 'off');
291              %set(AX(2), 'Ygrid', 'off');
292              %set(AX(2), 'Ylim', [0 105]);
293              %set(AX(2), 'YTick', 0:25:100);
294              % set(AX(2), 'YTickLabel', 0:25:100);
295              %set(AX(2), 'YTickLabel', []);
296              set(AX(2), 'FontSize',14);
297              set(AX(2), 'YDir','reverse')
298              if nargin >2
299
300
301              xlim(AX(2),[tmin tmax]);
302              xlim(AX(1),[tmin tmax]);
303              end
304              linkaxes(AX); % link the axis together.
```

```
305             end
306
307         end
308         function obj = WriteVtkOlf(obj)
309             %this function exports water depth into the VTK format.
310             %The output can be viewd with paraview visualization system.
311             triangles = obj.tri; %% turn to 0 array indexing....
312             iID = triangles(:,1) - 1;
313             jID = triangles(:,2) - 1;
314             kID = triangles(:,3) - 1;
315             OutputFile = strcat(obj.RootDir,obj.BaseName,pad(obj.i),num2str(
                    obj.i),'head_olf.vtk');
316             fid = fopen(OutputFile,'w');
317             if fid < 0
318                 error('could not open file for vtk output');
319             end
320             fprintf(fid,'# vtk DataFile Version 2.0\n'); % vtk version.
321             fprintf(fid,'Export to vtk by Karim Norouzi. Open Source Rocks
                    ;-) ! \n'); % title
322             fprintf(fid,'ASCII\n'); % file type is ascii.
323             fprintf(fid,'DATASET POLYDATA\n'); %
324             fprintf(fid,'POINTS %d float \n',length(obj.x));
325             for iInd=1:length(obj.x)
326                 fprintf(fid,' %f  %f  %f  \n',obj.x(iInd), obj.y(iInd),
                        obj.z(iInd));
327             end
328             fprintf(fid,'POLYGONS %d  %d\n',length(obj.tri), length(obj.tri
                    )*4 );
329             for iInd=1:length(iID)
330                 fprintf(fid,' 3  %d  %d  %d \n',iID(iInd), jID(iInd), kID(
                        iInd) );
331             end
332             fprintf(fid,'POINT_DATA %d \n',length(obj.x));
333
334             fprintf(fid,'SCALARS WaterDepth float 1\nLOOKUP_TABLE default\n'
                    );
335             fprintf(fid,'%f\n',obj.h);
336             fclose(fid);
337             disp([OutputFile,' processed']);
338         end
339         function obj = WriteVtkPm(obj)
340             % this function writes the head for porous meida in VTK
341             % use paraview to visualize head values
342             wedge = obj.prisim-1;
343             OutputFile = strcat(obj.RootDir,obj.BaseName,pad(obj.i),num2str(
                    obj.i),'.head_pm','.vtk');
344             fid = fopen(OutputFile,'w');
345             if fid < 0
346                 error('could not open file for vtk output');
347             end
348             fprintf(fid,'# vtk DataFile Version 2.0\n'); % vtk version.
349             fprintf(fid,'Export to vtk by Karim Norouzi. Open Source Rocks
                    ;-) ! \n'); % title
350             fprintf(fid,'ASCII\n'); % file type is ascii.
```

```
351             fprintf(fid,'DATASET UNSTRUCTURED_GRID\n'); %
352             fprintf(fid,'POINTS %d float \n',length(obj.xyz));
353             for iInd=1:length(obj.xyz)
354                  fprintf(fid,' %f   %f   %f  \n',obj.xyz(iInd,1), obj.xyz(
                        iInd,2), obj.xyz(iInd,3));
355             end
356             fprintf(fid,'CELLS %d   %d\n',length(wedge), length(wedge)*7 );
357             for iInd=1:length(obj.prisim)
358              fprintf(fid,' 6   %d   %d   %d   %d   %d   %d\n',wedge(iInd,1),
                    wedge(iInd,2),wedge(iInd,3),wedge(iInd,4),wedge(iInd,5),
                    wedge(iInd,6) );
359             end
360
361             fprintf(fid,'CELL_TYPES  %d\n',length(wedge) );
362             fprintf(fid,'%d\n',ones(length(wedge),1)*13);
363
364             fprintf(fid,'POINT_DATA %d \n',length(obj.xyz));
365             fprintf(fid,'SCALARS PMHead float 1\nLOOKUP_TABLE default\n');
366             fprintf(fid,'%f\n',obj.Hpm);
367             fclose(fid);
368             disp([OutputFile,' processed']);
369
370         end
371         function obj = WriteVtkPmVariable(obj,variable)
372             wedge = obj.prisim-1;
373             OutputFile = strcat(obj.RootDir,obj.BaseName,pad(obj.i),num2str(
                    obj.i),'.pm_sat','.vtk');
374             fid = fopen(OutputFile,'w');
375             if fid < 0
376                 error(' could not open file for vtk output');
377             end
378             fprintf(fid,'# vtk DataFile Version 2.0\n'); % vtk version.
379             fprintf(fid,'Export to vtk by Karim Norouzi. Open Source Rocks
                    ;-) ! \n'); % title
380             fprintf(fid,'ASCII\n'); % file type is ascii.
381             fprintf(fid,'DATASET UNSTRUCTURED_GRID\n'); %
382             fprintf(fid,'POINTS %d float \n',length(obj.xyz));
383             for iInd=1:length(obj.xyz)
384                  fprintf(fid,' %f   %f   %f  \n',obj.xyz(iInd,1), obj.xyz(
                        iInd,2), obj.xyz(iInd,3));
385             end
386             fprintf(fid,'CELLS %d   %d\n',length(wedge), length(wedge)*7 );
387             for iInd=1:length(obj.prisim)
388              fprintf(fid,' 6   %d   %d   %d   %d   %d   %d\n',wedge(iInd,1),
                    wedge(iInd,2),wedge(iInd,3),wedge(iInd,4),wedge(iInd,5),
                    wedge(iInd,6) );
389             end
390
391             fprintf(fid,'CELL_TYPES  %d\n',length(wedge) );
392             fprintf(fid,'%d\n',ones(length(wedge),1)*13);
393
394             fprintf(fid,'POINT_DATA %d \n',length(obj.xyz));
395             fprintf(fid,'SCALARS PMHead float 1\nLOOKUP_TABLE default\n');
396             fprintf(fid,'%f\n', variable);
```

```
397             fclose(fid);
398             disp([OutputFile,' processed']);
399         end
400         function area = TriangleArea( obj, x , y)
401             % calulates the area of a triangle with vertices at x[x1,x2,x3]
402             % and y[y1,y2,y3];
403             % this function will issue an error if the triangle is not
404             % orinted counter clockwise
405              area =(0.5*det([[ 1 x(1) y(1)];[1 x(2) y(2)];[1 x(3) y(3)]]));
406              if area <= 0
407                  error('negative area detected');
408              end
409         end
410         function  CalcMassMatrix(obj)
411             % this is a function to create the mass matrix that results from
412             % the use of Control volume finite element method. The matrix is
413             % diagonal dominient.
414              n_triangles = length(obj.tri);
415              obj.w = zeros(n_triangles,3);
416              for t_ind=1:n_triangles
417                  i = obj.tri(t_ind,1);
418                  j = obj.tri(t_ind,2);
419                  k = obj.tri(t_ind,3);
420                  x_m = (obj.x(i)+obj.x(j)+obj.x(k))/3;  % middle of the
                         triangle
421                  y_m = (obj.y(i)+obj.y(j)+obj.y(k))/3;  % middle of the
                         triangle
422                 %[x_m,y_m] = obj.circumcenter([obj.x(i),obj.x(j),obj.x(k)
                         ],[obj.y(i),obj.y(j),obj.y(k)]);
423                  x_mij = (obj.x(i)+obj.x(j))/2;
424                  y_mij = (obj.y(i)+obj.y(j))/2;
425                  x_mjk = (obj.x(j)+obj.x(k))/2;
426                  y_mjk = (obj.y(j)+obj.y(k))/2;
427                  x_mki = (obj.x(i)+obj.x(k))/2;
428                  y_mki = (obj.y(i)+obj.y(k))/2;
429                  x_i = obj.x(i); x_j = obj.x(j); x_k = obj.x(k);
430                  y_i = obj.y(i); y_j = obj.y(j); y_k = obj.y(k);
431
432                  %calc w
433                  obj.w(t_ind,1) = abs( (obj.y(i) - obj.y(j))*x_m - (obj.x(i)
                         -obj.x(j))*y_m + obj.x(i)*obj.y(j) - obj.y(i)*obj.x(j));
434                  obj.w(t_ind,2) = abs( (obj.y(j) - obj.y(k))*x_m - (obj.x(j)
                         -obj.x(k))*y_m + obj.x(j)*obj.y(k) - obj.y(j)*obj.x(k));
435                  obj.w(t_ind,3) = abs( (obj.y(i) - obj.y(k))*x_m - (obj.x(i)
                         -obj.x(k))*y_m + obj.x(i)*obj.y(k) - obj.y(i)*obj.x(k));
436
437                  obj.tA(t_ind) = obj.TriangleArea([x_i x_j x_k] , [y_i y_j
                         y_k]);
438
439                  Aij = obj.TriangleArea([x_i x_mij x_m],[y_i y_mij y_m]);
440                  Aik = obj.TriangleArea([x_i x_m x_mki],[y_i y_m y_mki]);
441                  Aji = obj.TriangleArea([x_j x_m x_mij],[y_j y_m y_mij]);
442                  Ajk = obj.TriangleArea([x_j x_mjk x_m],[y_j y_mjk y_m]);
443                  Aki = obj.TriangleArea([x_k x_mki x_m],[y_k y_mki y_m]);
```

```
444                 Akj = obj.TriangleArea([x_k x_m x_mjk],[y_k y_m y_mjk]);
445
446                 m = [[11/18*(Aij+Aik)   5/18*Aij+1/9*Aik    1/9*Aij+5/18*Aik
                        ];...
447                      [5/18*Aji+1/9*Ajk  11/18*(Aji+Ajk)     1/9*Aji+5/18*Ajk
                           ];...
448                      [5/18*Aki+1/9*Akj  1/9*Aki+5/18*Akj    11/18*(Aki+Akj)]];
449                 obj.MassMatrix(i,i) = obj.MassMatrix(i,i) + m(1,1);
450                 obj.MassMatrix(i,j) = obj.MassMatrix(i,j) + m(1,2);
451                 obj.MassMatrix(i,k) = obj.MassMatrix(i,k) + m(1,3);
452                 obj.MassMatrix(j,i) = obj.MassMatrix(j,i) + m(2,1);
453                 obj.MassMatrix(j,j) = obj.MassMatrix(j,j) + m(2,2);
454                 obj.MassMatrix(j,k) = obj.MassMatrix(j,k) + m(2,3);
455                 obj.MassMatrix(k,i) = obj.MassMatrix(k,i) + m(3,1);
456                 obj.MassMatrix(k,j) = obj.MassMatrix(k,j) + m(3,2);
457                 obj.MassMatrix(k,k) = obj.MassMatrix(k,k) + m(3,3);
458             end
459 %           [L,U,P] = lu(obj.MassMatrix,'vector');
460 %           obj.MassL = L;
461 %           obj.MassU = U;
462 %           obj.MassP = P;
463             obj.vA = full(sum(obj.MassMatrix))';
464         end
465         function [znu,dz] = evolve(obj,save_flag)
466             % this is the main routine for the calculation of of the
467             % sediment transport and evolution of the surface elevation.
468             % it calls flux function and uses a simple Trapozodial rule to
469             % integrate in time.
470              znu = obj.z;
471              i = 1;
472              t = 0;
473              obj.ReadHeadOlf(i);
474              if(obj.i)
475                  qs = obj.flux(obj.t, [obj.H obj.z]);
476                  tnu = obj.t;
477              end
478              while(obj.i )  % while there are files to
479
480                  qs_nu = obj.flux(obj.t, [obj.H obj.z]);
481                  %dHdt = dydt(1:obj.n);
482
483                  znu = znu + (tnu-t)/obj.Rs/(1-obj.teta)*(qs_nu+qs)/2;
484                  qs= qs_nu; % change the qs to qs_nu, ..
485                  t = tnu;
486
487                  %%%%%
488                  % trisurf(obj.tri,obj.x,obj.y,znu-obj.z,'edgecolor','none')
489                  % view(0,90)
490                  % colorbar
491                  % shading interp
492                  % drawnow
493                  %%%%5
494                  i=i+1;
495                  obj.ReadHeadOlf(i);
```

```
496                 tnu = obj.t;
497                 % temp output ....
498                 msg =['time step: ', num2str(obj.i),' time: ',num2str(tnu)
                        ];
499                 disp(msg);
500                 if(save_flag)
501                     filename = strcat( obj.RootDir,'znu',pad(i),num2str(i),
                            '.txt');
502                     fid = fopen(filename,'w');
503                     fprintf(fid, '%f ',znu');
504                     fclose(fid);
505                 end
506
507 %                 subplot(2,1,1);
508 %                 obj.Henv = max(obj.Henv,obj.H);
509 %                 trisurf(obj.tri, obj.x, obj.y, obj.Henv - obj.z);%shading
       interp
510 %                 view(0,90); shading interp
511 %                 colorbar
512 %
513 %                  subplot(2,1,2);
514 %                  trisurf(obj.tri, obj.x, obj.y, znu - obj.z);%shading
       interp
515 %                  view(0,90);shading interp
516 %                  title(msg);
517 %                  colorbar
518 %                  drawnow;
519               %%%%%%%%%%%%%%
520             end
521             dz = znu -obj.z;
522
523         end
524         function ids = SelectElements(obj, data, datamin,datamax)
525             % data is node data;
526             % a function to select nodes where the node value is between
527             % datamin and datamax. The ids can be used to select nodes in
528             % HSG
529             ids = [];
530             for tid=1:length(obj.tri)
531                 i_node = obj.tri(tid,1);
532                 j_node = obj.tri(tid,2);
533                 k_node = obj.tri(tid,3);
534                 trivalue = (data(i_node)+data(j_node)+data(k_node))/3;
535                 if (trivalue < datamax) && (trivalue > datamin)
536                         ids = [ids tid];
537                 end
538             end
539
540         end
541         function w = PointDistanceToLine(obj,x,y)
542             % this function calculates the distance of point 1 to the line
543             % identified with point 2 and 3.
544             % [x1, x2, x3], [y1, y2, y3] define the inputs
545             dx = x(3) - x(2);
```

```
546             dy = y(3) - y(2);
547             w = abs( (y(3) - y(2))*x(1) - (x(3)-x(2))*y(1) + x(3)*y(2) - y
                    (3)*x(2))/sqrt(dx*dx+dy*dy);
548
549         end
550         function [tsp] = StreamPowerfd(obj, H)  % total stream power
551             % This is a function that calculates the Stream Power using
552             % finite difference
553             %input is the water Head in surface.
554              tsp = zeros(size(H'));
555              qs = zeros(size(H'));
556              Z = obj.z;
557              C = 0.025; %manning rouphgness
558              gamma = 9.81*1000;
559              %qp = [0.1488743389816312, 0.4333953941292472,
                     0.6794095682990244, 0.8650633666889845, 0.9739065285171717];
560              %qw = [0.2955242247147529, 0.2692667193099963,
                     0.2190863625159821, 0.1494513491505806, 0.0666713443086881];
561             for t_id = 1:length(obj.tri)
562                  i = obj.tri(t_id,1);
563                  j = obj.tri(t_id,2);
564                  k = obj.tri(t_id,3);
565                  %%
566                  %Sx = 1/2/obj.triangle_area(t_id)*( H(i)*(obj.y(j)-obj.y(k)
                         )+ H(j)*(obj.y(k)-obj.y(i))+H(k)*(obj.y(i)-obj.y(j)));
567                  %Sy= 1/2/obj.triangle_area(t_id)*( H(i)*(obj.x(k)-obj.x(j))
                         + H(j)*(obj.x(i)-obj.x(k))+H(k)*(obj.x(j)-obj.x(i)));
568                  %S = sqrt(Sx*Sx + Sy*Sy);
569                  % if grad_H_s is less than both fluxes are zero.
570                  if H(i) > H(j)
571                      h = H(i) - Z(i);
572                      S = h/obj.L(t_id,3);
573                      Qs = gamma*h.^(5/3)*sqrt(S)/C*obj.w(t_id,3);
574                      %% second interface.
575                      qs(i) = qs(i) - Qs;
576                      qs(j) = qs(j) + Qs;
577                  else
578                      h = H(j) - H(j);
579                      S = h/obj.L(t_id,3);
580                      Qs = gamma*h.^(5/3)*sqrt(S)/C*obj.w(t_id,3);
581                      %% second interface.
582                      qs(i) = qs(i) + Qs;
583                      qs(j) = qs(j) - Qs;
584                  end
585
586                  if H(j) > H(k)
587                      h = H(j) - Z(j);
588                      S = h / obj.L(t_id,1);
589                      Qs = gamma*h.^(5/3)*sqrt(S)/C*obj.w(t_id,1);
590                      %% second interface.
591                      qs(j) = qs(j) - Qs;
592                      qs(k) = qs(k) + Qs;
593                  else
594                      h = H(k) - H(k);
```

```
595                     S = h/obj.L(t_id,1);
596                     Qs = gamma*h.^(5/3)*sqrt(S)/C*obj.w(t_id,1);
597                     %% second interface.
598                     qs(j) = qs(j) + Qs;
599                     qs(k) = qs(k) - Qs;
600                 end
601
602                 if H(k) > H(i)
603                     h = H(k) - Z(k);
604                     S = h / obj.L(t_id,2);
605                     Qs = gamma*h.^(5/3)*sqrt(S)/C*obj.w(t_id,2);
606                     %% second interface.
607                     qs(k) = qs(k) - Qs;
608                     qs(i) = qs(i) + Qs;
609                 else
610                     h = H(i) - H(i);
611                     S = h/obj.L(t_id,2);
612                     Qs = gamma*h.^(5/3)*sqrt(S)/C*obj.w(t_id,2);
613                     %% second interface.
614                     qs(k) = qs(k) + Qs;
615                     qs(i) = qs(i) - Qs;
616                 end
617             end % end qs
618              tsp=  qs'./obj.vA;
619         end
620         function [tsp] = StreamPower(obj, H)  % total stream power
621             % stream power with Quadrature formualtion.
622             % the Energy slope is calculated for each triangle using the the
623             % H for three nodes.
624              tsp = zeros(size(H'));
625              qs = zeros(size(H'));
626              Z = obj.z;
627              C = 0.025; %manning rouphgness
628              gamma = 9.81*1000;
629              qp = [0.1488743389816312, 0.4333953941292472,
                     0.6794095682990244, 0.8650633666889845, 0.9739065285171717];
630              qw = [0.2955242247147529, 0.2692667193099963,
                     0.2190863625159821, 0.1494513491505806, 0.0666713443086881];
631             for t_id = 1:length(obj.tri)
632                  i = obj.tri(t_id,1);
633                  j = obj.tri(t_id,2);
634                  k = obj.tri(t_id,3);
635                  H_m = (H(i)+H(j)+H(k))/3;
636                  H_ij = (H(i)+H(j))/2;
637                  H_jk = (H(j)+H(k))/2;
638                  H_ki = (H(i)+H(k))/2;
639                  Z_m = (Z(i)+Z(j)+Z(k))/3;
640                  Z_ij = (Z(i)+Z(j))/2;
641                  Z_jk = (Z(j)+Z(k))/2;
642                  Z_ki = (Z(i)+Z(k))/2;
643                 %%
644                 x_m = (obj.x(i)+obj.x(j)+obj.x(k))/3;  % middle of the
                        triangle
645                 y_m = (obj.y(i)+obj.y(j)+obj.y(k))/3;  % middle of the
```

```
646                 triangle
647                 x_ij = (obj.x(i)+obj.x(j))/2;
648                 y_ij = (obj.y(i)+obj.y(j))/2;
649                 x_jk = (obj.x(j)+obj.x(k))/2;
650                 y_jk = (obj.y(j)+obj.y(k))/2;
651                 x_ki = (obj.x(i)+obj.x(k))/2;
652                 y_ki = (obj.y(i)+obj.y(k))/2;
653
654                 %%
655                 Sx = 1/2/obj.tA(t_id)*( H(i)*(obj.y(j)-obj.y(k))+ H(j)*(obj
                        .y(k)-obj.y(i))+H(k)*(obj.y(i)-obj.y(j)));
656                 Sy= 1/2/obj.tA(t_id)*( H(i)*(obj.x(k)-obj.x(j))+ H(j)*(obj.
                        x(i)-obj.x(k))+H(k)*(obj.x(j)-obj.x(i)));
657                 S = sqrt(Sx*Sx + Sy*Sy);
658                 % if grad_H_s is less than both fluxes are zero.
659                 sqrt_S = sqrt(S);
660                 if S > 10e-12
661                     Hqp = (1-qp)*H_ij + qp*H_m;
662                     Zqp = (1-qp)*Z_ij + qp*Z_m;
663                     hqp = Hqp - Zqp;
664                     if any(hqp) < 0
665                         error('negetive water depth');
666                     end
667                     ssp = gamma*hqp.^(5/3)*sqrt_S/C;
668                     %qw_mij = obj.segment.integrate(qwx+qwy);  % flow
                            throuh the first segment
669                     L= sqrt( (x_ij - x_m)*(x_ij - x_m) + (y_ij - y_m)*(y_ij
                            - y_m));
670                     nx = (x_m - x_ij)/L;
671                     ny = (y_m - y_ij)/L;
672                     qs_mij = L*sum( qw .* ssp );
673                     %% second interface.
674                     Hqp = (1-qp)*H_jk + qp*H_m;
675                     Zqp = (1-qp)*Z_jk + qp*Z_m;
676                     hqp = Hqp - Zqp;
677                     if any(hqp) < 0
678                         error('negetive water depth');
679                     end
680                     ssp = gamma*hqp.^(5/3)*sqrt_S/C;
681                     %qw_mij = obj.segment.integrate(qwx+qwy);  % flow
                            throuh the first segment
682                     L= sqrt( (x_jk - x_m)*(x_jk - x_m) + (y_jk - y_m)*(y_jk
                            - y_m));
683                     nx = (x_m - x_jk)/L;
684                     ny = (y_m - y_jk)/L;
685                     qs_mjk = L*sum( qw .* ssp );
686                     %%
687                     Hqp = (1-qp)*H_ki + qp*H_m;
688                     Zqp = (1-qp)*Z_ki + qp*Z_m;
689                     hqp = Hqp - Zqp;
690                     if any(hqp) < 0
691                         error('negetive water depth');
692                     end
```

```
693                     %qw_mij = obj.segment.integrate(qwx+qwy);  % flow
                            throuh the first segment
694                     L= sqrt( (x_ki - x_m)*(x_ki - x_m) + (y_ki - y_m)*(y_ki
                             - y_m));
695                     nx = (x_m - x_ki)/L;
696                     ny = (y_m - y_ki)/L;
697                     qs_mki = L*sum( qw .* ssp );
698                     %%
699                     qs(i) = qs(i) + qs_mij - qs_mki;
700                     qs(j) = qs(j) + qs_mjk - qs_mij;
701                     qs(k) = qs(k) + qs_mki - qs_mjk;
702                 end
703             end % end qs
704
705              %tsp=  obj.MassU\(obj.MassL \ qs(obj.MassP)');
706              tsp = qs' ./ obj.vA;
707
708
709 %
710         end
711         function    CalcStreamPower(obj)
712             % calculation of the stream power for the transient case.
713             % calls StreamPower or StreamPowerfd
714             i = 1;
715             obj = obj.ReadHeadOlf(i);
716             if obj.i
717              t = obj.t;
718              H = obj.H;
719              csp = obj.StreamPower(H);
720             end
721             i = i+1;
722             obj.ReadHeadOlf(i);
723             while obj.i
724                  Hnu = obj.H;
725                  tnu = obj.t;
726                  cspnu = obj.StreamPower(Hnu);
727                  ssp = 9.81*1000*(Hnu.*(Hnu - obj.z) - H.*(H - obj.z))/(tnu
                         - t) ...
728                      + 0.5*(cspnu + csp);
729                  H = Hnu;
730                  t = tnu;
731                  csp = cspnu;
732                  ExportBaseleveltoGMS(strcat(obj.RootDir,'ssp',pad(obj.i),
                         num2str(i),'.gms'),ssp);
733                  disp([ obj.RootDir,'stream power for ',num2str(i)]);
734                  i = i+1;
735                  obj.ReadHeadOlf(i);
736             end
737         end
738         function [znu,Qb] =  erode(obj,step,stepsize)
739             % the newest version of the land surface evolution.
740             % can call Qs (Quadrature integration) or Qsfd (finite
                    difference)
741             if isempty(obj.vA)
```

```
742                 error('calculate geometries first');
743             end
744             znu = obj.z;
745             Qb = [];
746              i = 1;
747              t = 0;
748              obj.ReadHeadOlf(i);
749              if(obj.i)
750                  [qs,qb] = obj.Qsfd(obj.t, obj.H);
751                  tnu = obj.t;
752              end
753              Qb = [Qb qb];
754             %c =1/obj.beta/obj.Rs/(1-obj.teta);
755              c =1/obj.beta/obj.Rs;
756
757              while(obj.i < stepsize)  % while there are files to process
758                  [qs_nu,qb] = obj.Qsfd(obj.t, obj.H );
759                  Qb = [Qb qb];
760                  znu = znu + c*(tnu-t)*(qs_nu+qs)/2;
761                  qs= qs_nu; % change the qs to qs_nu, ..
762                  t = tnu;
763                  i=i+1;
764                  obj.ReadHeadOlf(i);
765                  tnu = obj.t;
766                  % temp output ....
767                  msg =[obj.RootDir,' - time step: ', num2str(obj.i),' time:
                         ',num2str(tnu)];
768                  disp(msg);
769                  if(step)
770                       ext = (step-1)*stepsize + i-1;
771                       filename = strcat( obj.RootDir,'znu',pad(ext),num2str(
                             ext),'.gms');
772                       ExportBaseleveltoGMS(filename,znu); % save in gms
                             format.
773
774                  end
775              end
776              filename = strcat( obj.RootDir,'Qsbnd.gms');
777              ExportBaseleveltoGMS(filename,Qb); % save in gms format.
778
779          end
780         function Hmax = MaxWaterDepth(obj)
781             %find the water depth Envelop.
782                 i=1;
783                 Hmax = obj.z;
784                 obj.ReadHeadOlf(i);
785                 Hmax = obj.H;
786                 while(obj.i);
787                      i = i+1;
788                      obj.ReadHeadOlf(i);
789                      Hmax = max(Hmax, obj.H);
790
791                      disp(['reading file ',num2str(i)]);
792                 end
```

```
793         end
794         function DiscretizeUsingInCenters(obj)
795             %% calculate vA,Lij, and w using incenters...
796             % discritizes the triangles using Incenters.
797             % the interface length, normals and each node area is
798             % calculated. The values are needed for the finite difference
799             % method.
800 
801              nNodes = length(obj.x);
802              nTri = length(obj.tri);
803              obj.L =zeros(nTri,3);
804              obj.w =zeros(nTri,3);
805              obj.nx =zeros(nTri,3);
806              obj.ny =zeros(nTri,3);
807              obj.vA = zeros(nNodes,1);
808              A = 1;
809              B = 2;
810              C = 3;
811              for t = 1:nTri
812                  i = obj.tri(t,1); j = obj.tri(t,2); k = obj.tri(t,3);
813                  a = obj.distance([obj.x(j) obj.x(k)],[obj.y(j) obj.y(k)]);
814                  b = obj.distance([obj.x(i) obj.x(k)],[obj.y(i) obj.y(k)]);
815                  c = obj.distance([obj.x(i) obj.x(j)],[obj.y(i) obj.y(j)]);
816                  s = a+b+c;
817                  ix = (a*obj.x(i) + b*obj.x(j) + c*obj.x(k))/(a+b+c);
818                  iy = (a*obj.y(i) + b*obj.y(j) + c*obj.y(k))/(a+b+c);
819 
820                  Area = obj.TriangleArea([obj.x(i), obj.x(j), obj.x(k)],[obj
                         .y(i), obj.y(j),obj.y(k)]);
821                  r = Area/2/s; % raduous of incenter.
822                  obj.L(t,A) = a; % a is opposite node A
823                  obj.L(t,B) = b; % b is opposite node B
824                  obj.L(t,C) = c; % c is opposite node C
825                  obj.w(t,A) = r;
826                  obj.w(t,B) = r;
827                  obj.w(t,C) = r;
828                  di = obj.distance([ix,obj.x(i)],[iy,obj.y(i)]); %distance
                         from node i to incenter
829                  dj = obj.distance([ix,obj.x(j)],[iy,obj.y(j)]);
830                  dk = obj.distance([ix,obj.x(k)],[iy,obj.y(k)]);
831                  bi = sqrt(di*di - r*r);
832                  bj = sqrt(dj*dj - r*r);
833                  bk = sqrt(dk*dk - r*r);
834                  obj.vA(i) = obj.vA(i) + r*bi;
835                  obj.vA(j) = obj.vA(j) + r*bj;
836                  obj.vA(k) = obj.vA(k) + r*bk;
837 
838                  obj.tA(t) = Area;
839                  obj.nx(t,C) = (obj.x(i)-obj.x(j))/c; % normal to the
                         interface 1 x dir
840                  obj.ny(t,C) = (obj.y(i)-obj.y(j))/c; % normal to the
                         interface 1 y dir
841                  obj.nx(t,B) = (obj.x(k)-obj.x(i))/b;
842                  obj.ny(t,B) = (obj.y(k)-obj.y(i))/b;
```

```
843                 obj.nx(t,A) = (obj.x(j)-obj.x(k))/a;
844                 obj.ny(t,A) = (obj.y(j)-obj.y(k))/a;
845
846             end
847
848
849         end
850         function DiscretizeUsingMedian(obj)
851             %% calculate vA,Lij, and w using Medians
852             % discritize the triangles using median values.
853             % values are needed for finite difference. When the triangles
854             % are equlateral, this is the same as DiscreitzeUsingInCenters()
855              nNodes = length(obj.x);
856              nTri = length(obj.tri);
857              obj.L =zeros(nTri,3);
858              obj.w =zeros(nTri,3);
859              obj.nx =zeros(nTri,3);
860              obj.ny =zeros(nTri,3);
861              obj.vA = zeros(nNodes,1);
862              for t = 1:nTri
863                  i = obj.tri(t,1); j = obj.tri(t,2); k = obj.tri(t,3);
864                  a = obj.distance([obj.x(j) obj.x(k)],[obj.y(j) obj.y(k)]);
865                  b = obj.distance([obj.x(i) obj.x(k)],[obj.y(i) obj.y(k)]);
866                  c = obj.distance([obj.x(i) obj.x(j)],[obj.y(i) obj.y(j)]);
867                  obj.L(t,1) = a;
868                  obj.L(t,2) = b;
869                  obj.L(t,3) = c;
870                  mx = (obj.x(i) + obj.x(j) + obj.x(k))/3; %meidan x coord
871                  my = (obj.y(i) + obj.y(j) + obj.y(k))/3; % meidan y coord
872
873                  mxij = (obj.x(i) + obj.x(j))/2;
874                  myij = (obj.y(i) + obj.y(j))/2;
875                  mxjk = (obj.x(j) + obj.x(k))/2;
876                  myjk = (obj.y(j) + obj.y(k))/2;
877                  mxki = (obj.x(k) + obj.x(i))/2;
878                  myki = (obj.y(k) + obj.y(i))/2;
879                  A = obj.TriangleArea([obj.x(i), obj.x(j), obj.x(k)],[obj.y(
                         i), obj.y(j),obj.y(k)]);
880                  obj.w(t,3) = obj.distance([mx mxij],[my myij]);
881                  obj.w(t,1) = obj.distance([mx mxjk],[my myjk]);
882                  obj.w(t,2) = obj.distance([mx mxki],[my myki]);
883                  obj.vA(i) = obj.vA(i)+obj.TriangleArea([obj.x(i), mxij, mx
                         ],[obj.y(i),myij  ,  my]);
884                  obj.vA(i) = obj.vA(i)+obj.TriangleArea([obj.x(i), mx, mxki
                         ],[obj.y(i), my, myki]);
885                  obj.vA(j) = obj.vA(j)+obj.TriangleArea([obj.x(j), mxjk, mx
                         ],[obj.y(j), myjk, my]);
886                  obj.vA(j) = obj.vA(j)+obj.TriangleArea([obj.x(j), mx, mxij
                         ],[obj.y(j), my, myij]);
887                  obj.vA(k) = obj.vA(k)+obj.TriangleArea([obj.x(k), mxki, mx
                         ],[obj.y(k), myki, my]);
888                  obj.vA(k) = obj.vA(k)+obj.TriangleArea([obj.x(k), mx, mxjk
                         ],[obj.y(k), my, myjk]);
889                  obj.tA(t) = A;
```

```
890                 obj.nx(t,1) =  -(my-myij)/obj.w(t,1);  % normal to the
                        interface 1 x dir
891                 obj.ny(t,1) = (mx-mxij)/obj.w(t,1); % normal to the
                        interface 1 y dir
892                 obj.nx(t,2) = - (my-myjk)/obj.w(t,2);
893                 obj.ny(t,2) = (mx-mxjk)/obj.w(t,2);
894                 obj.nx(t,3) = - (my-myki)/obj.w(t,3);
895                 obj.ny(t,3) = (mx-mxki)/obj.w(t,3);
896             end
897
898
899         end
900         function [dZdt] = Qs(obj,t,H)
901             %this function calculates sediment flux using Quadrature method.
902             %Energey gradient is calculated using head values for the 3
903             %nodes in triangle.
904              %np = obj.pool.NumWorkers;
905              Q_s = zeros(size(H));
906              Z = obj.z;
907
908              AA = (obj.Rs - obj.Rw)*obj.g*obj.D;
909              BB = obj.Ks*obj.D^(3/2)*sqrt((obj.Rs - obj.Rw)/obj.Rw*obj.g);
910              gamma = obj.g*obj.Rw;
911              qp = [0.1488743389816312, 0.4333953941292472,
                     0.6794095682990244, 0.8650633666889845, 0.9739065285171717];
912              qw = [0.2955242247147529, 0.2692667193099963,
                     0.2190863625159821, 0.1494513491505806, 0.0666713443086881];
913              A = 1;
914              B = 2;
915              C = 3;
916             for t_id = 1:length(obj.tri)
917                  ii = obj.tri(t_id,1);
918                  jj = obj.tri(t_id,2);
919                  kk = obj.tri(t_id,3);
920                  H_m = (H(ii)+H(jj)+H(kk))/3;
921                  H_ij = (H(ii)+H(jj))/2;
922                  H_jk = (H(jj)+H(kk))/2;
923                  H_ki = (H(ii)+H(kk))/2;
924                  Z_m = (Z(ii)+Z(jj)+Z(kk))/3;
925                  Z_ij = (Z(ii)+Z(jj))/2;
926                  Z_jk = (Z(jj)+Z(kk))/2;
927                  Z_ki = (Z(ii)+Z(kk))/2;
928                 %%
929                 Sx = 1/2/obj.tA(t_id)*( H(ii)*(obj.y(jj)-obj.y(kk))+ H(jj)
                         *(obj.y(kk)-obj.y(ii))+H(kk)*(obj.y(ii)-obj.y(jj)));
930                 Sy = 1/2/obj.tA(t_id)*( H(ii)*(obj.x(kk)-obj.x(jj))+ H(jj)
                         *(obj.x(ii)-obj.x(kk))+H(kk)*(obj.x(jj)-obj.x(ii)));
931                 S = sqrt(Sx*Sx + Sy*Sy);
932                 % if grad_H_s is less than both fluxes are zero.
933
934                 if S > 10e-16
935
936                     Hqp = (1-qp)*H_ij + qp*H_m;
937                     Zqp = (1-qp)*Z_ij + qp*Z_m;
```

```
938                 hqp = Hqp - Zqp;
939
940                 Texcess = max(0,(gamma*hqp*S/AA - obj.Tc));
941                 qs_seg = BB*(Texcess).^(3/2);
942                 qs_x = qs_seg*Sx/S;
943                 qs_y =  qs_seg*Sy/S;
944                 %qw_mij = obj.segment.integrate(qwx+qwy);  % flow
                        throuh the first segment
945
946                 qs_mij = obj.w(t_id,C)*sum( qw .* ( qs_x*obj.nx(t_id,C)
                        - qs_y*obj.ny(t_id,C)) );
947                 %% second interface.
948
949
950                 Hqp = (1-qp)*H_jk + qp*H_m;
951                 Zqp = (1-qp)*Z_jk + qp*Z_m;
952                 hqp = Hqp - Zqp;
953
954
955                 Texcess = max(0,(gamma*hqp*S/AA - obj.Tc));
956                 qs_seg = BB*(Texcess).^(3/2);
957
958                 qs_x =  qs_seg*Sx/S;
959                 qs_y =  qs_seg*Sy/S;
960
961                 qs_mjk = obj.w(t_id,A)*sum( qw .* ( qs_x*obj.nx(t_id,A)
                        - qs_y*obj.ny(t_id,A) ) );
962
963                 %%
964
965                 Hqp = (1-qp)*H_ki + qp*H_m;
966                 Zqp = (1-qp)*Z_ki + qp*Z_m;
967                 hqp = Hqp - Zqp;
968
969                 Texcess = max(0,(gamma*hqp*S/AA - obj.Tc));
970                 qs_seg = BB*(Texcess).^(3/2);
971
972                 qs_x = qs_seg*Sx/S;
973                 qs_y =  qs_seg*Sy/S;
974
975                 qs_mki = obj.w(t_id,B)*sum( qw .* ( qs_x*obj.nx(t_id,B)
                        - qs_y* obj.ny(t_id,B)));
976
977                 %%
978
979
980                 Q_s(ii) = Q_s(ii) - qs_mij + qs_mki;
981                 Q_s(jj) = Q_s(jj) - qs_mjk + qs_mij;
982                 Q_s(kk) = Q_s(kk) - qs_mki + qs_mjk;
983             end
984
985
986
987
```

```
988
989             end % end qs
990           dZdt = -Q_s./obj.vA;
991       end
992       function [dZdt] = QsCV(obj,t,H)
993           %This function calculates sediment flux using Control volume
994           %approach. This is called from erode function.
995            Q_s = zeros(size(H));
996            Z = obj.z;
997            %seg = obj.segment;
998            gamma = obj.g*obj.Rw;
999            AA = (obj.Rs - obj.Rw)*obj.g*obj.D;
1000           BB = obj.Ks*obj.D^(3/2)*sqrt((obj.Rs - obj.Rw)/obj.Rw*obj.g);
1001           A = 1;
1002           B = 2;
1003           C = 3;
1004           for t_id = 1:length(obj.tri)
1005                ii = obj.tri(t_id,A);
1006                jj = obj.tri(t_id,B);
1007                kk = obj.tri(t_id,C);
1008               %% testting flux
1009                    if H(ii) > H(jj)
1010                        S = (H(ii) - H(jj))/obj.L(t_id,C);
1011                        hqp = H(ii) - Z(ii);
1012                        Texcess = max(0,(gamma*hqp*S/AA - obj.Tc));
1013                        qs_seg = BB*(Texcess).^(3/2);
1014                        qs_mij = qs_seg*obj.w(t_id,C);
1015                        Q_s(ii) = Q_s(ii) - qs_mij;
1016                        Q_s(jj) = Q_s(jj) + qs_mij;
1017                    else
1018                        S = (H(jj) - H(ii))/obj.L(t_id,C);
1019                        hqp = H(jj) - Z(jj);
1020                        Texcess = max(0,(gamma*hqp*S/AA - obj.Tc));
1021                        qs_seg = BB*(Texcess).^(3/2);
1022                        qs_mij = qs_seg*obj.w(t_id,C);
1023                        Q_s(ii) = Q_s(ii) + qs_mij;
1024                        Q_s(jj) = Q_s(jj) - qs_mij;
1025                    end
1026
1027                    %% second interface.
1028
1029                    if H(jj) > H(kk)
1030                            S = (H(jj) -H(kk))/obj.L(t_id,A);
1031                            hqp = H(jj) - Z(jj);
1032                            Texcess = max(0,(gamma*hqp*S/AA - obj.Tc));
1033                            qs_seg = BB*(Texcess).^(3/2);
1034                            qs_mjk = qs_seg*obj.w(t_id,A);
1035                            Q_s(jj) = Q_s(jj) - qs_mjk ;
1036                            Q_s(kk) = Q_s(kk) + qs_mjk;
1037                    else
1038                           S = (H(kk) -H(jj))/obj.L(t_id,A);
1039                            hqp = H(kk) - Z(kk);
1040                            Texcess = max(0,(gamma*hqp*S/AA - obj.Tc));
1041                            qs_seg = BB*(Texcess).^(3/2);
```

```
1042                                qs_mjk = qs_seg*obj.w(t_id,A);
1043                               Q_s(jj) = Q_s(jj) + qs_mjk ;
1044                               Q_s(kk) = Q_s(kk) - qs_mjk;
1045                        end
1046
1047                        %%
1048                        if H(kk) > H(ii)
1049                            S = (H(kk) -H(ii))/obj.L(t_id,B);
1050                            hqp = H(kk) - Z(kk);
1051                            Texcess = max(0,(gamma*hqp*S/AA - obj.Tc));
1052                            qs_seg = BB*(Texcess).^(3/2);
1053                            qs_mki = qs_seg*obj.w(t_id,B);
1054                            Q_s(ii) = Q_s(ii) + qs_mki;
1055                            Q_s(kk) = Q_s(kk) - qs_mki;
1056                        else
1057                            S = (H(ii) -H(kk))/obj.L(t_id,B);
1058                            hqp = H(ii) - Z(ii);
1059                            Texcess = max(0,(gamma*hqp*S/AA - obj.Tc));
1060                            qs_seg = BB*(Texcess).^(3/2);
1061                            qs_mki = qs_seg*obj.w(t_id,B);
1062                            Q_s(ii) = Q_s(ii) - qs_mki;
1063                            Q_s(kk) = Q_s(kk) + qs_mki;
1064                        end
1065                    end
1066                dZdt =    Q_s./obj.vA; %obj.MassU\(obj.MassL \ (Q_s(obj.MassP,:))
                        );
1067                dZdt(obj.bnd_nodes) = 0;
1068            end
1069            function [dZdt,qb] = Qsfd(obj,t,H)
1070                % function to calculate sediment flux using finite difference.
1071                %
1072                 %np = obj.pool.NumWorkers;
1073                 Q_s = zeros(size(H));
1074                 Z = obj.z;
1075                 %seg = obj.segment;
1076                 gamma = obj.g*obj.Rw;
1077                 AA = (obj.Rs - obj.Rw)*obj.g*obj.D;
1078                 BB = obj.Ks*obj.D^(3/2)*sqrt((obj.Rs - obj.Rw)/obj.Rw*obj.g);
1079                for t_id = 1:length(obj.tri)
1080                     ii = obj.tri(t_id,1);
1081                     jj = obj.tri(t_id,2);
1082                     kk = obj.tri(t_id,3);
1083                     %% testting flux
1084                     H_ij = (H(ii)+H(jj))/2;
1085                     H_jk = (H(jj)+H(kk))/2;
1086                     H_ki = (H(ii)+H(kk))/2;
1087                     Z_ij = (Z(ii)+Z(jj))/2;
1088                     Z_jk = (Z(jj)+Z(kk))/2;
1089                     Z_ki = (Z(ii)+Z(kk))/2;
1090                     %%
1091
1092                         S = (H(jj) -H(ii))/obj.L(t_id,3);
1093                         hqp = H_ij - Z_ij;
1094                         Texcess = max(0,(gamma*hqp*abs(S)/AA - obj.Tc));
```

```
1095                    qs_seg = BB*(Texcess).^(3/2);
1096
1097                    qs_mij = qs_seg*obj.w(t_id,3);
1098                    if H(ii) > H(jj)
1099                        Q_s(ii) = Q_s(ii) - qs_mij;
1100                        Q_s(jj) = Q_s(jj) + qs_mij;
1101
1102                    else
1103
1104                        Q_s(ii) = Q_s(ii) + qs_mij;
1105                        Q_s(jj) = Q_s(jj) - qs_mij;
1106
1107                    end
1108
1109                    %% second interface.
1110
1111                    S = (H(kk) -H(jj))/obj.L(t_id,1);
1112                    hqp = H_jk - Z_jk;
1113
1114                    Texcess = max(0,(gamma*hqp*abs(S)/AA - obj.Tc));
1115                    qs_seg = BB*(Texcess).^(3/2);
1116
1117                    qs_mjk = qs_seg*obj.w(t_id,1);
1118                    if H(jj) > H(kk)
1119                            Q_s(jj) = Q_s(jj) - qs_mjk ;
1120                            Q_s(kk) = Q_s(kk) + qs_mjk;
1121                    else
1122                            Q_s(jj) = Q_s(jj) + qs_mjk ;
1123                            Q_s(kk) = Q_s(kk) - qs_mjk;
1124                    end
1125
1126                    %%third interface
1127
1128                    S = (H(ii) -H(kk))/obj.L(t_id,2);
1129                    hqp = H_ki - Z_ki;
1130
1131
1132                    Texcess = max(0,(gamma*hqp*abs(S)/AA - obj.Tc));
1133                    qs_seg = BB*(Texcess).^(3/2);
1134
1135
1136                    qs_mki = qs_seg*obj.w(t_id,2);
1137                    if H(kk) > H(ii)
1138                        Q_s(ii) = Q_s(ii) + qs_mki;
1139                        Q_s(kk) = Q_s(kk) - qs_mki;
1140                    else
1141                        Q_s(ii) = Q_s(ii) - qs_mki;
1142                        Q_s(kk) = Q_s(kk) + qs_mki;
1143                    end
1144                end
1145            dZdt =    Q_s./obj.vA; %obj.MassU\(obj.MassL \ (Q_s(obj.MassP,:))
                );
1146            ind = find(Q_s(obj.bnd_nodes)> 0);
1147            qb = sum(Q_s(obj.bnd_nodes(ind)));  % select and sum the
```

```
                positive flux out of the system.
1148            dZdt(obj.bnd_nodes(ind)) = 0;  % only the postive flux gets out
                of the system.
1149        end
1150        function plotproperty(obj,prop)
1151            % a quick way of plotting a surface property.
1152             tri = obj.tri;
1153             x = obj.x/1000;
1154             y = obj.y/1000;
1155             z = obj.z;
1156             max_x = max(x);
1157             min_x = min(x);
1158             max_y = max(y);
1159             min_y = min(y);
1160
1161             trisurf(tri,x,y, prop ,'edgecolor','none');
1162            % trisurf(tri,x,y,z, prop);
1163              shading interp
1164                 view(0,90);
1165                 %hc = colorbar;
1166                 set(gca,'ydir','reverse');
1167                 axis equal
1168
1169                 xlim([min_x max_x]);
1170                 ylim([min_y max_y]);
1171                 %caxis([-3.5 3.5]);
1172                 xlabel('X[Km]','fontsize',16);
1173                 ylabel('Y[Km]','fontsize',16);
1174
1175            end
1176        function [cx,cy] = circumcenter(obj,x,y)
1177            % finds the triangle circumcenter coordinates
1178                 DET = 2*(x(1)*(y(2)-y(3)) + x(2)*(y(3)-y(1)) + x(3)*(y(1)-y
                         (2)));
1179                 mx = (x(1)*x(1)+y(1)*y(1))*(y(2)-y(3))+(x(2)*x(2)+y(2)*y(2)
                         )*(y(3)-y(1))+(x(3)*x(3)+y(3)*y(3))*(y(1)-y(2));
1180                 my = (x(1)*x(1)+y(1)*y(1))*(x(3)-x(2))+(x(2)*x(2)+y(2)*y(2)
                         )*(x(1)-x(3))+(x(3)*x(3)+y(3)*y(3))*(x(2)-x(1));
1181                 cx =mx/DET;
1182                 cy =my/DET;
1183        end
1184        function [ix,iy] = incenter(obj,x,y)
1185            %% calculates the incenter of of the triagle.
1186            % finces the incenter coordinates for each triangle.
1187            a = obj.distance([x(2) x(3)],[y(2) y(3)]);
1188            b = obj.distance([x(1) x(3)],[y(1) y(3)]);
1189            c = obj.distance([x(1) x(3)],[y(1) y(3)]);
1190            ix = (a*x(1) + b*x(2) + c*x(3))/(a+b+c);
1191            iy = (a*y(1) + b*y(2) + y*x(3))/(a+b+c);
1192        end
1193        function d = distance(obj,x,y)
1194            % his function calculates the distance between two points.
1195            dx = x(2) - x(1);
1196            dy = y(2) - y(1);
```

```
1197                d = sqrt(dx*dx + dy*dy);
1198            end
1199        end  %end methods
1200
1201    end
```

Bibliography

[1] Richard John Huggett. *Fundamentals of Geomorphology*. Routledge, Milton Park, Abingdon, Oxon; New York, 3rd edition, February 2011.

[2] Garry Willgoose. Mathematical Modeling of Whole Landscape Evolution. *Annual Review of Earth and Planetary Sciences*, 33(1):443–459, 2005.

[3] Rebecca L. Reverman, Maria G. Fellin, Frederic Herman, Sean D. Willett, and Caroline Fitoussi. Climatically versus tectonically forced erosion in the Alps: Thermochronometric constraints from the Adamello Complex, Southern Alps, Italy. *Earth and Planetary Science Letters*, 2012.

[4] G. E. Hilley, C. P. Chamberlain, S. Moon, S. Porder, and S.D.Willett. Competition between erosion and reaction kinetics in controlling silicate-weathering rates. *Earth and Planetary Science Letters*, 2010.

[5] Sean D. Willett. Late Neogene Erosion of the Alps: A Climate Driver? *Annual Review of Earth and Planetary Sciences*, 38(1):411–437, April 2010.

[6] Joshua J. Roering, James W. Kirchner, and William E. Dietrich. Hillslope evolution by nonlinear, slope-dependent transport: Steady state morphology and equilibrium adjustment timescales. *Journal of Geophysical Research*, August 2001.

[7] P Zhang, P Molnar, and W.R. Downs. Increased sedimentation rates and grain sizes 2-4 Myr ago due to the influence of climate change on erosion rates. *Nature*, (410), 2001.

[8] Gregory E. Tucker and Gregory R. Hancock. Modelling landscape evolution. *Earth Surface Processes and Landforms*, 35(1):28–50, January 2010.

[9] Garry Willgoose, Rafael L. Bras, and Ignacio Rodriguez-Iturbe. A coupled channel network growth and hillslope evolution model: 1. Theory. *Water Resources Research*, 27(7):1671–1684, 1991.

[10] Gregory E. Tucker, Stephen T. Lancaster, Nicole M. Gasparini, Rafael L. Bras, and Scott M. Rybarczyk. An object-oriented framework for distributed hydrologic and geomorphic modeling using triangulated irregular networks. *Computers & Geosciences*, 27(8):959–973, 2001.

[11] Gregory E. Tucker, Stephen T. Lancaster, Nicole M. Gasparini, Rafael L. Bras, Scott M. Rybarczyk, and Scott M. An Object-Oriented Framework for Distributed Hydrologic and Geomorphic Modeling Using Triangulated Irregular Networks. *Computers and Geosciences*, 27:959–973, 1999.

[12] Gregory E. Tucker and Rudy L. Slingerland. Erosional dynamics, flexural isostasy, and long-lived escarpments: A numerical modeling study. *Journal of Geophysical Research: Solid Earth*, 99(B6):12229–12243, 1994.

[13] Jean Braun and Malcolm Sambridge. Modelling landscape evolution on geological time scales: a new method based on irregular spatial discretization. *Basin Research*, 9(1):27–52, 1997.

[14] S. Carretier and F. Lucazeau. How does alluvial sedimentation at range fronts modify the erosional dynamics of mountain catchments? *Basin Research*, 17(3):361–381, 2005.

[15] R. H. Whittaker. *Communities and Ecosystems*. Macmillan USA, New York, 2nd edition, August 1975.

[16] Recep Efe, Munir Ozturk, Ibrahim Atalay, and Donatella Termini. 3rd International Geography Symposium, GEOMED2013, 10-13 June 2013, Antalya, TurkeyBank Erosion and Secondary Circulation in a Meandering Laboratory Flume. *Procedia - Social and Behavioral Sciences*, 120:496–505, March 2014.

[17] Artemi Cerdà and Stefan H. Doerr. The effect of ash and needle cover on surface runoff and erosion in the immediate post-fire period. *CATENA*, 74(3):256–263, August 2008.

[18] Cristina Fernández and José A. Vega. Effects of mulching and post-fire salvage logging on soil erosion and vegetative regrowth in NW Spain. *Forest Ecology and Management*, 375:46–54, September 2016.

[19] A. Jordán and L. Martínez-Zavala. Soil loss and runoff rates on unpaved forest roads in southern Spain after simulated rainfall. *Forest Ecology and Management*, 255(3–4):913–919, March 2008.

[20] Maruxa C. Malvar, Martinho A. S. Martins, João P. Nunes, Peter R. Robichaud, and J. Jacob Keizer. Assessing the role of pre-fire ground preparation operations and soil water repellency in post-fire runoff and inter-rill erosion by repeated rainfall simulation experiments in Portuguese eucalypt plantations. *CATENA*, 108:69–83, September 2013.

[21] Peter R. Robichaud, Joseph W. Wagenbrenner, Fredrick B. Pierson, Kenneth E. Spaeth, Louise E. Ashmun, and Corey A. Moffet. Infiltration and interrill erosion rates after a wildfire in western Montana, USA. *CATENA*, 142:77–88, July 2016.

[22] Xu Jiongxin. Precipitation-vegetation coupling and its influence on erosion on the Loess Plateau, China. *CATENA*, November 2005.

[23] Ji Zhou, Bojie Fu, Guangyao Gao, Yihe Lü, Yu Liu, Nan Lü, and Shuai Wang. Effects of precipitation and restoration vegetation on soil erosion in a semi-arid environment in the Loess Plateau, China. *CATENA*, 137:1–11, February 2016.

[24] Kelin X. Whipple. The influence of climate on the tectonic evolution of mountain belts. *Nature Geoscience*, 2(2):97–104, February 2009.

[25] R. Allan Freeze and R. L. Harlan. Blueprint for a physically-based, digitally-simulated hydrologic response model. *Journal of Hydrology*, 9(3):237 – 258, 1969.

[26] Reed M. Maxwell, Mario Putti, Steven Meyerhoff, Jens-Olaf Delfs, Ian M. Ferguson, Valeriy Ivanov, Jongho Kim, Olaf Kolditz, Stefan J. Kollet, Mukesh Kumar, Sonya Lopez, Jie Niu, Claudio Paniconi, Young-Jin Park, Mantha S. Phanikumar, Chaopeng Shen, Edward A. Sudicky, and Mauro Sulis. Surface-subsurface model intercomparison: A first set of benchmark results to diagnose integrated hydrology and feedbacks. *Water Resources Research*, 50(2):1531–1549, February 2014.

[27] G. Gottardi and M. Venutelli. A control-volume finite-element model for two-dimensional overland flow. *Advances in Water Resources*, 16(5):277 – 284, 1993.

[28] Q. Li, A. J. A. Unger, E. A. Sudicky, D. Kassenaar, E. J. Wexler, and S. Shikaze. Simulating the multi-seasonal response of a large-scale watershed with a 3d physically-based hydrologic model. *Journal of Hydrology*, 357(3–4):317–336, August 2008.

[29] R. Therrien and E. A. Sudicky. Three-dimensional analysis of variably-saturated flow and solute transport in discretely-fractured porous media. *Journal of Contaminant Hydrology*, 23(1):1–44, June 1996.

[30] Sorab Panday, Peter S. Huyakorn, Rene Therrien, and Ralph L. Nichols. Improved three-dimensional finite-element techniques for field simulation of variably saturated flow and transport. *Journal of Contaminant Hydrology*, 12(12):3 – 33, 1993.

[31] Craig D. Allen, Alison K. Macalady, Haroun Chenchouni, Dominique Bachelet, Nate McDowell, Michel Vennetier, Thomas Kitzberger, Andreas Rigling, David D. Breshears, E. H. (Ted) Hogg, Patrick Gonzalez, Rod Fensham, Zhen Zhang, Jorge Castro, Natalia Demidova, Jong-Hwan Lim, Gillian Allard, Steven W. Running, Akkin Semerci, and Neil Cobb. A global overview of drought and heat-induced tree mortality reveals emerging climate change risks for forests. *Forest Ecology and Management*, 259(4):660–684, February 2010.

[32] A. P. Nicholas. Cellular modelling in fluvial geomorphology. *Earth Surf. Process. Landforms*, 2005.

[33] Keith Beven. How far can we go in distributed hydrological modelling? *Hydrology and Earth System Sciences Discussions*, 5(1):1–12, 2001.

[34] Keith Beven. Towards an alternative blueprint for a physically based digitally simulated hydrologic response modelling system. *Hydrological Processes*, 16(2):189–206, 2002.

[35] Gregory E. Tucker and Gregory R. Hancock. Modelling landscape evolution. *Earth Surface Processes and Landforms*, 35(1):28–50, January 2010.

[36] Peter Holmgren. Multiple flow direction algorithms for runoff modelling in grid based elevation models: An empirical evaluation. *Hydrological Processes*, 8(4):327–334, 1994.

[37] D. Collins, R. L. Bras, and G. E. Tucker. Modeling the effects of vegetation-erosion coupling on landscape evolution. *Journal of Geophysical Research: Earth Surface*, 109(F3), 2004.

[38] Peter B. Solyom and Gregory E. Tucker. Effect of limited storm duration on landscape evolution, drainage basin geometry, and hydrograph shapes. *Journal of Geophysical Research: Earth Surface*, 109(F3), 2004.

[39] Gregory E. Tucker, Nicole M. Gasparini, Rafael L. Bras, and Stephen T. Lancaster. A Stochastic Approach to Modeling Drainage Basin Evolution. *Water Resour. Res*, 36:1953–1964, 2000.

[40] Rebecca Doble, Philip Brunner, James McCallum, and Peter G. Cook. An Analysis of River Bank Slope and Unsaturated Flow Effects on Bank Storage. *Ground Water*, 50(1):77–86, 2012.

[41] Philip Brunner and Craig T. Simmons. HydroGeoSphere: A Fully Integrated, Physically Based Hydrological Model. *Ground Water*, 50(2):170–176, 2012.

[42] R. Therrien and E. A. Sudicky. Three-dimensional analysis of variably-saturated flow and solute transport in discretely-fractured porous media. *Journal of Contaminant Hydrology*, 23(1):1–44, June 1996.

[43] Svenja Bartsch, Sven Frei, Marianne Ruidisch, Christopher L. Shope, Stefan Peiffer, Bomchul Kim, and Jan H. Fleckenstein. River-aquifer exchange fluxes under monsoonal climate conditions. *Journal of Hydrology*, 509:601–614, February 2014.

[44] Jessica E. Liggett, Adrian D. Werner, and Craig T. Simmons. Influence of the first-order exchange coefficient on simulation of coupled surface–subsurface flow. *Journal of Hydrology*, 414-415:503–515, January 2012.

[45] Margaret Shanafield, James L McCallum, Peter G Cook, and Saskia Noorduijn. Variations on thermal transport modelling of subsurface temperatures using high resolution data. *Advances in Water Resources*, 89:1–9, March 2016.

[46] S. Frei and S. Peiffer. Exposure times rather than residence times control redox transformation efficiencies in riparian wetlands. *Journal of Hydrology*.

[47] L.A. Richards. CAPILLARY CONDUCTION OF LIQUIDS THROUGH POROUS MEDIUMS. *Physics*, November 1931.

[48] M. Th. van Genuchten. A Closed-form Equation for Predicting the Hydraulic Conductivity of Unsaturated Soils. *Soil Sci. Soc. Am. J.*, 44(5):892–898, 1980.

[49] Brian A. Ebel, Benjamin B. Mirus, Christopher S. Heppner, Joel E. VanderKwaak, and Keith Loague. First-order exchange coefficient coupling for simulating surface water groundwater interactions: parameter sensitivity and consistency with a physics-based approach. *Hydrological Processes*, 23(13):1949–1959, 2009.

[50] KJ KRISTENSEN and SE JENSEN. A model for estimating actual evapotranspiration from potential evapotranspiration. *Nordic Hydrology*, 6(3):170–188, 1975.

[51] Ruud P. Bartholomeus, Jan-Philip M. Witte, Peter M. van Bodegom, Jos C. van Dam, and Rien Aerts. Critical soil conditions for oxygen stress to plant roots: Substituting the Feddes-function by a process-based model. *Journal of Hydrology*, 360(1–4):147–165, October 2008.

[52] Richard G. Allen, William O. Pruitt, James L. Wright, Terry A. Howell, Francesca Ventura, Richard Snyder, Daniel Itenfisu, Pasquale Steduto, Joaquin Berengena, Javier Baselga Yrisarry, Martin Smith, Luis S. Pereira, Dirk Raes, Alain Perrier, Isabel Alves, Ivan Walter, and Ronald Elliott. *Agricultural Water Management*, 81(1–2):1–22, March 2006.

[53] Marcello Donatelli, Gianni Bellocchi, and Laura Carlini. Sharing knowledge via software components: Models on reference evapotranspiration. *European Journal of Agronomy*, 24(2):186–192, February 2006.

[54] Kell B Wilson, Paul J Hanson, Patrick J Mulholland, Dennis D Baldocchi, and Stan D Wullschleger. A comparison of methods for determining forest evapotranspiration and its components: sap-flow, soil water budget, eddy covariance and catchment water balance. *Agricultural and Forest Meteorology*, 106(2):153–168, January 2001.

[55] Jon D. Pelletier. *Quantitative Modeling of Earth Surface Processes*. Cambridge University Press, August 2008.

[56] Terence R. Smith and Francis P. Bretherton. Stability and the conservation of mass in drainage basin evolution. *Water Resources Research*, 1972.

[57] Joshua J. Roering, James W. Kirchner, and William E. Dietrich. Evidence for nonlinear, diffusive sediment transport on hillslopes and implications for landscape morphology. *Water Resources Research*, March 1999.

[58] E. Foufoula-Georgiou, V. Ganti, and W. E. Dietrich. A nonlocal theory of sediment transport on hillslopes. *Journal of Geophysical Research*, June 2010.

[59] John Wainwright and Mark Mulligan. *Environmental Modelling: Finding Simplicity in Complexity*. John Wiley & Sons, January 2013.

[60] Arjun M. Heimsath, William E. Dietrich, Kunihiko Nishiizumi, and Robert C. Finkel. The soil production function and landscape equilibrium. *Nature*, 388(6640):358–361, July 1997.

[61] Hafzullah Aksoy and Levent M. Kavvas. A review of hillslope and watershed scale erosion and sediment transport models. *25 Years of Assessment of Erosion*, December 2005.

[62] William E. Dietrich, Dino G. Bellugi, Leonard S. Sklar, Jonathan D. Stock, Arjun M. Heimsath, and Joshua J. Roering. Geomorphic transport laws for predicting landscape form and dynamics. In Peter R. Wilcock and Richard M. Iverson, editors, *Geophysical Monograph Series*, volume 135, pages 103–132. American Geophysical Union, Washington, D. C., 2003.

[63] Erkan Istanbulluoglu and Rafael L. Bras. On the dynamics of soil moisture, vegetation, and erosion: Implications of climate variability and change. *Water Resources Research*, 42(6), 2006.

[64] William E. Dietrich, Dino G. Bellugi, Leonard S. Sklar, Jonathan D. Stock, Arjun M. Heimsath, and Joshua J. Roering. *Geomorphic Transport Laws for Predicting Landscape form and Dynamics*. American Geophysical Union, 2013.

[65] J. Taylor Perron, William E. Dietrich, and James W. Kirchner. Controls on the spacing of first-order valleys. *Journal of Geophysical Research: Earth Surface*, 113(F4), 2008.

[66] Alan D. Howard. A detachment-limited model of drainage basin evolution. *Water Resources Research*, 30(7):2261–2285, 1994.

[67] Jon D. Pelletier. Fluvial and slope-wash erosion of soil-mantled landscapes: detachment- or transport-limited? *Earth Surface Processes and Landforms*, 37(1):37–51, 2012.

[68] M. Attal, G. E. Tucker, A. C. Whittaker, P. A. Cowie, and G. P. Roberts. Modeling fluvial incision and transient landscape evolution: Influence of dynamic channel adjustment. *Journal of Geophysical Research*, August 2008.

[69] Garry Willgoose. Mathematical Modeling of Whole Landscape Evolution. *Annual Review of Earth and Planetary Sciences*, 2005.

[70] Brian J. Yanites and Todd A. Ehlers. Global climate and tectonic controls on the denudation of glaciated mountains. *Earth and Planetary Science Letters*, 325-326:63–75, April 2012.

[71] Brian J. Yanites and Gregory E. Tucker. Controls and limits on bedrock channel geometry. *Journal of Geophysical Research F: Earth Surface*, 115(4), 2010.

[72] Jean Braun and Sean D. Willett. A very efficient O(n), implicit and parallel method to solve the stream power equation governing fluvial incision and landscape evolution. *Geomorphology*, 180-181:170–179, January 2013.

[73] Kelin X. Whipple and Gregory E. Tucker. Dynamics of the stream-power river incision model: Implications for height limits of mountain ranges, landscape response timescales, and research needs. *Journal of Geophysical Research: Solid Earth*, 104(B8):17661–17674, 1999.

[74] William B. Bull. Threshold of critical power in streams. *Geological Society of America Bulletin*, 90(5):453–464, 1979.

[75] Mitch D'Arcy and Alexander C. Whittaker. Geomorphic constraints on landscape sensitivity to climate in tectonically active areas. *Geomorphology*, 204:366–381, January 2014.

[76] Eric Kirby and Kelin Whipple. Quantifying differential rock-uplift rates via stream profile analysis. *Geology*, 29(5):415–418, May 2001.

[77] Dirk Scherler, Bodo Bookhagen, and Manfred R. Strecker. Tectonic control on 10be-derived erosion rates in the Garhwal Himalaya, India. *Journal of Geophysical Research: Earth Surface*, 119(2):2013JF002955, February 2014.

[78] Sean D. Willett. Orogeny and orography: The effects of erosion on the structure of mountain belts. *Journal of Geophysical Research: Solid Earth*, 1999.

[79] A. S. Abdul and R. W. Gillham. Laboratory Studies of the Effects of the Capillary Fringe on Streamflow Generation. *Water Resources Research*, 20(6):691–698, June 1984.

[80] Uli Maier, Matthias Flegr, Hermann Rügner, and Peter Grathwohl. Long-term solute transport and geochemical equilibria in seepage water and groundwater in a catchment cross section. *Environmental Earth Sciences*, 69(2):429–441, May 2013.

[81] Peter Grathwohl, Hermann Rügner, Thomas Wöhling, Karsten Osenbrück, Marc Schwientek, Sebastian Gayler, Ute Wollschläger, Benny Selle, Marion Pause, Jens-Olaf Delfs, Matthias Grzeschik, Ulrich Weller, Martin Ivanov, Olaf A. Cirpka, Ulrich Maier, Bertram Kuch, Wolfgang Nowak, Volker Wulfmeyer, Kirsten Warrach-Sagi, Thilo Streck, Sabine Attinger, Lars Bilke, Peter Dietrich, Jan H. Fleckenstein, Thomas Kalbacher, Olaf Kolditz, Karsten Rink, Luis Samaniego, Hans-Jörg Vogel, Ulrike Werban, and Georg Teutsch. Catchments as reactors: a comprehensive approach for water fluxes and solute turnover. *Environmental Earth Sciences*, 69(2):317–333, May 2013.

[82] Markus Kottek, Jürgen Grieser, Christoph Beck, Bruno Rudolf, and Franz Rubel. World map of the köppen-geiger climate classification updated. *Meteorologische Zeitschrift*, 15(3):259–263, 2006.

[83] Hermann Rugner, Marc Schwientek, Barbara Beckingham, Bertram Kuch, and Peter Grathwohl. Turbidity as a proxy for total suspended solids (TSS) and particle facilitated pollutant transport in catchments. *Environmental Earth Sciences*, 69(2):373–380, 2013.

[84] Marc Schwientek, Karsten Osenbruck, and Matthias Fleischer. Investigating hydrological drivers of nitrate export dynamics in two agricultural catchments in Germany using high-frequency data series. *Environmental Earth Sciences*, 69(2):381–393, 2013.

[85] Holger Frey and Frank Paul. On the suitability of the {SRTM} {DEM} and {ASTER} {GDEM}for the compilation of topographic parameters in glacier inventories. *International Journal of Applied Earth Observation and Geoinformation*, 18(0):480 – 490, 2012.

[86] GRASS Development Team. *Geographic Resources Analysis Support System (GRASS GIS) Software*. Open Source Geospatial Foundation, 2012.

[87] M. Neteler, M.H. Bowman, M. Landa, and M. Metz. GRASS GIS: a multi-purpose Open Source GIS. *Environmental Modelling and Software*, 31:124–130, 2011.

[88] Erkan Istanbulluoglu. An Eco-hydro-geomorphic Perspective to Modeling the Role of Climate in Catchment Evolution. *Geography Compass*, 3(3):1151–1175, 2009.

[89] Erkan Istanbulluoglu. Vegetation-modulated landscape evolution: Effects of vegetation on landscape processes, drainage density, and topography. *Journal of Geophysical Research*, 110(F2), 2005.

[90] Cameron W. Wobus, Gregory E. Tucker, and Robert S. Anderson. Does climate change create distinctive patterns of landscape incision? *Journal of Geophysical Research: Earth Surface*, 115(F4):n/a–n/a, 2010.

[91] Brian J. Yanites and Todd A. Ehlers. Global climate and tectonic controls on the denudation of glaciated mountains. *Earth and Planetary Science Letters*, 325-326:63–75, April 2012.

[92] Brent J. Zaprowski, Frank J. Pazzaglia, and Edward B. Evenson. Climatic influences on profile concavity and river incision. *Journal of Geophysical Research*, pages 10–1029, 2005.

[93] Peter Molnar, Robert S. Anderson, Grant Kier, and John Rose. Relationships among probability distributions of stream discharges in floods, climate, bed load transport, and river incision. *Journal of Geophysical Research: Earth Surface*, 111(F2), 2006.

[94] M. Louise Jeffery, Todd A. Ehlers, Brian J. Yanites, and Christopher J. Poulsen. Quantifying the role of paleoclimate and Andean Plateau uplift on river incision. *Journal of Geophysical Research: Earth Surface*, 118(2):852–871, 2013.

[95] Karen Hartshorn, Niels Hovius, W. Brian Dade, and Rudy L. Slingerland. Climate-Driven Bedrock Incision in an Active Mountain Belt. *Science*, 297(5589):2036–2038, 2002.

[96] J. V. Waters, S. J. Jones, and H. A. Armstrong. Climatic controls on late Pleistocene alluvial fans, Cyprus. *Geomorphology*, 2010.

[97] D. Lague. Reduction of long-term bedrock incision efficiency by short-term alluvial cover intermittency. *Journal of Geophysical Research: Earth Surface*, 115(F2):n/a–n/a, 2010.

[98] Erkan Istanbulluoglu. Modeling Catchment Evolution: From Decoding Geomorphic Processes Signatures toward Predicting Impacts of Climate Change. *Geography Compass*, 3(3):1125–1150, 2009.

[99] M. C. Quigley, M. Sandiford, and M. L. Cupper. Distinguishing tectonic from climatic controls on range-front sedimentation. *Basin Research*, 19(4):491–505, 2007.

[100] Ignacio Rodŕiguez-Iturbe and Juan B. Valdés. The geomorphologic structure of hydrologic response. *Water Resources Research*, 15(6):1409–1420, 1979.

[101] Ignacio Rodriguez-Iturbe, Marcelo Gonzalez-Sanabria, and Rafael L. Bras. A geomorphoclimatic theory of the instantaneous unit hydrograph. *Water Resources Research*, 18(4):877–886, 1982.

[102] On the effects of small scale space–time variability of rainfall on basin flood response. *Journal of Hydrology*, 514(0):313 – 327, 2014.

[103] L. Nicótina, E. Alessi Celegon, A. Rinaldo, and M. Marani. On the impact of rainfall patterns on the hydrologic response. *Water Resources Research*, 44(12), 2008.

[104] Efthymios I. Nikolopoulos, Emmanouil N. Anagnostou, Marco Borga, Enrique R. Vivoni, and Anastasios Papadopoulos. Sensitivity of a mountain basin flash flood to initial wetness condition and rainfall variability. *Journal of Hydrology*, 402(3-4):165 – 178, 2011.

[105] Erwin Zehe, Rolf Becker, András Bárdossy, and Erich Plate. Uncertainty of simulated catchment runoff response in the presence of threshold processes: Role of initial soil moisture and precipitation. *Journal of Hydrology*, 315(1-4):183 – 202, 2005.

[106] Peter S. Eagleson. Climate, soil, and vegetation: 2. The distribution of annual precipitation derived from observed storm sequences. *Water Resources Research*, 14(5):713–721, 1978.

[107] Ipcc. *IPCC Fourth Assessment Report: Working Group II Report "Impacts, Adaptation and Vulnerability"*. Cambridge University Press, 2007.

[108] A Burton, V Glenis, M.A. Jones, and C.G. Kilsby. Models of daily rainfall cross-correlation for the United Kingdom. *Environmental Modelling & Software*, 49(0):22 – 33, 2013.

[109] A Burton, C.G. Kilsby, H.J. Fowler, P.S. Cowpertwait, and P.E. OConnell. RainSim: A spatial temporal stochastic rainfall modelling system. *Environmental Modelling & Software*, 23(12):1356 – 1369, 2008.

[110] Gregory E. Tucker and Rudy Slingerland. Drainage basin responses to climate change. *Water Resources Research*, 33(8):2031–2047, 1997.

[111] Antonio Francipane, Valeriy Ivanov, Leonardo V. Noto, Erkan Istanbulluoglu, Elisa Arnone, and Rafael L. Bras. tRIBS-Erosion: A parsimonious physically-based model for studying catchment hydro-geomorphic response. {*CATENA*}, 92(0):216 – 231, 2012.

[112] Roman A. DiBiase and Michael P. Lamb. Vegetation and wildfire controls on sediment yield in bedrock landscapes: SEDIMENT STORAGE BEHIND VEGETATION DAMS. *Geophysical Research Letters*, 40(6):1093–1097, March 2013.

[113] Omer Yetemen, Erkan Istanbulluoglu, J. Homero Flores-Cervantes, Enrique R. Vivoni, and Rafael L. Bras. Ecohydrologic role of solar radiation on landscape evolution. *Water Resources Research*, 51(2):1127–1157, February 2015.

[114] A. Jordán and L. Martínez-Zavala. Soil loss and runoff rates on unpaved forest roads in southern Spain after simulated rainfall. *Forest Ecology and Management*, 255(3–4):913–919, March 2008.

[115] N. Romano, G. D'Urso, G. Severino, G. B. Chirico, M. Palladino, and Donatella Termini. Four Decades of Progress in Monitoring and Modeling of Processes in the Soil-Plant-Atmosphere System: Applications and ChallengesEffect of Vegetation on Fluvial Erosion Processes: Experimental Analysis in a Laboratory Flume. *Procedia Environmental Sciences*, 19:904–911, January 2013.

[116] Thomas Dunne, Weihua Zhang, and Brian F. Aubry. Effects of rainfall, vegetation, and microtopography on infiltration and runoff. *Water Resources Research*, 27(9):2271–2285, 1991.

[117] Christopher S. Heppner, Keith Loague, and Joel E. VanderKwaak. Long-term InHM simulations of hydrologic response and sediment transport for the R-5 catchment. *Earth Surface Processes and Landforms*, 32(9):1273–1292, August 2007.

[118] Christopher S. Heppner, Qihua Ran, Joel E. VanderKwaak, and Keith Loague. Adding sediment transport to the integrated hydrology model (InHM): Development and testing. *Advances in Water Resources*, 29(6):930–943, June 2006.

[119] Keith Loague, Christopher S. Heppner, Benjamin B. Mirus, Brian A. Ebel, Qihua Ran, Adrianne E. Carr, Susan H. BeVille, and Joel E. VanderKwaak. Physics-based hydrologic-response simulation: foundation for hydroecology and hydrogeomorphology. *Hydrological Processes*, 20(5):1231–1237, March 2006.

[120] Benjamin B. Mirus, Brian A. Ebel, Christopher S. Heppner, and Keith Loague. Assessing the detail needed to capture rainfall-runoff dynamics with physics-based hydrologic response simulation. *Water Resources Research*, 47(3):W00H10, March 2011.

[121] Qihua Ran, Christopher S. Heppner, Joel E. VanderKwaak, and Keith Loague. Further testing of the integrated hydrology model (InHM): multiple-species sediment transport. *Hydrological Processes*, 21(11):1522–1531, May 2007.

[122] Tom Gleeson, Lars Marklund, Leslie Smith, and Andrew H. Manning. Classifying the water table at regional to continental scales. *Geophysical Research Letters*, 38(5):L05401, March 2011.

[123] W. B. Langbein and S. A. Schumm. Yield of sediment in relation to mean annual precipitation. *Eos, Transactions American Geophysical Union*, 39(6):1076–1084, 1958.

[124] R. Allan Freeze. A stochastic-conceptual analysis of rainfall-runoff processes on a hillslope. *Water Resources Research*, 16(2):391–408, 1980.

[125] Joel E. VanderKwaak and Keith Loague. Hydrologic-Response simulations for the R-5 catchment with a comprehensive physics-based model. *Water Resources Research*, 37(4):999–1013, April 2001.

[126] Markus Kottek, Jürgen Grieser, Christoph Beck, Bruno Rudolf, and Franz Rubel. World Map of the Köppen-Geiger climate classification updated. *Meteorologische Zeitschrift*, 15(3):259–263, June 2006.

[127] Piedad M. Cristiano, Paula I. Campanello, Sandra J. Bucci, Sabrina A. Rodriguez, Oscar A. Lezcano, Fabian G. Scholz, Nora Madanes, Débora Di Francescantonio, Laureano Oliva Carrasco, Yong-Jiang Zhang, and Guillermo Goldstein. Evapotranspiration of subtropical forests and tree plantations: A comparative analysis at different temporal and spatial scales. *Agricultural and Forest Meteorology*, 203:96–106, April 2015.

[128] J. B. Stewart. Evaporation from the wet canopy of a pine forest. *Water Resources Research*, 13(6):915–921, December 1977.

[129] Kell B Wilson, Paul J Hanson, Patrick J Mulholland, Dennis D Baldocchi, and Stan D Wullschleger. A comparison of methods for determining forest evapotranspiration and its components: sap-flow, soil water budget, eddy covariance and catchment water balance. *Agricultural and Forest Meteorology*, 106(2):153–168, January 2001.

[130] Cornelissen Thomas, DiekkrÃŒger Bernd, and Bogena Heye. Using HydroGeoSphere in a Forested Catchment: How does Spatial Resolution Influence the Simulation of Spatio-temporal Soil Moisture Variability. *Procedia Environmental Sciences*, 2013.

[131] Michael P. Lamb, Mariya Levina, Roman A. DiBiase, and Brian M. Fuller. Sediment storage by vegetation in steep bedrock landscapes: Theory, experiments, and implications for postfire sediment yield: SEDIMENT STORAGE IN BEDROCK LANDSCAPES. *Journal of Geophysical Research: Earth Surface*, 118(2):1147–1160, June 2013.

[132] Francesco Ciocca, Ivan Lunati, and Marc B. Parlange. Effects of the water retention curve on evaporation from arid soils. *Geophysical Research Letters*, 41(9):3110–3116, 2014.

[133] Brian A. Ebel, Keith Loague, and Ronaldo I. Borja. The impacts of hysteresis on variably saturated hydrologic response and slope failure. *Environmental Earth Sciences*, 61(6):1215–1225, April 2010.

[134] Tomomi Kumagai, Makiko Tateishi, Yoshiyuki Miyazawa, Masahiro Kobayashi, Natsuko Yoshifuji, Hikaru Komatsu, and Takanori Shimizu. Estimation of annual forest evapotranspiration from a coniferous plantation watershed in japan (1): Water use components in japanese cedar stands. *Journal of Hydrology*, 508:66 – 76, 2014.

[135] Chandra Prasad Ghimire, Maciek W. Lubczynski, L. Adrian Bruijnzeel, and Diana Chavarro-RincÃ³n. Transpiration and canopy conductance of two contrasting forest types in the Lesser Himalaya of Central Nepal. *Agricultural and Forest Meteorology*, 197:76–90, October 2014.

[136] Josie Geris, Doerthe Tetzlaff, Jeffrey McDonnell, and Chris Soulsby. The relative role of soil type and tree cover on water storage and transmission in northern headwater catchments. *Hydrological Processes*, 29(7):1844–1860, March 2015.

[137] Xuan Yu, Anna Lama¡, Christopher Duffy, Pavel Kraim, and Jakub Hrus¡ka. Hydrological model uncertainty due to spatial evapotranspiration estimation methods. *Computers & Geosciences*, 90, Part B:90–101, May 2016.

[138] Q. Li, A.J.A. Unger, E.A. Sudicky, D. Kassenaar, E.J. Wexler, and S. Shikaze. Simulating the multi-seasonal response of a large-scale watershed with a 3d physically-based hydrologic model. *Journal of Hydrology*, 357(3-4):317–336, August 2008.

[139] David D. Bosch, Laura K. Marshall, and Robert Teskey. Forest transpiration from sap flux density measurements in a Southeastern Coastal Plain riparian buffer system. *Agricultural and Forest Meteorology*, 187:72–82, April 2014.

[140] Kate A Brauman, David L Freyberg, and Gretchen C Daily. Potential evapotranspiration from forest and pasture in the tropics: A case study in kona, hawai'i. *Journal of Hydrology*, 440–441:52 – 61, 2012.

[141] Piedad M. Cristiano, Paula I. Campanello, Sandra J. Bucci, Sabrina A. Rodriguez, Oscar A. Lezcano, Fabian G. Scholz, Nora Madanes, Débora Di Francescantonio, Laureano Oliva Carrasco, Yong-Jiang Zhang, and Guillermo Goldstein. Evapotranspiration of subtropical forests and tree plantations: A comparative analysis at different temporal and spatial scales. *Agricultural and Forest Meteorology*, 203:96–106, April 2015.

[142] C. Anthony Federer and Douglas Lash. *BROOK: a hydrologic simulation model for eastern forests.* Water Resource Research Center, University of New Hampshire, Durham, N.H., 1978.

[143] J. Canadell, R. B. Jackson, J. B. Ehleringer, H. A. Mooney, O. E. Sala, and E.-D. Schulze. Maximum rooting depth of vegetation types at the global scale. *Oecologia*, 108(4):583–595, 1996.

[144] R. Therrien and E. A. Sudicky. Three-dimensional analysis of variably-saturated flow and solute transport in discretely-fractured porous media. *Journal of Contaminant Hydrology*, 23(12):1 – 44, 1996.

[145] Benjamin B. Mirus and Keith Loague. How runoff begins (and ends): Characterizing hydrologic response at the catchment scale. *Water Resources Research*, 49(5):2987–3006, May 2013.

[146] R. Therrien, R. G. McLaren, E. A. Sudicky, and S. M. Panday. HydroGeoSphere: a three-dimensional numerical model describing fully-integrated subsurface and surface flow and solute transport. *Groundwater Simulations Group, University of Waterloo, Waterloo, ON*, 2010.

[147] Daniel Nepstad, Georgia Carvalho, Ana Cristina Barros, Ane Alencar, João Paulo Capobianco, Josh Bishop, Paulo Moutinho, Paul Lefebvre, Urbano Lopes Silva Jr., and Elaine Prins. Road paving, fire regime feedbacks, and the future of Amazon forests. *Forest Ecology and Management*, 154(3):395–407, December 2001.

[148] Sibyll Schaphoff, Wolfgang Lucht, Dieter Gerten, Stephen Sitch, Wolfgang Cramer, and I. Colin Prentice. Terrestrial biosphere carbon storage under alternative climate projections. *Climatic Change*, 74(1-3):97–122, January 2006.

[149] Gregory K. Gould, Mingliang Liu, Michael E. Barber, Keith A. Cherkauer, Peter R. Robichaud, and Jennifer C. Adam. The effects of climate change and extreme wildfire events on runoff erosion over a mountain watershed. *Journal of Hydrology*, 536:74–91, May 2016.

[150] R.j. Fensham and R.j. Fairfax. Drought-related tree death of savanna eucalypts: Species susceptibility, soil conditions and root architecture. *Journal of Vegetation Science*, 18(1):71–80, February 2007.

[151] Lee E. Brown, Joseph Holden, Sheila M. Palmer, Kerrylyn Johnston, Sorain J. Ramchunder, and Richard Grayson. Effects of fire on the hydrology, biogeochemistry, and ecology of peatland river systems. *Freshwater Science*, 34(4):1406–1425, November 2015.

[152] Jane G. Cawson, Petter Nyman, Hugh G. Smith, Patrick N. J. Lane, and Gary J. Sheridan. How soil temperatures during prescribed burning affect soil water repellency, infiltration and erosion. *Geoderma*, 278:12–22, September 2016.

[153] J. G. Cawson, G. J. Sheridan, H. G. Smith, and P. N. J. Lane. Effects of fire severity and burn patchiness on hillslope-scale surface runoff, erosion and hydrologic connectivity in a prescribed burn. *Forest Ecology and Management*, 310:219–233, December 2013.

[154] R. B. Foltz and N. S. Wagenbrenner. An evaluation of three wood shred blends for post-fire erosion control using indoor simulated rain events on small plots. *CATENA*, 80(2):86–94, February 2010.

[155] Jesús S. Notario del Pino and José-Reyes Ruiz-Gallardo. Modelling post-fire soil erosion hazard using ordinal logistic regression: A case study in South-eastern Spain. *Geomorphology*, 232:117–124, March 2015.

[156] N. Kettridge, R. E. Humphrey, J. E. Smith, M. C. Lukenbach, K. J. Devito, R. M. Petrone, and J. M. Waddington. Burned and unburned peat water repellency: Implications for peatland evaporation following wildfire. *Journal of Hydrology*, 513:335–341, May 2014.

[157] Peter R. Robichaud, Sarah A. Lewis, Joseph W. Wagenbrenner, Louise E. Ashmun, and Robert E. Brown. Post-fire mulching for runoff and erosion mitigation: Part I: Effectiveness at reducing hillslope erosion rates. *CATENA*, 105:75–92, June 2013.

[158] Vinod Mahat, Uldis Silins, and Axel Anderson. Effects of wildfire on the catchment hydrology in southwest Alberta. *CATENA*, 147:51–60, December 2016.

[159] D. C. S. Vieira, C. Fernández, J. A. Vega, and J. J. Keizer. Does soil burn severity affect the post-fire runoff and interrill erosion response? A review based on meta-analysis of field rainfall simulation data. *Journal of Hydrology*, 523:452–464, April 2015.

[160] Maria Cristina Rulli, Silvia Bozzi, Matteo Spada, Daniele Bocchiola, and Renzo Rosso. Rainfall simulations on a fire disturbed mediterranean area. *Journal of Hydrology*, 327(3–4):323–338, August 2006.

[161] Maria Rosa Darrigo, Eduardo Martins Venticinque, and Flavio Antonio Maës dos Santos. Effects of reduced impact logging on the forest regeneration in the central Amazonia. *Forest Ecology and Management*, 360:52–59, January 2016.

[162] Roberto Cazzolla Gatti, Simona Castaldi, Jeremy A. Lindsell, David A. Coomes, Marco Marchetti, Mauro Maesano, Arianna Di Paola, Francesco Paparella, and Riccardo Valentini. The impact of selective logging and clearcutting on forest structure, tree diversity and above-ground biomass of African tropical forests. *Ecological Research*, 30(1):119–132, December 2014.

[163] Yong Lin and Xiaohua Wei. The impact of large-scale forest harvesting on hydrology in the Willow watershed of Central British Columbia. *Journal of Hydrology*, 359(12):141–149, September 2008.

[164] David Costantini, David P. Edwards, and Mirre J. P. Simons. Life after logging in tropical forests of Borneo: A meta-analysis. *Biological Conservation*, 196:182–188, April 2016.

[165] David W. Peterson and Erich Kyle Dodson. Post-fire logging produces minimal persistent impacts on understory vegetation in northeastern Oregon, USA. *Forest Ecology and Management*, 370:56–64, June 2016.

[166] GR Hancock, JBC Lowry, TJ Coulthard, KG Evans, and DR Moliere. A catchment scale evaluation of the SIBERIA and CAESAR landscape evolution models. *Earth Surface Processes and Landforms*, 35(8):863–875, 2010.

[167] Robert E. Horton. The role of infiltration in the hydrologic cycle. *Eos, Transactions American Geophysical Union*, 14(1):446–460, June 1933.

[168] Keith Beven and Jim Freer. A dynamic TOPMODEL. *Hydrological Processes*, 15(10):1993–2011, July 2001.

[169] A Routschek, J Schmidt, and F. Kreienkamp. Impact of climate change on soil erosion — A high-resolution projection on catchment scale until 2100 in Saxony/Germany. {*CATENA*}, 121(0):99 – 109, 2014.

[170] Erkan Istanbulluoglu, Omer Yetemen, Enrique R. Vivoni, Hugo A. Gutiérrez-Jurado, and Rafael L. Bras. Eco-geomorphic implications of hillslope aspect: Inferences from analysis of landscape morphology in central New Mexico. *Geophysical Research Letters*, 35(14):L14403, July 2008.

[171] Javier H. Flores Cervantes, Erkan Istanbulluoglu, Enrique R. Vivoni, Chandra D. Holifield Collins, and Rafael L. Bras. A geomorphic perspective on terrain-modulated organization of vegetation productivity: analysis in two semiarid grassland ecosystems in Southwestern United States. *Ecohydrology*, 7(2):242–257, April 2014.

[172] Fortunat Joos, I. Colin Prentice, Stephen Sitch, Robert Meyer, Georg Hooss, Gian-Kasper Plattner, Stefan Gerber, and Klaus Hasselmann. Global warming feedbacks on terrestrial carbon uptake under the Intergovernmental Panel on Climate Change (IPCC) Emission Scenarios. *Global Biogeochemical Cycles*, 15(4):891–907, December 2001.

[173] C. Fernández, J. A. Vega, T. Fonturbel, P. Pérez-Gorostiaga, E. Jiménez, and J. R. Pérez. Runoff and soil erosion after rainfall simulations in burned soils. *Forest Ecology and Management*, 234, Supplement:S191, November 2006.

[174] Peter R. Robichaud, Sarah A. Lewis, Joseph W. Wagenbrenner, Louise E. Ashmun, and Robert E. Brown. Post-fire mulching for runoff and erosion mitigation: Part I: Effectiveness at reducing hillslope erosion rates. *CATENA*, 105:75–92, June 2013.

[175] Maria Cristina Rulli, Silvia Bozzi, Matteo Spada, Daniele Bocchiola, and Renzo Rosso. Rainfall simulations on a fire disturbed mediterranean area. *Journal of Hydrology*, 327(3–4):323–338, August 2006.